Impact of partial nitrogen and fluorine substitution on the interface properties of π-conjugated molecules adsorbed on inorganic substrates

A combined photoelectron-spectroscopy and X-ray-standing-waves study

Dissertation
der Mathematisch-Naturwissenschaftlichen Fakultät
der Eberhard Karls Universität Tübingen
zur Erlangung des Grades eines
Doktors der Naturwissenschaften
(Dr. rer. nat.)

vorgelegt von
Antoni Franco Cañellas
aus
Manresa, Spanien

Tübingen
2017

Gedruckt mit Genehmigung der Mathematisch-Naturwissenschaftlichen Fakultät der Eberhard Karls Universität Tübingen.

Tag der mündlichen Qualifikation:	24.04.2018
Dekan:	Prof. Dr. Wolfgang Rosenstiel
1. Berichterstatter:	Prof. Dr. Frank Schreiber
2. Berichterstatter:	Prof. Dr. Martin Oettel
3. Berichterstatter:	Dr. Jörg Zegenhagen

Abstract

Organic semiconductors are carbon-based materials with promising features aimed at substituting and/or complementing their inorganic counterparts (e.g. silicon, germanium or gallium arsenide). They can be cheaply mass-produced, they are flexible and their properties can be chemically tuned, all attractive characteristics for the consumer-electronics market. In recent years, remarkable progress has been made and one can already buy smartphones and TVs equipped with organic LEDs. Also, interesting prototypes of roll-up organic solar cells have been presented. Nonetheless, the real breakthrough for these materials is yet to come since fundamental aspects regarding the charge transport through metal electrodes (among others), important for the device circuitry, still limit the overall efficiency. In this context, the energy-level alignment (ELA) between the molecules and the electrode determines the charge injection/extraction energy barriers and, therefore, is responsible for an optimum charge transfer across the interface. A proper rationalization of the ELA requires a full description of the interface properties: electronic, chemical as well as structural, including adsorption distances and molecular distortions. Chemical functionalization of polymers or small molecules by adding side groups with strong electron donor or acceptor behavior has been a way to optimize the ELA. In this work, we employ element-specific techniques such as X-ray photoelectron spectroscopy (XPS) and X-ray standing waves (XSW) to infer how partial nitrogen and fluorine substitution in prototypical and well studied π-conjugated organic molecules affects the geometrical, chemical and electronic properties of these when deposited on metal single-crystal substrates with different reactivities. We show that the combination of high-resolution XPS with XSW is a powerful method to tackle this issue since the adsorption distance and molecular distortion can be readily connected to feature changes in the XP spectra. In particular, we deposit several perylene and pentacene derivatives on different metal and semiconductor surfaces, namely the (111) surface of gold, silver and copper and the polar surfaces (000$\pm$1) of zinc oxide (ZnO). Finally, we also show that this method can be extended successfully to study the evolution of the bare ZnO surface under different treatments in real-time. ZnO is a promising transparent inorganic semiconductor that can be engineered easily in different nanostructures. Its polar surfaces represent a conundrum, as the actual composition and conformation of the surface are still a topic of debate. Having extracted the chemical and structural information with a combination of XPS and XSW, we provide new results about the surface and its respective behavior under different treatment conditions.

Recorda d'on véns, per saber on vas.
Aquest treball va dedicat a tots els que m'han ajudat a arribar fins aquí

Contents

I. Introduction **13**

1. Motivation and outline **15**

2. Fundamental concepts: the inorganic-organic interface **19**
2.1. π-conjugated systems . . . 19
2.2. Interface energetics involving π-conjugated systems . . . 20
2.3. Beyond the monolayer coverage . . . 25
2.3.1. Growth modes . . . 25
2.3.2. Intermolecular forces . . . 26
2.4. Beyond the metal-organic interface . . . 27

3. Experimental methods and techniques **29**
3.1. Sample preparation . . . 29
3.1.1. Organic molecular beam deposition . . . 29
3.1.2. Substrate cleaning and preparation . . . 30
3.2. Photoelectron spectroscopy (PES) . . . 31
3.2.1. X-ray photoelectron spectroscopy (XPS) . . . 34
3.2.2. Ultraviolet photoelectron spectroscopy (UPS) . . . 37
3.3. The X-ray standing wave technique (XSW) . . . 39
3.3.1. Fundamentals of the technique . . . 40
3.3.2. Practical and technical considerations and data analysis . . . 45
3.4. Low-energy electron diffraction (LEED) . . . 48
3.5. Experimental setup . . . 50
3.5.1. The I09 beamline at the Diamond Light Source (DLS) . . . 50
3.5.2. Setup at Soochow University . . . 50

4. Materials **53**
4.1. Organic compounds . . . 53
4.2. Single-crystal substrates . . . 55
4.2.1. Coinage metals . . . 55
4.2.2. Zinc oxide (ZnO) . . . 57

II. Results and discussion **65**

5. Perylene adsorbed on coinage metals **67**
5.1. Context . . . 67

5.2. Results . . . 67
5.3. Discussion . . . 69
5.4. Conclusions . . . 70

6. PTCDI adsorbed on coinage metals 71
6.1. Context . . . 71
6.2. Results . . . 73
6.2.1. Coverage-dependent XPS and UPS . . . 73
6.2.2. High-resolution XPS of (sub)monolayer coverages . . . 77
6.2.3. LEED measurements . . . 82
6.2.4. XSW results: adsorption heights and molecular distortion . . . 83
6.3. Discussion . . . 86
6.4. Conclusions . . . 90

7. F4PEN adsorbed on coinage metals 93
7.1. Context . . . 93
7.2. Results . . . 94
7.2.1. Coverage dependent XPS and UPS . . . 94
7.2.2. High-resolution XPS of (sub)monolayer coverages . . . 100
7.2.3. LEED measurements . . . 103
7.2.4. XSW results: adsorption heights and molecular distortions . . . 104
7.3. Discussion . . . 108
7.3.1. Effect of the substrate . . . 108
7.3.2. Comparison with PEN and PFP . . . 108
7.4. Conclusions . . . 110

8. Characterization of the ZnO polar surfaces 113
8.1. Preparation of the ZnO substrates . . . 113
8.2. Characterization of the ZnO surfaces . . . 114
8.2.1. Surfaces prepared with the Standard Treatment . . . 115
8.2.2. Surfaces under different preparation conditions . . . 120
8.3. Discussion . . . 131
8.3.1. Influence of the termination on the bare surface properties . . . 131
8.3.2. Influence of the annealing and the sputtering to the surface . . . 132
8.3.3. Influence of a water overlayer . . . 134
8.4. Conclusions . . . 135

9. Perylene derivatives adsorbed on the polar surfaces of ZnO 137
9.1. Context . . . 137
9.2. Results . . . 138
9.2.1. Perylene derivatives adsorbed on the standard-treated O-ZnO surface 138
9.2.2. PTCDI adsorbed on the standard-treated Zn-ZnO surface . . . 147
9.2.3. Adsorption of PTCDI under different substrate conditions . . . 149
9.3. Discussion . . . 155
9.3.1. Influence of the functional groups . . . 156
9.3.2. Influence of the surface termination and preparation . . . 157

9.4. Conclusions 158

III. Summary and outlook **161**

10. Summary **163**

11. Outlook **167**

IV. Appendix **169**

A. XSW study of TAT deposited on the coinage metals **171**

B. F4PEN: beam-damage tests and additional measurements **173**

C. XSW study of PTCDA adsorbed on PbS **179**

D. Refinement of the O 1s core-level fitting model of O-ZnO **181**

E. F6TCNNQ adsorbed on the polar surfaces of ZnO **183**

F. Angular-dependent XSW analysis. Probing different depths **189**

G. Molecular bilayers and heterostructures investigated with XSW **193**

H. XSW measurements at KMC-1 beamline (BESSY II). Test beamtime **199**

I. Improvements of the triple-cell evaporator **201**

Bibliography **209**

Acronyms **254**

Publications **257**

Zusammenfassung **258**

Acknowledgements **261**

Part I.

Introduction

1. Motivation and outline

The Information Age [1] skyrocketed when the Internet and personal computers were made available and affordable for the broad public and got a decisive boost with the break of smartphones into the electronics market. However, this is still the beginning since concepts such as "Internet of Things", "Smart Grids" or "Domotics" are becoming increasingly popular. Along with the globalization of the economy and hyperconnection of essentially everything, concerns about the long- and mid-term sustainability of this growth model have brought up fundamental questions regarding the energy sources that are going to *fuel* this new era. During the last few decades, green and renewable energy sources have attracted paramount scientific and political attention. Huge efforts and hopes are devoted to Big-Science projects such as nuclear fusion [2] for a clean, *endless* energy source and quantum-based computers as the natural way to overcome the classical limits of transistor downscaling [3]. But these are long term solutions, if any at all.

At the core of this new age are semiconductor-based devices. It is thus clear that, in the short and midterm, further elaborations and breakthroughs will go along with improvements to these devices and their fundamental components. New materials and combinations thereof have laid the pathway to follow. This approach was already applied in the early years of the inorganic-semiconductor industry, where systems made of different chemical elements were first studied (for instance, gallium and arsenide, GaAs, or gallium and nitrogen GaN [4]), nowadays ubiquitous in commercial devices. Within this context, organic semiconductor (OSCs) materials appeared as an alternative and/or a complement to the traditional inorganic semiconductors. OSCs are carbon-based materials, mostly polymers [5] or small molecules [6–8] that contain a repeating carbon aromatic ring made of alternating single and double bonds that leave the perpendicular π-orbitals unaffected. This yields a delocalized π-electron system along the whole structure (see Sec. [2.1]). Organic light emitting diodes (OLEDs), field-effect transistors (OFETs) [9–11] and organic solar cells (OSC) [5, 9, 12], among others [13], have generated a fruitful field of study since the first semiconductor properties for a carbon-based material were reported [14]. The main advantages shown for organic materials are [15]:

- High chemical tunability.
- Low cost.
- Easier industrial production scaling.
- Mechanical flexibility [16].
- Biocompatibility.
- High exciton binding energies.

Of course, they also have some drawbacks especially regarding low crystallinity [17], low charge-carrier mobilities [11] and degradation [18, 19]. These issues have been the focus of most of the applied research carried out in the last decades. In addition, fundamental questions appeared when the theoretical framework used in the description of inorganic semiconductors and their interfaces did not hold for the organic case [20]. Thus, intense

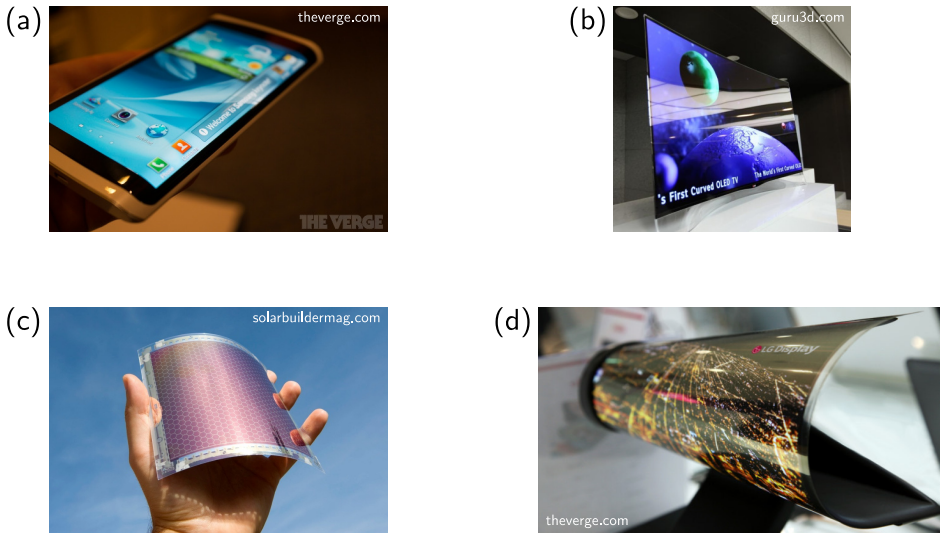

Figure 1.1.: Different devices employing organic semiconductors, being (a) and (b) commercially available and (c) and (d) just prototypes. (a) Smartphone equipped with an OLED screen with curved edges. (b) Curved TV with an OLED screen. (c) Prototype of a curved OPV cell. (d) Prototype of a curved display.

research was devoted to the understanding of the physics governing organic semiconductor materials, especially their interaction with metal electrodes [21–24] and the so-called energy-level alignment (ELA) [20, 25]. Despite these challenges, organic-based electronic devices are already commercially available with different degrees of penetration in the mainstream market. The most prominent examples are smartphones and TV with OLED screens [26] (see Fig. [1.1]). Nonetheless, the biggest commercial breakthrough is yet to come [27].

A key issue is the device efficiency, which, in most of the cases, has to do with charge separation, recombination, transport and/or transfer across an interface. It was already evident at the dawn of inorganic-semiconductor-based devices that interfaces have a central role [28], and it is even more true for organic-based devices, where the combination of different materials with complementary properties, such as charge-donor-like and -acceptor-like compounds, is a common approach to mitigate the shortcomings of single-component active materials [29]. Indeed, bicomponent systems at the (sub)monolayer [30, 31] as well as in the thin-film [32] regime have attracted remarkable interest. Moreover, the combination of an organic material with an inorganic counterpart, either as a doping mechanism [33, 34] or as a full hybrid system, further improves their capabilities [35]. It is thus clear that, either between two organic materials or between an organic and an inorganic one, interfaces are everywhere. In all cases, though, the necessary circuitry inherent to any electronic device introduces yet another interface between an (or several) organic material and a metal contact. This case is particularly important since the overall device efficiency is determined by the charge transport through the metal-organic interface [36]. As a practical example, Fig. [1.2] shows the different interfaces that are found in a prototypical organic photo-voltaic (OPV) device. The fundamental phenomena happening when OSCs are in contact with a metal or inorganic semiconductor substrates will be explained in Chapter [2], with particular emphasis on the correlation between the electronic character-

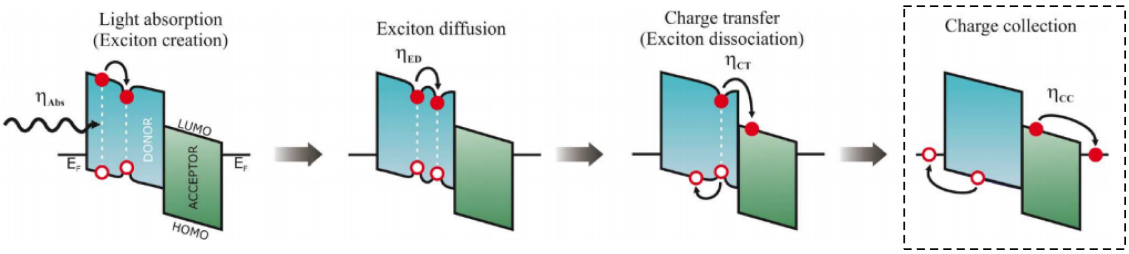

Figure 1.2.: Example of the different interfaces that one may find within an organic photo-voltaic (OPV) device, for instance. In this case, the light is absorbed and an electron is promoted from the highest occupied molecular orbital (HOMO) to the lowest unoccupied molecular orbital (LUMO), leaving a hole in the former. Next, the charges have to migrate towards the interface between a donor and the acceptor materials, so that the transport is efficient. Finally, the charges have to be extracted through the interface between the organic material and the metal electrode. Each of these processes has an associated efficiency η, which depends on the intrinsic characteristics of the material, but also on how the different compounds couple (structurally and electronically) at the interface. For the highlighted case, the metal may deeply influence the electronic and structural properties of the molecule. Thus, understanding how these changes occur is essential to rationalize and control the charge transfer across the metal-organic interface. This will be one of the goals of this thesis. Image adapted from Ref. [37].

istics of the interface with the conformational changes that the molecules undergo upon adsorption.

Within this particular context, the last two decades have seen tremendous progress towards the rationalization of the microscopic phenomena happening at the metal-organic interface. For this purpose, ideal systems[1] composed of prototypical conjugated organic molecules (COMs) deposited under ultra-high vacuum (UHV) conditions on well ordered and defined metal surfaces have been studied. With the same spirit, the materials employed in this research will be presented in Chap. [4]. In addition, the combination of numerous surface-science techniques has allowed for a deep understanding of the processes and mechanisms happening at the interface down to the atomic scale. In Chapter [3], we present the experimental details that involve most of the UHV-based studies of metal-organic interfaces. Also, we explain the basics of the probing techniques used during this project. Central to this work, photoelectron spectroscopy (PES), which has been used widely to investigate the electronic and chemical properties at the interface, and the X-ray standing wave technique will be discussed extensively.

As a further step towards a full understanding of the metal-organic interface, in chapters [5], [6], [7] and Appendix [A] we analyze systematically how different chemical modifications to well-studied COMs change the interface properties. In particular, the selective substitution of some of the atoms by nitrogen or fluorine in the prototypical π-conjugated molecules is considered. The electronegative character of these elements has the potential to modify the in-plane arrangement of the molecules as well as the substrate-molecule chemical, electronic and structural properties. The results yield a deeper understanding of the subtle mechanisms defining the molecule-metal and molecule-molecule interactions.

In the last two chapters, we devote ourselves to the study of the technologically relevant zinc-oxide (ZnO-)molecular interface. In recent years, a combination of surface-science studies of hybrid inorganic-organic systems (HIOS) made of ZnO and different COMs have pushed forward the atomistic understanding of these complex systems. Intimately

[1] Understood as systems that are in controlled conditions and environments differing from those found in real devices.

connected to it, state-of-the-art computational models have shed some light upon the complex surface of ZnO and its stabilization mechanisms. Prior to describing our different ZnO-molecule systems, in Chap. [8] we characterize the bare polar surfaces of ZnO, prepared under different conditions, with a set of PES and XSW measurements. The different surface properties are in Chap. [9] connected to the conformational, chemical and electronic changes observed for different adsorbed COM monolayers. More precisely, different perylene derivatives are deposited on the polar surface of ZnO and their adsorption distances are measured with XSW, whereas the chemical and electronic properties are studied with PES techniques. The occurrence of charge transfer from the substrate to the molecule are monitored for the different molecules and substrate characteristics. From these results, we rationalize which molecular features and substrate preparation maximize them.

Chapters [10] and [11] wrap up and summarize the prominent findings of this work and provide some direction towards addressing issues left open, serving as a guideline for future investigations. Finally, complementary results and projects are reported in the Appendix.

2. Fundamental concepts: the inorganic-organic interface

The common framework for the research presented here is the interface between a (sub)-monolayer of a π-conjugated molecule and an inorganic substrate, either a metal or a semiconductor. It is therefore important to devote some time to explain the main mechanisms and phenomenology governing these systems. Rather than an exhaustive description, emphasis will be put on the key concepts. For a comprehensive explanation, the reader is referred to the following references [20, 38–40] and references therein. Ref. [30] is especially recommended, since it provides an up-to-date, short review of the topics discussed in this chapter. References [41–43] also give a very simple explanation of the basic concepts discussed here, especially in the context of ELA and the electronic characteristics of interfaces.

2.1. π-conjugated systems

As we have anticipated in the previous chapter, π-conjugated systems (COMs) are a particular subset of organic (carbon-based) molecules that have a semiconductor character. In the following, we are going to explain where this behavior comes from and compare it to the traditional inorganic semiconductors.

COMs are aromatic structures that contain alternating single and double bonds stemming from the sp^2 hybridization of the atomic orbitals. sp^2 hybridization is the linear combination of $2p$-orbitals and a $2s$ one that renders three in-plane, equivalent, hybrid orbitals, 120° away from each other. They engage with the nearby atoms forming σ-bonds, leaving the remaining out-of-plane p_z-orbitals free to form π-bonds (see Fig. [2.1]). The maximum overlap of p_z-orbitals happens when these are parallel, thus forcing the sp^2-orbitals to be in the sample plane. The π-electrons are delocalized around the molecule, allowing them some degree of freedom and, consequently, being more likely to be excited to empty levels. In addition, owing to the weaker overlap of the p_z-orbitals, the splitting between occupied and unoccupied states is smaller than with the sp^2 hybrid orbitals. Therefore, the highest occupied molecular orbital (HOMO) and the lowest unoccupied molecular orbital (LUMO) are π-orbitals. The energy difference between the HOMO and the LUMO defines the molecular gap, which is the most important parameter when describing the electron-transport characteristics of the material. HOMO and LUMO are often called the *frontier orbitals* of the molecule. One of the most important advantages of organic semiconductors, compared to the inorganic counterparts, is that via chemical tuning the π-system can be modified and the relative position of the frontier orbitals can be shifted, for instance by adding electron-donating or -withdrawing functional groups to the molecule.

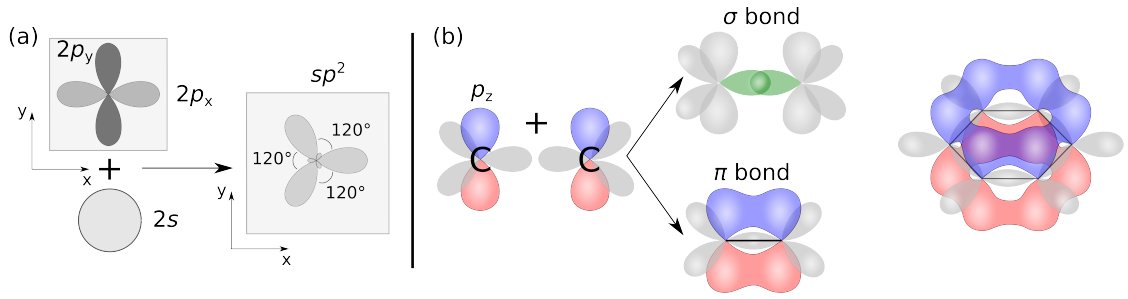

Figure 2.1.: Origin of the π-conjugated system of benzene. (a) sp^2 hybridization stemming from the combination of a $2s$ orbital and two $2p$ orbitals that render three in-plane sp^2 120° apart from each other. The out-of-plane orbital (p_z) remains unaffected. (b) Possible bond formation between two carbon atoms. In a cyclic molecule, all the carbon atoms are sp^2 hybridized, meaning that the in-plane orbitals engage in σ-bonds leaving the out-of-plane orbital (p_z) free to form a π-bond with the surrounding atoms. As seen in the picture, the π electrons become delocalized around the molecule. In the ground state, all the bonding orbitals are filled, whereas the antibonding ones are free, thus setting a highest occupied molecular orbital (HOMO) and the lowest unoccupied molecular orbital (LUMO). The π-bonds have a lower energy difference between HOMO and LUMO, thus electrons are more easily promoted to the "conduction band", for instance through light absorption. See Ref. [44, 45] for more details.

The π-system is also actively involved in intermolecular interactions (see also Sec. [2.3]), in particular with mutually induced dipoles. Hence, in the absence of functional groups with strong donor and/or acceptor groups, molecule-molecule interactions are mostly dominated by weak van der Waals (vdW). This has important consequences, not only for the thermal stability of molecular solids, but also for the electronic transport properties. For the latter, although COMs can be optically excited, the created electron-hole pair (the exciton) is strongly localized (Frenkel exciton), usually within the same molecule, thus limiting the charge mobility, which, in most cases, happens through hopping processes. This is in contrast to the band-like transport of inorganic semiconductors that originates from the stronger interaction of their atoms and favors the delocalization of the exciton (Wannier exciton) within the material, thus improving enormously the charge mobility. The hopping mechanism significantly depends on the degree of π-π overlapping between adjacent molecules. For instance, the transport will be more efficient if molecules face each other, as opposed to a perpendicular arrangement, hence rendering anisotropic transport characteristics. This implies that a proper understanding of the electronic and optical properties of these systems cannot be achieved without knowing the molecular arrangement and their structural properties.

Finally, the nature of the π-system also renders different phenomenology, compared to the inorganic case, when contacted with another material, for instance a metal or an inorganic semiconductor. In the following, we will devote ourselves to the particular case of the interface between a COM and an inorganic substrate, the core topic of this thesis.

2.2. Interface energetics involving π-conjugated systems

Figure [2.2] shows the energy levels of a metal and a COM before and after they are brought into contact. When this happens, the energy levels shift in order to find a common frame, this is called the energy-level alignment (ELA). The ELA determines the flow, if any, of charges either negative (electrons) or positive (holes) across the interface. From the device point of view this is a fundamental process: for LEDs, an efficient charge in-

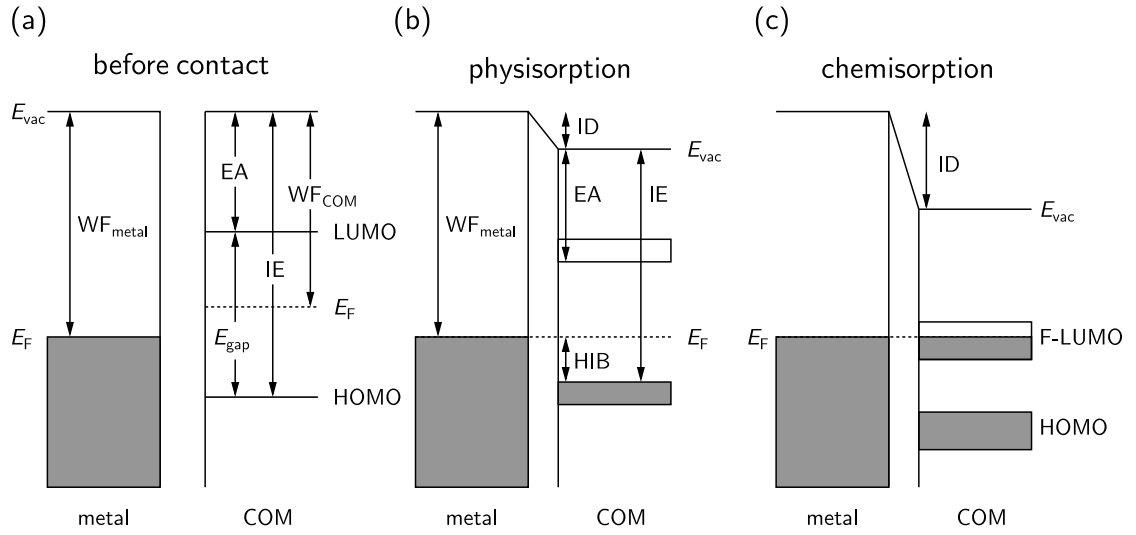

Figure 2.2.: Relevant magnitudes that govern the electronic properties of an isolated metal and a COM (a) and after they are in contact under a physisorptive regime (b) and a chemisorptive one (c). E_F is the Fermi level, WF the work function, E_{vac}, the local vacuum level, EA is the electron affinity, the IE is the ionization energy, HIB stands for hole injection barrier, and ID is the interface dipole appearing upon contact between metal and molecules. The frontier orbitals, HOMO and LUMO, are very sensitive to the environment and when brought close to the metal, the energy levels broaden. In the chemisorptive case, where shorter adsorption distances are usually expected, involving possible CT and/or bond formation, the frontier orbitals broaden even more and the LUMO may become (partially) filled due to CT from the metal. Figure adapted from Ref. [47].

jection through the metal electrode is desired; on the contrary, for solar cells one pursues an efficient charge extraction (Fig. [1.2]). In either case, charges have to overcome certain energy barriers, which, upon contact, have a common reference at the interface.

Starting with the isolated systems (Fig. [2.2a]), a metal substrate has electrons occupying energy levels up to the Fermi level (E_F)[1]. The energy to bring them to the vacuum corresponds to the metal work function (WF_{metal}). For an isolated molecule, electrons occupy positions until the HOMO. They can be promoted to the LUMO if they are given, at least, the energy of the gap (E_{gap}). Both HOMO and LUMO are the most important energy levels when discussing the electronic properties. They are very sensitive to the surroundings. Hence, one can obtain valuable information about molecule-molecule and molecule-substrate interactions by studying their spectroscopic changes, for instance with ultra violet photoelectron spectroscopy [46] (UPS, Sec. [3.2.2]). For semiconductors, the Fermi level is within the gap, therefore unfilled. Consequently, it is more convenient to define the energy barriers according to the frontier orbitals. Thus, the ionization energy (IE) is the energy necessary to move an electron from the HOMO to the vacuum. Conversely, the electron affinity (EA) is the energy necessary to bring an electron from the vacuum to the LUMO.

The Schottky-Mott theory describes correctly what happens to the energy levels at the interface between two inorganic semiconductors or an inorganic semiconductor and a

[1] Strictly speaking, the Fermi level is defined when $T = 0\,\mathrm{K}$, hence one should talk about the electron chemical potential at a given temperature, $\mu(T)$. Following the discussion by Ueno et al. in the preface of Ref. [40], we take $E_F = E_F(T) = \mu(T)$.

metal [48]. This theory assumes that both systems align their vacuum levels, i.e. an electron so far away (at an infinite distance) that does not feel the influence of the material will have the same energy independently of the system where it comes from, it is thus invariant. This means that, theoretically, just by knowing the work functions of both materials one could predict how the levels align. For organic semiconductors, however, it was found that, in many cases, the vacuum-level alignment did not describe the experimental results correctly [20]. From an experimental point of view (for instance with UPS), one cannot access the vacuum-level *at infinity* ($E_{\text{vac}}(\infty)$) [49]. What it is accessible, instead, is a local vacuum-level or the vacuum-level at the surface VL(s), with the corresponding energy $E_{\text{vac}}(s)$ [49]. It is defined as the energy of an electron at rest just outside the surface, not influenced by any interaction with it. This magnitude depends on the local characteristics of the surface. More precisely, this local effect stems from the fact that, for a clean metal surface in UHV, there is no sharp transition for the electron cloud, meaning that the atoms at the surface have their electron cloud spilling out into the vacuum. Consequently, the outer surface is partially negative and the subsurface partially positive, thus rendering the so-called *surface dipole*. If we now turn to the electron escaping the surface, it is clear that the potential energy exerted by the dipole will affect the electron energetics. Of course, local variations of the surface dipole will be also seen by the escaping electron, which can be used as a method to probe the surface conditions. Indeed, the magnitude of the dipole depends on the surface termination[2] as well its particular environment, namely, contamination, presence of adsorbates, etc. The breakdown of the vacuum-level alignment for OSCs (Schottky-Mott) model becomes clear when one recognizes that what is experimentally probed is $E_{\text{vac}}(s)$, which is not an absolute value, but it rather depends on the surface conditions.

The question is then, what happens to the surface vacuum level (and thus the WF) when we deposit a conjugated molecule? To answer this, one has to consider the precise nature of the surface dipole. Actually, upon deposition of an organic layer, the surface dipole becomes an *interface dipole*, hence having contributions intrinsic to the molecule and others stemming from the physical and chemical interactions of this with the surface [20, 30, 41]. As summarized in Fig. [2.3], such interactions may happen in various ways. In the context of the ELA between a COM overlayer and a metal substrate, those various phenomena or possible combinations thereof [50] have to be taken into account. For that purpose, one can distinguish two main, extreme and opposed scenarios: on the one hand, the molecules physisorb on the surface, meaning that only weak vdW forces are at play; on the other hand, the molecules are chemisorbed on the surface, implying the formation of bonds and possible charge transfer (CT) across the interface. Figures [2.2b] and [2.2c] summarize the impact on the ELA of these two extreme cases. It is worth noting that, as shown in Fig. [2.4], depending on the nature of the substrate-molecule interaction, the magnitude (and the sign) of the interface dipole changes. Therefore, adsorbing molecules that easily accept electrons from the substrate (they have an acceptor character) or molecules that easily cede molecules to the substrate (donor character) appeared as a mechanism to increase/decrease the metal WF. In a more refined approach, mixing molecules with opposite characters appears as a suitable way to fine-tune the WF [30].

[2] See the *Gedankenexperiment* described by Ishii et al. [20]: it exemplifies the surface-termination dependence of different magnitudes such as the work function (and thus the surface dipole).

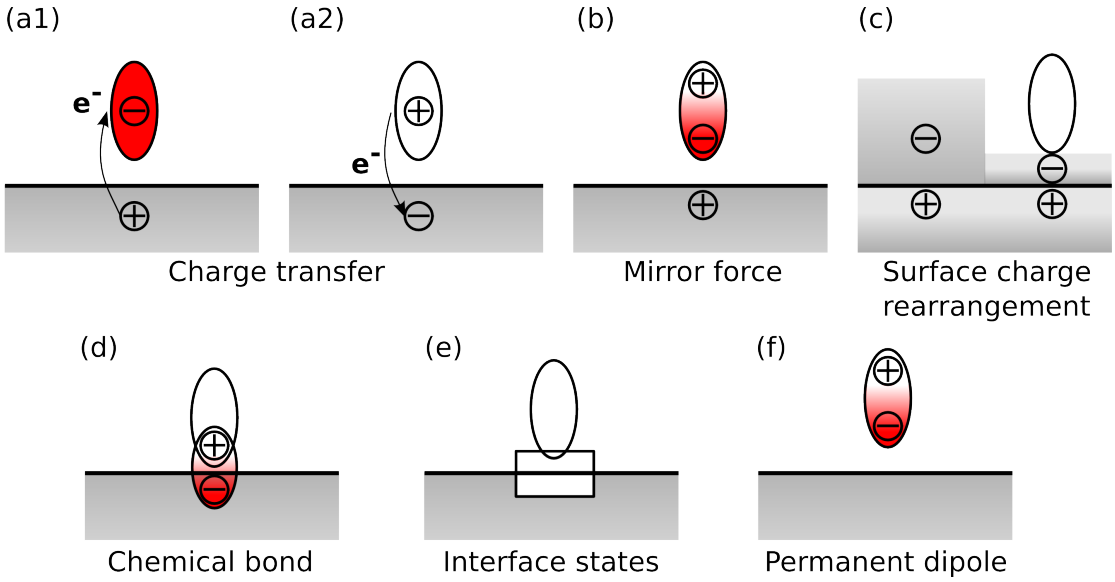

Figure 2.3.: Different effects between the molecular orbitals of an adsorbate and a metal substrate underneath that contribute to and/or affect the interface dipole. (a) Charge transfer from the molecule to the substrate (a1) and from the substrate to the molecule (a2). Depending on the combination of molecule and substrate only one of both occurs or both may happen in charge donation and back-donation processes [50]. The net charge transfer, which can be integer or fractional in terms of the elementary charge e [51], causes the negative and positive charges to be separated by the interface. (b) Formation of an image charge at one side of the interface induced by the presence of a charge of the opposed polarity at the other side. It is usually seen for interfaces involving insulators. (c) Push-back effect. The presence of an adsorbate pushes back to the surface the electron cloud spilling out, hence reducing the surface dipole [52]. It is of special importance for physisorbed molecules [53]. (d) Chemical-bond formation. It describes the case where chemical bonds at the interface are created or changed. The dipole direction depends on the specific case. (e) Interface states. Prominent in the case of inorganic-semiconductor substrates although it is ubiquitous in all kind of interfaces [54–56]. It is the case where the hybridization between the orbitals from both sides originates states that only belong to the interface. (f) Intrinsic molecular dipole moment. Most of the molecules are non-planar or undergo some sort of distortion when adsorbed on the surface. This leads to the formation of an intrinsic dipole that has to be taken into account when describing the interface energetics [57]. Note that these effects are not restricted to metal substrates, but may also take place when the molecules are adsorbed on inorganic semiconductors and insulators. Image based on Ref. [20].

Besides the impact on the electronic properties of the adsorbate-substrate interface, the phenomena shown in Fig. [2.3] also affect other fundamental parameters such as the adsorption energy and the adsorption distance, which are key to define the interaction strength between molecule and substrate and may be regarded as a quantitative way to distinguish between physisorption and chemisorption. They have been recurrently used as a benchmark [58,59] for the theoretical models studying the adsorption mechanisms [60,61]. Recently, the adsorption distance has been found to be the fundamental parameter that describes the energetics of the interface states [56]. It is thus clear that a precise knowledge of the adsorption adsorption distance is necessary for a proper description of the adsorption behavior.

The lack of systematic studies that precisely measure the said properties for a given molecule adsorbed on different substrates, together with the absence, until just a few years ago, of a reliable method to calculate adsorption geometries has hampered a systematic understanding and possible prediction of adsorption geometries. From the theoretical point of view, it is worth noting that the incorporation of vdW corrections to DFT calculations [62–64] has improved significantly the agreement between theory and exper-

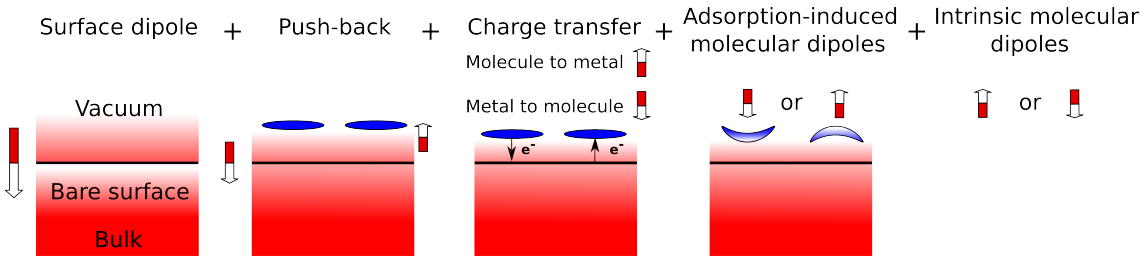

Figure 2.4.: Direction of the interface dipole. The overall interface dipole, in the range of weak chemisorption, i.e. excluding strong bond formation, stems from different contributions, each one having a particular direction. Knowing the specific contributions is crucial to rationalize the WF changes and is only possible if the electronic, chemical and structural properties of the adsorbate are considered. Image based on Ref. [30].

iments [61]. Nonetheless, notable discrepancies between the experimental description of intramolecular distortions, such as those of 3,4,9,10-perylene tetracarboxylic dianhydride (PTCDA) adsorbed on the copper surfaces [65, 66] an theory [61] indicate the need of further investigations.

Depending on the adsorption regime, i.e. chemisorptive, physisorptive or a situation in between, some trends in the adsorption distance may be expected as deduced from the available XSW studies [58, 67–69]. In particular, for physisorbed molecules, usually the case of COMs on Au(111) or graphite, where vdW forces dominate and the electronic coupling with the substrate is driven by the push-back effect (Fig. [2.3c]), the adsorbates show relatively high adsorption distances that are limited by the sum of the vdW radii of the substrate and adsorbate atoms [58, 70, 71]. This entails a rather planar adsorption geometry with no significant distortions of the functional groups and a prominent role of molecule-molecule interactions.

In the intermediate regime, where the presence of CT, weak chemisorption and hybridization may take place, the interplay of many factors defines the adsorption distance and the molecular distortion. In particular, the molecule-substrate and molecule-molecule interactions compete against each other and favoring one or the other may change the geometry [72]. Also, the presence of functional groups and their chemical nature may strongly modify the overall behavior [71]. Usually, the presence of certain heteroatoms increases the electronic coupling with the substrate. Thus, adding functional groups is a common mechanisms to enhance CT effects between substrate and adsorbate. When this happens, CT comes along with a bending towards the surface of the functional groups [68, 69, 71]. For the particular case of PTCDA adsorbed on silver substrates, which has become a canonical example, the reader is referred to Ref. [68] and references therein.

For the (strongly) chemisorptive regime, generally adsorbed systems on copper surfaces, the carbon structure adsorbs close to the substrate and the electronic coupling induces the filling of the molecular LUMO, with possible charge back-donation [50]. The molecular distortions are usually enhanced and in some cases may lead to a dissociative adsorption.

Despite being a topic still under debate, some recent attempts that have tried to rationalize the interplay between electronic, chemical and structural effects deserve to be mentioned [68, 71]. For instance, as outlined in the surface-induced aromatic stabilization (SIAS) model presented by Heimel et al. [71], the electronic, chemical and conformational properties of the molecules in contact with a metal are intimately related. In particular, this model rationalizes why some molecules undergo a partial or total LUMO filling,

whereas many others keep the LUMO pinned above the Fermi level of the metal upon contact. The authors identify the presence of functional groups with heteroatoms, such as (but not exclusively) keto groups (C=O), that bound to the surface as the mechanism that causes a reduction of the molecular gap that allows further CT to the LUMO. More precisely, the reductions of the gap is achieved by increasing the size of the π-conjugated system, which happens when the charge received from the substrate brings about modifications of the bond lengths going along with the change of the bond type from single to double and vice versa [71, 73]. In other words, the CT renders a resonant structure. Also, the bond formation with the substrate induces a bending of the functional groups towards the surface and a decrease of the adsorption distance. Actually, as reported recently [74, 75], the presence of heteroatoms is not necessary for the SIAS to happen, but only the ability of the molecule to form the resonant structure (implying also an increase of the size of the π-conjugated system) via the stretching/contractions of the molecular bonds. This model may be compatible with a precise description of the adsorption of PTCDA on different surfaces of silver [68] as well as for other systems such as perylene-3,4,9,10-tetracarboxylic-3,4,9,10-diimide (PTCDI, studied in Chap. [6]). Nonetheless, as the authors mention [71], this model may not apply to other molecules such as phthalocyanines. Therefore, more systematic studies are required.

2.3. Beyond the monolayer coverage: growth modes and intermolecular forces

In this section, we are going to devote a few lines to the concepts dominating a fully organic environment, i.e. away from the substrate influence. Although it is not an important part of this work, clarifying some concepts may help the reader to better understand some of the discussion later on. Before starting, it is important to keep in mind that the substrate influence may still be indirectly affecting the thin-film regime, for instance by determining the growth mode [76, 77]. Also, molecule-molecule interactions, which clearly dominate in the thin-film regime are also present within the first monolayer and may even be stronger than the interaction with the substrate [78].

2.3.1. Growth modes

The deposition of a material, either organic or inorganic, on a substrate and its subsequent growth follows three different mechanisms (Fig. [2.5]):

1. Island formation (**Vollmer-Weber**): as soon as the first molecules reach the surface they start aggregating and forming isolated islands, leaving some regions of the substrate uncovered.
2. Layer-by-layer (**Frank–van der Merwe**): molecules arrange in smooth layers covering completely the substrate. A new layer does not start growing until the previous one is fully closed.
3. Wetting layer(s)+island formation (**Stranski–Krastanov**): the first layer(s), close to the surface, are fully closed (wetting layer(s)), but at some point islands will start to form on top.

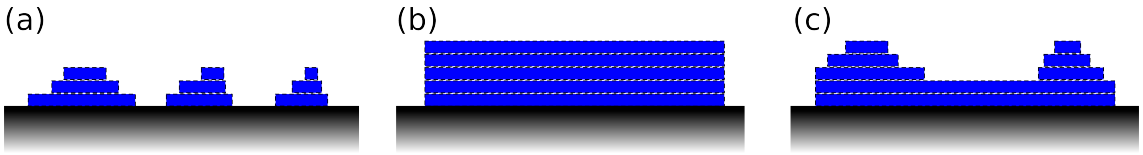

Figure 2.5.: Modes of thin-film growth: (a) Island (or Vollmer-Weber) growth. Islands are formed from the start to minimize the interface with the substrate. This gives rise to rough surfaces. (b) Layer-by-layer (or Frank-van der Merwe) growth: formation of a wetting layer(s) to minimize the surface energy. Closed layers are favorable, which renders very smooth surfaces.(c) Layer+island (Stranski-Krastanov) growth: formation of a wetting layer(s), which at some point turns into island growth. The first layer(s) is(are) strained to match the substrate and relax upon island formation.

Growth is driven/limited by kinetic and thermodynamic processes [79] and the ability of molecules to overcome different energy barriers [80] and diffuse around the surface, down/up step edges and between layers [81, 82]. The final configuration will be also influenced by the attractive/repulsive interaction between adjacent molecules and, in the first layer, also between the molecules and the substrate. Growth studies and characterization of thin films are of paramount importance for the understanding of electron-transport properties and their improvement [83] since it has been shown that the performance of organic-based optoelectronic devices, especially regarding their optical and electronic properties, depends intimately on the morphology [84].

Theoretically, the growth can be studied by means of Monte-Carlo simulations [85, 86]. Experimentally, within the first layers, any spectroscopic technique that can differentiate between the signals of the organic material and the substrate may provide different degrees of information about the growth. In articular, XPS allows for a quantitative analysis of the first layers [87]. Recently, low-energy electron microscopy has been used to provide real-time and -space information of the first stages of growth [88]. For thicker films see Ref. [89] and references therein.

It is worth noting that molecules can also undergo changes in their orientation during growth [90]. For instance, molecules that initially lay flat on the substrate at some point may flip to a standing orientation. Such changes are mostly related to the intermolecular interactions at play, as we will see next.

2.3.2. Intermolecular forces

Interactions between molecules are a key parameter when evaluating transport properties [91] since they determine how easily charge can move across an active material. Besides, as mentioned above, they play a major role in the growth dynamics. They are either attractive or repulsive and depend mostly on the chemical structure of the molecule and its functional groups. Let us, then, discuss which are the different types:

- Van der Waals interactions [92, 93]: are a generic name that includes several types of contributions, namely, Keesom or (permanent) dipole-dipole interactions; Debye or the interaction between an induced dipole and an induced one in a non-polar molecule and, lastly, London or interaction between temporary-induced dipoles. They are considered to be always attractive, although a recent theoretical study showed that in the absence of spherical symmetry happening in confined systems they may turn repulsive [94]. Its electrostatic nature is the weakest of the interactions discussed

here but have a long range and are ubiquitous, thus becoming dominant in the absence of other interactions. They are non-directional.

- Hydrogen-bond formation [95]: is of the type X–H···Y, where H is a hydrogen atom covalently bonded to an electronegative atom X that shifts the electron cloud away from the hydrogen atom, leaving it with a positive charge density that is electrostatically attracted to a nearby electronegative atom Y. The more electronegative X (and Y) the stronger will be the electrostatic interaction between H and Y. Contrary to vdW interactions, H-bonds are highly directional and have a wide range of energies (0.01–1.73 eV [96]). They play a major role in the formation of heteromolecular arrangements on well ordered surfaces [78] and can be tuned by modifying the molecular functional groups [97]. PTCDI, studied in Chap. [6], is widely used to form ordered supramolecular systems [78].
- π–π interactions: they happen between aromatic molecules with an extended π-electron system (see Fig. [2.1]). They are of paramount importance in the context of OSC growth, since most molecules in a purely organic environment rearrange to maximize/minimize them in the so-called π-stacking growth.
- Metal coordination: the interaction between organic compounds and metal atoms renders selective, directional and rather strong bonds, suitable for the formation of porous and well ordered systems.
- Covalent bonding: it is the strongest and most directional of all. It does not usually occur naturally among adsorbate compounds or at the thin-film regime, but rather is induced by thermal, optical or local reactions. They render stable systems but lack the self-error-correction mechanism seen in more flexibly-bound systems.
- Other electrostatic interactions: interactions between molecules that have permanent charges, dipoles or quadrupoles of significant magnitude.

It is worth noting that different interactions may happen simultaneously, the overall behavior being the net sum of their contributions.

We mention here a special type of intermolecular interactions that are promoted by the substrate, therefore only occurring within the first monolayer. They are called substrate-mediated interactions [98] and may have a rather long interaction range. Basically, these interactions occur when the adsorbed element, inorganic [98] as well as organic [99, 100], creates a perturbation on the electronic and/or crystal structure of the surface that favors the adsorption of additional molecules in the surroundings [98].

Intermolecular interactions within the first monolayer can be studied with scanning tunneling microscopy (STM), and if they are strong enough to leave an electronic or chemical fingerprint spectroscopy techniques can also be used [101–105].

2.4. Beyond the metal-organic interface: heteremolecular and inorganic-organic semiconductor interfaces

As an ending for this introductory chapter, we are going to shortly review some of the most recently studied systems in the context of inorganic-organic interfaces. They represent somehow an evolution of the typical metal-organic case, either from the conceptual

and/or experimental perspective.

We start by describing a rather recent elaboration of metal-organic interfaces, namely, those with incorporated metal dopants on the surface. Although the doping of organic semiconductors with alkali atoms was first examined a couple of decades ago [106] and the study of adsorbed atoms on metal surfaces is as old as surface science itself, it has been just rather recently that a set of surface-science techniques has been devoted to study the effect, at the atomic scale, of doping on the structural [107–110], chemical [111], magnetic [112] and electronic [110,113] properties of metal-organic interfaces. The typical examples are metal substrates with alkali or lead atoms implanted on the surface that modify the interface properties either by enhancing or reducing the metal-molecule coupling.

Another example that has been already mentioned is the combination of two molecules, a donor-acceptor pair, to populate the first monolayer. The interplay between molecule-molecule and substrate interactions is used as a mechanism to tune, for instance, the work function [114] and the ionization energy [29]. The relative concentration of the two molecules is used as the tuning mechanism. This elegant way to modify the charge injection/extraction energy barriers at metal electrodes, however, has only been partially rationalized in the last few years [30,31,115]. A slight variation of the same are systems composed of a first homomolecular layer adsorbed on a metal surface with another homogeneous layer of a different compound deposited directly above, the so-called bilayer systems [116]. These render the most simple case for the study of organic-organic interactions between two different components. From the applied point of view, adding a buffer layer of a given organic compound to tune the ELA between the metal electrode and an organic active material is also a valid way to improve the charge transport across the electric "soft" contact. However, the integrity of the first layer may be hampered by diffusion of the active material towards the metal surface. This indicates that the interactions at the atomic level and the influence of the metal beyond the first layer need not be neglected for a proper control of these systems. More information on this topic can be found in Appendix [G].

Finally, since the combination of organic and inorganic semiconductors was demonstrated to be a feasible mechanism to reduce the shortcomings of the separate components [117–120], plenty of research has been devoted to the design and investigation of hybrid inorganic-organic systems (HIOS). In recent years, research has increasingly focused on the detailed understanding of their interface processes. Thus, a more surface-science approach has been adopted to rationalize these systems. A good example of it is the first XSW results presented in this thesis (Chap. [9]) that provide a precise adsorption geometry of several organic adsorbates on ZnO[3]. In this context, besides zinc oxide (ZnO), titanium dioxide (TiO_2) [124–130] has become quite popular, although some studies on the technologically relevant gallium nitride (GaN) are also available [131]. As a particular case of hybrid inorganic-organic semiconductor systems, perovskites have also attracted remarkable interest recently [132], especially in the context of solar cells [133].

[3] We note that the study, even including XSW experiments [121], of small molecules adsorbed on semiconductor surfaces is not a new topic [122]. Nonetheless, large COMs deposited on metal oxides, the case of this work, is more recent [35,123].

3. Experimental methods and techniques

In the following, the experimental details of the research carried out during this thesis are explained. To begin with, the preparation of the samples is described. This includes any ex-situ as well as in-situ treatment. Next, the fundamentals of the main techniques employed are outlined. Finally, a brief description of the setups where the experiments were carried out is given. Despite ultra-high vacuum (UHV) being central in all the measurements reported here, we refrain from commenting on the specific technical and scientific details of it. The reader is referred to Ref. [134] for a concise introduction to vacuum technology and Refs. [135, 136] for a deeper, more specialized insight.

3.1. Sample preparation

Organic materials contain carbon (C) and hydrogen (H) as well as other atoms, most commonly oxygen (O), nitrogen (N) and fluorine (F), all being also present in atmospheric gases such as carbon dioxide (CO_2), carbon monoxide (CO), nitrogen dioxide (NO_2) and water (H_2O). It is therefore desirable to avoid any contamination that could mask, influence or damage the samples. This is even more important in the present work where, in most cases, just a monolayer of organic molecules is studied. Last but not least, since the techniques employed here use electrons, which interact strongly with matter, as the primary source of information, it is important to reduce the amount of molecules and atoms that they encounter before reaching the spectrometer. For this reason, the cleaning of the substrates and the subsequent deposition of the π-conjugated molecules are performed in situ, under ultra-high vacuum (UHV) conditions, at the same setup where the measurements are carried out.

3.1.1. Organic molecular beam deposition

The samples studied throughout this work, (sub)monolayers as well as multilayers, were prepared via organic molecular beam deposition (OMBD) [137, 138]. The films studied with high-resolution XPS (HR-XPS) and XSW were grown with the same home-made Knudsen-cell as the one described in Ref. [47]. It consists of three thermally-insulated evaporators that are resistively heated using a tantalum wire. Thermocouples are used to measure the temperature of each separate evaporator. The compounds are placed inside quartz-glass crucibles that are held with a stainless-steel structure and surrounded with the aforementioned heating wire. In order to avoid shortcuts, Macor® ceramic pieces are used to insulate the conducting parts. A shutter is placed in front of the aperture to prevent cross-contamination of the crucibles and to immediately stop the deposition. The cells are mounted on UHV-compatible equipment that can be easily attached to any UHV chamber. During this project, some modifications were made to improve the stability of the cell. A detailed description can be found in Appendix [I]. All the molecular compounds

studied had been previously purified via a two-cycle sublimation process [44, 139].

The deposition rates and the nominal coverages were calibrated using a quartz-crystal microbalance (QCM) available in the UHV system. Unless stated, no further annealing treatment was applied upon deposition of the molecules. The intensity of the C $1s$ core-level peak, compared to the substrate signal attenuation was used to make sure that coverages higher than one monolayer were not exceeded.

3.1.2. Substrate cleaning and preparation

Due to the central role of the interface in this work, having a clean, well-defined substrate surface is a conditio sine qua non. In addition, the technical requirements of the XSW technique (Sec. [3.3]) demand a high crystal quality at the surface as well as in the bulk. Consequently, the single-crystal substrates (Sec. [4.2]) have to be treated to achieve both a clean surface and an excellent crystal quality with a low mosaicity.

3.1.2.1. Sputtering and annealing

Sputtering/annealing cycles are a standard cleaning procedure in surface science that consist of two steps: first, the surface is bombarded with ionized noble-gas atoms, usually argon (Ar^+), and secondly, the surface is annealed at relatively high temperatures to remove the atoms that might have been located within the crystal lattice and heal the surface. In more detail, a stream of Ar is let in the chamber, then ionized through the interaction with free electrons emitted from a filament and subsequently accelerated, via a voltage difference, towards the substrate surface. The posterior annealing is achieved via the heating system attached to the sample holder/manipulator. This process can be repeated many times until the desired surface conditions are achieved. The objective of the sputtering/annealing cycles is twofold: to remove undesired adsorbates from the surface, including deposited organic thin films, and to make the surface more homogeneous. One has to keep in mind that this procedure is destructive since layers of atoms from the substrate surface are removed. Therefore, the parameters (see Tab. [3.1]), yielding a sample drain currents of $\sim 5\,\mu$A in our case, have to be adapted for each specific sample to avoid undesired damage. As it will be seen in Chap. [8] this is especially important when treating the ZnO substrates. On the contrary, for metal single crystals, one can be more relaxed about the sputtering and annealing time, the kinetic energy of the ions and the annealing temperature. Nonetheless, one can accidentally melt the crystal if the temperature is not carefully chosen (annealing close to the melting point may help to improve the crystal quality, though). Table [3.1] summarizes the specific parameters used to treat the different crystals.

Substrate	**Sputtering**			**Annealing**	
	Ar pressure (mbar)	Ar^+ E_{kin} (keV)	Time (min)	Temp. (°C)	Time (s)
Au(111)	5.10^{-5}	0.5	30	550	30
Ag(111)				520	
Cu(111)				520	
ZnO			15	420	10

Table 3.1.: Sputtering/annealing-cycle parameters used for the different substrate crystals.

3.1.2.2. Furnace annealing

For the specific case of ZnO (Chapters [8] and [9]), in order to improve the crystallinity of the substrates, previous to any UHV treatment, the crystals were annealed in a quartz-tube furnace under ambient conditions. They consist of a quartz (SiO_2) tube that is inserted inside a cylindrical, resistive-heating furnace. The furnace used was a Carbolite mtf 12/38/250 (maximum temperature 1200°C, maximum continuous temperature 1100°C).

3.2. Photoelectron spectroscopy (PES)

Photoelectron spectroscopy (PES) makes use of the photoelectric effect[1] to extract information from a given material and its environment. The very basic idea is that an incoming photon transfers all the energy to a bound electron, which is then released with a certain kinetic energy. From the energy-conservation principle, the kinetic energy of the freed electron (E_{kin}) is given by the difference between the initial photon energy ($h\nu$) and the energy necessary to bring this electron from its bound state to a free one, namely, the binding energy (E_{B} or BE through this work). Due to the quantum nature of the atom, E_{B} is unique for each element and energy transition and hence chemically specific. By recording how many freed electrons have a certain E_{B} one is probing the density of states (DOS) of the particular system, i.e. the number of electrons that populate each specific energy level. Furthermore, as it will be explained below, any variation of the E_{B} position and peak shape can be related to changes in the chemical and electronic environment.

Experimentally, provided that $h\nu$ is known, by measuring the E_{kin} of the electron one can access the atomic information contained in E_{B}:

$$E_{\text{B}} = h\nu - E_{\text{kin}} - \phi_{\text{A}} \tag{3.1}$$

where ϕ_{A} is the work function (WF) of the electron analyzer, which is the device employed to measure the kinetic energies of the released electrons [141]. Importantly, one needs to define a reference. If one omits ϕ_{A} in the previous equation, the reference is the vacuum level, which is adequate for free atoms and molecules. However, for solids the appropriate is to refer the energies to the Fermi level E_{F}, hence ϕ_{A} has to be included[2].

In Eq. [3.1], it is implicit that those electrons with E_{kin} have not lost energy, due to scattering events, on the way to the spectrometer/analyzer. The inelastic mean free path λ of electrons in solids is very short thus giving PES an intrinsic surface sensitivity (10–50 Å) and, at the same time, constraining it to UHV conditions[3]. Actually, the probing

[1] The photoelectric effect was first observed by Heinrich Hertz, in 1887, when shining UV light onto a metal. Albert Einstein, using the new concepts of energy quantization gave a proper theoretical framework in 1905. Einstein received the Nobel Prize in 1921 for it [140].

[2] When sample and electron analyzer share a common electric ground, their Fermi levels align, meaning that the vacuum level (VL) is different for each case. Thus, an electron leaving the sample has to overcome the sample work function ϕ_{s} to reach the vacuum level, then move to the analyzer VL and finally overcome ϕ_{A} in order to be collected: $E_{\text{kin}} = h\nu - E_{\text{B}} - \phi_{\text{s}} - (\phi_{\text{A}} - \phi_{\text{s}}) = h\nu - E_{\text{B}} - \phi_{\text{A}}$ [49].

[3] Ambient-pressure X-ray photoelectron spectroscopy partially overcomes the limitation of using UHV environment by creating a differential pressure along the path towards the electron analyzer, which allows to carry out experiments at nearly ambient pressures [142].

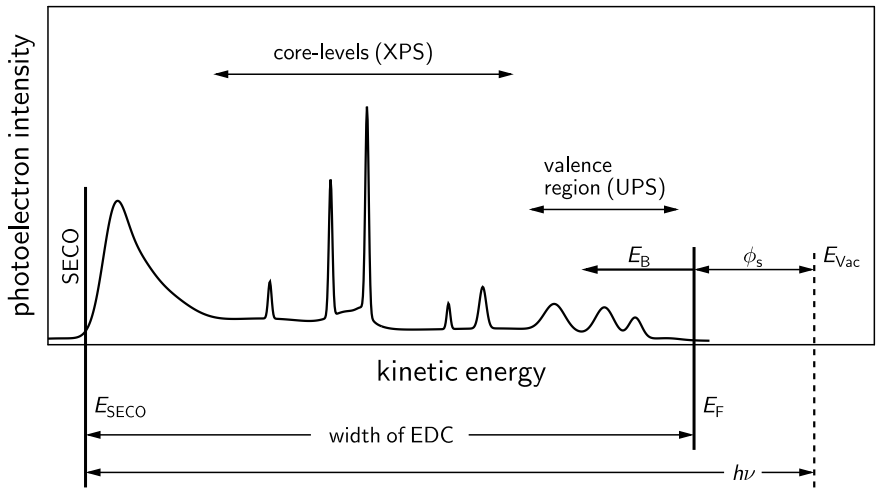

Figure 3.1.: Energy-distribution curve (EDC). The intensity of photemitted electrons (which is proportional to the DOS) for a given atom or compound versus the energy of the exciting photons represents the energy-distribution curve (EDC). The EDC takes a range equal to $h\nu$ minus the sample WF (ϕ_s) and goes from the Fermi edge (E_F) to the secondary-electron cutoff (SECO). For a system involving many atoms, one distinguishes two regions within the EDC: first, the deep core-levels stemming from the electronic states of each particular atom that are not involved in bond formation; secondly, the valence band (VB) region stemming from the electronic states of the outermost shells, more likely to participate in transport and bond formation events. The energy of the photons used determines which states can be accessed and with which resolution. Core-levels have a higher E_B and can only be accessed with X-rays. Valence band electrons have much lower E_B, thus being accessible with both X-rays and ultraviolet light. However, the resolution is much higher if UV is used, owing to its much higher cross section at this energy range. Figure adapted from Ref. [47].

depth can be tuned, to some extend, by using different photon energies and/or varying the angle between the source and the surface.

In addition to varying the probing depth, changing the photon energy also exploits the energy-dependence of the photoemission cross-sections, which allows to improve the sensitivity and resolution of certain regions of the energy-distribution curve (Fig. [3.1]). In this context, two main subgroups within PES are distinguished: ultraviolet PES (UPS) and X-ray PES (XPS). As shown in Fig. [3.1], the lower photon energy employed in UPS is more suitable for studying the outer energy levels, i.e. the valence-band electrons. Since these are more likely to be involved in transitions to the conduction band, UPS is one of the best suited techniques to study the electronic properties of materials. The higher energies of X-rays can also access the deeper energy levels, those with higher E_B, the so called core-levels of the atom. Such levels are occupied by electrons that remain rather unperturbed under external effects, thus retaining the chemical state of the atom or compound.

Before moving to the specific details of UPS and XPS, we shortly outline the main ideas behind the photoemission process. We refrain from a detailed mathematical description of it (see Refs. [141, 143, 144] for this purpose and Ref. [145] for a concise explanation). According to the *Three-Step model* [141], the photoemission process can be divided into three parts: first, the creation of the photoelectron within the sample; secondly, the migration of the photoelectron towards the sample surface and thirdly, the escape of the photoelectron from the sample to the vacuum.

The first step deals with the probability that an incoming photon will excite an electron

from an initial state ψ_i to a final state ψ_f. The wave function of the atom, within the *Born-Oppenheimer approximation*, can be described as the product of the nuclear and the electronic part. Being the timescale of the photoexcitation (and subsequent relaxation) much faster than the nuclear motion, only the electronic component is relevant to describe the photoemission process[4]. Usually, the transition probability is calculated within the *dipole approximation* (i.e. resolving the Hamiltonian of the transition with first order perturbation theory), which neglects quadratic and higher-order dependences on the exciting electromagnetic field. Also, it is worth noting that photoexcitation is a many-body problem, meaning that, for a system of N electrons, the photoexcited state is coupled to the final state of the $N-1$ electrons. Nonetheless, such an extremely complex problem can be enormously simplified thanks to the *Koopmann's theorem*, also called *sudden approximation*, which states that the ionization leaves the wave function of the remaining electrons unaltered. In particular, as soon as the electron is ejected, it has no Coulomb interaction with the hole left behind. In virtue of this theorem, measuring the electron kinetic energy can be readily converted to its initial E_{B}. Experimentally, there are spectral features that cannot be explained without considering violations to the Koopmann's theorem. This specific cases will be explained in the XPS subsection.

The second step deals with the electron transport through the solid. Two main factors are into play: the Coulomb attraction between the photoelectron and the photohole left behind upon ionization and the scattering with the atoms. Although the sudden approximation considers that the Coulomb interaction with the hole left behind does not influence the creation of the photoelectron, its migration towards the surface is hindered by the electrostatic interaction with it. How strong this interaction is depends on the polarizability of the material, which determines its efficiency to screen the photohole. Indeed, materials that have (nearly) free charges can reorganize around the vacancy and reduce the Coulomb force. For instance, metals are very good at screening the photoholes created within the solid as well as within overlayers adsorbed on their surface. In general, the Coulomb interaction reduces the kinetic energy of the photoelectron, thus shifting the E_{B} to higher values than the actual one. This effect will be elaborated in the following subsection. Moving to the second effect, the inelastic scattering of the photoelectron on its way to the surface, as described by the inelastic mean free path (IMFP, λ), has a dependence on the photoelectron E_{kin}, as well as the material [147]. Interestingly, the material dependence is very small, thus $\lambda(E_{\mathrm{kin}})$ can be regarded as a universal curve, which has a minimum at $\sim$10 eV and it increases for smaller and higher energies. Besides the surface sensitivity and the need of UHV equipment, the intrinsically small IMFP implies that most of the electrons lose energy on the way to the analyzer. The scattered electrons render an inhomogeneous background across the whole spectra and contribute, mostly in metals, to the asymmetric line shape of the high E_{B} side of the core-level peaks, since an electron can lose energy but not gain it. A proper understanding of the energy losses is fundamental to evaluate the background, which has to be decoupled from the actual core-level signal. This is especially true if a quantitative PES analysis is pursued.

Finally, the escape from the surface towards the vacuum is mostly affected by the charge distribution on the surface and its dipole moment, which basically connects to the dis-

[4] This is important for the XSW technique, as it will be seen in Sec. [3.3], because one can effectively use photoemission to determine the position of the atoms [146].

cussion presented in Sec. [2.2]. In particular, the escaping photoelectron has to overcome the energy barrier rendered by the surface dipole. Consequently, the measured E_B will depend on its magnitude. For a given core-level, different E_B are reported depending on the precise nature of the surface or interface. A clear example is given in Chap. [6], where the carbon C 1*s* core-level of PTCDI (sub)monolayer has different E_B depending on the substrate material.

3.2.1. X-ray photoelectron spectroscopy (XPS)

XPS is most suited to study the deep core-levels of atomic, molecular, bulk as well as adsorbed species (see Ref. [148] for an overview on XPS and its applications). Due to the discrete nature of these levels, the information obtained from XPS is inherently chemically sensitive, which represents one of the most powerful characteristics of this technique[5]. Thus, XPS is most popularly used to identify elements and compounds of a sample with unknown composition. By recording the E_B of the intensity peaks and comparing its position to tabulated values (such as those of Ref. [150]), chemical elements and even compounds can be determined. Owing to the extensive energy range of X-rays, XPS is divided into two main groups. The first one uses photon energies between 0.1 and 2 keV and is called soft XPS (SXPS). The other uses higher photon energies (2–20 keV) and is known as Hard XPS (HAXPS or HXPS). HAXPS is considered a discipline of its own and in the context of material science is employed to study bulk electronic and chemical properties [151]. On the contrary, by using soft X-rays, one gains surface sensitivity and also resolution since the electron-photon cross-section is higher at lower energies.

Although not directly involved in the formation of chemical bonds, core-levels *feel* changes in the surrounding electronic configuration, thus providing valuable information about the chemical state of the probed element and its environment. In the context of inorganic-organic interfaces, this means that any molecule-molecule and/or substrate-molecule interactions will leave a fingerprint in the XP spectrum. Also, changes in the local charge density, for instance due to charge transfer (CT) from/to the substrate may well be observed. Of course, modifications of the chemical bonding are also clearly seen in XPS. Obtaining this information, however, is intricate and most of the times it requires complementary techniques [69, 152] and/or theoretical calculations [152–155]. In a typical XP spectrum, this information is hidden in the relative peak intensities, peak broadening and asymmetry, relative binding-energy shifts, also called core-level shifts (CLS), appearance of new peaks, etc. Previous to a more detailed explanation [156–158], focused on the context of inorganic-organic interfaces [152, 159] and organic solids [160–162]. Tab. [3.2] summarizes those most relevant.

The peak broadening is quantified via the full width at half maximum (FWHM) and its origin is twofold: broadening extrinsic to the photoemission processes, i.e. experimental contributions, and intrinsic or inherent to it. For the former, the resolution of the electron analyzer being too low to distinguish two transitions with very similar energy or the poor monochromaticity of the beam are the most important contributions. The experimental broadening is described with a Gaussian shape. More interesting are the intrinsic con-

[5] Initially, XPS was named Electron Spectroscopy for Chemical Analysis (ESCA) precisely for its chemical sensitivity. The technique was developed by Kai Siegbahn at the University of Uppsala, Sweden [149].

Origin of the main spectral features in PES		
Broadening	Extrinsic	Analyzer resolution Beam monochromaticity Charging
	Intrinsic	Lifetime broadening Sample inhomogeneities Unresolved final states Vibrational broadening
E_B shifts	Initial-state contributions	Chemical environment Hybridization
	Final-state contributions	Satellite structure Screening of the core-hole
Peak intensities		Stoichiometry Beam damage Charging

Table 3.2.: Summary of the main contributions to a PES spectrum.

tributions. The natural (or lifetime) broadening stems from the Heisenberg's uncertainty principle that couples the finite lifetime of a quantum state with its energy uncertainty. In particular, the core-hole, left upon photoexcitation, is an excited state and therefore has a relatively short lifetime [163]. Any external influence to the core-hole will have an impact on the peak broadening [164]. For instance, a strong substrate influence that screens or even fills the core-hole, reduces its lifetime, thus the same core-level peak may appear broader in the case of strong hybridization with the substrate compared to a physisorbed case [165, 166]. Another intrinsic source of broadening is the possible excitation of vibrational modes upon photoemission [167], which may explain why temperature has a strong influence on the peak FWHM. Also, inhomogeneities within the studied material, for instance, different arrangements of the molecules within the sample (e.g. island vs. monolayer [168]) or, in the case of semiconductor surface, local differences in the work function (e.g. different local doping concentrations) may contribute as well. Finally, a peak broadening may actually be two non-equivalent atoms of a given species very close in energy to each other that cannot be resolved as two separate peaks. This effect is clearly seen if the size of the molecule is increased [162]. The natural broadening is best described by a Lorentzian contribution to the peak shape.

Binding-energy or core-level shifts (CLS) are classified between those that can be explained via the initial-state picture and those which can only be understood when final-state contributions are taken into account [169]. The former has to do with the chemistry of the atomic ground state (that is why the CLS are also called chemical shifts), whereas the latter deal with processes that involve the excited core-hole. The most clear example of initial-state contributions is the chemical environment, for instance, atoms bound to electronegative atoms see their electron cloud slightly shifted away, hence the Coulomb interaction with the positive atomic nucleus is less screened by the other electrons and the E_B is higher. An example of this can be seen in Fig. [3.2] for the carbon C $1s$ core-level signal, which shows different contributions depending on how electronegative is the bonding atom. In the same direction, hydrogen-bond formation [101, 102, 170, 171] (and proton transfer [172]) can also be distinguished in XPS since charges are shifted closer/away from the nucleus thus inducing CLS in one or another direction depending on whether the proton donor or acceptor is being measured. The major contribution (although a non-depreciable

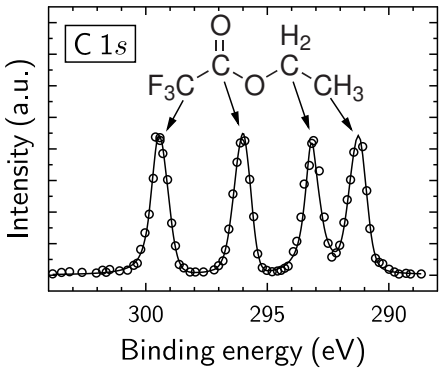

Figure 3.2: Example of the chemical sensitivity of XPS. The spectrum corresponds to the C 1*s* core-level of ethyl-trifluoroacetate. This technique is able to resolve different chemical environments, even within a given element. Depending on the surrounding atoms, the charge density of carbon is pulled away, as it happens for the bonding with electronegative atoms such as fluorine and oxygen. Consequently, the screening of the Coulomb interaction exerted by the atomic nucleus is less effective and the electrons are more strongly bound. Figure taken from Ref. [47], which was initially adapted from Ref. [149].

screening contribution is also present) to the hydrogen-bond-induced CLS comes from the initial-state [173]. Finally, changes in the environment, e.g. via sample charging, may also play a role [174].

Final-state contributions arise from violations of the Koopmann's theorem [158]. On the one hand, as depicted in Fig. [3.3], the interaction of the escaping electron with the remaining electron cloud may induce some energy transfer to the valence electrons, which may be promoted to the conduction band (shake-up process) or even completely ejected (shake-off process). A shake-up transition to an unoccupied state will be very favorable if it helps to transfer charge within the molecule to screen the core-hole [160, 161]. These processes are seen as small peaks at the high binding energy side of the main core-level peak (see for instance Fig. [6.5] in Chap. [6]). On the other hand, the screening of the core-hole by the surrounding is determined by its polarization. A highly polarizable environment is able to screen the core-hole more efficiently. This is the reason why adsorbed monolayers on metals have very well screened core-holes compared to the thin-film regime. Closer to the metal the core-hole will be strongly screened by the (nearly) free electrons of the substrate [175]. Therefore, increasing the coverage will shift the E_B towards higher values. It is worth noting that the substrate screening is usually stronger for the peaks corresponding to bonds with electronegative atoms, where the moving electrons of the substrate counteract the lower density of electrons around the less electronegative atom. This is clearly seen in the (sub)monolayer regime, where there is not a rigid shift of the E_B, for instance C–F or C=O peaks show higher shifts towards lower E_B than C–C or C–H peaks (see for instance Fig. [6.6] in Chap. [6]). Comparing shifts between multilayer and (sub)monolayer regimes can be used as an indicator of the interaction strength between molecule and substrate: larger shifts will highlight a stronger influence of the substrate. A similar effect is observed when comparing a given signal stemming from the surface to that originating in the bulk [169, 176, 177]: the fewer atoms surrounding a surface element compared to the bulk provide a less efficient screening. In the particular case of organic materials [178], the size of the molecule [161, 162] as well as the presence of functional groups [152, 161] also affect the screening efficiency. Indeed, functional groups with electronegative atoms will act as acceptors whereas the π-conjugated system will act as a donor. Hence, varying the electronegativity and/or the size of the aromatic ring modifies the relative donor-acceptor strength within the molecule. A larger π-conjugated system is also related to higher shake-up intensities, since the stronger donor character will be

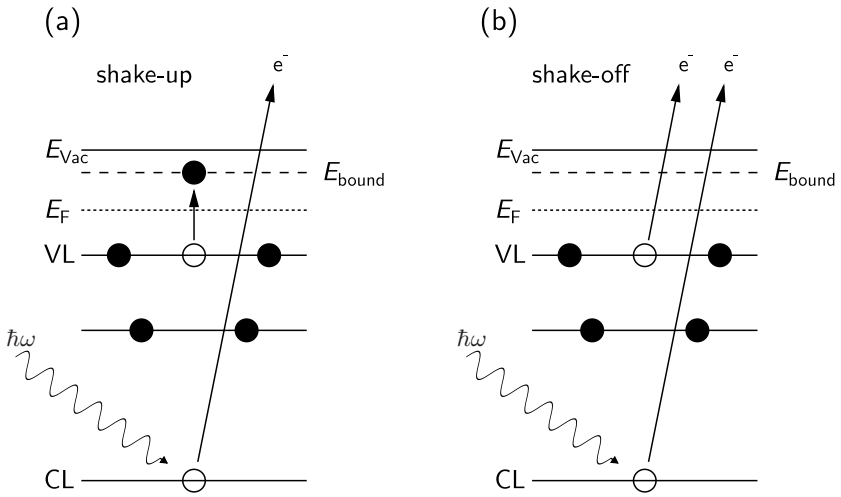

Figure 3.3.: Processes contributing to a typical XP spectra that cannot be explained with the Koopmann's theorem. (a) Shake-up transition: the photoelectron, on the way out, transfers part of its energy to a VB electron that is promoted to the conduction band. For COMs, this transitions is usually from the HOMO to the LUMO, thus, the shake-up appearing at the high binding energy side of the main peak is called HOMO-LUMO shake-up. (b) Shake-off transition, which is the same as before but in this case the transmitted energy is enough to free the valence electron. They usually appear in metals. Figure taken from Ref. [47].

able to transfer charge to core holes created in the acceptor part [161]. The molecular packing (i.e. strength of intermolecular interactions) within the first monolayer has been shown to have an important effect on the shake-up intensity as well [159]. For a deeper understanding of CLS, the reader is referred to Refs. [157, 158] and references therein. Their prediction and even a detailed knowledge of their origin require state-of-the-art calculations [179, 180].

Finally, relative peak intensities also provide important information about the studied system. In the particular case of COMs, they may reflect the stoichiometry (shake-up intensities may have to be accounted for though). Other external effects such as sample charging (critical when using insulator substrates) or beam damage due to overexposure may also change the intensity of the core-level peaks.

3.2.2. Ultraviolet photoelectron spectroscopy (UPS)

Although XPS can be used to study the weakly bound and less localized electrons of the VB, the photon energies are far above the photoionization threshold and the cross-section for such energies are low. Therefore, ultraviolet light is used instead. Typical lab sources use helium (He) gas discharge lamps, which have two main excitation lines: He I (21.2 eV) and He II (40.8 eV). One of the two lines is selected and usually a monochromator is attached to decrease the line width and the photon flux (to reduce possible beam damage). UPS gathers mostly surface-sensitive information [135]. The interpretation of UPS spectra has some particularities that will be outlined next. Before that, it is worth noting two specific UPS-based techniques important in the context of inorganic-organic interfaces, namely, angle-resolved UPS (ARUPS) [181, 182] and its rather recent upgrade called orbital tomography [183]. Basically, ARUPS is used to map (experimentally probe) the band

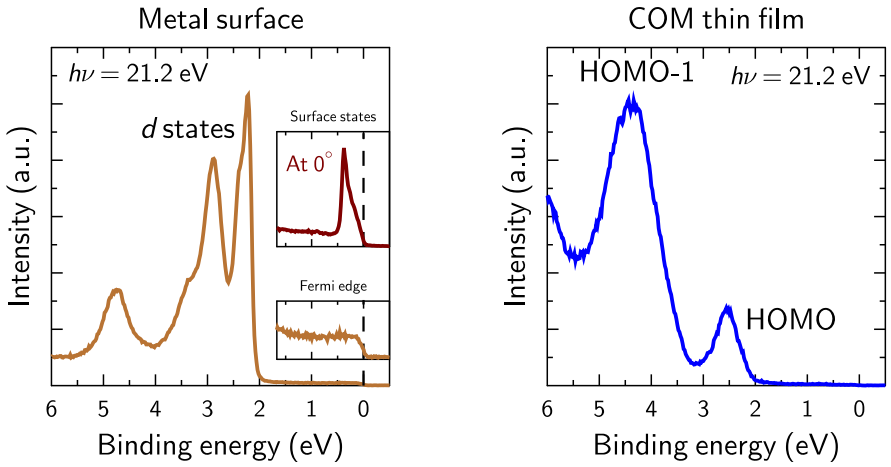

Figure 3.4.: Selected scans to illustrate the features observed in UPS. Unless stated within the plot, the electrons were collected at a take-off angle of 45°. The source employed is a helium lamp where the He I line is selected ($h\nu = 21.2\,\text{eV}$). At the left, the outer energy levels, close to the Fermi edge, of a Cu(111) surface are shown. The bottom inset is a zoom to the Fermi edge, whereas the top inset shows the same magnification but the take-off angle is 0°. The change of the angle makes the surface states of the metal visible. At the right, a thin film of PTCDI deposited on Cu(111) is measured. The metal *d*-band has disappeared and the molecular levels of the VB are visible. Most prominently, the HOMO and related levels are mapped.

structure. By considering the angular-dependence of photoemission, the kinetic energy of the electrons as well as its momentum are recorded, thus one obtains $E(\boldsymbol{k})$ [181,182]. Orbital tomography is an extension of it, which has been applied to study the frontier orbitals of molecular adsorbates. The particularity is that it renders a 3D reconstruction of the molecular orbitals and their changes upon contact with a substrate and/or intermolecular interactions [105,184–188].

UPS has direct access to the molecular HOMO and other related valence-band levels (Fig. [3.4]). Together with inverse photoemission spectroscopy (IPES), which probes the empty conduction band and thus it accesses the LUMO, they give a direct measurement of the transport gap [189,190][6]. Another important magnitude that can be readily obtained with UPS (provided that the sample is biased with an external voltage) is the work function. Indeed, as shown schematically in Fig. [3.1], by measuring the position of the secondary electron cutoff (SECO), one can directly measure the sample work function [191] and, even more important, the comparison of the SECO position before and after COM deposition allows to measure the interface dipole. UPS is, therefore, especially suited to obtain the charge injection/extraction barriers and hence the energy-level alignment at inorganic-organic, organic-organic as well as inorganic-inorganic interfaces [49].

Similarly to XPS, spectral changes such as broadening, peak (binding energy) shifting and splitting provide details of the electronic, chemical and structural changes at the

[6] Note that the transport gap is different from the optical gap (probed in photoluminescence experiments). In some materials with large exciton binding energies, such as organic semiconductors, the absorption of a photon may produce an exciton without actually decoupling the electron from the hole. Thus, the optical gap is the minimum energy required for a photon to be absorbed, whereas the transport gap is the minimum energy to separate a hole from its coupled electron. The transport gap is usually considered as the optical gap plus the exciton binding energy. Note that for materials with low exciton binding energies, such as inorganic semiconductors, both gaps may be almost identical.

inorganic-organic interface and within the organic material as well. In particular, enhanced screening by the substrate compared to the thin-film regime is also typically observed by shifts of the HOMO-related peak(s). Pure interface phenomena such as charge transfer from the substrate to the LUMO can also be observed in UPS. More precisely, features around the Fermi edge are typically related to LUMO filling (labeled former LUMO, since it is not unoccupied anymore), which can only be seen for coverages around one monolayer (provided that the growth is layer by layer). Vibrational effects have to be considered when interpreting valence-band spectra since they are of special importance to assess the transport properties of organic materials [46, 192, 193]. Besides some general peak broadening, it has been recently shown that even some angular-dependent intensity changes are connected to electron coupling with some specific vibrational modes [194]. Not only vibrational properties of the material can be derived from UPS, but also structural ones. The appearance/disappearance of spectral features in coverage-dependent studies may reveal the growth mode of a certain molecule on a certain substrate. The molecular orientation has also an impact on the UPS signal [195,196]. Indeed, the ionization potential (understood as the position of the HOMO with respect to the vacuum level) depends on the molecular axis (long vs. short) that is being excited [195].

Finally, similarly to the filling of the LUMO, gap states in organic as well as inorganic semiconductors can be revealed with UPS, especially high-resolution UPS, which can be identified as intensity features appearing within the gap. Such features may be, in some cases, very weak. Thus, it is very important to have a good signal-to-noise ratio to destinguish them from the background. This requires special experimental considerations, for instance a well electrically-insulated UHV chamber. The gap states have been revealed to be very important for the transport properties of organic materials and interfaces [197–199] as well as a mechanism to facilitate the charge transfer between an inorganic-organic semiconductor interfaces [127].

3.3. The X-ray standing wave technique (XSW)

At the core of this work is the X-ray standing wave (XSW) technique. Shortly (see Fig. [3.5]), *it is an interferometric technique that uses photoexcited signals, produced in the overlapping region of two Bragg-diffracted X-ray beams, to obtain high-precision and chemically sensitive adsorption distances of adsorbed species on single crystals.*

Before starting with the scientific part, we historically contextualize this technique so as to give a broad overview of its applications. For the interested reader, Ref. [200] collects the memories, thoughts and experiences of those who pioneered the development of the XSW technique.

Boris W. Batterman first reported that the fluorescence intensity emitted from a single crystal, illuminated with X-rays, changed when rocking the crystal around the Bragg condition, thus highlighting the presence of an X-ray standing wave field [201][7]. By matching the maxima and minima of the fluorescence signal with the reflected X-ray intensity around the Bragg angle and using dynamical diffraction theory, he correlated them with the relative position of the atomic planes of the crystal. A few years later, he used this principle

[7] Interesting enough, a similar effect had been found several years before by measuring the γ-rays, around the Laue condition, created from the interaction of neutrons with a calcite crystal [202].

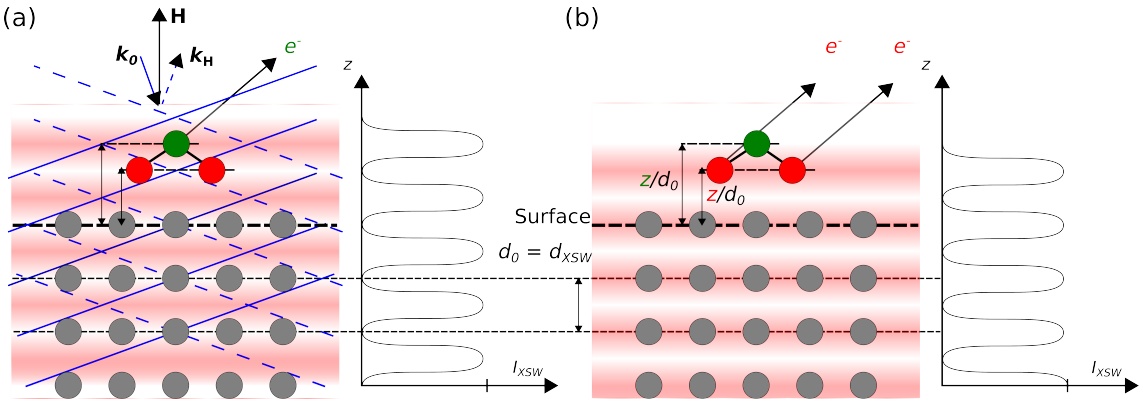

Figure 3.5.: Sketch that shows the core idea of the XSW technique. (a) An incoming X-ray $\boldsymbol{k}_0$ overlaps with the Bragg-reflected beam $\boldsymbol{k}_\mathrm{H}$ and creates an interference field inside as well as above the crystal surface. The periodicity between maxima (or minima) of intensity (d_XSW) is the same as the lattice spacing (d_0) along the diffraction direction **H**. (b) Although the interference field is stationary, if one scans the incident angle or beam energy around the Bragg condition, the intensity profile (I_XSW) can be shifted by half a lattice spacing. Consequently, if an atom is initially in an intensity maximum, after the scan will be in a minimum. By monitoring the absorption of X-rays around the Bragg condition, the absorption rate can be linked to the relative position of the atoms within the field (z/d_0). Since the absorption rate can be related to the number of emitted photoelectrons, by measuring the core-level signal of a given element around the Bragg condition, the adsorption distance can be obtained for different elements within the molecule.

to locate the position, relative to the silicon atomic planes, of dopant arsenic atoms embedded in the crystal [203]. Soon thereafter, it was shown that the XSW field extended outside the crystal surface [204], opening up the door to not only the mapping of dopants within a crystal structure [205] and the study of buried interfaces [206–208] but also the location of adsorbed species on the crystal surface [209]. For the latter, the one of interest in this work, first, adsorbed atoms were studied [209, 210], Langmuir-Blodgett films [211] and atomic layers followed [212]. Larger molecules adsorbed on different surfaces started to be studied in the 90s [213, 214]. Finally, the first measurements of COM molecules adsorbed on metal surfaces came only in the beginning of the new century [215–218].

3.3.1. Fundamentals of the technique

In the following, we are going to clarify the different phenomena involved in this quite exotic technique and explain how the adsorption distances are obtained. Emphasis is put more on the concepts rather than the mathematical description, which can be found in Refs. [47, 121, 205, 219, 220].

The key point that this section wants to explain is how one is able to obtain chemical and structural information of an atom, in this case adsorbed on the surface, by using X-ray diffraction. For this, one has to start considering how X-rays propagate through a crystal. This is better explained with dynamical diffraction theory [221], which goes beyond the typical kinematic diffraction model used to explain textbook scattering experiments. It takes into account multiple reflections of the X-rays, possible absorption, extinction and interference effects. By considering the Maxwell equations to describe the incoming X-rays and the dielectric constant of the material, under some assumptions[8], one can express the

[8] The X-ray-incidence angle is close to 90° (we will elaborate more on this below), the X-rays are σ-polarized, centrosymmetric crystals are used (to simplify the calculations), there is no conductivity at

incoming wave $\mathcal{E}_0$ and the Bragg-diffracted one along the crystal direction $\mathbf{H}$ $\mathcal{E}_\mathrm{H}$ as:

$$\mathcal{E}_0 = \mathscr{E}_0 \exp\left[2\pi\mathrm{i}\left(\omega t - \boldsymbol{k}_0 \cdot \boldsymbol{r}\right)\right] \tag{3.2}$$

$$\mathcal{E}_\mathrm{H} = \mathscr{E}_\mathrm{H} \exp\left[2\pi\mathrm{i}\left(\omega t - \boldsymbol{k}_\mathrm{H} \cdot \boldsymbol{r}\right)\right] \tag{3.3}$$

where ω and $\boldsymbol{k}$ are the angular frequency and the wave vector, respectively, and $\mathscr{E}$ is the electric field amplitude. The initial and the reflected complex amplitudes are related, assuming of course that they are coherent[9], via $\mathscr{E}_\mathrm{H} = \sqrt{R}\mathscr{E}_0 = \exp(\mathrm{i}\nu_\mathrm{H})$, with ν_H the phase between the two amplitudes and R the reflectivity, which can be further described as:

$$\sqrt{R} = \frac{\mathscr{E}_\mathrm{H}}{\mathscr{E}_0} = -\sqrt{\frac{F_\mathrm{H}}{F_0}}\left(\eta \pm \sqrt{\eta^2 - 1}\right), \tag{3.4}$$

where F is the complex structure factor and η the normalized angle parameter:

$$\eta = \frac{2(E_\mathrm{Bragg} - h\nu)/E_\mathrm{Bragg} \sin^2(\Theta_\mathrm{Bragg}) - \Gamma F_0}{\Gamma \left|F_\mathrm{H}\right|}. \tag{3.5}$$

with $\Gamma = \frac{r_\mathrm{e}\lambda^2}{\pi V}$, being r_e the classical radius of the electron, V the volume of the unit cell and λ the wavelength of the X-rays. These two equations describe how the reflectivity changes when either the angle, Θ, or the energy $E = hc/\lambda$ via the Bragg condition $\lambda = 2d_0 \sin\Theta_\mathrm{Bragg}$ (being d_0 the spacing of diffraction planes) of the incoming beam are scanned around the Bragg condition. At this point, it is worth noting that the presence of multiple scattering events, taken into account in dynamical diffraction theory, extends the possibility of having Bragg diffraction also for an interval around E_Bragg (Θ_Bragg). Indeed, Fig. [3.6] shows the reflectivity (or Darwin) curve, R, obtained by scanning the beam energy[10], $h\nu$, around E_Bragg.

By knowing the reflectivity, one is able to describe the intensity at a position $\boldsymbol{r}$ within the overlapping region between the incoming and the Bragg-reflected beam:

$$I_\mathrm{XSW}(\nu_\mathrm{H}, \boldsymbol{r}) = \frac{\left|\mathscr{E}_0 + \mathscr{E}_\mathrm{H}\right|^2}{\left|\mathscr{E}_0\right|^2} = 1 + R + 2\sqrt{R}\cos(\nu_\mathrm{H} - 2\pi\mathbf{H}\cdot\boldsymbol{r}). \tag{3.6}$$

This equation describes the intensity of the XSW field, which is spatially and phase modulated as we see from the cosine term. Noteworthy, the time dependence has been removed indicating that the maxima and minima do not change with time, they are stationary. However, as seen in Fig. [3.6], when scanning through the Bragg condition, the phase changes from π, for $h\nu \ll E_\mathrm{Bragg}$, to 0, for $h\nu \gg E_\mathrm{Bragg}$, effectively shifting the maxima and minima position by half a lattice plane. Hence, a fixed position within the XSW field will see a shifting intensity. On the contrary, for a fixed phase, the intensity will be different depending on the position we are at. Interestingly, only the z component of $\boldsymbol{r}$

X-ray frequencies ($\sigma_c = 0$), there is a periodic dielectric constant and the magnetic behavior is that of the vacuum ($\mu_r = 1$).

[9] The quality of the single crystal, i.e. the periodicity and homogeneity, are very important for this to happen.

[10] Nowadays, with synchrotron facilities widely available, tuning the X-ray energy has become the standard method. Also, note that many references use E, instead of $h\nu$, to label the beam energy. Hence, $E - E_\mathrm{Bragg}$ is usually found as the x-axis label of many XSW plots.

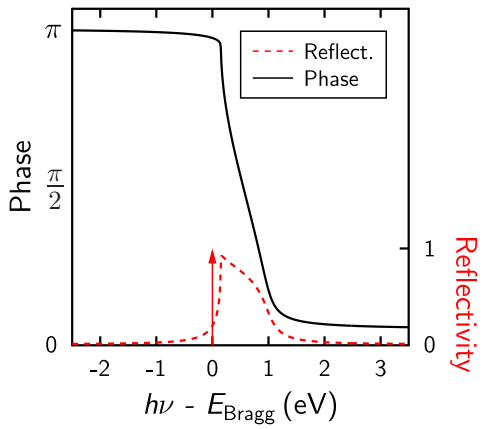

Figure 3.6: Example of reflectivity (or Darwin) curve (dashed red line) and phase difference (solid black line) between incident and reflected beam obtained when the beam energy $h\nu$ is scanned around the Bragg condition, as described by dynamical diffraction theory. For comparison, the red arrow would correspond to the reflectivity as described by kinematic diffraction theory, where Bragg diffraction happens only at a particular beam energy (or diffraction angle). It is worth noting that the asymmetric shape of the reflectivity stems from the fact that there are losses due to absorption. The parameters of the (111) reflection of a copper single crystal were used for the simulation. Figure adapted from Ref. [47].

is meaningful because $\mathbf{H}$ is a vector perpendicular to the lattice planes. Actually, since the system is periodic, z/d_0 is relevant. The spatial dependence of the XSW field can be seen in Fig. [3.7], where it becomes clear that small variations of $\mathbf{H} \cdot \boldsymbol{r}$ produce extreme intensity changes, giving rise to the outstanding spatial resolution of the technique.

Now, we have to see how one can exploit the spatial dependence of the intensity field to extract the position of the atoms. For that, we take advantage of the fact that the atoms of the material absorb X-rays. In particular, the atoms within the XSW field will absorb more or less radiation depending on the intensity that they experience. The absorption of radiation induces different processes, summarized in Fig. [3.8], that can be used to infer the intensity of the field. In our case, however, we restrict ourselves to photoemission. Therefore, one has to see how the measured signal (photoelectrons) can be traced back to the position of the atoms within the field.

The absorption of photons and subsequent photoelectron emission has been already

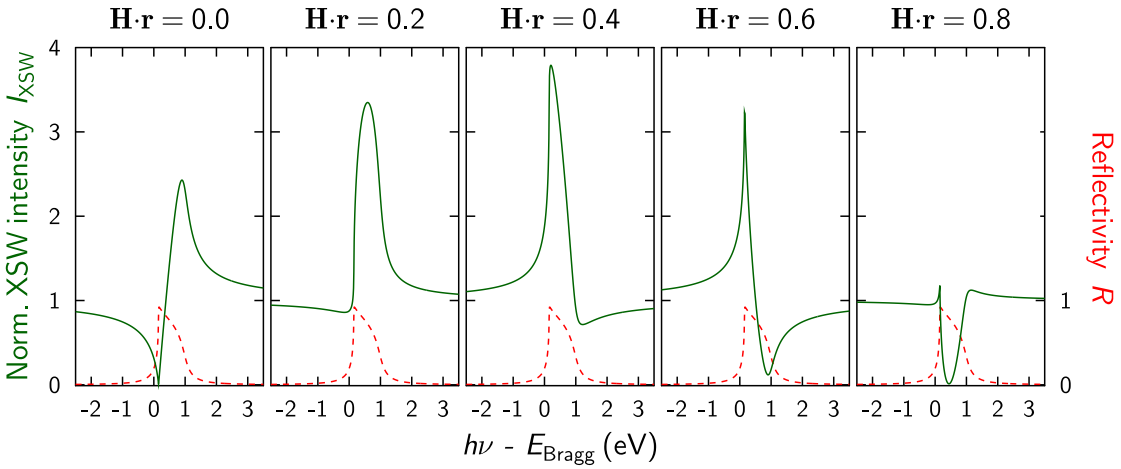

Figure 3.7.: Normalized intensity of the XSW field for different values of $\mathbf{H} \cdot \boldsymbol{r}$, i.e. at different z/d_0 positions within the standing wave field. The intensity can take ideal (without considering absorption of X-rays) values of 4, in the constructive case, and 0, for the totally destructive case. Note that positions very close to each other see very different intensities, rendering a highly precise way to distinguish between two different positions. Figure adapted from Ref. [47].

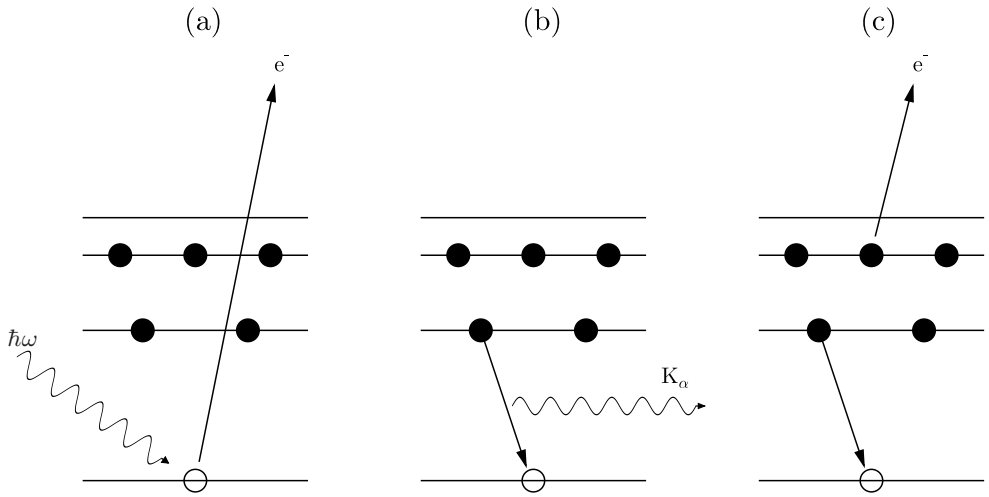

Figure 3.8.: Different processes that can be used in an XSW experiment to obtain information about the photon absorption. (a) Emission of an electron (photelectric effect). (b) Fluorescence [208] and (c) Ejection of Auger electrons [222]. Figure taken from Ref. [47].

discussed in Sec. [3.2]. Though, we remark that, when describing the photoexcitation by the XSW field, the probability of getting an electron to a certain excited state is evaluated within the dipole approximation, which considers it to be proportional to the intensity of the (XSW) field. Therefore, the number of collected electrons, i.e. the photoelectron yield, is proportional to the XSW field. Hence, one can write Eq. [3.6] as:

$$Y_{\mathrm{P}}(\nu_{\mathrm{H}}, \boldsymbol{r}) = 1 + R + 2\sqrt{R}\,\cos(\nu_{\mathrm{H}} - 2\pi.\mathbf{H}\cdot\boldsymbol{r}) \tag{3.7}$$

where Y_{P} is the photoelectron yield. As we have mentioned before the spatial dependence $\mathbf{H}\cdot\boldsymbol{r}$ is actually z/d_0 and so far we have considered that only one atom at a given z/d_0 participates. In reality, since static disorder and thermal vibrations are present, a given species or set of equal atoms do not occupy the same position but are distributed around a mean value. One takes this into account by setting a distribution function for z, $G(z)$, where $\int_0^{d_0} G(z)\mathrm{d}z = 1$, indicating that a given species is totally localized within an XSW period[11], which in z is equal to the crystal lattice spacing along $\mathbf{H}$. Then, Eq. [3.7] takes the following form:

$$Y_{\mathrm{P}}(\nu_{\mathrm{H}}, z) = 1 + R + 2\sqrt{R}\int_0^{d_0} G(z)\cos(\nu_{\mathrm{H}} - 2\pi\,\frac{z}{d_0})\mathrm{d}z \tag{3.8}$$

Since it is the structural information of the measured species, contained in $G(z)$ and z, what we want to find out, two parameters are used to compact this information. The coherent position P_{H} and the coherent fraction f_{H} will be the parameters that we have to infer from the measurements. At this point, we note that, although not explicitly written, R and ν_{H} depend on the parameter $h\nu - E_{\mathrm{Bragg}}$, as seen in Fig. [3.6]. Consequently, from

[11] Remember that the distance between two maxima (or minima) of the XSW field is the same distance as two lattice plane of the crystal, $d_{\mathrm{XSW}} = d_0$.

an experimental point of view, for a fixed system and setup geometry, the only varying parameter is the photon energy that is scanned around the Bragg condition. Hence, the working condition for the data analysis takes the following form:

$$Y_{\mathrm{P}}(h\nu) = 1 + R + 2\sqrt{R}\, f_{\mathrm{H}} \cos(\nu_{\mathrm{H}} - 2\pi P_{\mathrm{H}}) \tag{3.9}$$

The coherent position takes values between 0 and 1 (being both geometrically equivalent) and is directly related to the (mean) position of the species being considered via:

$$d_{\mathrm{H}} = (n + P_{\mathrm{H}})d_0 \quad n = 0, 1, 2, \ldots \tag{3.10}$$

where n introduces an ambiguity that stems from the periodicity of the XSW field, but can be removed with common sense and the physical constraints of the system[12].

The coherent fraction also takes values between 0 and 1 and describes how ordered are the atoms contributing to d_{H}. 0 corresponds to the case where they are randomly distributed around d_{H} and 1 is for the case where all atoms are exactly at d_{H}. The information contained in f_{H} is intimately related to the atomic behavior of the emitters. More precisely, f_{H} is the scalar product of all the separate effects that influence the distribution of atoms along **H**: thermal vibrations, described with the Debye-Waller factor D_{H}; static disorder of the atoms contained in the geometric factor α_{H} and the portion of atoms C not randomly distributed along **H**. All influence the coherent fraction: $f_{\mathrm{H}} = Ca_{\mathrm{H}}D_{\mathrm{H}}$ and have to be equal to 1 for a perfect ordering. The other extreme case, $f_{\mathrm{H}} = 0$, can be obtained from different ways. The obvious one is a random distribution along **H**, i.e. $C = 0$, but the same situation can be achieved if the contributions to the electron yield, originating from the static distribution of different positions cancel each other ($\alpha_{\mathrm{H}} = 0$). α_{H} is the only one that also influences the coherent position. We note that, for the case of adsorbates, the coverage has to be equal or below 1 monolayer. The main reason is that adsorption distances only make sense for the first layer, but also, adding extra layers just artifically increases the coherent fraction because the collected photoelectron yield would come already from different positions in z.

By taking a deeper look at the coherent fractions, one can obtain, for instance the vibration of amplitude of the studied species [210] and even reconstruct a full unit cell, thus bypassing the phase problem found in diffraction experiments [223]. Without elaborating much, f_{H} can be arranged as:

$$f_{\mathrm{H}} \mathrm{e}^{2\pi \mathrm{i} P_{\mathrm{H}}} = \int_0^{d_0} G(z) \mathrm{e}^{2\pi \mathrm{i}\ z/d_0} \mathrm{d}z \tag{3.11}$$

In this equation, f_{H} can be interpreted as the first Fourier component of the distribution function $G(z)$ times a phase factor that contains P_{H}. It is therefore possible to reconstruct $G(z)$ if f_{H} and P_{H} are measured for sufficient diffraction directions **H**. This method has been applied, for instance, to unambiguously reconstruct the unit cell of complex crystals [224, 225], in what is called XSW imaging. Triangulation can also be employed to well-ordered adsorbates in order to find their position with respect to the substrate [66].

[12] An example on how to deal with the ambiguity n for an adsorbed species is shown in Fig. [B.2] of Appendix [B].

3.3.2. Practical and technical considerations and data analysis

The popularity of this technique, with its chemical sensitivity and high precision, is limited by its demanding technical prerequisites. In the following, we are going to describe the main requirements needed to perform the XSW technique. But, let us first shortly recall how an XSW experiment works. Taking Eq. [3.9], we want to obtain f_H and P_H. For that, one needs to know the photoelectron yield and the reflectivity. Thus, for a fixed diffraction geometry, one uses different beam energies around the Bragg condition of the given diffraction direction and simultaneously measures, at each point, the reflectivity and an XPS scan for the core-level of interest to obtain the photoelectron yield. Usually, 30 to 40 data points are measured within $\pm 3\,\mathrm{eV}$ around E_{Bragg}.

3.3.2.1. Beam and beamline requirements

The main purpose of using synchrotron facilities[13] for XSW experiments is that the X-ray energy has to be tuned. In addition, it has to be monochromatic and without higher harmonics, which may add undesired contributions to the reflectivity. Also, the beam has to be defocused in order to reduce possible beam damage to the organic compounds but this has to go along with a high photon flux to keep the count rate high. The beam has to be stable, meaning that there has to be a proper feedback system that corrects the position of the crystal monochromators every time that they move to tune the energy. Also, one has to take into account the influence of the monochromator on the beam profile. After the reflection by the monochromator crystal (in our case made of silicon), the beam width changes. Thus, a reflection of the crystal monochromator has to be chosen that renders an energy width smaller than that of the sample substrate. In any case, the convolution between the monochromator and the sample reflectivities has to be considered in the data analysis. Besides, one has to be able to measure the beam current, which is usually used as the normalization parameter when adding up the different scans. For further details, Ref. [224] gives information about one of the first dedicated XSW facilities, namely, beamline ID32 (closed in 2012) at the European Synchrotron Radiation Facility (ESRF), France. For comparison, in Appendix [H], we discuss the improvements needed in beamline KMC-1, at BESSY (Berlin), and its HIKE end-station to satisfactorily accommodate XSW experiments for adsorbed systems.

Finally, since only (sub)monolayer coverages are measured, excellent UHV conditions are required (low $10^{-10}\,\mathrm{mbar}$). Also, the sample manipulator inside the chamber needs to move in 3 spatial directions as well as to rotate in the polar and azimuth directions to optimize the sample position with respect to the reflectivity screen and the analyzer.

3.3.2.2. Experimental geometry

As the sharp reader may have already guessed, this technique is overall limited by the quality of the substrate used to generate the XSW field. The periodicity and intensity of the field relies on a well-ordered and homogeneous (with low mosaicity) crystal structure along the diffraction direction **H**. Although really high-quality crystals are available, this

[13] The reader is referred to Ref. [226] for a detailed explanation of the mechanisms involving the generation and handling of synchrotron radiation.

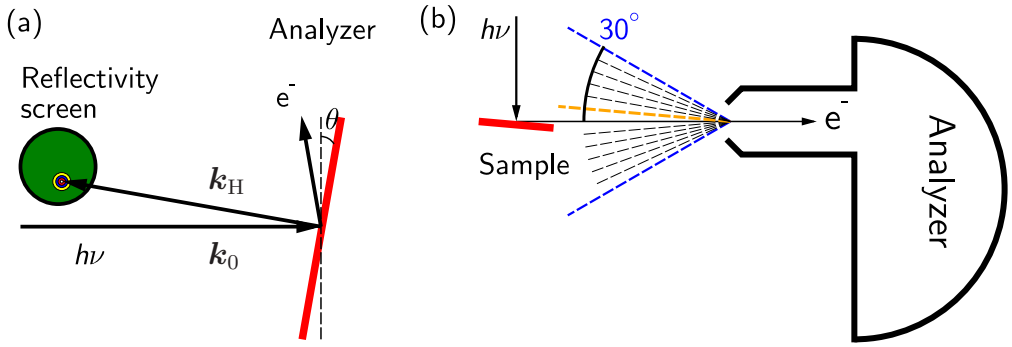

Figure 3.9.: Sketch of the relevant geometries in a normal-incidence XSW (NIXSW) experiment. The sample is depicted in red. (a) A strict normal-incidence (NI) geometry would prevent a proper measurement of the reflectivity. Consequently, the sample is slightly tilted (by θ) to facilitate that the reflected beam impinges on the reflectivity screen. As it is discussed in the main text, it is desirable to collect the electrons at very small emission (take-off) angles, which is achieved by placing the detector at 90° with respect to the incoming beam. (b) Sketch of the electron analyzer and the implications of the ±30° large acceptance angle (in blue). The electrons collected at grazing angles have negligible non-dipole contributions. Therefore, they are desirable for a simplified analysis of the XSW data. The large acceptance angle of the detector also takes electrons photoemitted under conditions where there are substantial non-dipole contributions. In transmission mode, all the electrons within the blue cone are integrated. In angular mode, the electrons are sorted out by their emission angle. Thus, one can consider only the grazing-emission electrons by selecting the proper slice (in orange).

still represents a hard constraint for the applicability of this technique. At the end of the 80s, a variation of the XSW technique was developed that tolerates some degree of imperfection in the crystal quality. The so-called normal-incidence (NI) XSW technique, uses a backreflection geometry to create the XSW field, i.e. the incoming beam impinges at $\sim$ 90° with respect to the crystal planes [227] (sketch in Fig. [3.9a]). The reason is that the intrinsic angular width of the reflectivity (see Fig. [3.6]) curve is highest when the diffraction angle is 90°. This is the diffraction geometry used in all our experiments.

Another important experimental parameter is the position of the electron analyzer with respect to the incoming beam. As already mentioned, the XSW analysis is enormously simplified if the photoemission process is considered within the dipole approximation. Without much detail, it can be seen that the photelectron yield is asymmetric with respect to the incoming and reflected beam (forward/backward asymmetry). However, when detecting the electrons at 90° with respect to the incoming photon, this difference disappears. It is common, in dedicated XSW beamlines, to have the analyzer and beam at 90° from each other so that a NI geometry can be configured and the non-dipole contributions can be greatly removed, simplifying the experimental conditions and the subsequent data analysis.

3.3.2.3. Non-dipole corrections and recording mode

As it has been stated above, collecting the photoelectrons at grazing emission in a NI geometry (the analyzer is placed at ∼90° with respect to the incoming beam) minimizes possible non-dipole contributions to the photoemission process, thus enormously simplifying the XSW analysis. Besides, they can be further minimized if the photoelectron yield is obtained from symmetrical core-level states, namely, *s*-orbitals. However, the electron analyzer available at the beamline has a relatively large acceptance angle of ±30°

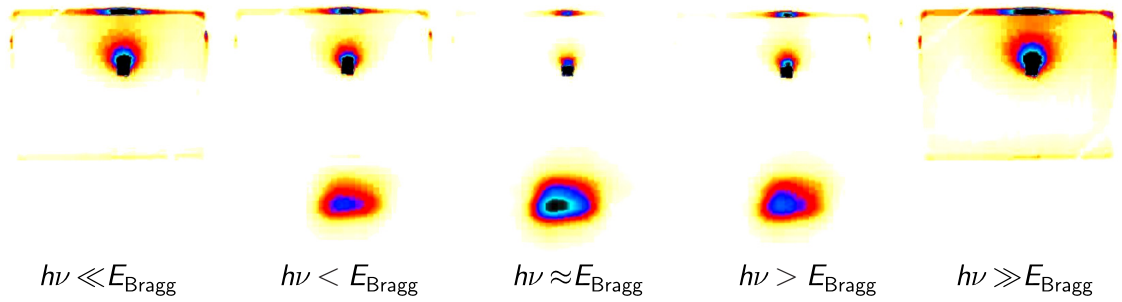

Figure 3.10.: Beam reflection on a ZnO substrate for different X-ray energies around the Bragg condition (E_{Bragg}). Top row: owing to the X-ray-induced fluorescence one can see, with a camera installed inside the chamber, how the beam impinges on the substrate. Note that the fluorescence dramatically decreases around E_{Bragg} because the X-rays penetration is drastically reduced. Bottom row: the fluorescence produced by the reflected beam impinging on the reflectivity screen is shown for each corresponding image above. The intensity of the fluorescence (also recorded with a camera inside the chamber) as it changes when the beam energy is scanned around E_{Bragg} is used as the experimental measurement of the reflectivity.

(Fig. [3.9b]), which implies that a portion of the electrons will not be collected at grazing angles. Furthermore, for practical purposes, a strict NI is not possible and the sample is tilted 2–3°, slightly deviating from the ideal geometry. Ref. [228] studies in detail all this contributions to the final coherent fractions and positions, although using a deviation of 7° from the NI geometry for their calculations thus overvaluing the actual changes of the coherent positions.

The electron analyzer has two collecting modes: in transmission mode the electrons are collected regardless of their emission angle, whereas in angular mode they are sorted out by their incoming angle (Fig. [3.9b]). For this purpose, the acceptance angle of the analyzer can be divided in different slices, in our case 24 slices with 2.5°. This allows one to select the electrons that enter the analyzer at grazing angles thereby minimizing all the effects mentioned above. As shown in Appendix [F], angular-dependent XSW measurements performed on a bare ZnO crystal concluded that the impact on the coherent position is relatively small and the transmission mode can be safely used, although the contributions to the coherent fractions may become relevant in some cases (not yet well understood).

3.3.2.4. Reflectivity measurements

The reflectivity is measured using a fluorescent screen conveniently located such that the reflected beam can easily impinge on it and only small corrections to the sample position are required. To experimentally account for the reflectivity, either the fluorescent light can be collected with a suitable camera (and/)or the drain current generated on the screen can be measured. As an example, Fig. [3.10] shows, for different beam energies around the Bragg condition, how the beam is impinging on a ZnO substrate and the corresponding changes in reflected beam on the fluorescent screen.

3.3.2.5. Photoelectron yield and data evaluation

As stated before, the photoelectron yield is extracted from XP spectra. More precisely, the area below the curve is used to evaluate the photoelectron yield. The chemical sensitivity

also implies that adsorption distances for inequivalent atoms within a given species can also be resolved as long as the separate contributions to the photoelectron yield can be decoupled. Consequently, by just taking the total area under a particular core-level signal, and applying suitable background subtraction, the average position of all the possible inequivalent species is obtained. Then, with the right fitting model, the positions for the different inequivalent species can also be resolved. Chapters [6] and [7] provide some nice examples of this. Nowadays, with dedicated beamlines available, the real challenge is finding a suitable model that can resolve as many inequivalent species as possible, in order to maximize the structural information.

At the synchrotron, data points are obtained with different X-ray energies around the Bragg condition, each containing a value for the reflectivity, one XPS scan, the beam current as well as the sample drain current. The beam current is used to normalize the data and effectively remove any undesired fluctuations of the beam flux. The sample drain current is recorded to check for abnormalities in case the measurements show unexpected features. For the results reported here, the software CASAXPS [229] was used to evaluate the XPS data, fit it and extract the relevant peak areas (i.e. the photoelectron yield). The experimental data (reflectivity, photoelectron yield and beam current) were fitted, using Eq. [3.9], with a Scilab [230] script, which also can include non-dipole corrections [218], provided by Tien-Lin Lee, beamline scientist at I09, DLS (see Sec. [3.5.1]). Finally, the script also allowed to correct possible mosaicity contributions by convoluting the rocking curve with a Gaussian function of a certain FWHM (typically $\sim$0.3 eV).

3.4. Low-energy electron diffraction (LEED)

Low-energy electron diffraction (LEED) is employed to characterize the in-plane structure of single-crystal surfaces, either clean or with adsorbates on them (it is implied that the investigated structure must hold some degree of symmetry). Due to the high cross section of electron-electron interactions, this technique is very surface sensitive (thus requiring UHV). Electrons (in the 10–200 eV of LEED) have a smaller de Broglie wavelength than X-rays, becoming especially suited to study surfaces at the atomic scale.

As in any scattering technique, not only diffraction directions (spots) but also their intensity contain information. A qualitative analysis of the diffraction spots can already tell which kind of symmetry the surface or adsorbate has, if any at all. More elaborate techniques, such as I–V LEED [231] and spot profile analysis LEED (SPA-LEED) [232], also analyze the intensity profiles providing information of the surface roughness. With dynamical-diffraction analysis of the I–V LEED one can reconstruct the surface unit cell with high precision (similarly to SPA-LEED [233]) and even obtain a full 3D description of the adsorbate geometry, including the adsorption distance [234–236]. However, fitting the I–V curves is computationally expensive and, at the end, is also an indirect method since the information stems from the refinement of a structural model that requires some initial guess [237]. Finally, low-energy electron microscopy (LEEM) [238, 239] can be used to investigate real-time growth of adsorbates [88, 115, 240]. Ref. [241] provides a good summary of LEED-based techniques. Some disadvantages are that LEED is not chemically-sensitive, does not provide information of the bulk and, in most cases [237], requires a long-range order, limiting its application to disordered systems.

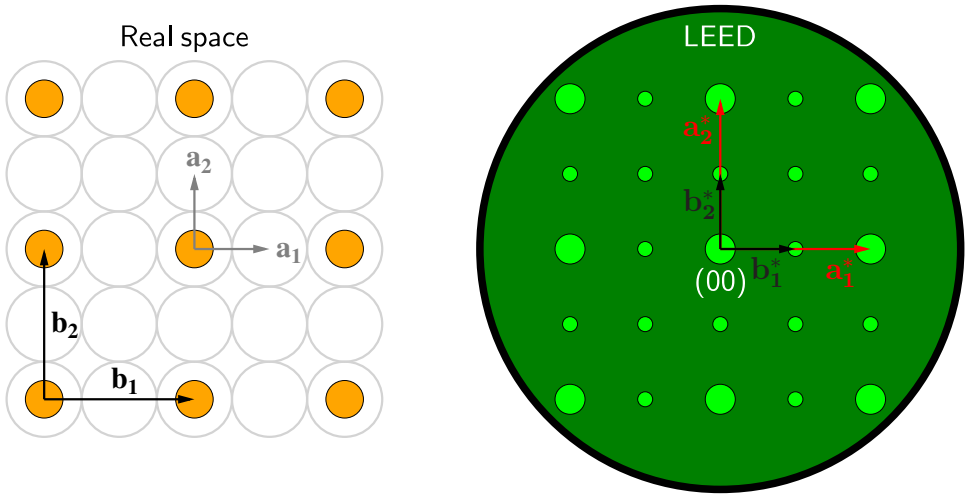

Figure 3.11.: Real vs. reciprocal space as obtained by LEED. At the left, as an example, a fcc(100) surface (gray) is covered with a (2×2) overlayer adsorbing on top sites (orange). In real space, the unit cell of the adsorbate is two times bigger than that of the substrate. At the right, the corresponding LEED pattern, as seen in the reflectivity screen, is depicted. Note that the adsorbate vectors (in black) are half the length in reciprocal space.

LEED devices consist of an electron gun (commonly using a thermionic cathode), which produces a monochromatic stream of electrons, and some optic elements, required to collimate and focus the beam. Electrons impinge normally on the surface, being subsequently back-scattered. By means of a fluorescent screen placed in front of the sample (and around the electron gun), the scattered electrons that interfere constructively produce bright spots on it. Beam damage is a very important issue and some experimental modifications have been implemented in order to reduce it when studying organic overlayers. Of particular interest here is the addition of microchannel plates (MCP) aimed at reducing the beam current required to have a detectable signal. The MCP increases the detection sensitivity thus requiring less electrons to obtain a good signal.

The qualitative information, which is the one exploited in this work, is obtained by scanning the reciprocal space and observing the diffraction spots on the screen that are representative of the symmetry of the surface and/or adsorbate in the real space. The electron energy can be tuned as a way to effectively change the reciprocal space region being probed. Indeed, according to Laue's condition for constructive interferences, $\boldsymbol{k}_f - \boldsymbol{k}_i = \mathbf{G}$, where $\boldsymbol{k}_i$ and $\boldsymbol{k}_f$ are the final and initial wave vectors, respectively, and $\mathbf{G}$ a vector in the reciprocal space, the higher (lower) the electron energy, the smaller (larger) its wavelength and, consequently, larger (smaller) the wave vector $\boldsymbol{k}$[14]. It is worth noting that, due to the extreme surface sensitivity, as a first approximation the interference along the surface normal can be neglected and it becomes a 2D scattering problem. Surface unit cells can be obtained from the position of the diffraction spots as well (Fig. [3.11]). Beyond this, a precise analysis of the spot distribution is required, using a matrix analysis of the data, which enables a full in-plane characterization of the adsorbed layer and its epitaxy [242].

[14] de Broglie's theory states that any subatomic particle can be treated as a wave, with a certain wavelength λ given by $\lambda = h/p$, where h is the Planck's constant and p is the particle momentum. Therefore, the electron wavelength is related to its energy via $\lambda = h/\sqrt{2mE}$, where m is the electron mass and E the energy. Finally, the modulus of the wave vector $\boldsymbol{k}$ is equal to $2\pi/\lambda$.

Some reviews in this matter can be found here [243, 244].

3.5. Experimental setup

Next, a brief description of the setups employed to perform the different experiments is given. In addition to the main locations, namely, the beamline I09 at Diamond Light Source and the Soochow University, additional UPS measurements were performed at the Humboldt Universität in Berlin, within the context of the ZnO project. The specific details of the setup will be given in the corresponding chapter.

3.5.1. The I09 beamline at the Diamond Light Source (DLS)

The XSW and soft-XPS experiments were carried out at the beamline I09 of the Diamond Light Source (DLS) at the Harwell Science & Innovation Campus, Didcot, UK. It is a rather new beamline (the first experiments, still in commissioning time, started in 2013). Consequently, during the period where our experiments were performed, the end-station underwent different extensions and improvements (see Refs. [47, 245] for a description of the early setup). For instance, two additional preparation chambers were installed next to the analysis chamber. The main chamber is composed by the lower analysis section and an upper preparation chamber, both separated by a gate valve. Each separate chamber is equipped with LEED and the preparation chambers also allocate a sputtering gun and a double e-beam/resistive heater. The main manipulator also contains a double resistive/e-beam heater (up to 1500 K) and has 5 degrees of freedom, namely, x, y, z plus polar (θ) and azimuth (φ) rotation angles. It also allows sample cooling through liquid nitrogen ($T < 100\,\mathrm{K}$) or liquid helium ($T < 50\,\mathrm{K}$). Gases and/or water can be dosed in the main preparation chamber through a leak valve. The electron analyzer attached to the analysis chamber (base pressure 3×10^{-10} mbar) is a VG Scienta EW4000 HAXPES with an acceptance angle of $\pm30^\circ$ that allows a transmission as well as an angular recording mode. A UPS setup is also attached to the analysis chamber (He lamp with monochromator). The data acquisition is controlled through the dedicated software GDA [246] that allows to tune and modify virtually all the parameters of the measurement. The visualization software DAWN [247] is also available at the experimental hutch to visualize the data.

The beamline (layout in Fig. [3.12]) delivers a soft and a hard X-ray beam that are both focused on the same spot of the sample. The soft X-ray beam ($h\nu = 230 - 2000\,\mathrm{eV}$) is monochromatized with a plane grating monochromator, whereas the hard X-ray beam ($h\nu = 2.1 - 18\,\mathrm{keV}$) has a silicon double crystal monochromator. The beam can be defocused up to a size of $300\,\mu$m.

3.5.2. Setup at Soochow University

The UPS measurements, the coverage-dependent XPS and the LEED measurements presented in Chap. [6] and [7] reported in this work were carried out at Prof. Steffen Duhm's group, part of the Institute of Functional Nano & Soft Materials (FUNSOM), at Soochow University, China. The setup (Fig. [3.13]) consists of three interconnected chambers [69, 77, 249]: evaporation chamber (base pressure 3×10^{-10} mbar), annealing and sputtering chamber (3×10^{-10} mbar) and analysis chamber (base pressure: 2×10^{-10} mbar).

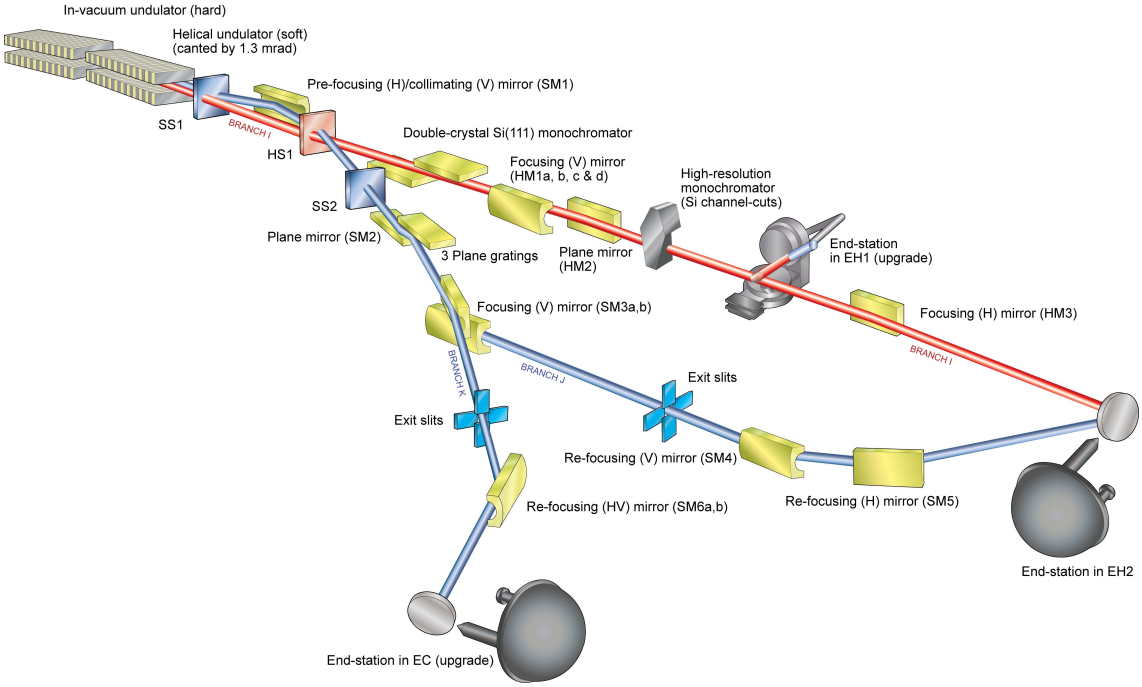

Figure 3.12.: Sketch of beamline I09 at the Diamond Light Source, Didcot, UK. Note the hard X-rays (I) and the soft X-rays (J) branches can be focused on the same spot of the sample. Additional end-stations are to be built (branch K), where only the soft beam is used. Taken from [248].

The LEED system is a Micro-Channel-Plate OCI BDL800IR-MCP. UPS experiments were performed using monochromatized He I radiation ($h\nu = 21.2\,\mathrm{eV}$) and a Specs PHOIBOS 150 analyzer. The energy resolution was always set to 80 meV. The angle between the incident beam and the sample was fixed to 40°. The spectra were collected at photoelectron take-off angles (θ) of 45° with an acceptance angle of ±10° along the $\Gamma - M$ direction of the substrate. The SECO was measured in normal emission with a bias potential of -3 V. XPS was done using a monochromatized AlK$_\alpha$ source ($h\nu = 1486.6\,\mathrm{eV}$). The error of E_B values in UPS is estimated to be $\pm 0.05\,\mathrm{eV}$.

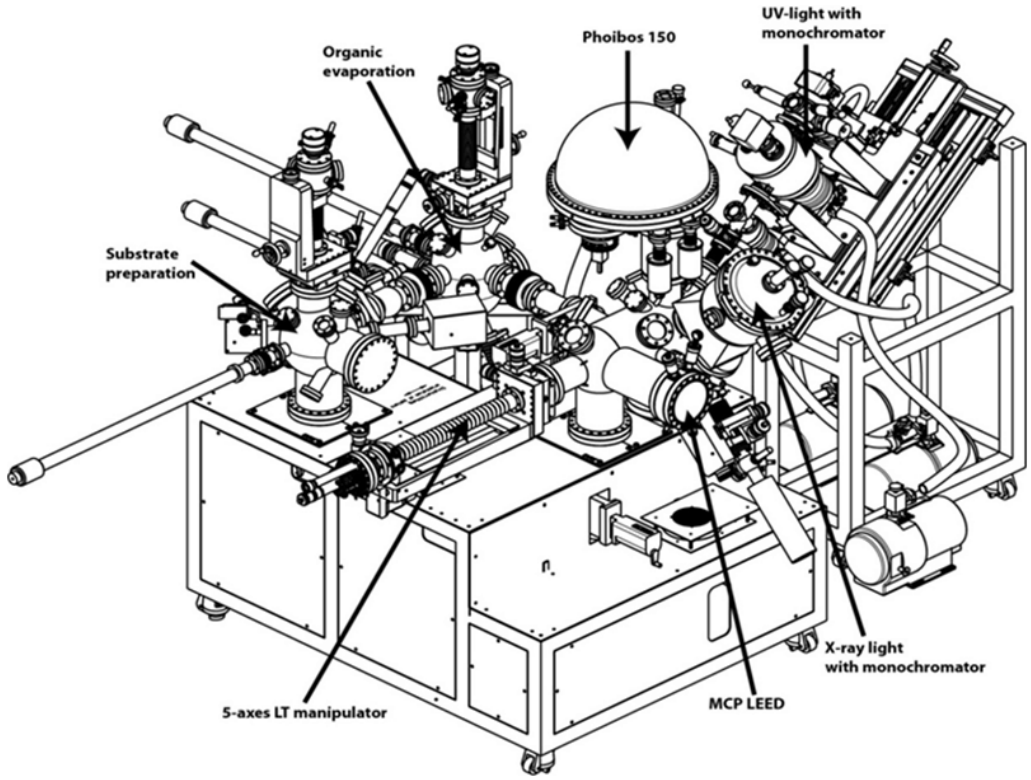

Figure 3.13.: Sketch of the UHV setup at FUNSOM, Soochow University. Picture courtesy of SPECS GmbH.

4. Materials

In this chapter, we briefly describe the materials used in the different projects included in this work. We start with the organic compounds and continue with the substrates where they were deposited.

4.1. Organic compounds

One of the main advantages of organic semiconductors, compared to their inorganic counterparts, is the high degree of tunability offered by the manifold synthesis processes. It is thus common that new compounds with promising new features or improved electronic, optical or stability characteristics regularly appear. In this thesis, we rather focus on prototypical π-conjugated organic semiconductor molecules and simple derivatives thereof. In particular, perylene and pentacene (PEN) derivatives are mostly considered through this work. For an extensive review on other application-oriented materials see, for instance, Ref. [250]. Figure [4.1] summarizes the molecular structures of all the compounds investigated.

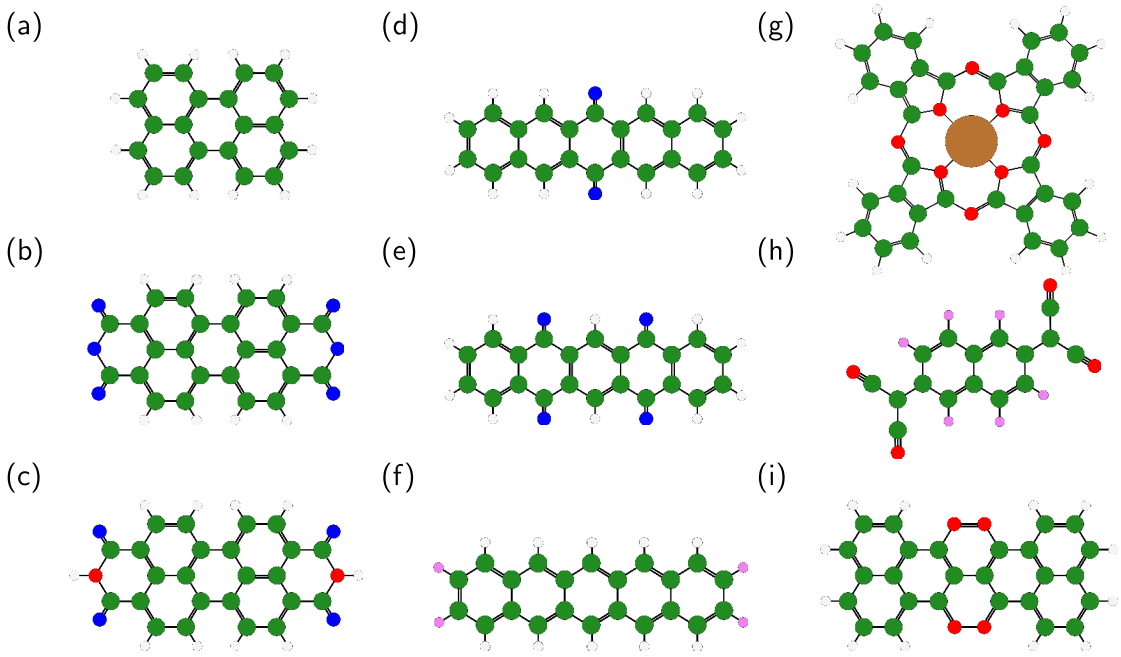

Figure 4.1.: Organic compounds used in this work with the different chemical species colored, namely, carbon (green), oxygen (blue), nitrogen (red), fluorine (violet) and hydrogen (white). (a) Perylene, (b) PTCDA, (c) PTCDI, (d) P2O, (e) P4O, (f) F4PEN, (g) CuPc, (h) F6TCNNQ and (i) TAT.

(a) Perylene

- Formula: $C_{20}H_{12}$
- Character: donor.
- Optical gap: 2.83 eV [251].
- Transport gap: 2.82 eV [252].

(b) Perylene-3,4,9,10-tetracarboxylic dianhydride (PTCDA)

- Formula: $C_{24}H_8O_6$
- Character: acceptor.
- Optical gap: 2.22 eV [189].
- Transport gap: 2.74 eV [189].

(c) Perylene-3,4,9,10-tetracarboxylic-3,4,9,10-diimide (PTCDI)

- Formula: $C_{24}H_{10}O_4N_2$
- Character: acceptor.
- Optical gap: 2.17 eV [189].
- Transport gap: 2.37 eV [189].

(d) 6,13-pentacenequinone (P2O)

- Formula: $C_{22}H_{12}O_2$
- Character: acceptor.
- Optical gap: 2.8 eV [253].
- Transport gap: not found/measured.

(e) 5,7,12,14-pentacenetetrone (P4O)

- Formula: $C_{22}H_{10}O_4$
- Character: acceptor.
- Optical gap: not found/measured.
- Transport gap: not found/measured.

(f) 2,3,9,10-tetrafluoropentacene (F4PEN)

- Formula: $C_{22}H_{12}F_4$
- Character: acceptor.
- Optical gap: not measured.
- Transport gap: not measured.

(g) Copper(II) phthalocyanine (CuPc)

- Formula: $C_{32}H_{16}N_8Cu$
- Character: donor.
- Optical gap: 1.7 eV [189].
- Transport gap: 2.2 eV [189].

(h) 2,2'-(perfluoronaphthalene-2,6-diylidene)dimalononitrile (F6TCNNQ)

- Formula: $C_{16}F_6N_4$
- Character: (strong) acceptor.
- Optical gap: 2.1 eV [254].
- Transport gap: 1.93 eV [255].

(i) 7,8,15,16-tetraazaterrylene (TAT)

- Formula: $C_{26}H_{12}N_4$.
- Character: acceptor [249].
- Optical gap: 1.98 eV [256].
- Transport gap: 2.66 eV [249].

The reported gaps were all measured for thin films of the corresponding material.

4.2. Single-crystal substrates

Besides the organic compounds, the substrates are also very relevant for the experiments performed in this work. Next, the main properties of the materials used as support for the COMs are explained.

4.2.1. Coinage metals

Gold (Au), Silver (Ag) and Copper (Cu) are standard materials for studies of metal-organic interfaces. On the one hand, owing to fundamental reasons, they have different degrees of reactivity, being Au the least and Cu the most reactive of the three. This allows to systematically test how different substrate reactivities modify the structural and electronic properties. On the other hand, owing to technological reasons, for most of the optoelectronic devices, electrical contacts are made of either Au, Ag or Cu.

Besides the substrate material, the crystallographic orientation of the surface also plays an important role. Thus, depending on the direction through which a crystal is cut different crystallographic planes are exposed. Surface atoms originate from the break of chemical bonds, therefore, they expose atomic orbitals that are not bound (or saturated). This is a source of instability per se and is behind many surface reactions, which seek to minimize this instability by filling (or saturating) the unbound orbitals. Hence, the less neighbors a surface atom has, the less stable it is (since less orbitals are paired). In other words, the most densely packed a surface is, the most stable becomes. In a simple picture, the reactivity of a surface plane can be categorized by the number of missing neighbors of a surface atom compared to the same atom in the bulk. The coinage metals have a face-centered cubic (fcc) structure. This means that the most densely packed surface is the (111) one, thus the most stable and least prone to become covered by undesired adsorbates, compared to other more open surfaces such as the (100) and (110).

The electronic properties are obviously influenced by the surface structure. As it has been discussed in Sec. [2.2], if an electron wants to leave the metal it has to overcome the metal work function (WF), which has a surface contribution that stems from the surface dipole. Since it depends on the number of charges available, which in turn directly depends on the number of surface atoms, the most densely packed structures will present a stronger dipole, hence increasing the surface contribution to the total work function. Thus, (111) fcc surfaces present the highest WF. It is worth noting that the presence of impurities and/or local reconstructions also contribute to WF variations within a given surface. To know more see [257].

(111) surfaces of the coinage metals have become a standard in surface-science experiments and studies of metal-organic interfaces. Interestingly, hexagonal close-packed (hcp)

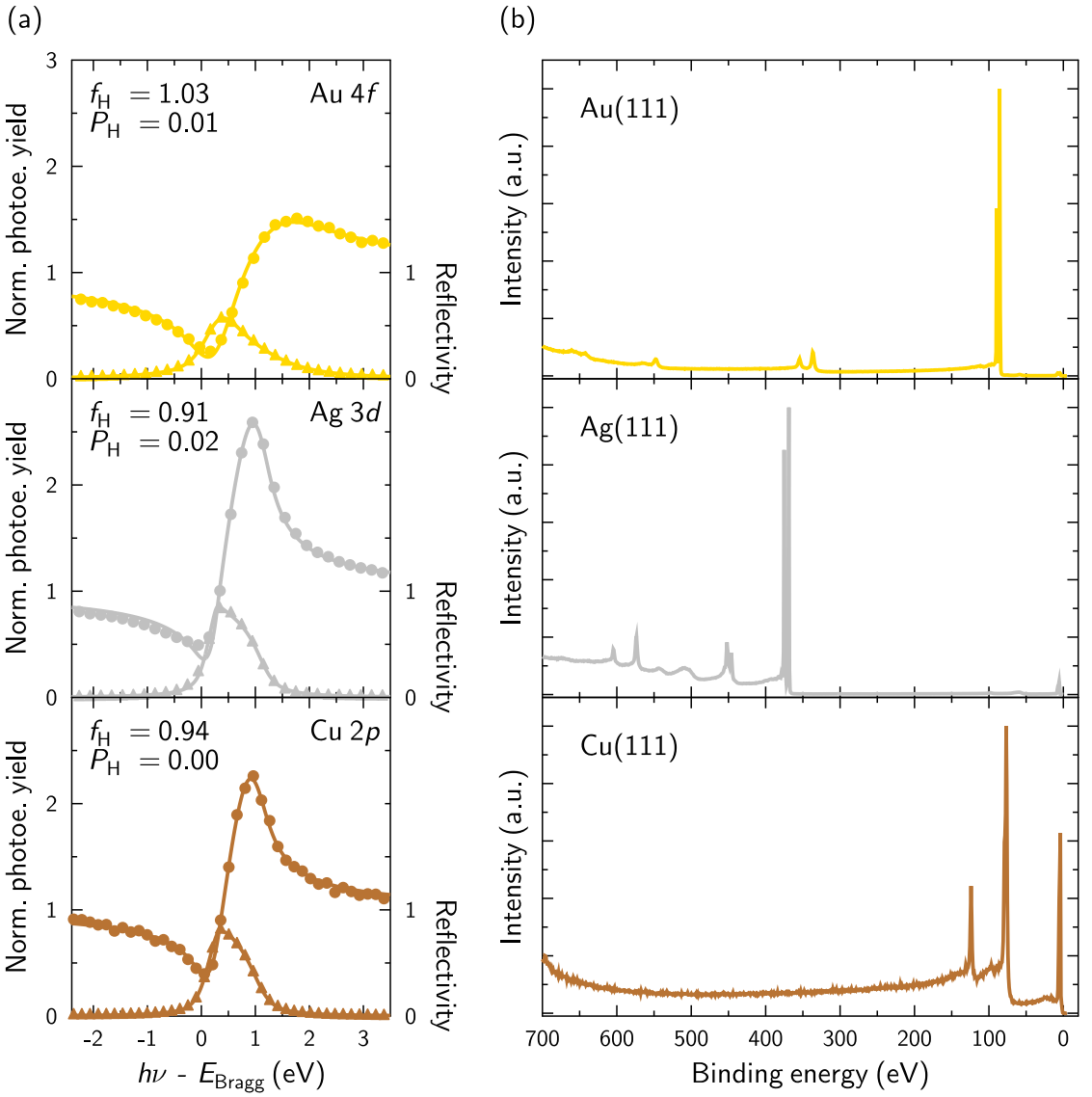

Figure 4.2.: (a) XSW measurements on the (111) clean surfaces of the coinage metals along $\mathbf{H} = [111]$. The high coherent fractions point out to a high vertical ordering of the atomic layers, whereas the coherent position being virtually 0 (or 1, which is the same due to the periodicity of the field) indicates that the atomic position of these layers corresponds to the extremes of the standing wave field. (b) Survey scans of the same clean surfaces. The energy used was 800 eV.

surfaces along the (0001) direction, such as those of the zinc oxide polar surfaces discussed in the next section, have the same packing structure as that of the fcc (111). Metal-organic interfaces studied in this project are restricted to the Au(111), Ag(111) and Cu(111) standard surfaces. Fig. [4.2] shows typical XSW scans for these clean surfaces together with a survey XPS scan. It is worth mentioning that interesting XSW experiments have been carried out in other more reactive surfaces, for some examples see [66, 258, 259].

As discussed by Hammer and Nørskov, the nobility of a metal depends on two factors: the degree of filling of the antibonding states upon adsorption and the degree of orbital

	Au(111)	Ag(111)	Cu(111)
(111) lattice spacing at RT (d_0 in Å)	2.353	2.357	2.086
Bragg energy at 88° (keV)	2.634	2.630	2.972
FWHM of the (111) Bragg reflection (eV)	1.12	1.18	0.87
Unit cell constant (Å)	4.078	4.085	3.615

Table 4.1.: Relevant parameters of the (111) faces of gold, silver and copper in the context of XSW experiments: the crystal lattice spacing, the Bragg energy close to normal-incidence, the theoretical FWHM of the reflectivity curve and finally the unit cell parameter.

overlap with the adsorbate [260], which influences the strength of the substrate-adsorbate interaction, among other parameters. Thus, Au is the least reactive compared to Ag and Cu and is mostly responsible for a phyisisorptitve interaction [58, 67, 70]. The Au(111) surface undergoes a reconstruction to a $(22 \times \sqrt{3})$ herringbones structure [261–263] that lifts the first atomic layer by 3% compared to the bulk [261, 263] and shows a sinusoidal arrangement with an amplitude of 0.15 Å and a lateral periodicity of 63 Å. This surface reconstruction has to be taken into account when studying molecular adsorbates [58, 70]. Interestingly, it has been reported that the adsorption of different OSC molecules may modify the reconstruction pattern [264]. The Au(111) surface has a work function of 5.31 eV [265]. Ag(111) is an intermediate situation, between physisorption and chemisorption, and mostly depends on the molecule [71]. It has a work function of 4.74 eV [265]. Cu(111) is the most reactive surface of all three and is mostly responsible for a chemisorptive adsorption [71, 77]. It has a work function of 4.98 eV [265].

Finally, Tab. [4.1] includes some important parameters for the three coinage-metal substrates that are useful in the context of XSW experiments, namely, the Bragg energy close to normal-incidence (∼90°) corresponding to the [111] direction for each substrate, the lattice spacing along the said crystal direction and the crystal unit cell parameter.

4.2.2. Zinc oxide (ZnO)

Zinc oxide (ZnO) is a II-VI semiconductor[1]. In nature, it can be found within the rare zincite mineral, which has a major preference for the wurtzite hcp crystal structure, although under some special conditions zinc-blende and rock-salt crystal structures (both fcc) can also be obtained [266]. Its wide-band gap in the UV, 3.3 eV at RT, makes it colorless and transparent/translucent[2]. Its hexagonal wurtzite-type structure can be seen as a superposition of planes composed of tetrahedrally coordinated O^{2-} and Zn^{2+} ions, as seen in Fig. [4.3a], which results in a non-central symmetric structure with four atoms per unit cell. ZnO is a direct gap semiconductor with the transition at the Γ point ($\boldsymbol{k} = 0$) in the reciprocal space (Fig. [4.3b]) and its exciton binding energy (60 meV) is well above the thermal energy at room-temperature. Due to the presence of defects, ZnO has an intrinsic n-type character [268]. p-doping of ZnO, however, remains challenging and intense research has been devoted to achieve it [269]. As a summary, the main properties of ZnO are listed in Tab [4.2]. For a comprehensive review see also Refs. [266, 270–273].

One of the most promising features of ZnO, together with its optoelectronic properties

[1] Binary compounds between Zn, Cd or Hg and O, S, Se or Te and their alloys.
[2] The precise electronic and optical properties will depend on many parameters such as the growth method and defect concentration [267].

Properties	Features
Stable phase at 300 K	Wurtzite (hcp)
Lattice parameters at 300 K:	
a_0	3.2496 Å
c_0	5.2069 Å
a_0/c_0	1.602 (1.633 for ideal wurtzite [274])
u	0.345 (0.375 for ideal wurtzite [274])
Density	5.606 g/cm^3
Melting point	1975°C
Thermal conductivity	0.6, 1–1.2
Linear expansion coefficient (/°C)	a_0: 6.5.10^{-6}, c_0: 3.0.10^{-6}
Static dielectric constant	8.656
Refractive index	2.008, 2.029
Energy gap	3.1–3.4 eV (direct)
Intrinsic carrier concentration	$< 10^6$/cm^3
Exciton binding energy	60 meV
Electron effective mass	$0.24m_e$
Electron hall mobility at 300 K for low n-type cond.	200 cm^2/Vs
Hole effective mass	$0.59m_e$
Hole Hall mobility at 300 K for low p-type cond.	5–50 cm^2/Vs

Table 4.2.: Main properties of ZnO, adapted from Ref. [275]. A very detailed explanation of these and other properties can also be found in the first chapter of Ref. [274]. u is a factor used to describe the z position of the atoms in the unit cell in terms of c. Thus, one atom occupies a position of $z = 0$ and the other $z = uc$ (see Fig. [4.3]).

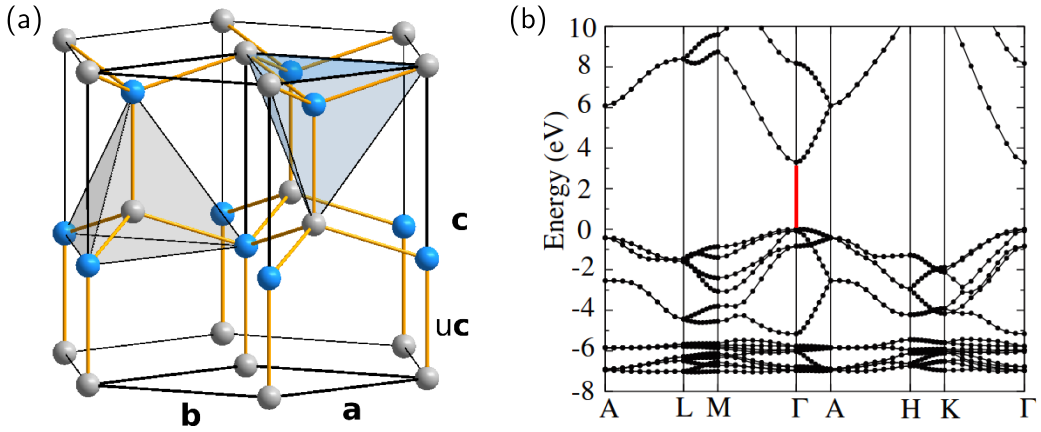

Figure 4.3.: Structural and electronic characteristics of ZnO. (a) Wurtzite crystal structure of ZnO where the unit cell, highlighted in black, has the following parameters: **a** = **b** = 3.250 Å, **c** = 5.204 Å, u = 0.345 and the angle between **a** and **b** is 120°. Zinc and oxygen atoms are in 1:1 concentration and occupy equivalent positions within the crystal structure, being each atom tetrahedrally coordinated, as shown in the figure with an example for each case. (b) Calculated band structure with the direct band gap transition highlighted in red. Figure adapted from Ref. [272].

is that it can be engineered in multiple nanostructured forms (Fig. [4.4]): nanowires and nanorods, tetrapods, nanorings as well as ordered thin films, among others, have been reported [270]. Furthermore, specific properties can be tuned to some extend by varying the growth parameters [276].

The properties of ZnO are remarkably different depending on the crystal orientation, the surface treatment (during as well as after growth), the presence of defects (desired or

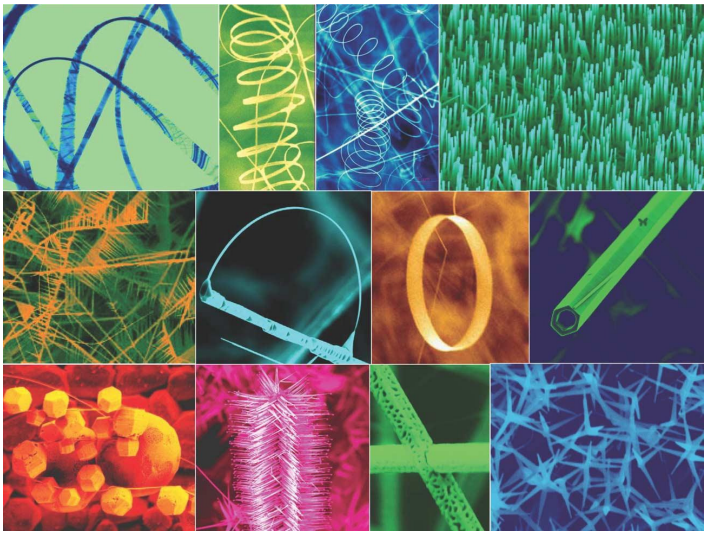

Figure 4.4.: Several examples of ZnO nanostructures. Taken from Ref. [280].

undesired) and the growth method. A clear example is the work function, whose values have been reported to be remarkably different depending on the particular conditions above mentioned [277]. Likewise, optical [267,278] and electronic attributes [277,279] are bound to the particular characteristics of the crystal. Therefore, ZnO properties can be tuned through many different ways. This is a double-edged sword since it makes complicated to untangle contributions from different parameters to a given effect. This will be further exemplified in the discussions below regarding the surface structure and chemistry.

As summarized by Hewlett and McLachlan in a recent review [35], besides doping, the ZnO-surface properties can be further modified by the growth of thin layers of inorganic or organic materials. Since this work is devoted to the study of organic adsorbates, the reader is referred to the mentioned review for information on the inorganic adlayers [35] as well as to Ref. [281] for a specific focus on surface functionalization of nanostructures.

In recent years, the combination of organic semiconductor materials with inorganic (nano)structures has attracted significant attention, especially for ZnO, since it has proven a way to overcome the drawbacks presented by the separate materials, but also as a source of new and interesting phenomenology [120]. In this context, a proper understanding of the surface structural, chemical and electronic properties of ZnO is a basic requirement to properly describe how the organic-inorganic interface behaves and a necessary step towards a rational tuning of its properties. As it will become clear below, the intrinsic nature of ZnO makes its surfaces a challenging and controversial case of study. Therefore, we will devote Chap. [8] to the characterization of the surface under our specific treatment conditions as a previous, and necessary step, before focusing, in Chap. [9], on their interface with various organic compounds.

4.2.2.1. The ZnO polar surfaces

Due to the symmetry of the wurtzite structure along the [0001] direction (c axis), the lattice plains contain either Zn cations or O anions. Cutting the crystal along the c-direction

yields one surface with only oxygen atoms that corresponds to the $(000\bar{1})$ plane, named O-terminated ZnO (O-ZnO), and another one with only zinc atoms corresponding to the (0001) plane, named Zn-terminated ZnO (Zn-ZnO). Both terminations form the polar surfaces of ZnO[3].

Before continuing with the description of these surfaces, we devote a few lines clarifying their crystallographic notation. In cubic crystal structures, the crystallographic planes are denoted by three Miller indices (hkl) that are related to the real-space coordinates (x, y, z) of the unit cell. However, in hexagonal (and rhombohedral) lattices some confusion may arise when reporting permutation symmetries. Thus, an additional coordinate u is introduced, which refers to a direction within the (x, y) plane. Then, the Miller-Bravais indices $(hkil)$ are used instead, being h, k and l the Miller indices and i a redundant index since $h + k + i = 0$. Consequently, one can draw a correlation between the 3-index and 4-index notations. For our particular case, the polar surfaces are along the [0001] direction that is the same as the [001]. For ZnO, however, the (0001) plane is forbidden in diffraction experiments and the [0002] equivalent direction is used instead. In this work, the Zn-terminated surface will be denoted as (0001), (0002) and (002) interchangeably, whereas $(000\bar{1})$, $(000\bar{2})$ and $(00\bar{2})$ will be used for the O-terminated one (in some cases, for typographic convenience, the -1 may be used instead of the $\bar{1}$).

The stacking of layers with opposed charges renders an accumulating dipole moment along the mentioned direction, as shown in Fig. [4.5]. From a pure ionic description, surfaces with a nonzero dipole moment have a diverging surface energy and therefore are theoretically unstable [283, 284]. However, as the ZnO polar surfaces can be found in nature, there have to be some stabilizing processes at work. Although there is no full consensus, yet, regarding the stabilization of these surfaces, three main mechanisms and combinations thereof have been proposed [285,286]: first, the charge transfer from one surface to the opposite one; secondly, changing the surface stoichiometry, either by removing or adding zinc and/or oxygen atoms; thirdly, adsorption of charged adsorbates [284,287]; and very recently, entropic disorder on the surface has also been reported to contribute to the stability of polar surfaces [286]. The surface preparation method and ambient conditions may favor which mechanisms predominates over the others.

Polarity plays a major role in the thin-film growth [288], optoelectronic [289,290] properties, catalytic performance [291] and interface properties of ZnO [292]. Thus, although crystallographically equivalent, the surface properties differ quite substantially between the Zn-terminated and the O-terminated faces. For a comprehensive review of the properties of polar surfaces see Refs. [282,284].

Another aspect that cannot be decoupled from the stabilization of the ZnO polar surfaces is their possible surface reconstructions and/or relaxation. Both mechanisms involve the rearrangement of the surface atoms with respect to the bulk. In particular, a given surface undergoes reconstruction when its in-plane symmetry (parallel to the surface) is lower than that shown by the bulk. On the contrary, relaxed surfaces show the same in-plane symmetry but the lattice spacing is changed, being an outward/inward relaxation if the topmost layer(s) show(s) a higher/smaller lattice spacing than the bulk [293]. Cleaving a crystal produces dangling bonds on the surface, which increase the surface energy. In

[3] ZnO has also the so-called non-polar surfaces, being the $(10\bar{1}0)$ and $(11\bar{2}0)$ the most abundant. They contain zinc as well as oxygen atoms at each layer. See Ref. [282] for more information.

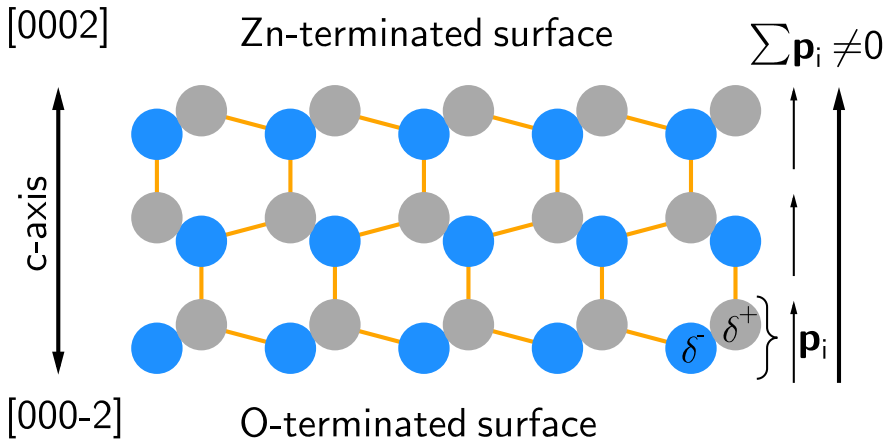

Figure 4.5.: 2D sketch of a ZnO slab along the c axis with the oxygen anions in blue and zinc cations in gray. Each bilayer yields an electric dipole $\mathbf{p}_i$ that adds up to those of the other bilayers thus rendering an accumulating dipole, which is the source of the surface instability.

order to minimize the free energy, the surface atoms will rearrange to form the most stable structure that is accessible under the corresponding thermodynamic conditions. Therefore, different experimental conditions may produce different surface geometries. In this context, plenty of experimental and theoretical studies have investigated the polar surface of ZnO under many different conditions, reporting several reconstructions, predicting some others and even showing contradictory results. Although it is certainly beyond the scope of this work to provide an extensive context for all of them, in the paragraphs below we summarize the surface structures that have been both observed experimentally and obtained from theoretical calculations.

The (0001) Zn-terminated surface Following the argument of atom removal from the surface to reach a stable configuration, STM studies found triangular islands and pits with the height of one layer (2.7 Å) and the sides decorated with oxygen atoms [294, 295]. It was found that these triangular motifs were the most energetically-favorable way to accommodate zinc vacancies on the surface [295, 296]. Such a mechanism appears to be promoted under poor hydrogen environments [295, 296]. Grazing-incidence X-ray diffraction (GIXD) experiments seem to support the creation of vacancies since their best data fit was obtained upon a random removal of 1/4 of the surface atoms [297]. Also, regions showing a (1×3) reconstruction, arising from missing Zn-rows that coexist with hydrogen decoration of the remaining Zn atoms, have been found together with regions showing the aforementioned triangular nanostructures [298]. More recent calculations have shown that entropic contributions are key to decide which reconstruction prevails among the manifold possibilities with very similar surface energies [299]. In particular, at low hydrogen concentrations, increasing the temperature makes the entropic contributions to stabilize the (2×2)-O reconstruction. Otherwise, with more humid conditions, the $(\sqrt{3} \times \sqrt{3})R30° + (2 \times 1)$H dominates [299]. Going beyond equilibrium conditions, the (1×1)-H surface was reported [300], explaining its previous experimental discovery [301, 302]. It is suggested that such a termination appears when the oxygen dangling bonds at the step edges and the zinc ones at the surface are passivated via adsorption of hy-

drogen/hydroxyl groups. Actually, a more recent study showed that the triangular pits are lifted upon water adsorption (which at low coverages dissociates on the surface) [303]. In the same direction, artificially creating more Zn vacancies by high-temperature annealing in UHV creates metastable reconstructions that can exist only with the help of hydrogen adsorption [304]. Besides, another mechanism to electrostatically compensate the surface polarity has been reported, namely, the strong faceting of the surface [305, 306]. At this point, it is worth noting that early theoretical studies detailed the transfer of 0.17 electrons from one surface to the other with the subsequent appearance of metallic states at the surface [307]. However, such a metal states have not been observed so far [294, 308]. As it has become clear above, the adsorption of species, most notably hydrogen and hydroxyl groups is a common mechanism accompanying any of the surface modifications described. Several studies have reported on the specific role of such adsorbates [309–312], which even readily appear for a UHV in-situ cleaved crystal [310], implying that their adsorption is extremely favored. Finally, studies of the surface relaxation have also yielded contradictory results. For instance, ion scattering experiments showed a bulk-like topmost layer [313], which is supported by surface X-ray diffraction experiments that could not resolve any sign of relaxations beyond the error bars [309] and angle-resolved photoelectron diffraction (PhD) [314]. Conversely, a combination of ion scattering spectroscopy and reflection high-energy electron diffraction (RHEED) showed an outward relaxation of 7% [315]. In a similar direction, transmission-electron microscopy (TEM) showed that the Zn atoms are randomly displaced outwards [316]. As discussed in Ref. [314], old studies wrongly derived an inward relaxation from intensity-profile analysis of LEED measurements because an inaccurate lattice spacing was used.

The $(000\bar{1})$ O-terminated surface Owing to the different polarity, the O-ZnO surface shows a quite different behavior, which is attributed to the minor flexibility of the oxygen *s*-orbital to form bonds compared to the outer *d*-shell of zinc [317]. Consequently, the number of different reconstructions is lower for this termination. In fact, the (1×1) unreconstructed surface is the most widely reported (see for instance Refs. [301, 307, 313]) and its stability is attributed to the adsorption of hydrogen [318, 319]. Indeed, removing the hydrogen overlayer renders the (1×3) reconstruction with O vacancies along the [100] directions [319–321]. Most prominently, (5×5) hexagonal holes have been reported [322] and predicted theoretically [317]. Also, most recently, a rather elusive (3×3)-Zn vacancy arrangement in the subsurface that only exists combined with hydrogen adsorption [323] has been experimentally found. From an electrostatic point of view, the stabilization of the surface is achieved by removing 1/4 of the charges [324]. The aforementioned reconstructions support the partial charge removal. However, they also need the adsorption of hydrogen to be fully stable, which seems the most preferred stabilization mechanism. It is worth noting that a $(\sqrt{3} \times \sqrt{3})R30°$ reconstruction achieved under very low hydrogen background [325] and claims of a hydrogen-free (1×1) O-ZnO surface [326] can be found in the literature. Noteworthy, very recent theoretical studies have shown that the actual hydrogen coverage may depend on the doping concentration (number of oxygen vacancies) [327]. Also, contrary to the Zn-terminated surface, the adsorption of hydrogen seems to induce surface metallicity [308]. Finally, regarding possible lattice relaxations, ion-scattering measurements reported a virtually bulk-like lattice spacing for the topmost

layer [313], which is supported by TEM experiments [316]. On the contrary, X-ray diffraction studies reported a contraction of the topmost layers [328], in line with a photoelectron diffraction study that measured a contraction of 25% with respect to the bulk spacing [329] and LEED measurements reporting a 16% contraction [330].

Part II.

Results and discussion

5. Perylene adsorbed on coinage metals

The XSW results found in this chapter were published in Ref. [69].

5.1. Context

Perylene (see paragraph [4.1]) constitutes the building block for a large family of COMs, e.g. diindenoperylene (DIP), PTCDI and PTCDA and their derivatives. Despite its core role, the study of perylene adsorbed on different substrates has not attracted as much attention as DIP or PTCDA. There are some remarkable exceptions, though. For instance, the work of Eremtchenko et al. [331–333] on Ag(111), Manandhar and coworkers [334,335] on the different coinage metals and the recent work of Bobrov et al. [336,337] on Ag(110), among other structural and theoretical studies on different metal surfaces [264, 338–340] and semiconductor substrates [123,126,128,341]. To the best of our knowledge, however, the experimental determination of vertical adsorption geometries of perylene has not been addressed so far. In this chapter, we present XSW measurements for perylene adsorbed on Au(111) and Cu(111). Far from complete, they provide a useful reference to discuss the impact of functional groups on perylene derivatives with emphasis on its adsorption geometry. Last but not least, they provide experimental evidence that contradicts some recurrently used ideas regarding the correlation between a short adsorption distance and a substrate-to-molecule charge transfer (CT).

5.2. Results

Several films of perylene with coverages below 1 monolayer (ML) were deposited on Au(111) and Cu(111). Only hard X-rays were used during the beamtime. Two typical XP spectra are shown in Fig. [5.1], which are used to illustrate the fit employed to analyze the XSW data rather than to extract quantitative conclusion since the BE was not calibrated. Nonetheless, one can appreciate a broadening in the Cu(111) spectra compared to that on gold and an increase of the satellite structure. The peak position is also shifted towards lower BE on copper. Unfortunately the magnitude of the shift cannot be taken as a solid value. However, a similar trend has been observed for DIP [58].

For the evaluation of the XSW data, the total area of the carbon peak was used to evaluate the photoelectron yield since the individual components did not provide a coherent fit. This implies that the adsorption distances obtained correspond to the average position of all the carbon atoms within the molecule. An example of these measurements are shown in Fig. [5.2]. On Cu(111), one of the samples was also cooled down with liquid nitrogen. By considering the change in Bragg energy and knowing the thermal expansion of copper, the LT was estimated to be 200 K (higher than expected). The fitting parameters and the obtained adsorption distances are summarized in Tab. [5.1] and, for a more visual

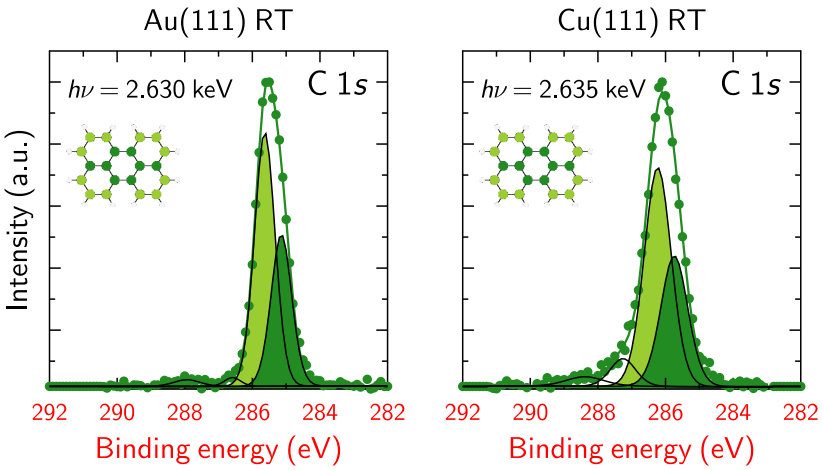

Figure 5.1.: Core-level spectra of the carbon C 1*s* signal corresponding to perylene adsorbed on Au(111) (left) and Cu(111) (right), both measured at room temperature (RT) and at normal incidence (X-rays impinging almost perpendicular to the sample surface). The BE was not calibrated, therefore the reader is advised not to trust the x-scale. The fitting model takes into account the two inequivalent species, namely carbon atoms bound only to other carbon atoms (dark green) and carbon atoms bound to hydrogen as well as other carbon atoms (yellow green). Both components were set to have the same FWHM and a Voigt-function line shape with a Lorentzian contribution of 30%. Two shake-ups (Gaussian lineshape) were included to complete the fit. We note here the broadening of the peak on copper compared to that on gold and the higher intensity of the sake-up structure. The energy used on gold is 4 eV lower than the Bragg energy of the (111) reflection on gold.

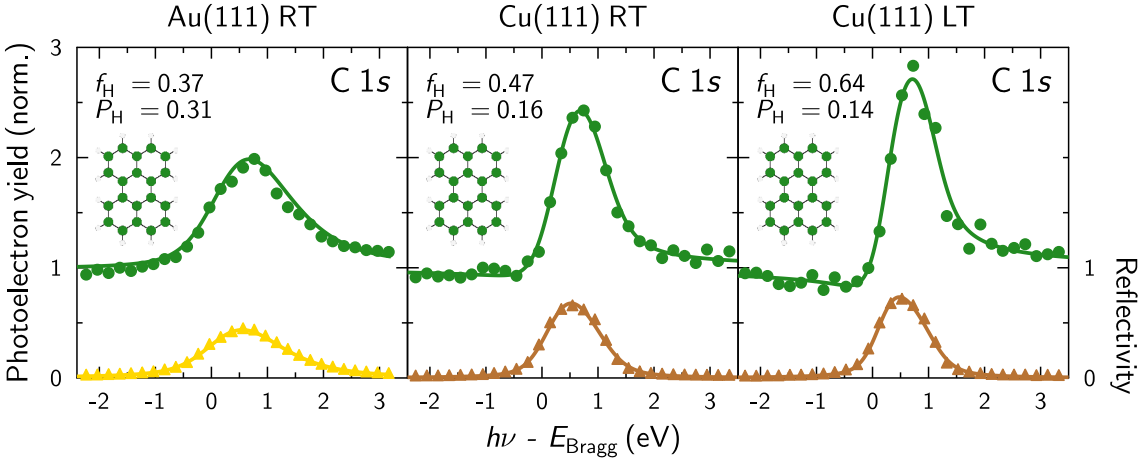

Figure 5.2.: XSW measurements along **H** = [111] for perylene deposited on Cu(111) and Au(111). On Cu(111) the measurements were performed at room temperature (RT) and at low temperature (LT) cooling down with liquid nitrogen (only $T \sim 200$ K could be achieved). The fitting parameters are included, namely, the coherent fraction (f_H) and the coherent position (P_H).

representation, the vertical adsorption geometry is sketched in Fig. [5.3].

As stated in Sec. [4.2.1], the (111) surface of gold undergoes a reconstruction that lifts the topmost layer by a 3% and thus has to be considered when providing the adsorption distance to the surface [70]. In practice, it means subtracting $0.03 \times d_0$ to the measured adsorption distance (where d_0 is the bulk lattice spacing of gold) [70].

Perylene on Cu(111) adsorbs at a much lower adsorption distance compared to gold, as it has been reported before for many other systems [58,67,71,342]. The effect of cooling can

Substrate	Component	f_{111}	P_{111}	d_{111} (Å)
Au(111) RT	**C1*s* total**	0.37	0.31	3.01 ± 0.06
Cu(111) RT		0.47	0.16	2.43 ± 0.02
Cu(111) LT		0.64	0.14	2.38 ± 0.02

Table 5.1.: Summary of the XSW parameters extracted from the measurements in Fig. [5.2]. The adsorption distance of perylene on Au(111) takes into account the surface reconstruction. See text for more details.

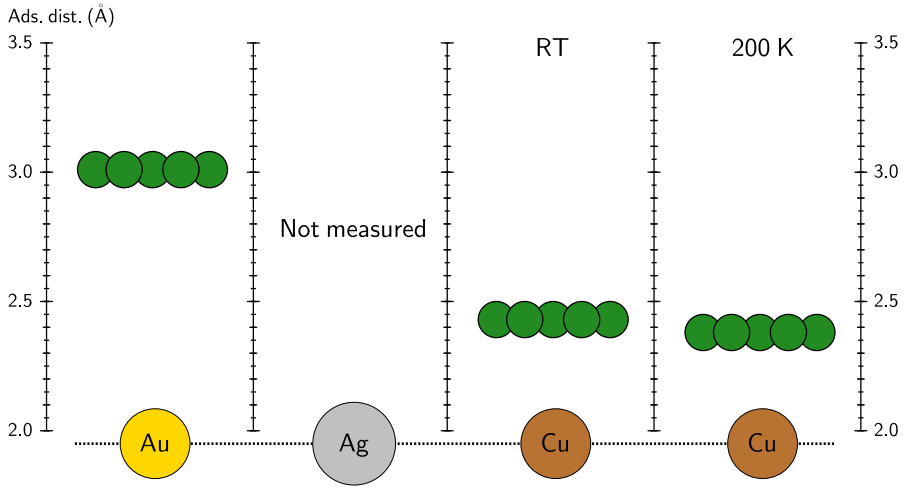

Figure 5.3.: Sketch of the vertical adsorption geometry of perylene adsorbed on the (111) surfaces of gold and copper. On copper the measurements were performed at RT and at 200 K. For the precise adsorption distances see Tab. [5.1]. The origin of the scale is the topmost substrate atoms, but it is shifted 2 Å for a clearer data display.

be seen in the increased coherent fraction. This is typically seen for XSW measurements at LT [245, 342, 343], which can be tentatively explained by lower thermal vibrations of the adsorbed molecules.

5.3. Discussion

During the last decades, the experimental characterization of metal-organic interfaces has allowed one to correlate the electronic and conformational changes happening upon adsorption. Among all the observed features, two main parameters have been recurrently used to point out the existence of a strong coupling between substrate and adsorbate, namely, CT features at the valence band through (partial) LUMO filling and a short adsorption distance of the molecule on a particular substrate. Certainly, in numerous examples studied both phenomena go hand in hand and the system showing the lowest adsorption distance also shows the major degree of LUMO filling [67, 68, 71]. The results presented here show that this cannot be taken as a general rule [68]. Measurements presented by Manandhar and coworkers [334, 335] and supported by additional synchrotron measurements [74, 344] show no CT features for perylene on any of the coinage metals. In a first approximation, one can explain that considering the large gap of perylene [251], which keeps the LUMO above the Fermi edge even on copper. It is therefore surprising to see a remarkably short adsorption distance on Cu(111), close to those of PEN [57] and other systems with extended π-conjugated systems [245]. Therefore, a notable short adsorption distance does

not necessarily mean a strong electronic coupling. Interestingly enough, for bicomponent monolayers of donor-acceptor molecules it has been seen that the molecule that accepts the charge from the metal does not necessarily come closer to the substrate [345,346] (see Appendix [G] for more details on heteromolecular adsorbate systems).

Information of the adsorption distance of perylene on gold and copper also allows us to address the substrate-dependence of the peak broadening observed in the core-level spectra shown in Fig. [5.1]. A similar effect has been reported for other systems [165,166,347], which has been explained in terms of the lifetime broadening of the core-hole [165]. More precisely, the probability of an electron filling the hole left by the photoemitted electron decreases with an increasing adsorption distance since the electronic coupling is reduced. Thus, increasing the lifetime of the hole is accompanied by a decrease in the energy uncertainty (in virtue of the uncertainty principle, where in a simple way $\Delta t \cdot \Delta E = \text{constant}$). Consequently, shorter adsorption distances *a priori* come along with broader core-level peaks.

Another interesting aspect that can be discussed with our measurements is the lifting of the surface reconstruction of gold upon adsorption of perylene [264], but not PTCDA [348, 349], nor PTCDI [350]. Indeed, Sun et al. [264] showed in a STM study that the gold surface is slightly perturbed upon perylene adsorption. Conversely, when its derivative PTCDA is evaporated on the surface no changes are observed [348]. This might be explained by the shorter adsorption distance of perylene reported here, compared to that of PTCDA [70], that causes the molecular orbitals to be closer to the surface and thus being able to slightly lift the surface reconstruction.

5.4. Conclusions

The results presented here provide a good reference to discuss, in the next chapter, the particular effect of different functional groups on the adsorption distance of perylene. As a foretaste, though, the short adsorption distance on Cu(111) despite the absence of CT features in the valence band, in stark contrast to what is observed for its derivatives, indicates that one cannot establish a general relationship between a short adsorption distance and CT features.

6. PTCDI adsorbed on coinage metals. Influence of the lateral and vertical order on the core-level spectra

The results presented in this chapter were published in Ref. [69]. They were carried out in collaboration with Prof. Steffen Duhm's group at FUNSOM, Soochow University, in Suzhou, China. Qi Wang, supervised by Prof. Duhm, performed the coverage-dependent UPS, XPS and LEED and analyzed the LEED and UPS data contained in the following.

6.1. Context

Despite the tremendous progress achieved in the last decades, there is still a lot to know about the metal-organic interface and new experiments and theoretical models invite to rethink the current knowledge. One example is, as shown experimentally in the previous chapter, that the often assumed causal relation between short adsorption distance and CT cannot be taken as a universal trend as often done in the past. Some recent attempts to find a general explanation for the energy-level alignment have identified the presence of functional groups with heteroatoms [71] as a key element that determines why CT happens for some systems and not for others. Recent HR-UPS measurements, however, have extended the surface-induced aromatic stabilization (SIAS) mechanism presented by Heimel et al. [71] (see Sec. [2.2]) to other π-conjugated systems that are pure aromatic hydrocarbons (no heteroatoms present), such as DIP [74, 75, 351]. Interestingly, perylene, another pure hydrocarbon, does not show CT states [334, 335] indicating that, in any case, functional groups have to be added to perylene in order to bring the LUMO closer to the Fermi edge. It is thus clear that more experimental and theoretical input has to be presented in order to achieve a unified picture of the mechanisms governing the metal-organic interface. In particular, systematic studies where only one parameter is varied help enormously to rationalize the particular effects of the given control parameter. In this direction, the results contained in this chapter study the electronic, chemical and conformational properties of PTCDI adsorbed on Au(111), Ag(111) and Cu(111). Consequently, one can see how the different interface characteristics change with the substrate reactivity. Furthermore, these experiments complete the necessary framework for the results presented in Chap. [9], where different perylene derivatives are adsorbed on ZnO. Of course, the different nature of the substrates does not allow a one-to-one comparison, but it provides some useful trends.

PTCDI, an acceptor-like semiconductor molecule and red dye (see paragraph [4.1]), is a perylene derivative that contains two imide radicals as functional groups (see Fig. [6.1]). The attachment of additional chains or side groups through the nitrogen atoms increases the versatility and tunability of the molecular properties [352–354], which add up to pos-

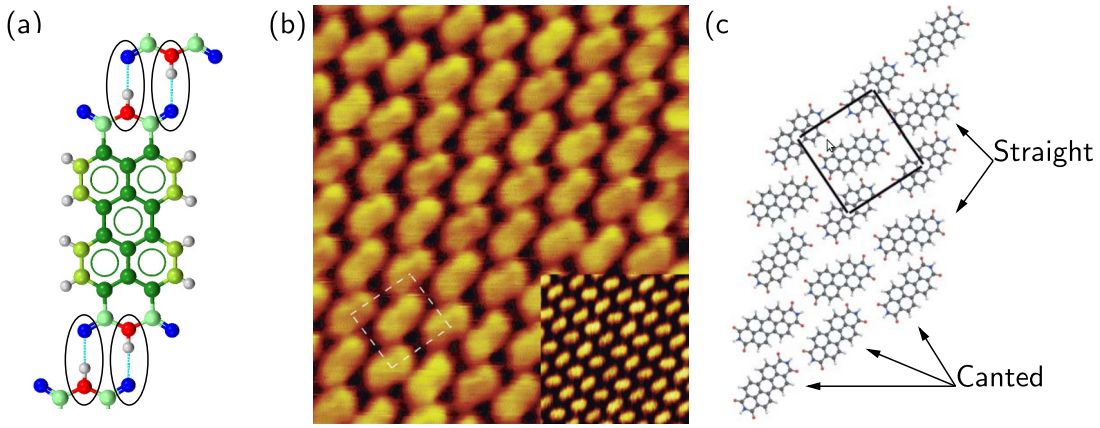

Figure 6.1.: (a) Sketch of the PTCDI molecule with the color code used to sketch the vertical adsorption geometry in the following sections: nitrogen atoms are colored in red, the carboxylic-oxygen atoms in blue and the different inequivalent carbon atoms are depicted in different shades of green. The preferential interaction between adjacent molecules is highlighted in black, typical for the straight PTCDI rows shown in many STM studies (example shown in (b)). (b) STM image of PTCDI deposited on Au(111). The inset shows a zoomed-out area. The unit cell is displayed in white. (c) Schematics of the PTCDI ordering on Au(111) extracted from the STM image. The row-like arrangement is clearly seen and two different types of columns can be distinguished, namely, the straight columns that show a parallel interaction of adjacent imide groups as displayed in (a) and the so-called canted columns where the PTCDI molecules are oriented towards the straight columns with a tilt angle of 11° [363, 364]. The unit cell is represented with a black square. As discussed in the main text, this arrangement has been reported for PTCDI on other weakly interacting substrates. Figures (b) and (c) were adapted from Ref. [364].

sible modifications to the perylene core [355–357]. Thus, PTCDI derivatives have been successfully employed in different functional devices [358–361]. The plain PTCDI, where a single hydrogen atom is attached to the nitrogen, shows already some very interesting properties compared to other well-known perylene derivatives, namely PTCDA and DIP. Indeed, the supramolecular arrangement is drastically affected since the molecules maximize the contact between adjacent imide groups through the N–H···O hydrogen-bond formation [103, 362–364]. This favors a parallel orientation as opposed to the dominating perpendicular arrangement between PTCDA molecules, which is driven by quadrupolar interaction that renders the typical herringbone structure seen for PTCDA in different substrates [362, 365]. Due to the strong directional interaction, PTCDI has been widely employed in self-assembly studies of bicomponent monolayers on metal surfaces (see Ref. [78] and references therein).

Past research with PTCDI (see Ref. [366] for the crystal structure) has been mostly focused on its supramolecular arrangement when deposited on weakly interacting substrates such as Au(111) [103, 363, 364], Ag–Si(111)$\sqrt{3}\times\sqrt{3}R30°$ [362, 367, 368], graphite [369] and MoS_2 [369]. In all of them, the typical arrangement of PTCDI forming rods, dominated by an imide–imide interaction, could be observed (see Fig. [6.1]), although several domains and multiple defects have been reported for PTCDI monolayers on Au(111) [363], NaCl [370], graphite [369] and MoS_2 [369]. Furthermore, different coverages of PTCDI have been also studied on KBr(100) [371], Pt(100) [372, 373], Pt(111) with a silver overlayer [374], TiO_2 [125–127], CaF_2(111) [375], NaCl [370], sulfur-passivated GaAs(100) with [376] and without [189] additional deposition of magnesium, ZnO [377], SiC(0001) [378], graphene [379–381], polymer [382], Ni(111) [383], Si(111) [383] as well as theoretical studies of the vibrational, electronic and absorption properties of the molecule in the gas phase

and in solution [384–388]. To the best of our knowledge, however, fewer interest has been devoted to study the PTCDI-(coinage)metal interface with photoelectron spectroscopy techniques [152, 389].

6.2. Results

The results shown next yield a comprehensive characterization of the interface between PTCDI and the (111) surface of the different coinage metals. The lateral arrangement of the first layer is inferred by LEED measurements. The vertical adsorption geometry and the chemical properties of (sub)monolayer coverages are accessed with XSW and HR-XPS measurements, respectively. Further coverage-dependent XPS and UPS highlight the chemical and electronic properties of the interface as opposed to those of the multilayer.

6.2.1. Coverage-dependent XPS and UPS

We start by presenting the coverage-dependent measurements. Fig. [6.2] shows survey scans of the valence-band (VB) region collected at normal-emission and at 45°. The substrate features decrease in intensity with the increasing coverage until they disappear completely, leaving only the molecular features in the spectra. It can be extracted, therefore, that at least the first layers of PTCDI are completely closed. One cannot say, however, whether it is a layer-by-layer growth or islands start growing after the first layers. Unfortunately, no information could be found for the growth mode of PTCDI on coinage metals. For PTCDA on Ag(111) and Au(111) it was reported that, upon formation of the first (closed) layers, the growth mode depends on various factors such as the film thickness, substrate temperature and growth rate [390, 391].

Of particular interest are CT effects from the substrate, which are visible through a (partial) filling of the molecular LUMO, usually only involving the first layer in contact with the substrate. As seen in Fig. [6.3], this is the case for PTCDI on Ag(111) and on Cu(111) (features labeled as L'). In the first case, the partially-filled LUMO is cut at the Fermi edge, which means that the PTCDI monolayer (ML) on silver becomes metallic [71]. For copper, the LUMO filling is complete since it appears entirely below the Fermi edge, rendering a semiconducting behavior. On the contrary, the LUMO of PTCDI on Au(111) remains unfilled at any coverage. Thus, we can conclude that the electronic coupling increases in the order Au-Ag-Cu, similarly to PTCDA [67]. Additional PTCDI deposition leads to interface dipoles on all substrates, as deduced from the secondary-electron cutoff (SECO) shifts in Fig. [6.3]. On gold, it can be mainly attributed to the push-back effect [30] and on silver and copper to the complex interplay of push-back and charge rearrangements by the net electron transfer from the substrate to PTCDI [50]. The different vacuum level (VL) energies for PTCDI multilayers are in contrast to PTCDA thin films deposited on coinage metals, which show the same VL regardless of the substrate underneath [67]. The evolution of these values with the coverage is plotted in Fig. [6.4]. The different shift of the VL, depending on the substrate, is clearly seen and it is responsible for both the relative position of the HOMO as well as the core-level shifts seen at the multilayer regime (Fig. [6.5]). It is thus clear that the substrate has an influence beyond the first layers. It is very interesting and yet unclear why some molecules do show a substrate-dependence [249]

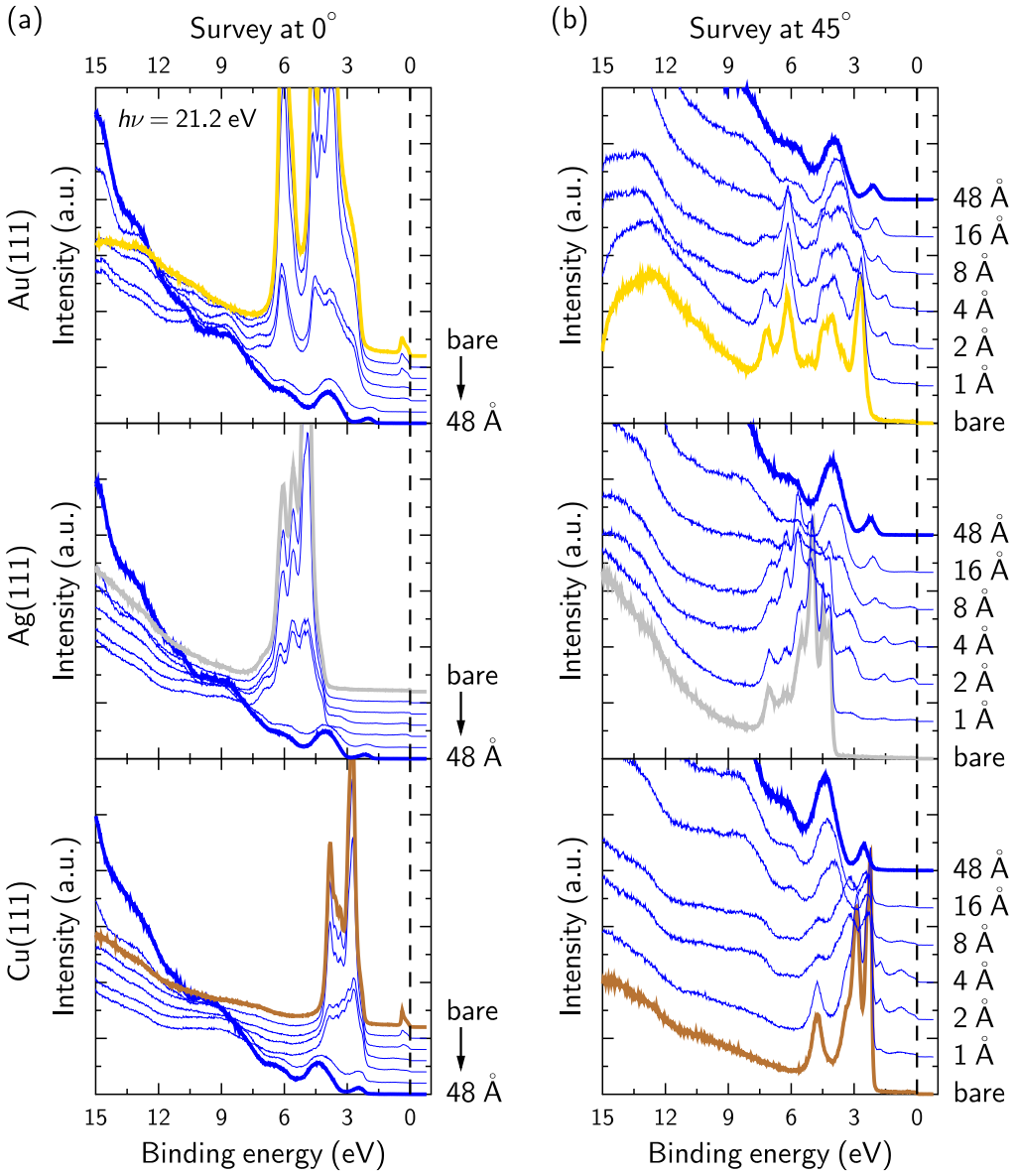

Figure 6.2.: Coverage-dependent survey scans of the valence-band region of PTCDI deposited on the three coinage metals (monochromatized He I source, $h\nu = 21.2\,\text{eV}$). Scans measured at (a) normal incidence and (b) at 45°. The surface states, close to $E_\text{B} = 0\,\text{eV}$ (visible only in (a)), and the metal d bands, $E_\text{B} = [2.5 - 8]\,\text{eV}$, belonging to the substrate (scans for the bare substrates highlighted), clearly decrease in intensity with increasing PTCDI coverage. For a final deposition of 48 Å (also highlighted in blue) the substrate features have disappeared and only PTCDI contributions are present, meaning that the molecules cover completely the surface.

even at the multilayer regime and others do not [67]. The precise values of the HOMO position and the WF function for the different coverages are summarized in Tab. [6.1].

For the different coverages, additional core-level spectra for carbon, nitrogen and oxygen were recorded using a monochromatized lab X-ray source with an Al anode ($h\nu = 1486.6\,\text{eV}$). Fig. [6.5] shows the spectra corresponding to the 48 Å (roughly 10 ML). From the (sub)monolayer coverage until the multilayer regime all the spectra shift towards higher

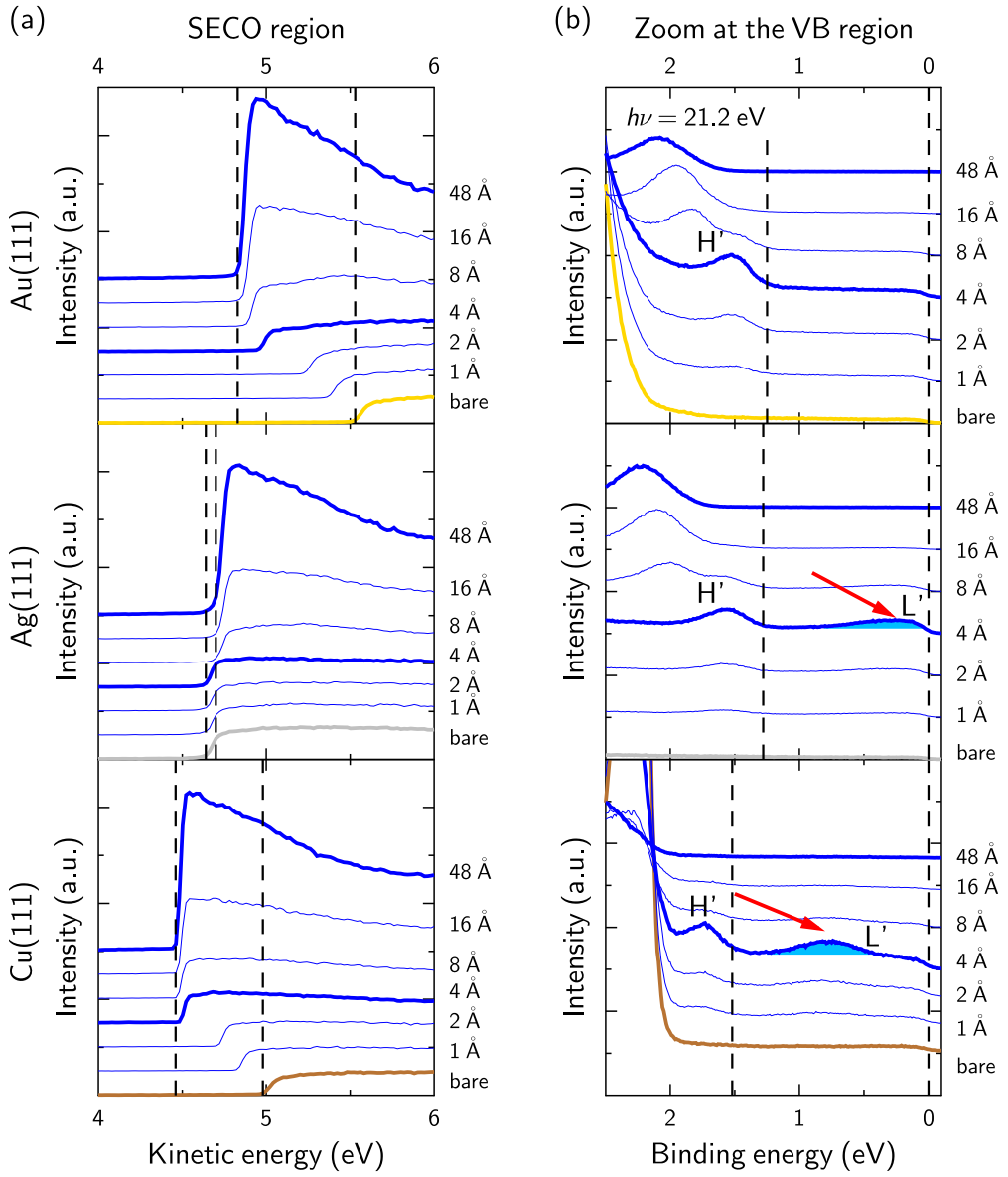

Figure 6.3.: Coverage-dependent valence-band spectra of PTCDI deposited on the coinage metals taken with a monochromatized He I source ($h\nu = 21.2\,\text{eV}$). Values shown in Table [6.1]. (a) SECO region (sample bias -3 V) that displays the vacuum-level shift with increasing coverage. Vertical lines highlight the bare substrate WF and the corresponding value for the highest coverage, which yields the WF employed to discuss the multilayer regime. (b) Zoomed VB region. Molecule contributions close to the Fermi level corresponding to the molecular former LUMO are labeled as L' and marked with an arrow for silver, where the former LUMO cuts the Fermi edge, and for copper, where it appears at higher BE and is completely filled. On the contrary, no feature appears for gold. The nominal monolayer (4 Å) and the multilayer regime are highlighted. The vertical lines highlight the relaxed HOMO (H') position at the nominal monolayer coverage.

BE as a result of the weakening of the substrate screening (intermediate plots not shown). The features of the core-level spectra away from the substrate reflect the chemistry of the molecule as well as the screening and polarization effects of the surroundings, in this case other equal PTCDI molecules. By comparing the scans, one clearly sees that there

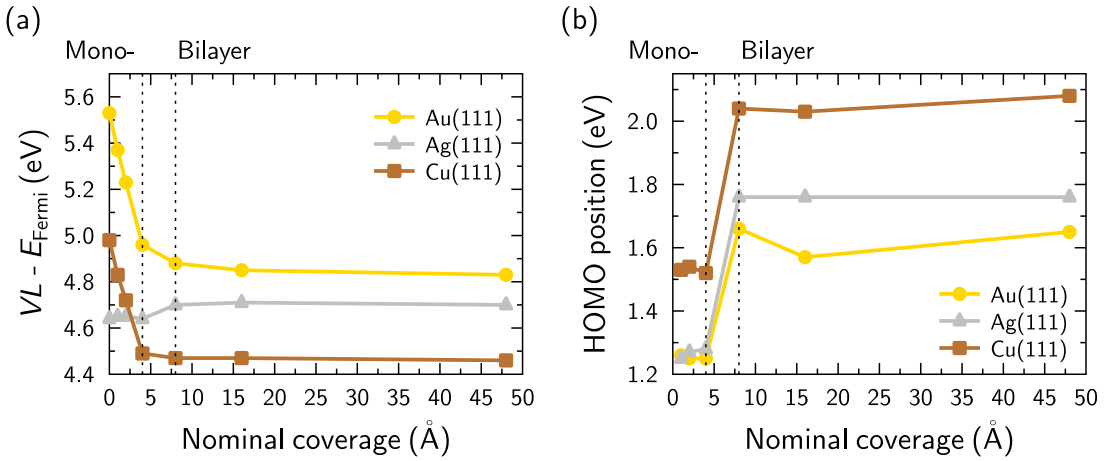

Figure 6.4.: (a) Vacuum-level shift with increasing coverage for PTCDI deposited on the three studied substrates. (b) HOMO position with increasing coverage. The nominal coverages corresponding to one and two full layers are marked with dashed lines.

		Coverage (Å)						
		Bare	**1**	**2**	**4**	**8**	**16**	**48**
Au(111)	WF (eV)	5.53	5.37	5.23	4.96	4.88	4.85	4.83
	HOMO (eV)	–	1.26	1.25	1.25	1.66	1.57	1.65
Ag(111)	WF (eV)	4.64	4.65	4.65	4.64	4.70	4.71	4.70
	HOMO (eV)	–	1.25	1.27	1.28	1.76	1.76	1.76
Cu(111)	WF (eV)	4.98	4.83	4.72	4.49	4.47	4.47	4.46
	HOMO (eV)	–	1.53	1.54	1.52	2.04	2.03	2.08

Table 6.1.: Summary of work functions (WF) and HOMO BE positions (HOMO) extracted from the UPS measurements in Fig. [6.3].

are no specific differences in the molecular environment that can be traced back to the substrate underneath since the spectra have the same shape regardless of the substrate. A closer look, however, shows that the spectra are rigidly shifted in energy compared to each other, following the same VL trend reported above. Considering the chemical environment, the two nitrogen atoms are equivalent, so are the four oxygen atoms. Consequently, one expects a single symmetric peak, which is clearly the case for the multilayer regime (Fig. [6.5]). The peak at the high BE side is attributed to HOMO-LUMO shake-ups [161, 162]. For carbon, four main inequivalent sites are identified[1], namely carbon atoms bound only to other carbon atoms (C–C), carbon atoms also linked to hydrogen atoms (C–H), the carbon atoms of the functional group (C=O) and finally the carbon atoms at the bridge position between the perylene core and the functional group (C–C–O). For stoichiometry reasons, the most intense peak, around 286 eV, is attributed to the perylene core, i.e. a combination of C–C, C–H and C–C–O. The carbon atoms of the functional groups are assigned to the peak shifted ∼3 eV towards higher BE. This BE shift is explained by the fact that these carbon atoms are linked to oxygen and nitrogen, which are more electronegative and attract the electrons towards them, leaving the carbon atoms

[1] PTCDI has a D_{2h} point symmetry that renders 7 nonequivalent carbon atoms, similar to PTCDA [392]. Their very small differences in BE, though, would make the fitting rather speculative. Therefore, only those carbons with clearly distinguished chemical environment are considered.

Component	Area			FWHM (eV)			BE (eV)			BE shift (eV)		
	Au	Ag	Cu	Au	Ag	Cu	Au	Ag	Cu	Au	Ag	Cu
Oxygen O 1*s*												
Low BE peak	0.00	0.02	0.02	0.36	0.88	0.76	529.85	529.97	530.27	-1.42	-1.42	-1.42
Main	1.10	1.11	1.08	1.02	1.05	1.01	531.27	531.39	531.69	0.00	0.00	0.00
Shake-up	0.20	0.23	0.19	1.73	1.86	1.75	532.95	533.07	533.38	1.68	1.68	1.68
Nitrogen N 1*s*												
Main	1.06	1.08	1.09	1.03	1.11	1.02	399.98	400.12	400.43	0.00	0.00	0.00
Shake-up	0.02	0.05	0.05	0.65	1.00	1.00	402.18	402.32	402.63	2.20	2.20	2.20
Carbon C 1*s*												
C–C	0.43	0.42	0.43	0.84	0.89	0.86	284.54	284.67	284.98	0.00	0.00	0.00
C–H	0.43	0.42	0.43	0.84	0.89	0.86	284.94	285.07	285.38	0.40	0.40	0.40
C–C–O	0.21	0.21	0.21	0.71	0.71	0.66	285.05	285.18	285.49	0.51	0.51	0.51
Shake-up 1	0.01	0.01	0.01	0.61	0.79	0.61	286.76	286.89	287.19	2.21	2.21	2.21
C=O	0.12	0.12	0.12	0.71	0.71	0.66	287.96	288.09	288.40	3.42	3.42	3.42
Shake-up 2	0.04	0.05	0.04	1.22	1.22	1.22	289.11	289.25	289.55	4.57	4.57	4.57

Table 6.2.: Summary of the XPS parameters for the different components used to fit the PTCDI multilayers deposited on the (111) surfaces of the coinage metals. The plots are shown in Fig. [6.5]. The BE positions for the multilayer on Ag(111), as well as the relative BE (BE shift) of the C=O component with respect to the main line, agree very well with those previously reported by Häming et al. [152].

slightly positive [161]. Consequently, the nucleus is less screened by the electron cloud and the Coulomb interaction is stronger thereby increasing the binding energy. Also, for the different carbon peaks, shake-up satellites are identified, similarly to what it is observed for PTCDA [161]. More information can be obtained by fitting the data. As explained in Sec. [3.2], a proper fit is very complicated and ideally is supported by theoretical calculations. In our case, we based our model in the work of Schöll and coworkers [161] done for PTCDA, which considers separate components for C–C and C–C–O, in contrast to the fit employed by O'Shea et al [389] for PTCDI or Gustafson and coworkers for PTCDA [393]. Also, when assuming 3 different components for the perylene core, the relative position of the C–C and C–H remains controversial. For instance, Zahn and coworkers [376, 394], in contrast to Schöll et al. [161], identify the lowest BE component as the C–H instead of C–C. Our decision to assign the C–H peak at a higher BE than the C–C is based on the comparative study of different perylene derivatives adsorbed on ZnO, which will be presented in Chapter [9], and the data displayed in the previous chapter. Indeed, as shown in Fig. [5.1], unsubstituted perylene presents an asymmetric carbon core-level peak stemming from the inequivalent C–C (8 atoms) and C–H (12 atoms) contributions. Thus, the most intense component corresponds to C–H and is situated at the high BE part of the peak. PTCDI (or PTCDA) loses 4 hydrogen atoms from the core to accommodate the functional group, yielding the inequivalent C–C–O sites. Since there are no reasons to assume that the relative positions of the C–C and C–H change when functional groups are attached, we decide to keep the same assignment as for unsubsituted perylene, only applying the new stoichiometry. We also note that XPS studies of the hydrogenation of carbon nanotubes locate the C–H at the high BE side of the pure C–C component [395].

6.2.2. High-resolution XPS of (sub)monolayer coverages

In order to obtain a deeper insight about the chemical changes happening at the different PTCDI-metal interfaces, we performed HR-XPS ($h\nu$ = 800 eV) measurements of

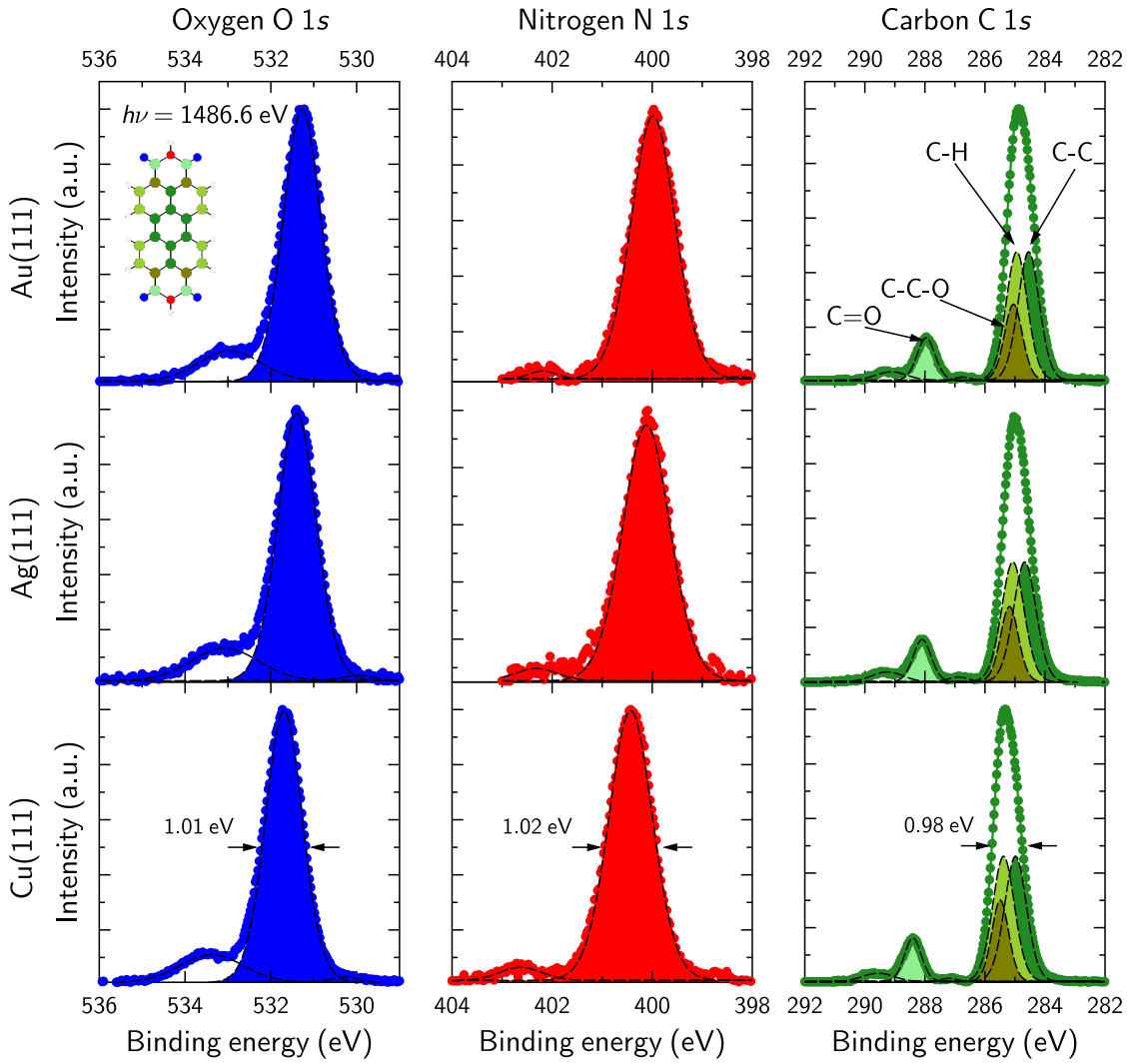

Figure 6.5.: Core-level spectra of PTCDI multilayers (nominal coverage 48 Å, which corresponds to roughly 10 ML) deposited on the (111) surface of the coinage metals. The fits were done considering the molecule stoichiometry and the additional peaks were attributed to shake-up satellites. Voigt profiles were used for the main components with a Lorentzian contribution of 30%. The shake-ups were fitted with a pure Gaussian line shape. As an example, the width of the main lines are included in the spectra of PTCDI on Cu(111), which are virtually the same for the other substrates, within ±0.05 eV, with the exception of the nitrogen peak on silver, which is slightly broader (see Tab. [6.2] for the precise values).

(sub)monolayer coverages. The results are included in Fig. [6.6]. The relevant fitting parameters of the main components are summarized in Tab. [6.3].

As clearly seen by comparing Figs. [6.5] and [6.6], in contrast to what happens at the multilayer regime, the line shape is extremely affected by the substrate underneath, highlighting the different levels of molecular coupling with the metal atoms. The peak broadening, the shake-up structure and the asymmetry of the peaks provide valuable information about the molecule-substrate interaction. A proper identification and understanding of all the mechanisms contributing to the line shape requires state-of-the-art theoretical calculations since the substrate influence, in some cases involving a strong hybridization with the

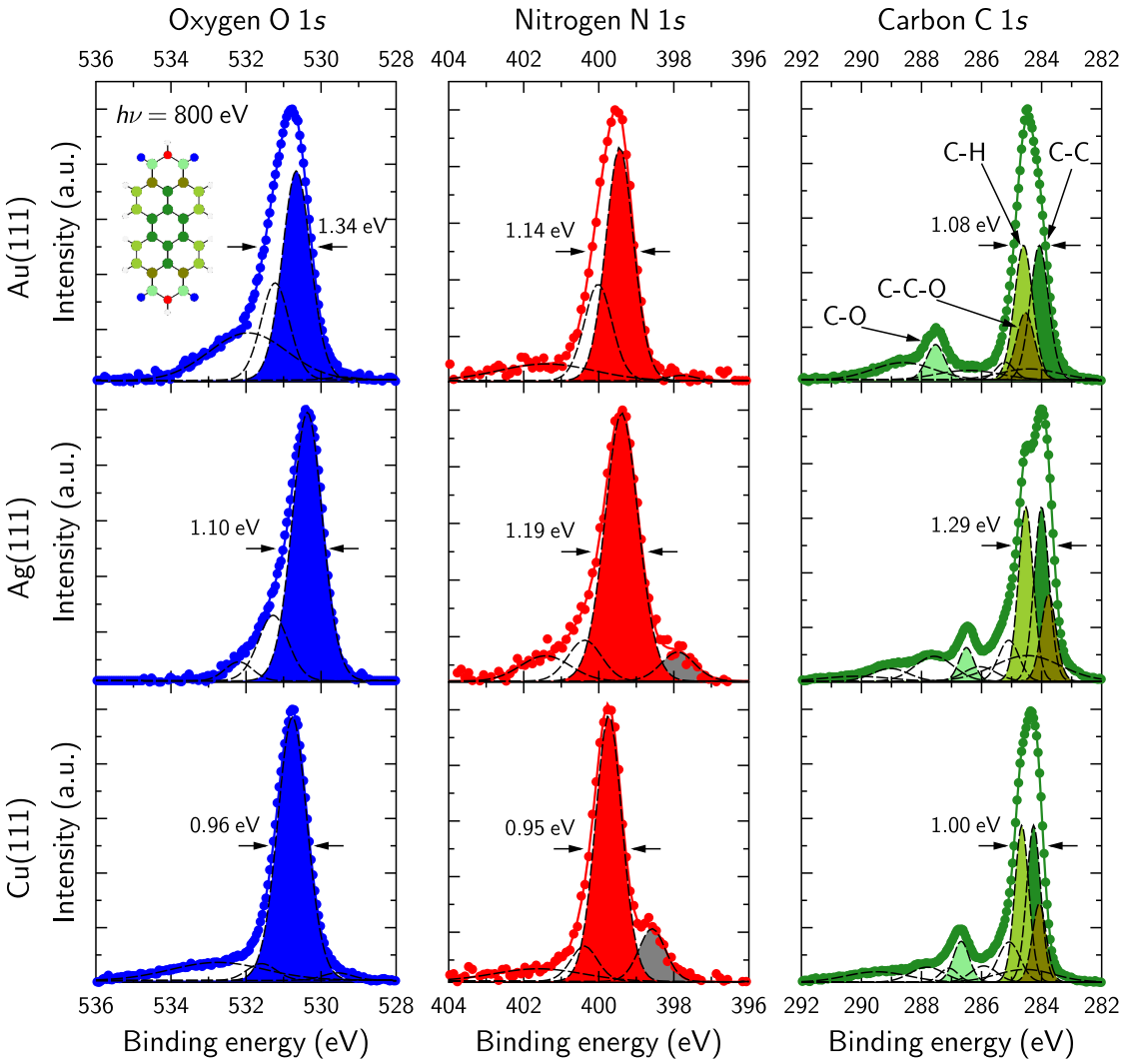

Figure 6.6.: Core-level spectra of PTCDI (sub)monolayers adsorbed on the different coinage metals and measured with a beam energy of $h\nu = 800\,\text{eV}$, 100 eV pass energy, at a take-off angle of 60° (beam impinging at 30° of the surface). The color code follows that of the picture inset of PTCDI. To keep a clean and simple layout, the shake-up satellites are not filled. The width of the main lines are included. Of special interest are the line profile changes happening from one substrate to the other, especially those of the C 1*s*, which are attributed to energy shifts of the different inequivalent components originating the perylene core peak. In dark gray, the unexpected side peaks observed in the nitrogen signal for silver and copper are highlighted. Their origin is discussed in the main text.

molecular orbitals, modifies the vibrational and electronic characteristics of the molecule compared to the isolated and thin-film scenario [159], which are very difficult to account for experimentally.

Starting with the spectra on Au(111), the three elements render a line shape very similar to those at the multilayer regime, but rigidly shifted towards lower BE by ∼0.45 eV, typical for weakly interacting systems, owing to the more efficient core-hole screening by the substrate. A more efficient screening is also responsible for the shake-up satellites moving closer to the main line [162]. More importantly, the BE difference between the C 1*s* peak related to the perylene core and that related to the functional groups remains the same as

Component	Area			FWHM (eV)			BE (eV)			BE shift (eV)		
	Au	Ag	Cu	Au	Ag	Cu	Au	Ag	Cu	Au	Ag	Cu
Oxygen O 1*s*												
Main	0.74	0.99	0.97	0.89	0.95	0.93	530.66	530.37	530.77	0.00	0.00	0.00
Data	–	–	–	1.34	1.10	0.96	530.77	530.42	530.77	–	–	–
Nitrogen N 1*s*												
Main	0.78	1.08	0.87	0.87	1.05	0.84	399.44	399.39	399.73	0.00	0.00	0.00
Data	–	–	–	1.14	1.19	0.95	399.57	399.37	399.77	–	–	–
Carbon C 1*s*												
C–C	0.39	0.40	0.34	0.72	0.58	0.55	284.08	284.00	284.27	0.00	0.00	0.00
C–H	0.39	0.40	0.34	0.72	0.58	0.55	284.60	284.53	284.66	0.53	0.52	0.39
C–C–O	0.19	0.20	0.17	0.72	0.58	0.55	285.54	283.77	284.08	0.47	-0.23	-0.19
C=O	0.10	0.08	0.10	0.72	0.58	0.58	287.53	286.50	286.68	3.46	2.50	2.41

Table 6.3.: Parameters for the main components employed to fit the HR-XP spectra shown in Fig. [6.6]. The information of the shake-up satellites is not included. The column with the BE shifts refers to the relative energy with respect to the main component. We note that the main components for nitrogen and oxygen refer to the colored ones. Especially in the case of gold, due to its asymmetry, the BE of these differ slightly from the maxima defined by the experimental points, labeled as "Data",whose BE is also included.

in the multilayer regime (∼3 eV). Overall, the C 1*s* spectrum resembles very much that of PTCDA on the same surface [396], but it shows differences with the PTCDI one reported by O'Shea et al. [389]. Indeed, they reported a coverage-dependent change of the carbon core-level spectrum [389] and observed a strong shift of the C=O component towards the perylene peak at coverages below 1 ML, which was attributed to the chemical bonding of the functional groups with the substrate atoms [389]. With increasing coverage, their C 1*s* spectrum becomes more and more similar to that reported in Fig. [6.6]. Thus, it was discussed that only part of the molecules/functional groups are involved in the chemical interaction with the substrate [389]. Since we did not record HR-XPS for different coverages, we can neither directly confirm nor deny the behavior reported by O'Shea and coworkers [389]. However, from our C 1*s* spectrum we cannot see any evidence of a shifted imide carbon component. Also, our spectra for oxygen and nitrogen (not reported by O'Shea et al. [389]) do not show the presence of different chemical states, which is expected if bonding and non-bonding groups coexist. Also, no lifting of the Au(111) surface reconstruction has been reported upon adsorption of PTCDI [350]. Last but not least, our coverage-dependent UPS measurements (see Fig. [6.3]) do not show any traces of chemical bonding at the (sub)monolayer regime and our XSW measurements (see Sec. [6.2.4] below) do not show any distortion of the nitrogen atoms (the information for the oxygen atoms is not available as it will be discussed). For the sake of discussion, we note that a study of PTCDI derivative on SiC reported the local bond formation between two (of the four) carboxylic oxygens and the substrate atoms, but without any CT to the molecular LUMO [397]. However, this situation would still leave a fingerprint in the O 1*s*. Despite this conundrum, we prioritize the internal coherence of our results stemming from a set complementary techniques and do not consider this possible coverage-dependence, which, in any case, deserves a closer look in the future. A last point on this worth considering is the different gold surfaces employed: in our case a single crystal whereas in Ref. [389] a gold thin film (150 nm) deposited on mica.

Continuing with the discussion of the nitrogen and oxygen spectra of PTCDI on gold, we have already mentioned the rigid shift towards lower BE compared to the multilayer

regime, but it is also important to highlight the asymmetry of the main lines of these elements. Certainly, a fitting of the peak using a single component is not possible owing to the slight asymmetry at the high BE side. Changes in the line shape and broadening are usually due to differences in the chemical environment, which in the case of the first layer is mainly due to the substrate influence. However, we propose that in this case it is the enhanced intermolecular interactions reported by PTCDI on Au(111) [364] the responsible for that. A detailed reasoning will be given in Sec. [6.3]. Nonetheless, in light of the discussion of the previous paragraph, we feel the need to rule out a relevant substrate contributions to the broadening. Starting for nitrogen, the presence of the hydrogen atom makes it very sensitive to the substrate influence. As it has been reported for PTCDI on TiO_2 [127] as well as on ZnO (Chap. [9]) and we will discuss next for silver and copper, any strong interaction/bond formation with the substrate may foster the deprotonation of nitrogen, i.e. the loss of the hydrogen atom, thus showing two different peaks in the N 1*s* core-level spectra, which are clearly not seen here. For the oxygen atoms, the existing asymmetry can hardly account for two rather different chemical environments, such those of oxygen atoms chemically bound to the substrate and oxygen atoms weakly interacting with the surrounding molecules. For comparison, a PTCDI derivative with alkyl chains attached to the imide group, reported to chemisorb on Au(111), shows rather broader core-level profiles for the O 1*s* signal [398].

The core-level spectra corresponding to PTCDI adsorbed on Ag(111) change dramatically compared to those of the multilayer regime (see Fig. [6.5]) as well as to those of Au(111). Häming and coworkers already discussed the manifold features shaping the core-level profiles [152, 399], which they complemented with calculation based on the Newns-Anderson model for chemisorption [400]. In particular, the metallic character of the first PTCDI layer on Ag(111) has an impact on the core-level spectra. The high BE edge for the C 1*s*, O 1*s* and N 1*s* peaks shows an extended asymmetric tail, similar to what is observed for small molecules adsorbed on metals [401]. The asymmetry stems from the continuum of interface states appearing upon hybridization of the molecular orbitals with the metal atoms [152], also responsible for the overall intensity increase of the shake-up structure. Interestingly, the C=O component shows a shift of ∼1.7 eV towards lower BE with respect to the multilayer regime, i.e. ∼1.1 eV more compared to C–C and C–H, meaning that the benefit from the substrate screening is higher for the carbon atoms with electron deficiency (due to the bond with the more electronegative oxygen and nitrogen atoms). This trend extends to the C–C–O carbon atoms, according to the fits in Fig. [6.6], where this component experiences a strong shift towards lower BE and is responsible for the split of the perylene-core peak, similar to what is reported for PTCDA on Ag(111) [109].

The core-level spectra corresponding to PTCDI deposited on Cu(111) show a decrease of the line width and an increased peak symmetry, in particular for nitrogen and oxygen. The BE shift in the C 1*s* XP spectrum with respect to the multilayer follows a similar trend as for silver. In particular, the C=O and C–C–O components move towards lower BE. It is interesting to note that this decreased line width compared to gold appears rather counterintuitive. Despite the different energies employed, the XP spectra of perylene shown in the last chapter (see Fig. [5.1]), shows a clear broadening of the spectra on Cu(111) compared to that on Au(111). Also, other comparative studies of phtalocyanines on coinage metals show broader peaks for the copper substrate [166]. More on this will

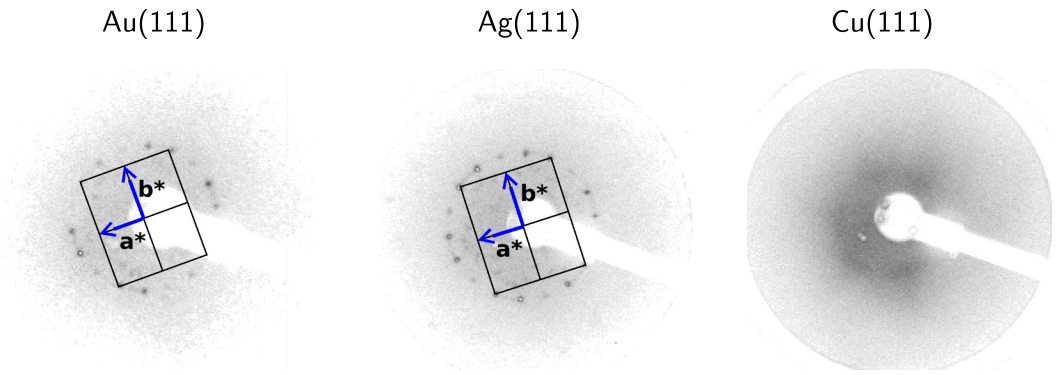

Figure 6.7.: LEED patterns for PTCDI coverages of 1 ML (4 Å), the unit cell is superimposed. Electron energies: $E = 51$ eV for Au(111), $E = 55$ eV for Ag(111) and $E = 29$ eV for Cu(111). The values of the unit cell vectors are found in Tab. [6.4]. Figure taken from Ref. [69].

be discussed in Sec. [6.3].

Finally, we note the presence of the low BE peak (gray component in Fig. [6.6]) seen for N 1*s* on Cu(111), less pronounced for Ag(111) and also reported for TiO_2 [127] and ZnO (see Chap. [9]). Its origin appears controversial. On Ag(111), the most intense peak is attributed to a giant satellite, whereas the low BE shoulder is considered the main line [152]. On the contrary, for PTCDI on TiO_2, the low BE peak is attributed to nitrogen atoms that lose the hydrogen (deprotonation) due to substrate CT [127]. Our findings for the PTCDI-ZnO interface (Chap. [9]) seem to support the latter since by varying the number of defects at the surface the intensity ratio varied accordingly.

As a final remark, we are aware that our fitting model may overlook some aspects, for instance, no asymmetry profile is included in the Voigt peaks employed to fit the main lines, in particular for the spectra of PTCDI on copper and silver. Also, the Lorentzian contribution to the Voigt profiles was set arbitrarily to be of 30% (the shake-ups were set to have a pure Gaussian profile [159, 161]), although having a ±10% difference does not modify much the fit. However, we tried to be consistent with the number of components employed for each core-level and only additional ones were added when the recorded profile made it necessary for a satisfactory fit. All in all, the trends discussed along this chapter, especially regarding BE positions and shifts may not be critically compromised, despite our simplifications.

6.2.3. LEED measurements

The LEED patterns for a nominal coverage of 4 Å (roughly 1 ML) are shown in Fig. [6.7]. It is inferred from the presence/absence of diffraction spots that PTCDI forms an ordered overlayer on Au(111) and Ag(111) but not on Cu(111). The extracted unit cell parameters are included in Tab. [6.4]. The distribution of the diffraction spots and the values of the unit cell indicate that the molecular arrangement is the same on both substrates.

The ordered arrangement seen on Au(111) is in line with the results of many STM studies of PTCDI on the mentioned substrate, see for instance Refs. [103,350,363,364,402]. However, small discrepancies appear between the unit cell parameters calculated here and those reported in STM studies [350, 363, 364, 402], which, by the way, also report

Substrate	Parameters		
	a (Å)	b (Å)	**a∠b** (°)
Au(111)	13.8	10.7	89.5
Ag(111)	12.9	11.0	89.4
Cu(111)	–	–	–

Table 6.4.: Unit cell parameters extracted from the LEED measurements shown in Fig. [6.7]. We note that the unit-cell area is bigger for gold than for silver, meaning that the molecular density is higher for the latter, which may well be due to the low-resolution of the diffraction pattern.

dissimilar values depending on the study. In particular, the parameters reported for the aforementioned scanning-probe studies show slightly longer axis (∼3 Å) and higher angles (from 5° to 10°). A possible explanation for this discrepancy is the fact that LEED patterns are averaged over the sample, whereas the STM measurements consider very small regions.

The authors are not aware of any STM study on Ag(111) nor Cu(111) for PTCDI. However, NEXAFS measurements on Ag(111) show flat-laying molecules at the monolayer as well as at the multilayer regime [399], whereas UPS measurements point out to the formation of closed layers [399], both in agreement with our XSW and UPS measurements. Also, DFT calculations (without vdW corrections) of PTCDI on Ag(111) [403] report slightly higher unit-cell parameters than those reported here. It is worth mentioning that the very similar molecule N,N′-dimethylperylene-3,4,9,10-bis(dicarboximide) (DM-PBDCI) does show an ordered arrangement on Ag(111) [404].

6.2.4. XSW results: adsorption heights and molecular distortion

Information of the vertical arrangement of the first PTCDI layer in contact with the three different surfaces was obtained by means of the XSW technique. In order to evaluate the photoelectron yield for the different core-level signals a model adapted from the HR-XPS (see Fig. [6.6]) was used and is shown in Fig. [6.8]. Due to the lower resolution of the hard X-rays (smaller cross-section for the light elements analyzed here), the fitting model could be simplified. In particular, for some cases less shake-up satellites were employed and, most importantly, the difference between C–C–O and C–C was neglected for the C $1s$ signal on Ag(111) and Cu(111) since both species are at almost the same BE[2]. As fitting constraints for the XSW data analysis, the BE was fixed for all the components and the FWHM was let free within an interval of ±0.2 eV. The area was let as a completely free parameter for all the components.

The fitting of the XSW data is shown in Fig. [6.9], where a remarkable number of inequivalent species are satisfactorily analyzed. This is taken as an independent validity test of our fitting model because the evaluation of the photoelectron yield is very sensitive to it. Interestingly, although the model renders very good results for PTCDI adsorbed on Cu(111) and Ag(111), on Au(111) coherent modulations of the photoelectron yield were obtained only for the total area stemming from the perylene core (i.e. the main

[2] One can also argue that, despite the slightly different chemical environment between C–C and C–C–O, the structural difference is not as pronounced since the C–C–O carbons are still carbons surrounded by other carbons and most importantly, they are part of the perylene core, justifying, this way, the assumption of one peak for C–C and C–C–O carbons.

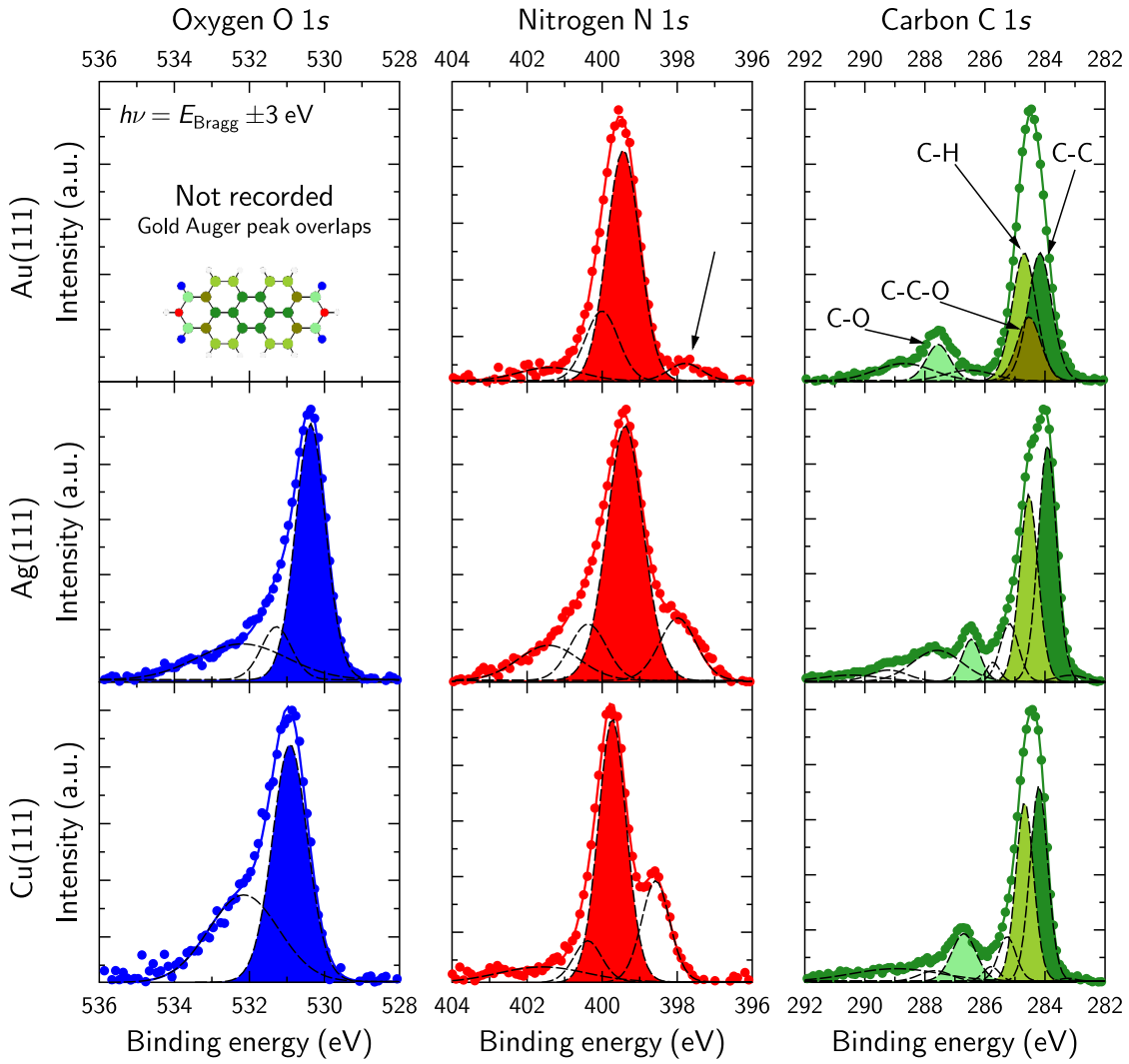

Figure 6.8.: Core-level model employed to fit the XSW data. The spectra shown here stem from the superposition of all the different XPS scans recorded during an XSW measurement, i.e. 31 scans within an interval of ±3 eV around the Bragg energy corresponding to the [111] direction of each substrate. Taking the superposition of different scans allows for a better signal-to-noise ratio, and thus clearer identification of different spectral features. We note that the N 1*s* core-level spectra for the gold case shows a feature at the low BE side of the main line (marked with an arrow), similarly to what it is observed on Ag(111) and Cu(111). Interestingly, though, this component is not present in the measurements performed with the soft X-ray beam (see Fig. [6.6] for comparison). See Sec. [6.3] for more details on this.

peak around 284 eV). For this case, different fitting models were employed (with two or three components) and none of them produced a good fit of the inequivalent carbon species, which naively could be explained by the disperse adsorption heights of the molecules within the supramolecular arrangement on gold [364] (see Sec. [6.3] for more details). Finally, the presence of a gold Auger peak around the O 1*s* BE region hinders a clean evaluation of the oxygen photoelectron yield, thus limiting the available structural information for the gold case. The fitting parameters are summarized in Tab. [6.5] and a sketch of the different adsorption geometries is displayed in Fig. [6.10].

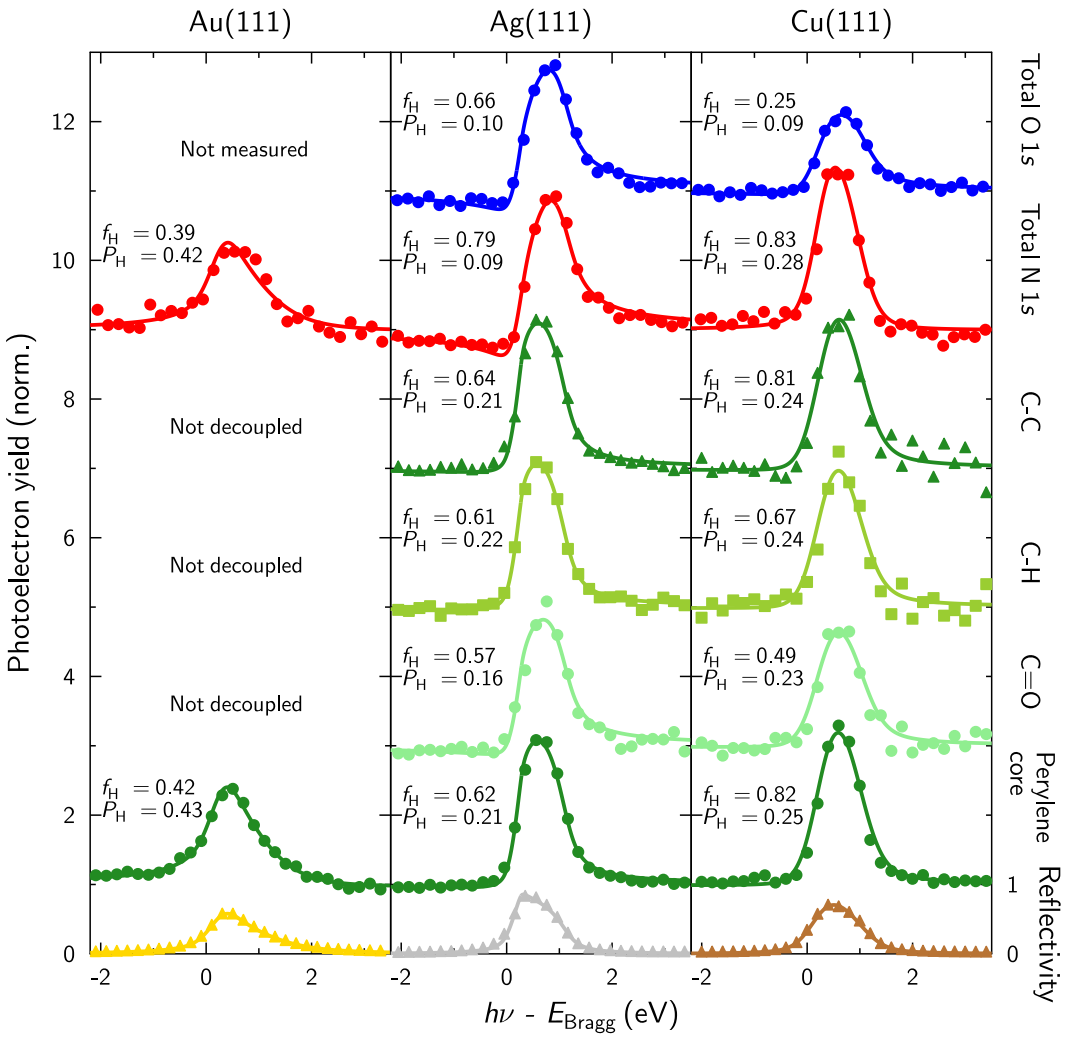

Figure 6.9.: XSW measurements along the **H** = [111] direction for PTCDI (sub)monolayers adsorbed on the three coinage metals. The different inequivalent species that could be resolved are included with the corresponding fitting parameters, namely the coherent fraction (f_H) and the coherent position (P_H). As discussed in the main text, the separation of the different inequivalent carbons was not possible for PTCDI on gold. For the same system, the oxygen adsorption distance is not accessible due to an overlapping substrate Auger peak at the O 1*s* region. Figure adapted from Ref. [69].

The coherent fractions for the different species are typical for flat-laying molecules. The perylene core shows remarkably high coherent fractions on copper and silver and slightly smaller on gold, but still within the range observed for other COM molecules [47]. The difference between the adsorption distance of C–H and C–C carbon atoms of the perylene core is virtually non-existent meaning that the peripheral carbons, on average, present no significant distortion compared to the inner ones. On the contrary, the functional carbon does show a lower adsorption distance for silver and copper, which is attributed to the pulling effect exerted by the heteroatoms adsorbing much closer to the substrate. Indeed, for silver, both the oxygen and nitrogen atoms are ∼0.25 Å below the perylene core, which pull down the C=O atoms by ∼0.1 Å with respect to the average carbon distance. On

Substrate	Component	f_{111}	P_{111}	d_{111} (Å)
Au(111)	N 1*s* total	0.39	0.42	3.26 ± 0.03
	Perylene core	0.42	0.43	3.29 ± 0.02
Ag(111)	O 1*s* total	0.66	0.10	2.60 ± 0.03
	N 1*s* total	0.79	0.09	2.58 ± 0.03
	C–C	0.64	0.21	2.85 ± 0.02
	C–H	0.61	0.22	2.87 ± 0.02
	C=O	0.57	0.16	2.73 ± 0.03
	Perylene core	0.62	0.21	2.86 ± 0.02
Cu(111)	O 1*s* total	0.25	0.09	2.28 ± 0.02
	N 1*s* total	0.83	0.28	2.68 ± 0.02
	C–C	0.81	0.24	2.59 ± 0.05
	C–H	0.67	0.24	2.59 ± 0.04
	C=O	0.49	0.23	2.56 ± 0.04
	Perylene core	0.82	0.25	2.61 ± 0.02

Table 6.5.: XSW parameters extracted from the data fitting shown in Fig. [6.9]. All the components that gave a coherent result are included. Due to the presence of an overlapping Auger peak in the O 1*s* BE region, the adsorption distance for this element could not be analyzed [70]. Also for PTCDI on gold, the separate components of the perylene core (C–H and C–C) and the C=O component did not yield a coherent fit, therefore they are not included. Also for Au(111), the actual adsorption distance was calculated taking into account the surface reconstruction occurring for this metal [70].

copper, though, the oxygen atoms are ∼0.3 Å below the core, whereas the nitrogen atoms are ∼0.1 Å above, consequently the opposing forces leave the functional-carbon atoms virtually at the same distance as carbon backbone (0.03 Å below). It is worth noting that the coherent fraction of the oxygen atoms on Cu(111) is lower than the other elements, although it is within the range observed for other molecules adsorbed on copper [47].

The vertical ordering shown by PTCDI is very similar to that of PTCDA, but some small differences appear due to the different functional group. For instance, on Ag(111), the nitrogen atoms are located below the perylene core, whereas the anhydride oxygen of PTCDA is above it [217, 405]. On copper, though, the oxygen atoms of PTCDI are bent towards the substrate and nitrogen adsorbs away from it. Interestingly, the anhydride oxygen of PTCDA is also adsorbing above the core, but in this case the carboxylic oxygens do it as well [65]. The adsorption distance of the perylene core is almost the same as for PTCDA on Au(111) and Ag(111). However, the PTCDI core adsorbs 0.05 Å closer to Cu(111) than PTCDA, intuitively assigned to the pulling effect of the oxygen atoms. State-of-the-art DFT calculations including vdW corrections, which have successfully reproduced the experimental values for PTCDA and DIP [61] are, unfortunately, not yet available for PTCDI. We note, however, that a DFT study of PTCDI on Ag(111) published in 2008 [403], correctly reports the bending of the oxygens towards the surface (adsorbing 2.74 Å atop of a silver atom), but predicts an adsorption distance of 3.41 Å for the central phenyl ring of the perylene core, which is sitting in a bridge position with respect to the substrate atoms [403]. This discrepancies might stem from the fact that vdW corrections were not used [403].

6.3. Discussion

The experimental data presented above renders a comprehensive description of different PTCDI-metal interfaces, which allows us to correlate the different features seen in the

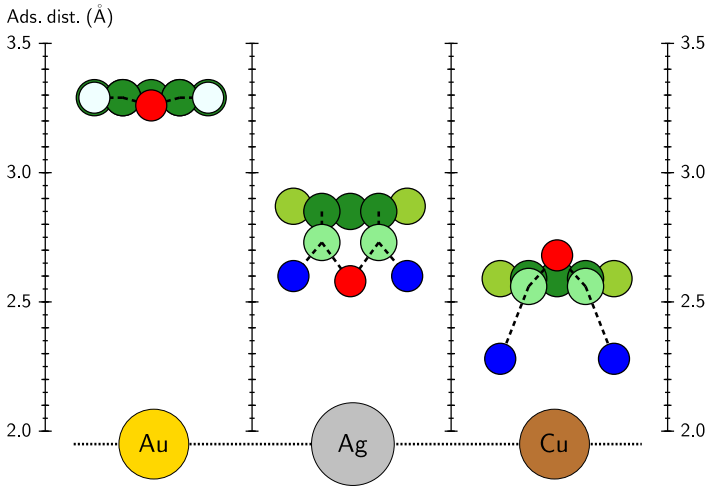

Figure 6.10.: Sketch of the adsorption geometry of PTCDI adsorbed on the (111) surfaces of gold, silver and copper. Precise adsorption distances for the different elements and inequivalent carbon atoms could be obtained thanks to the chemical sensitivity of the XSW technique and a proper fitting model. The precise values are summarized in Tab. [6.5]. The origin of the scale is the topmost substrate atom, but it is shifted 2 Å for a clearer data display.

electronic properties of the molecule with the different structural changes induced by the different substrates. Thus, PTCDI shows no ordered arrangement on Cu(111), as inferred from the LEED measurements. The interaction with the substrate is particularly strong as it is deduced from the completely filled LUMO, consequence of a significant CT from the substrate to the molecule, and the shortest adsorption distance exhibited by the perylene core within the three cases studied. Furthermore, the molecular distortion, with the oxygen atoms bending towards the substrate and the nitrogen ones adsorbing above the core, shows that the substrate influence is particularly affecting the functional groups. In light of this, one can argue that the strong bonding with the copper substrate hinders the molecular mobility over the surface, thus preventing the formation of an ordered layer. We note that a similar reasoning was made for the strongly interacting PTCDI on Si(111) [383] where near edge X-ray fine structure (NEXAFS) spectroscopy measurements showed a lack of molecular order and a remarkable distortion in the first layer.

The opposite situation is observed for PTCDI on Au(111), where the LEED patterns show the formation of a laterally ordered first layer, thus indicating a favored intermolecular interaction that, as seen in the numerous STM studies, mostly consists of an imide-imide group bonding [103,362,364]. Also, the electronic coupling with the substrate atoms is rather weak, since the molecular adsorption only induces an interface dipole due to the push-back effect, typical for weakly interacting systems [30], but no additional features at the VB are observed. In line with this, the adsorption distance is found to be the highest of the three cases. Although the adsorption geometry of the functional group is not complete, the position of the nitrogen atoms, virtually at the same distance as the perylene core indicates that no significant molecular distortion is induced by the substrate.

Lastly, PTCDI on silver shows an intermediate situation, where the molecules form a supramolecular arrangement on the surface as inferred by the existence of diffraction spots in LEED. Yet, the molecule-substrate electronic interaction is significant due to CT from the substrate that partially fills the LUMO and the remarkable molecular distortion, as

inferred by XSW, with the functional groups bending towards the surface.

Having established a clear framework for the structural and electronic properties we can now discuss how the different adsorption scenarios affect the core-level spectra. In particular, we aim at correlating the specific spectral features, namely, broadening and BE shifts with the specific electronic and structural arrangements mentioned before. To make the discussion more visual, Fig. [6.11] shows the BE shifts of the main components with respect to their corresponding BE at the multilayer regime for each substrate. What is basically plotted is the substrate-screening effect (nonexistent at the multilayer regime) for the different species. For gold, all the components show a rather homogeneous shift towards lower BE of around ∼0.45 eV, typical for physisorbed molecules, in full agreement with the rather high adsorption distance and the missing VB features. More importantly, the functional-carbon component (C=O) rigidly shifts with the core-carbons atoms, meaning that no specific interaction of these with the substrate is at work. This appears in stark contrast to the silver and copper cases. First, the perylene core components are shifted further towards lower BE, most likely due to the even more efficient substrate screening provided by the shorter adsorption distance, as reported by XSW (see Tab. [6.5]). Secondly and most remarkably, the strong shift towards lower BE of the C=O component and, slightly less pronounced, the bridge-carbon one (C–C–O), which goes in line with the strong bending of the functional groups towards the surface[3]. One can fairly ask why the shift is lower for the oxygen and nitrogen atoms. A plausible answer is that, since the end-group carbons are electron deficient because of the bonding to atoms with strong electron affinities, the screening has a more noticeable impact on these species than on the oxygen and nitrogen atoms [399], which already have an electron-rich environment, suitable for an efficient screening of the nucleus.

At this point, only the peak broadening is left for discussion. As mentioned in the corresponding results subsection [6.2.2], the core-level spectra measured on Au(111) show an increased broadening compared to those on Cu(111), which represent opposed adsorption scenarios as explained above. We note that the trend is also observed with hard X-rays (Fig. [6.8]. This behavior appears to contradict that shown for perylene in the previous chapter and other measurements reported for phtalocyanines [165, 166, 347] and DIP [58, 165, 347]. It is discussed that the lifetime broadening depends on the distance to the substrate, whereby a shorter adsorption distance goes along with broader peaks. Other contributions to the peak width, such as thermal and instrumental are ruled out, since they affect equally all the cases. Also, contributions from different film morphologies [168] are not considered at submonolayer coverages, where all the molecules are laying flat on the surface. Thus, a likely explanation is the influence of the molecular environment, i.e. molecule-molecule interactions, which are present on Au(111) and not on Cu(111) as inferred from the LEED measurements (see Fig. [6.7]). Indeed, the many STM studies available in the literature [103, 363, 364] show arrangements such as that in Fig. [6.1], where a highly directional imide-to-imide hydrogen bonding between nearby molecules (the so-called straight PTCDI rows) is accompanied by imide-to-core interactions (the canted PTCDI rows). Also, local-probe spectroscopy measurements show intermolecular electronic states that extend through various molecules [103]. Even more interesting, it

[3] We note that we do not have information about the position of the C–C–O, however, a slightly lower adsorption position compared to the carbon core position would not be surprising.

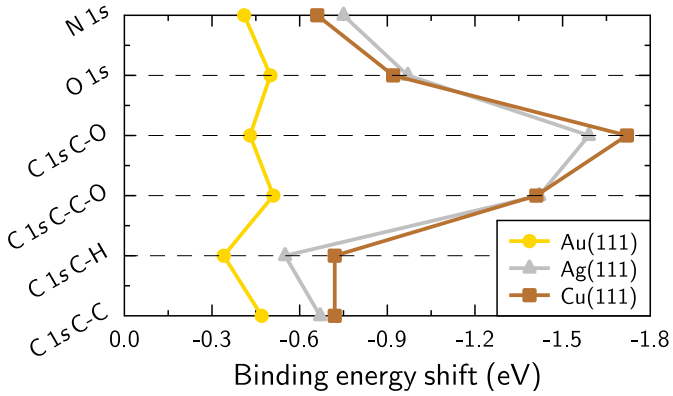

Figure 6.11.: Binding-energy shifts corresponding to the different inequivalent species at the (sub)monolayer regime with respect to the multilayer value (a 0 eV shift would be the case for a component appearing at the same BE as in the multilayer regime). The lines connecting the data points are included just as a guide for the eye. We note that, to account for the BE shifts of the O 1*s* and N 1*s* core-level signals, the maxima of the experimental data points are used instead of the main fitting component (see Tab. [6.3] for the precise values). The trend for gold shows neither element-specific nor site-specific shift, but a general shift of ∼0.45 eV, meaning that the substrate screening is rather homogeneous through the molecule, typical for weakly adsorbed species. On the contrary, PTCDI on copper and silver shows a strong shift of the functional-carbon species towards lower BE, clearly higher than for the other components. This indicates a specific substrate influence on the functional groups, which partially involves the bridge carbon atoms (C–C–O). The other carbon atoms of the core have a higher shift than on gold, most likely due to a shorter adsorption distance, which enhances the substrate screening. Figure adapted from Ref. [69].

turns out that the molecular influence is fostered by a mild annealing at 50°C, as reported by Hieulle and Silly [364], who also reported structural changes that favor the imide-to-imide arrangement, with various rows of straight PTCDI lines imaged, which appear to have different heights [364] (a possible contribution to the low coherent fractions reported in the XSW measurements in Fig. [6.9]). We therefore conclude that the enhanced intermolecular interactions reported on Au(111) and missing on Cu(111) are behind the spectral broadening appearing for the first in comparison to the latter.

It is then plausible to assume that PTCDI on Ag(111) represents an intermediate case, where the hybridization of molecular orbitals with those of the substrate atoms and the decreased adsorption distance (as seen in UPS and XSW) still leaves some freedom for the molecules to laterally rearrange (as shown in LEED), although the latter cannot be unambiguously assigned to any particular core-level feature beyond a reasonable broadening analogous to what happens on Au(111). Nonetheless, different studies of the similar PTCDA molecule on various silver surfaces showed that molecule-molecule interactions have an effect on the frontier orbitals as seen by orbital tomography [68, 105]. Also, the loss of lateral ordering upon cooling of a PTCDA monolayer on Ag(111) was shown to strengthen the bonding with the substrate, as indicated by a decrease in the adsorption distance, higher bending of the functional groups and, most importantly, further filling of the LUMO [72], similar to what we observe on copper.

One last point needs to be addressed regarding the core-level spectra and it is why we do not see stronger BE shifts as those reported for other systems showing hydrogen bond formation. Certainly, one can find in the literature many examples of XPS studies of hydrogen bonds [101, 102, 406], supported by theoretical calculations of the expected core-level shifts for the element acting as a proton donor and those expected for the proton acceptor [173] and, in some cases, the core-level shifts are higher than 1 eV rendering two

clearly distinguishable core-level features. A possible explanation may be given by the fact that some of these studies are for small molecules adsorbed on surfaces where the chemical environment is well defined, namely, H-bond formation with the surface but not within the following layers [101,102]. Also, for other cases, the bond formation between different small molecules is studied at the gas phase [171] where no other interactions are at play. Conversely, molecules on the surface also feel the substrate influence (although possibly weak), steric repulsion between nearby molecules or any other effects that may (slightly) disrupt the molecular ordering [407], thereby downplaying the H-bond formation.

As a closing remark for this section, we address the adsorption behavior of PTCDI on the coinage metals within the context of the SIAS model [71], outlined in Sec. [2.2]. This rationalizes the presence of CT from the metal to the molecular LUMO. PTCDI is a fair candidate to undergo SIAS, as already pointed out by Heimel et al. [71]. Now we are in position to proof experimentally whether this is the case. The LUMO filling, which is partial on Ag(111) and total on Cu(111), suggests that the Fermi-level pinning is overcome. The bending of the functional groups towards the surface and the core-level shift of the C=O species suggest that there is a preferential interaction between them and the silver and copper surface, which may well increase the resonant structure of the molecule. However, the chemical shift of the C=O component is less pronounced since it is clearly distinguishable from the perylene core peak, compared to the cases shown in Ref. [71], pointing out that the transition from C=O to C–O may not be fully achieved. Consequently, we conclude that PTCDI possesses virtually all the experimental fingerprints that accompany the SIAS mechanism but small discrepancies suggest that this might not be the only mechanism at work. In any case, without theoretical calculations, one cannot elaborate on the discussion further.

6.4. Conclusions

The high-quality experimental data presented here yields a comprehensive characterization of the structural, chemical and electronic (visually summarized in Fig. [6.12]) properties of a complex metal-organic interface, with particular emphasis on the substrate reactivity as a mediator between molecule-molecule and molecule-substrate interactions and their impact on the core-level spectra. As a summary, on Au(111), PTCDI adsorbs undistorted at the highest adsorption distance for the three coinage metals. The LUMO remains above the Fermi level, indicating that the electronic coupling with the substrate is rather weak. The core-level spectra show a line shape similar to the multilayer case but with a rigid shift towards lower BE, typical for physisorbed molecules. Most importantly, the BE difference between perylene core and functional carbon atoms remains the same as in the multilayer regime, supporting the statement that no specific interactions with the substrate occur. Interestingly, the spectra show an unexpected broadening and asymmetry, especially for the nitrogen and oxygen signals, compared to those for Cu(111) and the multilayer regime. Based on our LEED measurements and the numerous STM studies available, we attribute this to the molecule-molecule interaction, especially strong through the arrangement that favors a directional imide-imide interaction between adjacent molecules [364]. Moving to the least noble substrate, PTCDI on Cu(111) shows the lowest adsorption distance with a strong bending of the oxygen atoms towards the surface, but having the nitrogen

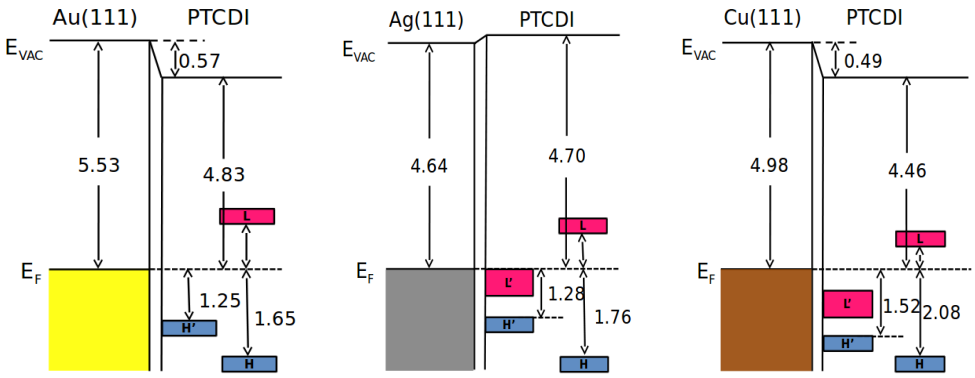

Figure 6.12.: Energy-level alignment between PTCDI and the different metals studied, derived from the measured electronic properties. The position of the LUMO (not included) was estimated by the transport gap of PTCDI (2.37 eV) as measured in a combined UPS and inverse photoemission study [189].

close to the perylene core distance. The strong molecular distortion is accompanied by a completely filled LUMO that falls entirely below the metal Fermi level. Thus, PTCDI shows a strong interaction with the substrate and a significant electronic coupling, both pointing out towards a rather strong chemisorptive behavior. It is argued that the strong bonding with the substrate hinders the mobility of the molecules [72], thus preventing a supramolecular arrangement, which is supported by the lack of diffraction spots in LEED. Surprisingly, the core-level spectra show the narrowest line width, especially compared to those on Au(111), challenging the, *a priori*, dominating lifetime broadening associated with a shorter adsorption distance. This supports our assumption that, for PTCDI, the molecular environment has an impact on the core-level spectra through a remarkable broadening, which is present for the Au(111) case but not for the Cu(111) one. Finally, an intermediate scenario is observed for PTCDI on Ag(111), where a half-filled LUMO appears in the VB spectra since it is cut by the Fermi edge, thus rendering a metallic character to the first monolayer. The molecule-metal coupling is followed by a bending of the oxygen and nitrogen atoms towards the surface and a decreased core adsorption distance compared to PTCDI on Au(111). The PTCDI-silver coupling does not prevent the molecules to laterally organize, as it is inferred from the existence of a LEED pattern. The metallic character has a strong impact on the core-level spectra that show a significant tailing towards the higher BE side due to the continuum of states appearing at the interface [152]. As another sign of the increasing interaction from Au to Cu, we highlight the side peak appearing for the nitrogen N 1*s* core-level spectra, which increases in intensity following the same order.

Overall, we can conclude that, due to the presence of the imide groups that facilitate a directional and strong molecule-molecule interaction, fingerprints of this may be observed in core-level spectra. This would be in stark contrast to other molecular films that lack these preferential interaction groups, such as phtalocyanines [165, 166, 347] or DIP [165, 347]. Finally, the complementary dataset presented here, allows one to further test the SIAS model introduced by Heimel et al. [71], highlighting the importance of the functional groups as a mechanism to induce a charge transfer from the surface, as it is evidenced by the comparison with unsubstituted perylene, presented in the previous chapter (Chap. [5]).

However, as also discussed for perylene, the presence of functional groups is not crucial for the molecules to exhibit a short adsorption distance.

7. F4PEN adsorbed on coinage metals. Effect of the fluorination on the adsorption distance

The results presented in this chapter were carried out in collaboration with Prof. Steffen Duhm's group at FUNSOM, Soochow University, in Suzhou, China. Qi Wang, supervised by Prof. Duhm, analyzed the LEED and UPS data contained in the following.

7.1. Context

Pentacene (PEN, $C_{22}H_{14}$) and its fluorinated derivative perfluoropentacene (PFP, $C_{22}F_{14}$) are prototypical rod-like π-conjugated molecules with donor and acceptor character, respectively. They have been extensively studied in thin films [162, 408, 409], single crystals [410], blends [32, 408, 411, 412] and as overlayers adsorbed on different metal [57, 76, 77, 100, 343, 413–423], semiconductor and insulating [187, 424–426] substrates. The effects induced by partial or total fluorination on different π-conjugated molecules [29] has attracted significant attention since it renders a way to make the molecule more stable against oxidation [18], to change the electron affinity as well as to tune the charge injection barriers between those and a metal electrode. For the latter, the substitution of hydrogen by fluorine increases the ionization energy (IE) of the molecule, which, in a simple picture, decreases (increases) the electron (hole) injection barrier [57, 427]. In addition, conformational changes upon adsorption introduce effects that one has to take into account in order to fully understand the energy-level alignment (ELA) at the interface [57]. This has already been studied for PEN and PFP on different prototypical nobel metal surfaces [57, 417, 418]. For instance, on Cu(111), PEN submonolayers are chemisorbed and can be imaged even at room temperature (RT) with STM, whereas PFP is weakly chemisorbed and only at low temperature (LT) the molecules can be imaged [417]. Furthermore, PFP on Cu(111) undergoes an adsorption-induced distortion that renders a higher adsorption distance for the fluorine atoms, on average, than the carbon backbone [57]. Interestingly, PEN on Ag(111) shows a similar behavior as PFP on Cu(111) [343]. Because of the weak interaction, PFP physisorbs on Ag(111) without distortion [418], similarly to both molecules on Au(111) [428, 429]. Temperature and coverage effects have been also reported [57, 343, 417]. Of particular interest is the effect of the distorted PFP on Cu(111), which renders a dipole moment that strongly influences the ELA and adds up to the typical push-back effect [57]. Besides, the induced molecular dipole, intramolecular dipole moments stemming from the C–F polar bonds within the molecule have a strong impact on the energy levels and the growth of the multilayer [418]. Thus, a proper characterization of the first monolayer is not only important for correctly describing the charge injection but also has implications for the thin film growth [76]. Additionally, state-of-the art DFT calculations with

vdW corrections show the radically different adsorption geometries of PEN and PFP on Cu(111), with the former adsorbing rather flat on the surface with a slight curvature and the latter showing a sharp bending, being the central atoms much closer to the surface than the edge carbons [430].

In order to further investigate how partial fluorination affects the metal-organic interface, we deposited the PEN derivative 2,3,9,10-tetrafluoropentacene F4PEN [431], synthesized by Prof. Bettinger's group at the University of Tübingen (see paragraph [4.1] for more details) [432, 433] on Ag(111) and Cu(111). In particular, a multi-technique approach was taken to assess the structural, chemical and electronic properties of the first layer as well as the subsequent ones until the thin-film regime. With this comprehensive characterization, the impact of partial fluorination on the structural and electronic characteristics of the organic-metal interface are further tested and discussed in the context of the extensive literature available for the non- and fully-fluorinated PEN counterparts.

Despite some remarkable research involving rubrene [18, 434–437], pthalocyanines [438–442] and PEN derivatives (including F4PEN) [432, 433, 443–445], available references for the chemical functionlization via fluorination of organic semiconductors are rather scarce, most likely due to the complexity inherent to the synthesis process [446, 447]. Therefore, we are optimistic that the results presented here will bring new and fresh input, especially related to the interface properties.

7.2. Results

The following results tackle the vertical adsorption geometry (via XSW) and in-plane arrangement (via LEED) of F4PEN adsorbed on Ag(111) and Cu(111). The chemical and electronic characteristics, from the first layer to the thin-film regime, deposited on the same substrates, are inspected with coverage-dependent XPS and UPS. Finally, the precise chemical state of the first (sub)monolayer is measured with synchrotron-based XPS.

7.2.1. Coverage dependent XPS and UPS

Following the same order as in the previous chapter, we start by presenting the coverag-dependent UPS and XPS measurements that highlight the specific interface features, as opposed to those originating at the purely organic environment. Fig. [7.1] shows the VB survey scans of the F4PEN-Ag(111) and F4PEN-Cu(111) systems. In both cases, the substrate features decrease in intensity with increasing F4PEN coverage pointing out that the formation of at least a wetting layer occurs, which significantly attenuates the photoemitted metal electrons. The molecular features seen at the highest coverage (nominally 48 Å, ∼10 ML) are substrate-dependent thus hinting at different growth modes and probable different intermolecular arrangements depending on the substrate. As a comparison, the same coverages for PTCDI, which grows layer-by-layer, show the same molecular features regardless of the substrate (Fig. [6.2]).

The VL shift with increasing coverage extracted from the SECO region, displayed in Fig. [7.2a], goes in line with the formation of at least a wetting layer around 4 Å on both substrates since the shift saturates at this coverage. In particular, the VL is reduced by ∼0.6 eV for both cases. The coverage evolution of the VL and the HOMO positions are

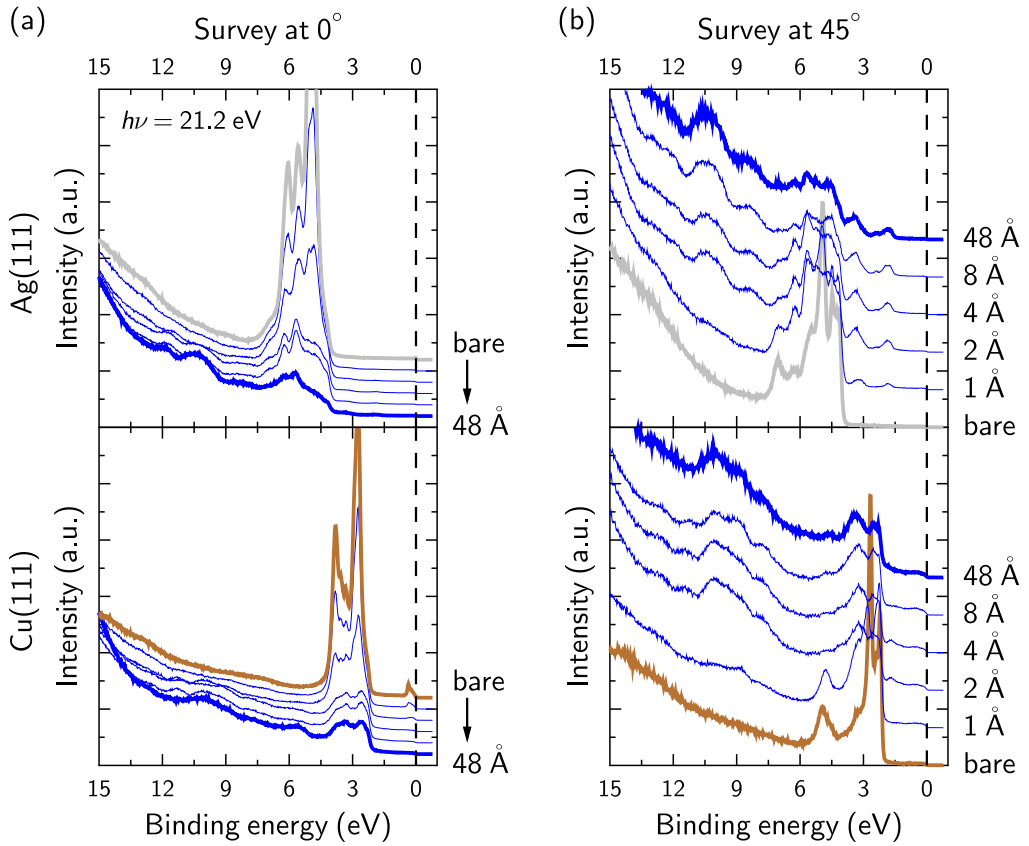

Figure 7.1.: Coverage-dependent survey scans of the valence-band region of F4PEN deposited on Ag(111) and Cu(111) (monochromatic He I source, $h\nu = 21.2\,\text{eV}$) measured at (a) normal incidence and (b) at 45°. The metal d bands, $E_\text{B} = [2.5 - 8]\,\text{eV}$, belonging to the substrate (scans for the bare substrates highlighted), clearly decrease in intensity with increasing F4PEN coverage. For a final deposition of 48 Å (also highlighted in blue) the substrate features have almost disappeared and only F4PEN contributions are present, meaning that at least a wetting layer exists on the surface. We note that, comparing F4PEN deposited on copper and on silver, the molecular features differ, thus showing a substrate-dependence also at the thin-film regime.

plotted in Fig. [7.3], with the precise energy positions also included in Tab. [7.1]. A closer look to the VB region, near the Fermi edge (Fig. [7.2b]), shows clearly the evolution of the F4PEN frontier orbitals. For silver, the relaxed HOMO (labeled as H' in Fig. [7.2b]) appears around 1.6 eV for the first coverages and remains around this position for the higher ones. Of special interest is the feature labeled as F*, which appears at the high BE side of the HOMO peak at monolayer coverages and becomes more pronounced in the subsequent depositions. Such a feature is tentatively attributed to a portion of molecules undergoing an energy-level (the HOMO in this case) splitting induced by dimer formation [448] between molecules of adjacent layers[1]. For this effect to happen, already around the nominally-deposited monolayer coverage (4 Å), the molecules in direct contact with the substrate should not hybridize with the surface atoms, which seems the case for F4PEN

[1] Being more specific, the electronic coupling between adjacent molecules can be theoretically described through the intermolecular transfer integral (t), which can be naively seen as a measurement of the orbital overlapping. In some cases, where the systems hold the right properties and grow well ordered, the electronic coupling may cause the splitting of the frontier orbitals already at the bilayer regime through the formation of dimers. Such a splitting is called $2t$-splitting (details in Refs. [192, 448]).

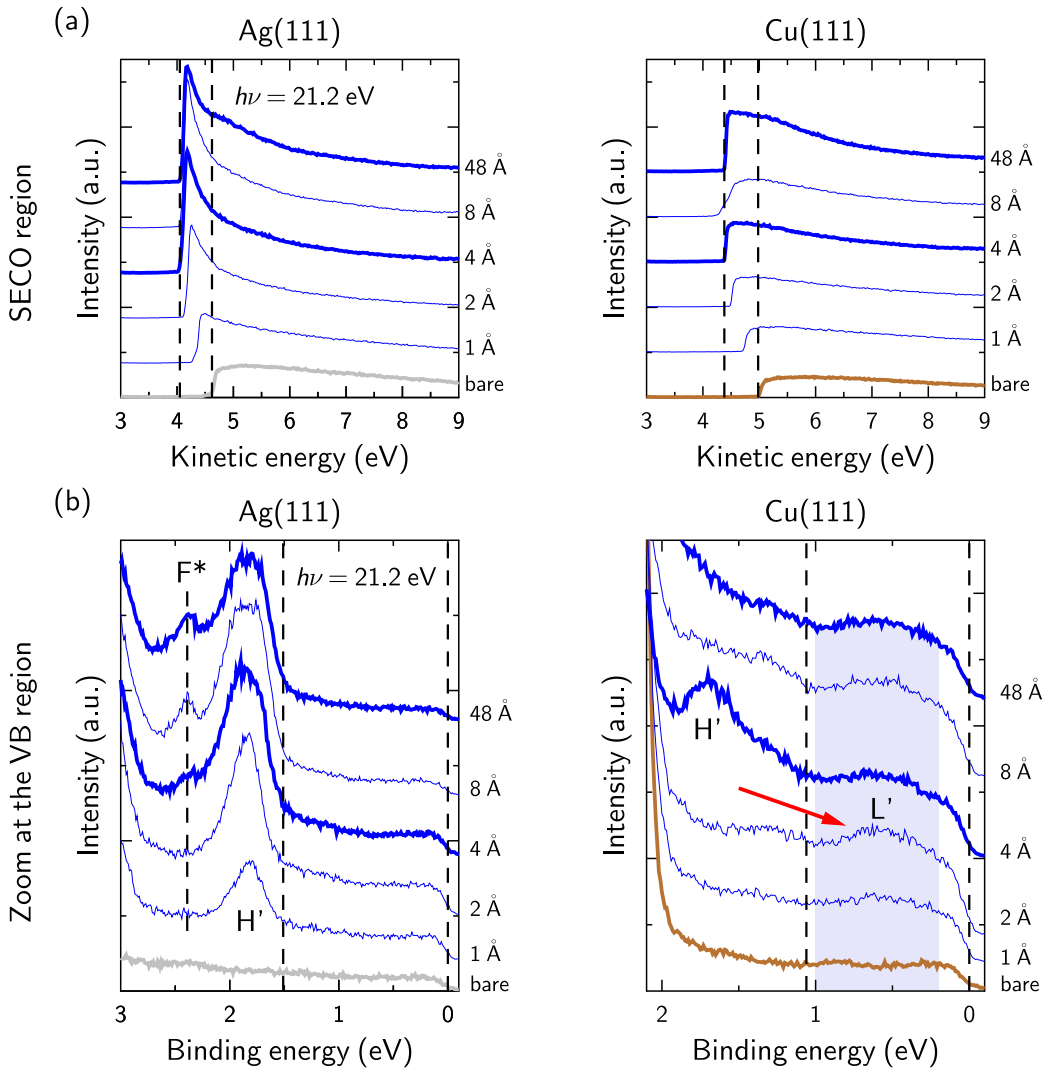

Figure 7.2.: SECO region (a) and valence-band region close to the Fermi edge (b) for F4PEN deposited on the Ag(111) and Cu(111) surfaces (monochromatic He I source, $h\nu = 21.2\,\text{eV}$). (a) SECO region (sample bias -3 V) that displays the vacuum-level shift with increasing coverage. Vertical lines highlight the bare substrate WF and the corresponding value for the highest coverage. (b) Zoomed VB region close to the Fermi edge that displays the changes undergone by the frontier orbitals in contact with the surface and their evolution with increasing coverages. The relaxed HOMO is labeled as H', whereas the filled LUMO for F4PEN on Cu(111) is highlighted and labeled as L'. For F4PEN on Ag(111) the energy-level splitting induced by possible dimerization (see text for more details) is labeled as F*.

on silver, as deduced from the non-existence of LUMO-filling features. The fact that the relative intensity of F* and the HOMO is more balanced towards the latter indicates that not all the molecules are involved in the dimerization. As a possible explanation, the formation of islands upon the wetting layer may be a reason why the dimerization does not involve all the molecules. Nonetheless, these conjectures definitely need additional measurements that support them.

Considering now the zoomed VB region close to the Fermi edge for F4PEN deposited on the Cu(111) surface, very interesting differences appear compared to the silver case. Most

		Coverage (Å)					
		Bare	**1**	**2**	**4**	**8**	**48**
Ag(111)	WF (eV)	4.62	4.31	4.12	4.05	4.05	4.05
	HOMO (eV)	–	1.56	1.60	1.51	1.48	1.51
Cu(111)	WF (eV)	4.98	4.70	4.47	4.37	4.37	4.38
	HOMOv(eV)	–	–	0.98	1.06	2.04	2.07
	F-LUMO (eV) (center)	–	–	0.48	0.48	0.48	0.48
	F-LUMO (eV) (range)	–	–	0–0.81	0–0.81	0–0.81	0–0.81

Table 7.1.: Summary of work functions (WF), HOMO and filled-LUMO BE for the different coverages of F4PEN deposited on Ag(111) and Cu(111) as extracted from Fig. [7.2].

notably, the feature labeled as L' shows up around 0.5 eV already for the lowest coverages and is attributed to the filling of the LUMO. It is remarkable to see that such a feature is seen in all the subsequent depositions, clearly pointing out towards the formation of islands on top of the wetting layer (Stranski-Krastanov growth). Unfortunately, the strong intensity of the substrate bands mask the HOMO, which is only observed for the nominal monolayer. The presence of a filled LUMO, similarly to PEN on the same substrate [77], is indicative of a strong electronic coupling with the substrate atoms.

We now move to the coverage-dependent XP spectra. Fig. [7.4] and [7.5] show the fluorine F 1*s* and the carbon C 1*s* core-level signals, respectively, for different coverages deposited on the studied metals. The line widths and BE positions of the fitting components are summarized in Tab. [7.2]. Additionally, at the bottom of both plots, the high-resolution XPS measurements of the (sub)monolayer coverages are included for comparison. Starting with the F 1*s* core-level (Fig. [7.4]), the increasing coverage on Ag(111) does not render appreciable spectral changes rather than a progressive BE shift towards higher energies, attributed to the less efficient core-hole screening provided by the intermolecular environment, compared to the metal surface. Next to the main spectral line, at the high BE side, one can distinguish a shake-up. Unfortunately, for copper, already for the bare substrate, a feature at the high BE side overlaps with the F 1*s* region and a clear

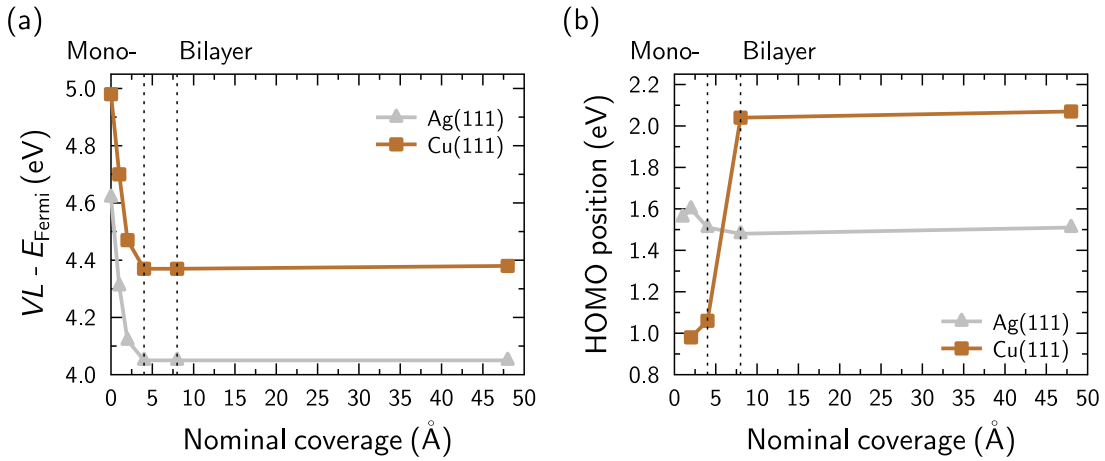

Figure 7.3.: (a) Vacuum-level shift with increasing coverage of F4PEN deposited on the two studied substrates. (b) HOMO position with increasing coverage. The nominal coverages corresponding to one and two full layers are marked with dashed lines.

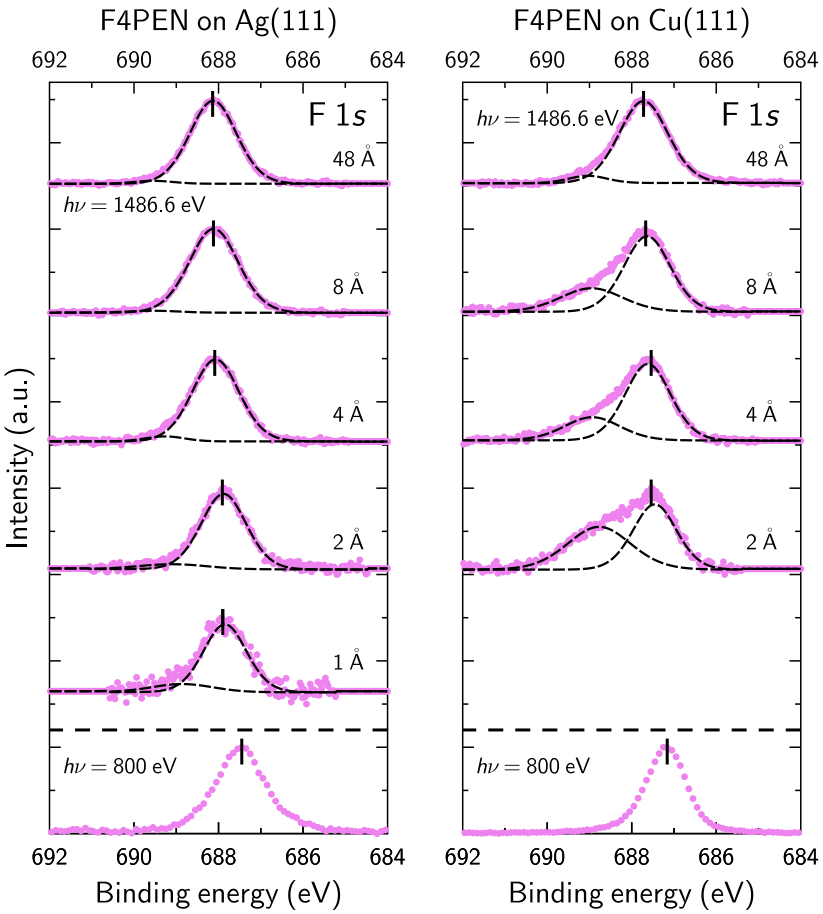

Figure 7.4.: XPS measurements of the F 1*s* core-level signal for different F4PEN coverages deposited on Ag(111) and Cu(111). The bottom spectra, added for comparison, correspond to the HR-XPS measurements recorded at the synchrotron ($h\nu$ = 800 eV) for a F4PEN (sub)monolayer. The top spectra were taken with a monochromatic X-ray lab source, $h\nu$ = 1486.6 eV (Al K_α line). The coverage-dependent spectra are fitted with Voigt profiles (Lorentzian contribution of 30%) for the main components and pure Gaussian profiles for the shake-ups. We note that the coverage-dependent spectra measured on Cu(111) have, already for the clean substrate (not shown), a feature around 689 eV that overlaps with the F 1*s* core-level signal. For the first deposition, distinguishing the molecule signal was very difficult, therefore the spectrum is not included. For increasing coverages, the substrate feature is still visible, appearing as a small shoulder at the higher BE side for the 48 Å nominal coverage. Despite this issue, the fluorine core-level signal appears rather symmetric and, besides a progressive shift towards higher BE with increasing coverage, no other spectral changes are noticeable.

comparison is not possible. However, since the HR-XPS already shows a rather symmetric peak for the interface case, no particular changes are expected at higher coverages rather than a shift towards higher BE, similarly to the silver case.

The C 1*s* core-level (Fig. [7.5]) appears more interesting. On silver, following the trend of fluorine, the spectra have the same line shape regardless of the coverage, and only a shift towards higher BE is observed. This is indicative of a physisorptive behavior. The spectra have two main features: the broad peak around 285 eV, attributed to the PEN core, and the smaller one at ∼287.5 eV belonging to the C–F carbon atoms at the short molecular edges. This assignment is done based on the stoichiometry of the molecule (C–C + C–H):(C–F) = 18:4 and also considering previous work carried out by Savu et al. on

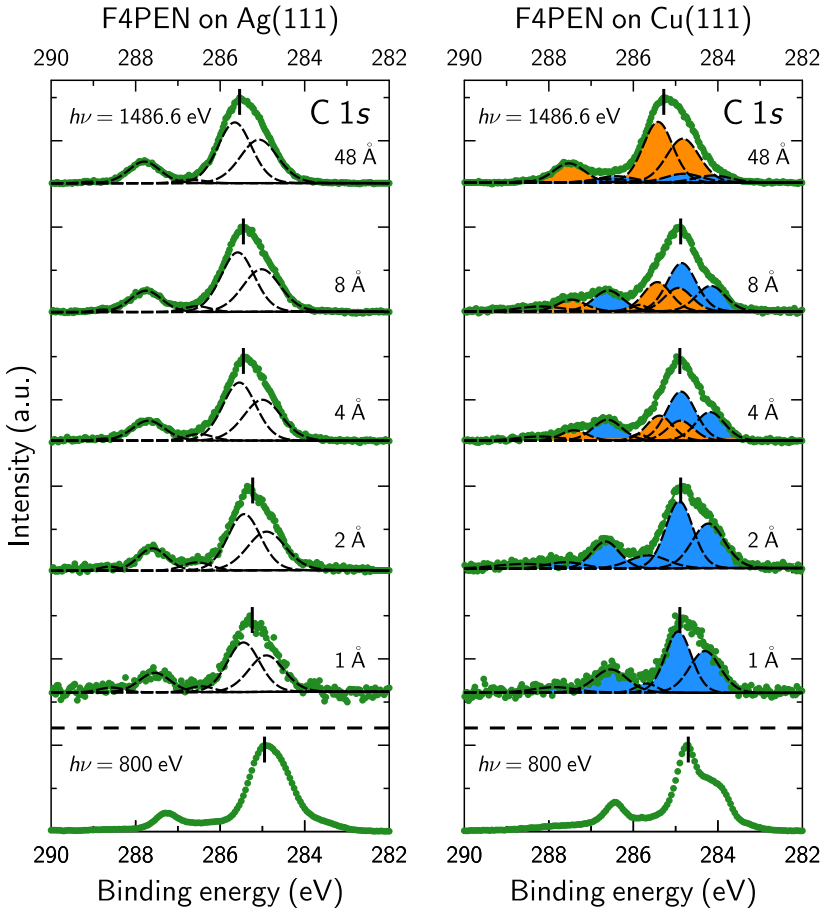

Figure 7.5.: XPS measurements of the C 1*s* core-level signal for different F4PEN coverages deposited on Ag(111) and Cu(111). The bottom spectra, added for comparison, correspond to the HR-XPS measurements recorded at the synchrotron ($h\nu$ = 800 eV) for a F4PEN (sub)monolayer. The coverage-dependent scans were recorded with a monochromatic X-ray lab source, $h\nu$ = 1486.6 eV (Al K_α line). The spectra are fitted with Voigt profiles (Lorentzian contribution of 30%) for the main components and pure Gaussian profiles for the shake-ups. Although the line profiles do not show striking differences, as it is the case of the monolayers measured with HR-XPS, a careful fit of the data shows that the first monolayer on Cu(111) (in blue) is visible even at the highest coverage, ∼10 ML (nominal coverage 48 Å). This appears in strong contrast to F4PEN on Ag(111), where, besides a progressive shift towards higher BE, the spectra can be perfectly reproduced with one set of components.

this molecule and similar ones [432, 433, 444]. For the (sub)monolayer regime, comparing the HR spectra to those measured in the lab, no significant differences appear besides a prominent tailing of the low BE side of the main peak observed for the former. Its origin will be addressed in the following section. On copper, however, the HR spectrum shows a particular line shape that cannot be resolved in the lab-recored ones. Such features will also be discussed below. Interestingly, the different lab scans show unexpected coverage-dependent changes. For the (sub)monolayer coverage, the low BE side of the backbone peak is more asymmetric than for silver, likely due to the poor resolution that does not allow one to properly distinguish the particular shoulder seen with the soft X-ray beam. The line shape starts to change already around the nominal monolayer coverage (4 Å). This is attributed to the coexistence of molecules in direct contact with the substrate and

Ag(111)											
Coverage (Å)		1	2	4	8	48	1	2	4	8	48
Core-level	**Component**	FWHM (eV)					Binding energy (eV)				
F 1*s*	Main	1.20	1.26	1.31	1.35	1.30	687.85	687.88	688.07	688.11	688.13
	Shake-up	1.70	1.90	1.08	1.91	1.11	688.86	689.08	689.27	689.53	689.54
C 1*s*	C–C	0.98	1.06	1.06	1.05	1.05	284.91	284.90	285.00	285.02	285.08
	C–H	0.90	0.91	0.93	0.93	0.93	285.45	285.43	285.54	285.58	285.66
	Shake-up 1	0.71	0.81	0.76	0.76	0.76	286.45	286.55	286.50	286.55	286.68
	C–F	0.86	0.80	0.91	0.88	0.88	287.55	287.60	287.70	287.75	287.80
	Shake-up 2	0.70	0.60	0.50	0.51	0.51	288.57	288.61	288.73	288.77	289.08
Cu(111)											
F 1*s*	Main	–	1.21	1.27	1.29	1.36	**687.32**	687.45	687.62	687.64	687.72
	Substrate signal	–	1.76	1.56	1.73	1.08	–	688.77	688.93	688.95	689.04
C 1*s*	C–C mono	0.86	0.91	0.81	0.81	1.01	284.31	284.23	284.19	284.17	284.12
	C–H mono	0.73	0.76	0.81	0.81	1.01	284.94	284.91	284.87	284.85	284.81
	Shake-up 1 mono	0.57	1.09	0.42	0.42	1.03	285.69	285.65	285.87	285.85	286.41
	C–F mono	0.92	0.77	0.81	0.81	1.01	286.54	286.66	286.61	286.59	286.55
	Shake-up 2 mono	1.14	1.04	1.23	1.23	0.47	287.86	287.61	288.21	288.19	288.52
	Shake-up 3 mono	–	1.63	–	–	–	–	288.56	–	–	–
	C–C multi	–	–	0.73	0.77	0.92	–	–	284.88	284.94	284.83
	C–H multi	–	–	0.73	0.77	0.83	–	–	285.38	285.43	285.42
	C–F multi	–	–	0.73	0.77	0.86	–	–	287.40	287.46	287.52

Table 7.2.: Summary of line widths and binding energies of the components used to fit the coverage-dependent XPS shown in Fig. [7.4] and [7.5]. For the copper case, where a spectroscopic feature at the F 1*s* region overlaps with the molecular signal, the BE of the parasitic component is also reported. Furthermore, for the 1 Å coverage, not shown in Fig. [7.5] due to a bad energy range, the BE, in bold, is reported for the molecule feature obtained upon subtracting the intensity of the substrate feature.

molecules at the second layer. Indeed, the core-level spectra can be fitted with two equal sets of components (blue for the contact layer and orange for the subsequent overlayers) that are rigidly shifted from each other. As the coverage is increased, the relative intensity of both sets changes, since more and more molecules occupy multilayer positions. This finding is totally in line with the UPS results, which support the formation of a wetting layer on copper and the subsequent island growth that already starts before the first layer is totally closed. Furthermore, the fact that the molecules in contact with the copper substrate have a distinctive chemical environment compared to the multilayer is indicative of the electronic and chemical coupling with the substrate that, however, only involves the carbon atoms since there is no evidence for the same features for fluorine. Also, the clearly differentiated behavior of F4PEN on Ag(111) compared to Cu(111) supports the rather physisorptive behavior on silver and rather chemisorptive on copper, similarly to PEN. The parameters of the fitting components can be found in Tab. [7.2]. As a concluding remark for this paragraph, the fitting model employed considers the stoichiometry of the molecule to assign the different components. Thus, C–C, C–H and C–F components are used for both substrates plus additional shake-ups that complete the fitting. As it will be discussed in more detail next, the poor resolution of the lab source makes the assignment of further components too speculative.

7.2.2. High-resolution XPS of (sub)monolayer coverages

As already anticipated in the previous section, the high resolution measurements of the chemical state of the F4PEN molecules at the interface provides additional details that are not resolved in the coverage-dependent study measured with a lab source. Starting again

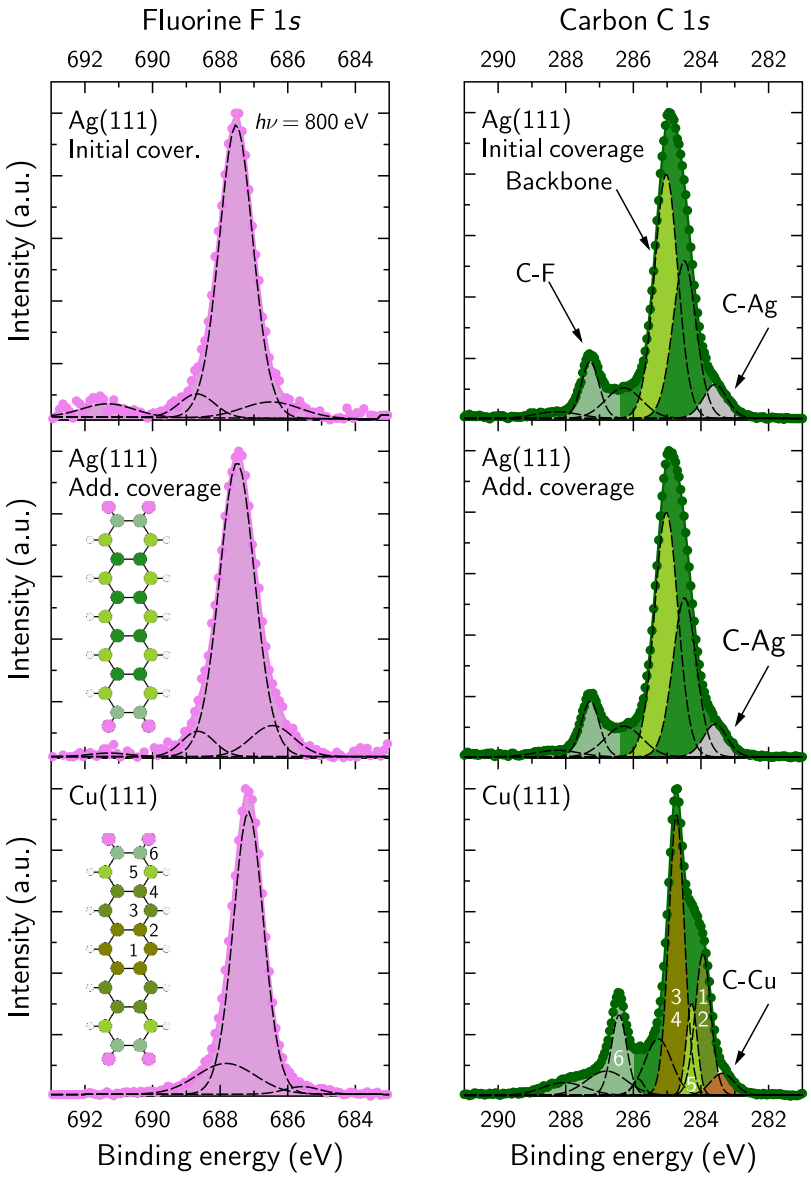

Figure 7.6.: HR-XPS scan measured at the synchrotron ($h\nu = 800\,\text{eV}$). The different components used to fit the spectra follow the color code of the inset molecules. We note that the numbering of the different carbon species is done following other spectroscopy studies [153, 449, 450] and has no connection to the IUPAC nomenclature used to define the chemical name of F4PEN. A Shirley background was applied for both the fluorine and carbon core-level signals. Voigt functions (Lorentzian contribution of 30%) were used for the different components and a Gaussian function for the shake-ups. The main components were set to have the same FWHM within an interval of $\pm 0.2\,\text{eV}$.

with the Ag(111) surface, two different coverages were studied within the (sub)monolayer regime, this being inspired by the behavior of PEN molecules adsorbed on Ag(111), which show a coverage-dependent adsorption distance stemming from the balance between intermolecular and molecule-substrate interactions [343]. Thus, the top and middle rows of Fig. [7.6] depict the two studied coverages of F4PEN deposited on the silver surface, the initial being, nominally, 0.5 ML and the final 0.75 ML. By comparing the position and the

shape of the features one can conclude that there is no evident coverage influence on the chemical environment of the molecules within the first monolayer, appearing, therefore, in contrast to PEN. The F 1s peak is remarkably symmetric and the shape can be reproduced with a single component, although two additional ones have to be added to fully reproduce the edges of the signal. The intensities of these additional components as well as the intensity of the shake-up peak at around 691 eV slightly change when the coverage is increased. This difference can be attributed to subtle changes in the molecular environment or being reminiscent of a small portion of fluorine atoms having the C–F bond slightly perturbed, either for the beam or the substrate. The latter is further supported by considering the corresponding C 1s spectra, which show a small shoulder at the low BE side that is attributed to a small portion of carbon atoms that are directly bound to silver, most likely close to step edges. Such a behavior has been observed for PFP [417,420] but also for a boronated tetracene derivative [451]. In both cases, the partial loss of the heteroatoms (fluorine or boron), either by the influence of the substrate or by an annealing treatment, comes along with an intensity increase of the low BE shoulder of the carbon signal. In our case, as shown in Appendix [B], this effect can be fostered by overexposing the sample to the soft X-ray beam ($h\nu = 800$ eV), thus providing further evidence of the connection between the loss of fluorines and the intensity increase of the C–substrate feature. Actually, as it will be discussed later, the XSW analysis of this shoulder renders a much lower adsorption distance than the carbon backbone, further proving the bonding with the substrate.

Overall, the fluorine and carbon core-level spectra for F4PEN adsorbed on silver resemble much the spectra corresponding to the multilayer case. This is indicative of a rather weak chemical interaction between the molecules and the substrate, as we have extensively discussed for PTCDI. Actually, this becomes even clearer when comparing them to those copper. Indeed, the backbone feature of the carbon core-level spectrum radically changes compared to the same on silver and the multilayer regime. In particular, the main peak becomes narrower and a pronounced shoulder appears towards the low BE side. Furthermore, the BE difference between the C–F and the backbone components is reduced and the shake-up structure increases in intensity. All these signs can be related to the strong chemical and electronic coupling of the molecule with copper. Similar features are also observed in the case of PEN adsorbed on different copper surfaces [57,450,452]. Noteworthy, a small shoulder also appears at the low BE edge, which is also associated to a small amount of carbon atoms bound directly to the copper surface. Nonetheless, the intensity of this feature is weaker than that on silver. As already mentioned before, the profound changes induced by the surface are not observed in the fluorine signal. It displays a single, narrow and rather symmetric peak, which, however, requires two additional components to obtain an optimum fit. The smaller FWHM compared to the silver case may be explained by a minor effect of the beam and/or by a reduced intermolecular influence, similarly to the discussion on PTCDI, and/or by a higher adsorption distance (as we shall see later).

Fitting the different core-level spectra provides a more detailed analysis of the chemical changes happening at the F4PEN-metal interface. Thus, following the color code of the insets, components for different inequivalent carbon species are included. Initially, only three inequivalent carbon species were included, namely, C–C, C–H and C–F, being the most intense component attributed to the carbon atoms bound to hydrogen [444]. Such

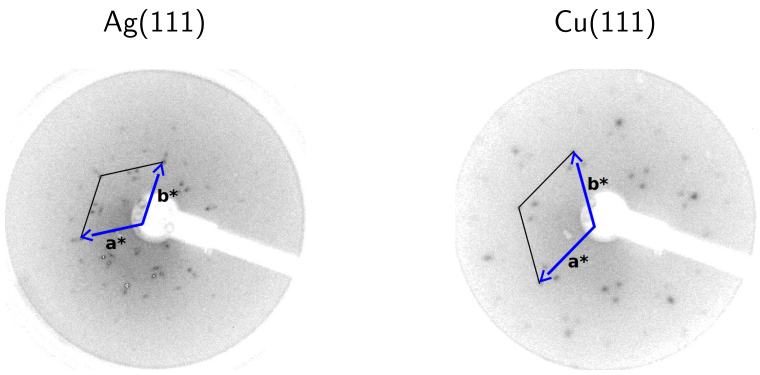

Figure 7.7.: LEED patterns for F4PEN coverages of 1 ML (4 Å), the unit cell is superimposed. Electron energies: $E = 29$ eV for Ag(111) and $E = 30$ eV for Cu(111). The values of the unit cell vectors are found in Tab. [7.3].

a fitting model works very well on silver, of course also adding additional shake-ups and a component for the C–Ag. Also, the carbon spectra have the area separated by colors following the stoichiometry of 18:4 between the backbone and the C-F carbon atoms.

Owing to the particular shape of the carbon signal for the copper case, which stems from the inequivalent chemical environments induced by the substrate, we are able to provide a more detailed fitting of the spectrum. We assign the different inequivalent carbons following the numbering of the bottom-most inset, which is partially based on previous work for PEN on different substrates [153, 450]. As the reader will see when checking the aforementioned references, the labeling is not exactly the same and it also conflicts with that used for silver. The reason for our specific choice is based on the XSW analysis in Sec. [7.2.4], whereby we can associate an adsorption distance to each component, thus linking the molecular structure to each component. As for the discrepancy with silver, it is known that the specific effect of the substrate induces different energy shifts [153, 155], thus making a one-to-one comparison unreliable. In any case, we acknowledge that the fitting model may be a topic of debate and theoretical input is desirable.

7.2.3. LEED measurements

The in-plane ordering of the F4PEN (sub)monolayers can be inferred from the LEED pictures presented in Fig. [7.7], where the unit cells are also highlighted and the corresponding values are included in Tab. [7.3]. The relatively low resolution of the LEED images does not allow a detailed and quantitative analysis of the in-plane arrangement. Therefore, the diffraction patterns for F4PEN are to be compared with those of PEN [77] and PFP [417, 423] and thus indirectly get the ordering through the multiple STM studies that have been performed for the parent molecules of F4PEN. Starting with the silver case, F4PEN shows a completely different diffraction pattern compared to PEN, which at RT shows no LEED pattern [77], and PFP, which shows a temperature-dependent behavior and only at cryogenic temperatures a 6-fold symmetry LEED pattern arises [421]. For the copper case, the LEED pattern is the same as the one for PEN on the same surface [77], which adds to the other similarities of PEN and F4PEN already seen in UPS.

The non-existence of LEED spots at RT for PEN and PFP on Ag(111) is attributed to is high mobility that renders a liquid-like behavior. Indeed, PFP molecules order

Substrate	Parameters		
	a (Å)	b (Å)	**a∠b** (°)
Ag(111)	9	9	120
Cu(111)	10	10	122

Table 7.3.: Unit cell parameters extracted from the LEED measurements shown in Fig. [7.7].

on the surface only at RT, as seen in different STM studies [419, 423]. Therefore, the partial fluorination of PEN seems to modify the molecular arrangement as distinctive LEED patterns can be imaged at RT already. The interaction will most likely involve the formation of C–F···H hydrogen bonds.

7.2.4. XSW results: adsorption heights and molecular distortions

We conclude this section with the XSW measurements performed on the very same systems that were studied with HR-XPS (Sec. [7.2.2]). The results are summarized in Fig. [7.8] and the fitting parameters, together with the adsorption distances for all the resolved species are included in Tab. [7.4]. In order to analyze the data, a fitting model very similar to that shown in Fig. [7.6] was employed to account for the photoelectron yield.

Starting with silver, adsorption distances could be obtained only from the total fluorine

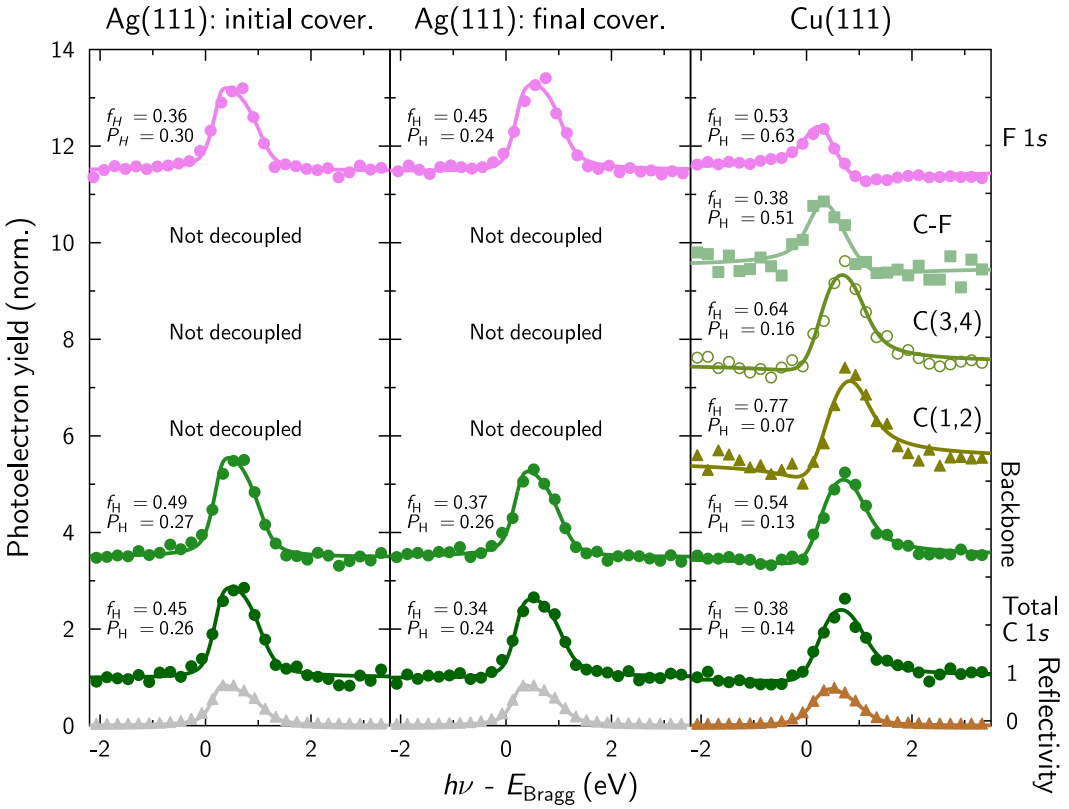

Figure 7.8.: XSW measurements along **H** = [111] corresponding to F4PEN (sub)monolayers adsorbed on Ag(111) and Cu(111). For silver, two different coverages were deposited. We note the shape differences/similarities of the photoelectron yield between the carbon backbone and the fluorine.

and carbon signal as well as from the carbon backbone. Unfortunately, the separate components within the C 1*s* could not be decoupled, although different fitting model were tried. Nonetheless, the very similar adsorption distance of the carbon backbone and the fluorine atoms indicates that F4PEN adsorbs virtually undistorted on the silver surface. This is further supported by the very similar coherent fractions of the backbone and the total carbon signal. This indicates that the inclusion of the C–F component in the evaluation of the photoelectron yield does not render a higher disorder thus suggesting a very similar adsorption distance of these compared to the backbone carbons. Increasing the coverage leaves the coherent positions unchanged, within the error bars, implying that the coverage does not have an influence on the adsorption distance in clear contrast to PEN [343]. Yet, the coherent fractions do change: those of carbon decrease and those of fluorine increase. Such a dissimilar behavior beyond the error bars is tentatively attributed to the increased intermolecular environment that, through the formation of C–F···H bonds, may perturb the peripheral C–H atoms without affecting the average adsorption distance. Since the hydrogen bonds are highly directional, its formation may foster a higher degree of ordering within the fluorine atoms. In any case, the overall flat-laying adsorption remains unperturbed.

On copper, the results turn out to be far more interesting. Adapting the core-level model used to fit the HR-XPS (Fig. [7.6]), we are able to obtain the adsorption distances for three different inequivalent carbon sites. This is a quite remarkable achievement per se, since we can infer internal distortions of a purely hydrocarbon environment, which has been one of the historical limitations of XSW, namely, only average adsorption were provided without resolving inequivalent species within a core-level signal. In this case, the strong coupling of the backbone with the substrate renders specific adsorption sites that induce marked core-level shifts that allow one to clearly distinguish some of the components. Therefore, with the particular fitting model they can be decoupled and analyzed in the XSW measurements. The role of the substrate interaction that induces specific adsorption sites may be the reason why the decoupling for F4PEN on Ag(111) (or PTCDI on Au(111), see Sec. [6.2.4] from the previous chapter) is not as successful. The obtained

Substrate	**Component**	f_{111}	P_{111}	d_{111} **(Å)**
Ag(111) initial coverage	F 1*s* total	0.36	0.30	3.05 ± 0.04
	Backbone	0.49	0.27	3.00 ± 0.03
	Total C 1*s*	0.45	0.26	2.97 ± 0.05
Ag(111) final coverage	Total F 1*s*	0.45	0.24	2.93 ± 0.05
	Backbone	0.37	0.26	2.97 ± 0.04
	Total C 1*s*	0.34	0.24	2.91 ± 0.05
Cu(111)	Total F 1*s*	0.53	0.63	3.40 ± 0.02
	C–F(6)	0.38	0.51	3.15 ± 0.05
	C(5) (*)	0.41	0.20	2.50 ± 0.36
	C(3,4)	0.64	0.16	2.42 ± 0.02
	C(1,2)	0.77	0.07	2.24 ± 0.08
	Backbone	0.54	0.13	2.36 ± 0.02
	Total C 1*s*	0.38	0.14	3.37 ± 0.04

Table 7.4.: XSW parameters extracted from the data fitting shown in Fig. [7.8]. The Total C 1*s* was calculated using the photoelectron yield from the whole carbon core-level signal, whereas the backbone only accounts for the components/features linked to the PEN core inequivalent carbons, thus excluding the C–F ones. All the components that gave a coherent result are included. (*) Although C(5) was not directly inferred from the measurements but from the vector analysis shown in Fig. [7.9], we include it here for completeness.

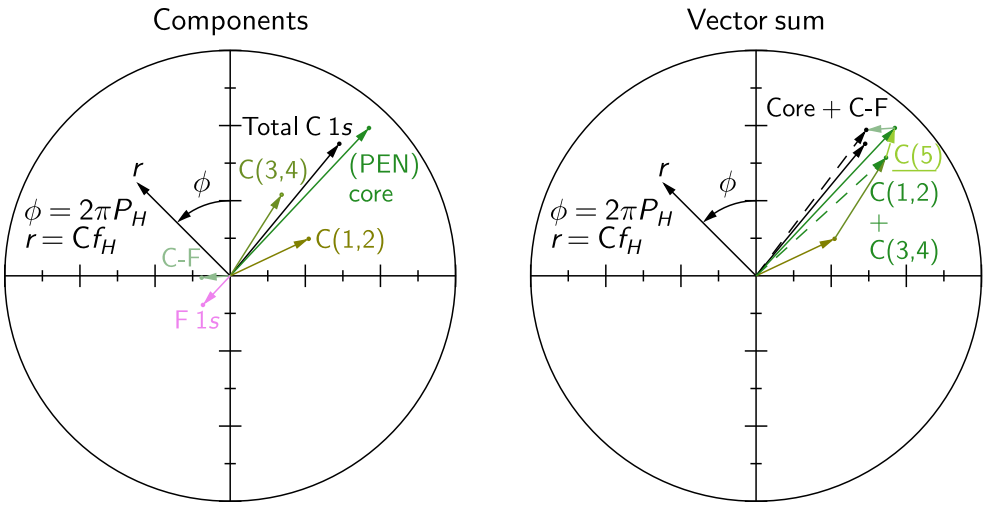

Figure 7.9.: Argand diagram of the XSW measurements corresponding to F4PEN adsorbed on Cu(111). A polar representation is used to plot the XSW fitting parameters: the angle is related to the coherent position P_{H} via $\phi = 2\pi P_{\mathrm{H}}$, whereas the radius is directly related to the coherent position via $r = Cf_{\mathrm{H}}$, where C is the number of atoms that contribute to each specific component. The left panel depicts the vectors for all the measured components, together with the PEN core (backbone) average adsorption distance and the total carbon average adsorption distance. The right panel shows the vector sum of the different components that contribute to the different average adsorption distances. For instance, the total carbon average adsorption distance is made of the C–F vector plus the PEN core one, whereas the PEN core vector stems from the contribution of the C(1,2), C(3,4) and C(5) (not resolved in XSW) carbon vectors. The number of atoms (C) for C(1,2) is 6, for C(3,4) is 8 and C(5) and C(6) have 4 atoms each.

adsorption distances show that the bottom-most carbons (component C(1,2)) are adsorbing at 2.24±0.08 Å, whereas the C–F ones (component C(6)) are situated ∼0.9 Å above, yielding a remarkable bottom-to-top vertical distance for carbon. This rises the question of how the molecule accounts for this carbon spread. Does it form a swift transition in a U-shape or it is rather a sharp bending in a more V-shape? To answer this question, we consider the other measured adsorption distances. The second lowest component, C(3,4), yields an adsorption distance of 2.42±0.02 Å, very close to the total carbon average adsorption distance 3.37±0.04 Å as well as to the average backbone distance (all carbon species except the fluorinated ones) 3.36±0.02 Å. The fact that the average adsorption distance are closer to the lowest part of the molecule is already indicative of a rather unequal distribution of adsorption distances. In order obtain a more detailed information of the different weights to the average adsorption distances it is useful to plot the XSW parameters in a polar form.

Figure [7.9] shows the Argand diagram (polar representation) of the coherent fractions and positions for the different evaluated signals. Since the average adsorption distances stem from the individual contributions of the different components, one can use the vector sum of these as a comparison with the corresponding measured vector. Thus, in the left panel of Fig. [7.9] all the measured components are depicted, whereas in the right one the vector sums are displayed, with the obtained vectors plotted in dashed lines. At this point, it is worth stressing that the contribution of an individual component to the average adsorption distance, as shown in the picture, is weighted by the number of carbon atoms contributing to the given component (C) as well as the precise value of P_{H} and f_{H}. First,

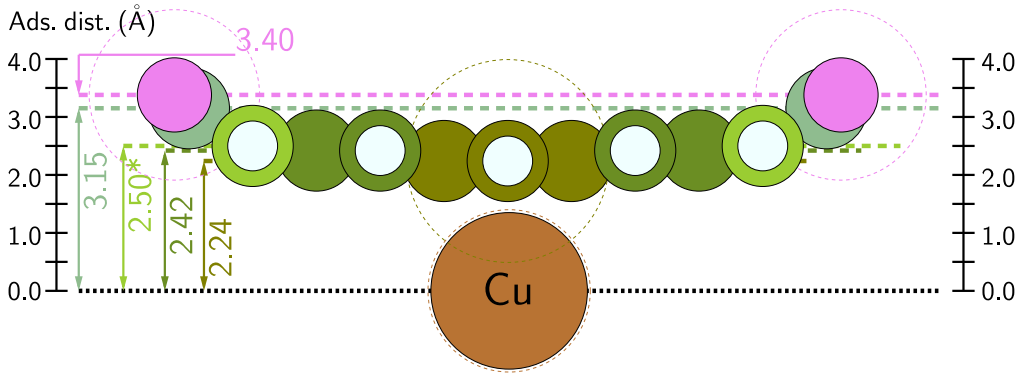

Figure 7.10.: Sketch of the vertical adsorption geometry of F4PEN on Cu(111) (in Å) as inferred from the XSW measurements (Figure [7.8]). The dashed circles represent the van-der-Waals radii. (*) The adsorption distance of component C(5) is not directly measured but inferred from the vector analysis of the XSW results (see Fig. [7.9]).

we consider the total carbon average adsorption distance (Total C $1s$) as the sum of the backbone and C–F contributions: we obtain a vector very close to the measured one, thus proving that the overall contribution of the fluorinated carbons to the average adsorption distance is very small. Secondly, turning to the carbon backbone, which is composed of the measured C(1,2) and C(3,4) components and C(5) (not resolved) we see that the sum of C(1,2) and C(3,4) renders a vector close to the measured backbone average adsorption distance. Nonetheless, the difference can well be attributed to C(5), which renders an adsorption distance of 2.50±0.36 Å when doing the back transformation, agreeing quite well with the relatively low backbone average adsorption distance.

The different obtained (measured and inferred) adsorption distances shown in the sketch of Fig. [7.10] hint at two different adsorption behaviors. Actually, by considering the shape of the photoelectron yield modulation in Fig. [7.8] one can already suspect that. The first one involves the backbone carbon atoms, namely, components C(1,2), C(3,4) and C(5), whereas the second one involves the fluorinated carbon atoms at the short molecular edge and of course the fluorine atoms. The virtually identical average adsorption distance of the molecule compared to PEN [57] appears in line with the other experiments that show a PEN-like behavior for F4PEN in direct contact with the Cu(111) surface. In addition, the precise measurements for the inequivalent carbon sites within the backbone support the DFT calculations performed by Shi et al. that show a gentle curvature of PEN, in stark contrast to PFP that displays a sharp bending [430]. Hence, we can safely conclude that the F4PEN backbone retains the PEN adsorption geometry. Nonetheless, the fluorinated edges are in discordance with the backbone trend since they abruptly move further up by ∼0.6 Å with respect to C(5). This is due to the repulsive effect exerted by the fluorine against the copper atoms. Actually, the distance of 3.15 Å of the short-edge, fluorinated carbon atoms is very similar to that calculated for PFP [430].

Before concluding this section, we comment on the coherent fractions of the copper case. The highest value is reported for the lowest carbon atoms, which act as anchoring sites and thus, may be less influenced by thermal vibrations or local disorder. This is supported by the fact that the values decrease when moving from the center to the edges. In any case, the coherent fractions correspond to a flat-laying molecule with a significant degree of ordering.

7.3. Discussion

The results presented in this chapter can be discussed from two main perspectives. On the one hand, one can focus on the particular effect of the substrate on the adsorption properties of F4PEN, similarly to the study of PTCDI. On the other hand, the degree of fluorination, as opposed to the non-fluorinatated and the totally fluorinated PEN, can be taken as the relevant parameter. In the following, we present our findings from this two perspectives. In some of the cases, however, the nature of the behavior observed stems from the interplay of different factors, namely, the substrate-molecule interaction, dominated by the substrate and the molecule-molecule interaction, which is mostly influenced by the partial fluorination of the PEN molecule, hence drastically changing the intramolecular dipole and fostering the formation of C–H···F hydrogen bond formation.

7.3.1. Effect of the substrate

The set of complementary measurements presented in this chapter for F4PEN adsorbed on Ag(111) and Cu(111) suggest a rather physisorptive behavior for silver and a rather strong chemisorptive behavior on copper that induces hybridization between the molecular orbitals and the subtrate atoms. Indeed, the relatively high adsorption distances of the molecule on silver, the absence of intramolecular distortions, similarly to PTCDI physisorbed on Au(111), together with the absence of LUMO filling and changes between the (sub)monolayer and the multilayer core-level spectra are all indications of a physisorptive behavior with vdW forces dominating the interaction. The fact that in the VB spectra dimerization-induced energy-level splitting is observed is also a clear indication of the absence of hybridization with the substrate. Exactly the opposite is observed for copper, adsorption-induced intramolecular distortions accompanied with a very short average adsorption distance, LUMO filling and strong influence of the substrate on the carbon core-level spectrum. Furthermore, the coverage-dependent XPS shows the contrast between first and subsequent layers.

7.3.2. Comparison with PEN and PFP

The most interesting here is, however, to compare F4PEN with its parent molecules, PEN and PFP, to find out how different degrees of fluorination affect the interface as well as the growth properties. The most evident case is F4PEN deposited on copper. The LEED pattern is identical to that of PEN [77], so are the VB features for the first layer in contact with the substrate [77], both pointing clearly to a PEN-like behavior of the F4PEN-Cu(111) interface. Most interesting is the XSW results that show a PEN-like backbone with a gentle curvature, but with a dramatic increase of the adsorption distance of the fluorinated carbons owing to the major repulsion between the copper atoms and the F $2p$ fluorine orbitals [443]. Consequently, the selective fluorination of PEN is not enough to modify the interface properties with copper since the effect is only conformational and localized at the fluorinated edges. Noteworthy, this situation changes at higher coverages. Released from the dominating substrate coupling, intermolecular interactions become the dominating parameter and, in this case, the partial fluorination does play a decisive role. Certainly, the highly electronegative character of the fluorine atoms increases the asym-

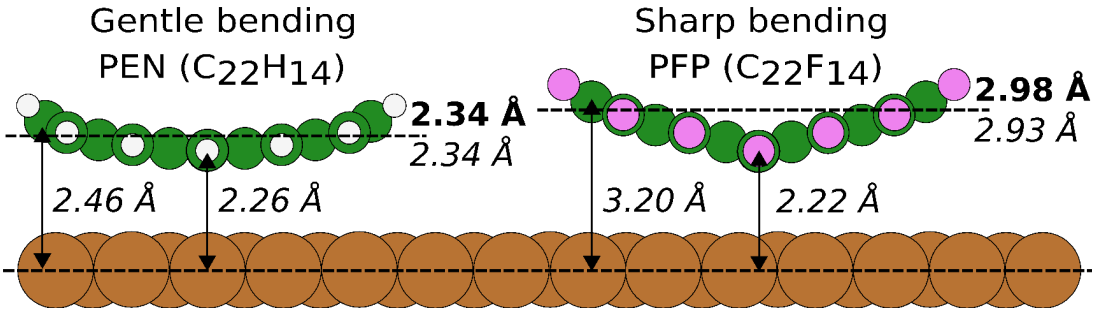

Figure 7.11.: Sketch of the vertical adsorption geometry of PEN and PFP adsorbed on Cu(111) as extracted from DFT calculations (see Ref. [430]). The adsorption distances in bold are XSW measurements [57], whereas those in italic correspond to the calculated values [430]. The complete fluorination of PEN renders a significantly different adsorption geometry, governed by the major repulsion between the substrate and the fluorine atoms.

metry of the intramolecular dipole and fosters intermolecular interactions through the formation of C–H···F hydrogen bonds, both changing the growth mode and the multilayer electronic properties compared to PEN and PFP.

Turning back to the vertical adsorption geometry, Fig. [7.11] summarizes the PEN and PFP cases on Cu(111) as extracted from XSW [57] and state-of-the-art DFT calculations [430]. If we now compare it to the adsorption geometry obtained for F4PEN (Fig. [7.10]) it is easy to identify the PEN-like behavior of the carbon backbone and the PFP-like character of the fluorinated carbons at the short edge. Actually, the calculated values for both cases are very similar to those presented here for F4PEN. In particular, the adsorption distance of the C–F carbons is very close to the 3.20 Å calculated for the short-edge carbons of PFP. Also, the magnitude of the bending for PEN (0.2 Å) falls within the range of the F4PEN backbone bending. We note that, from XSW measurements, the fluorine atoms of PFP are ∼0.1 Å above the average carbon distance [57].

On silver, both PEN[2] and PFP have a rather physisorptive behavior, as we have also seen for F4PEN. The weaker electronic coupling with the substrate cedes the prominent role to the intermolecular interactions. The LEED measurements are the first indication of the particular molecule-molecule arrangement of F4PEN compared to the other two. Certainly, the genuine diffraction pattern for F4PEN indicates a new arrangement different from those of PEN and PFP. PEN at RT has a liquid-like behavior [77] with no ordering and only at LT molecules can be visualized in STM [419]. On the contrary, PFP can be imaged already at RT [100] but it changes the arrangement if the temperature is decreased due to a change in the optimal balance between molecule-substrate and molecule-molecule interactions [100]. Here, however, it is likely that the intermolecular arrangement will be driven by the hydrogen formation between the C–F of one molecules and the C–H from the adjecent ones. Indeed, it seems a very likely hypothesis considering what has been reported for similar systems with fluorinated and nonfluorinated molecules coexisting [347,453,454]. However, without STM studies for our system, one cannot totally assure it. The increased

[2] As discussed by Duhm et al. [343], PEN on Ag(111) could be considered as *soft chemisorption*, since the adsorption distance falls between those of purely physisorbed and those with stronger chemisorption (see for instance Ref. [71]). Furthermore, the liquid-like behavior may arise from a similar strenght of the substrate-molecule and molecule-molecule interactions that confers the system a thermal-dependent equilibrium for the mobility [343].

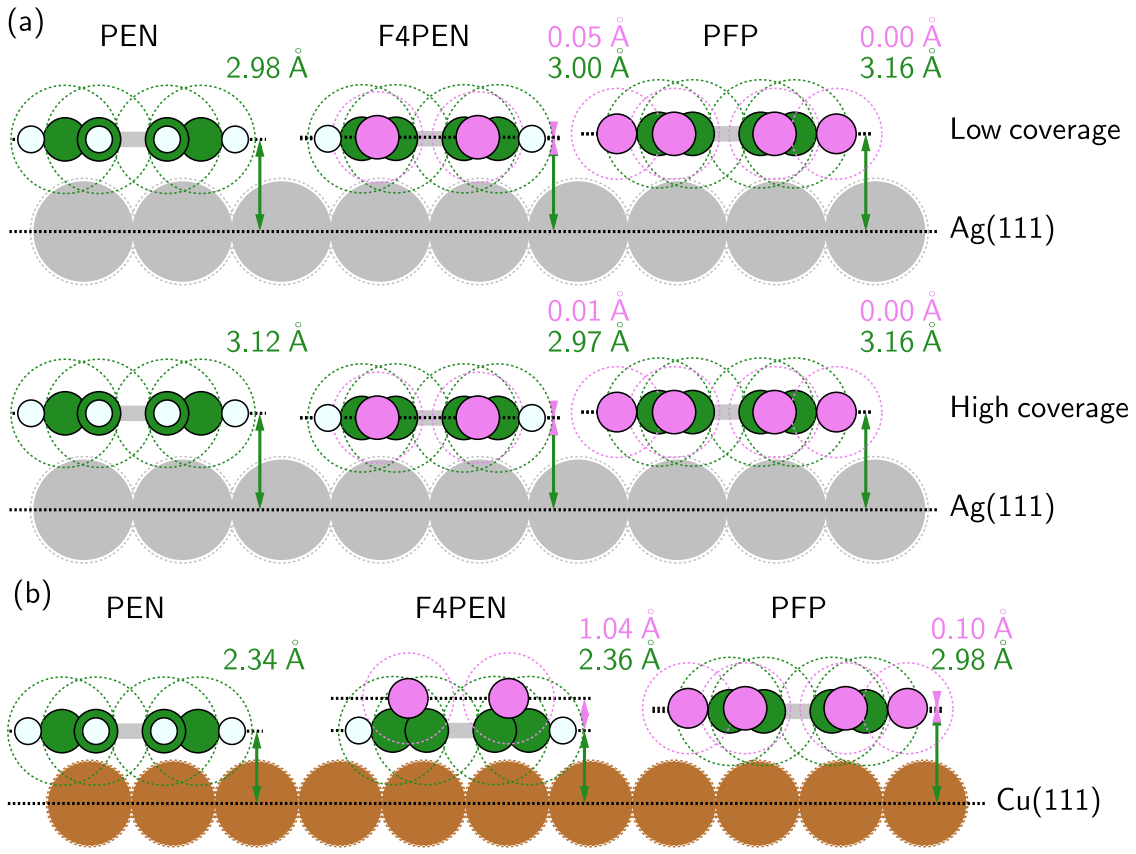

Figure 7.12.: Adsorption geometry (short edge depicted) of PEN, F4PEN and PFP adsorbed on Ag(111) (a) and on Cu(111) (b). (a) Measurements for two different coverages of PEN (from Ref. [343]) and F4PEN are shown (adsorption distances are only available for one coverage of PFP [418]). (b) The adsorption distance of PEN and PFP adsorbed on Cu(111) are obtained from Ref. [57].

intermolecular interaction seems to not also happen within the same layer but also between adjacent layers, if we consider the dimerization-induced splitting of the F4PEN HOMO, which has been also measured for PFP deposited on Ag(111) [455].

Finally, we shortly discuss the vertical adsorption geometry of the three PEN-related molecules. F4PEN shows no appreciable coverage-dependent changes in the adsorption distance and it displays virtually no distortion between the position of the fluorines and the carbon backbone, making its behavior close to that of PFP. However, the average adsorption distance is almost identical to that of a low-coverage PEN submonolayer, pointing out to an interplay between the carbon backbone as the channel for the substrate interaction, but being the fluorinated edges key to stabilize the molecule-molecule coupling and suppress the coverage-driven changes of the adsorption distance. Figure [7.12] summarizes the available adsorption distance for the three molecules on silver, as well as on copper.

7.4. Conclusions

In this chapter, we have presented a multitechnique study of the partially fluorinated PEN derivative, F4PEN, adsorbed on Ag(111) and Cu(111). The results have been compared to

the available literature for PEN and PFP adsorbed on the same surfaces. This has allowed one to acquire a deeper insight into how partial fluorination affects the different interface properties. Similarly to what has been shown in the previous chapter, the interface characteristics stem from the balance between the molecule-substrate and molecule-molecule interactions, having the heteroatoms a crucial role in this balance since they are the main channel whereby these interactions occur. Contrary to the PTCDI case, however, where the functional groups are prone to couple with the substrate atoms, the fluorine substitution in PEN decreases the molecule-to-substrate coupling through the repulsion of the F $2p$-orbitals [443], being this effect stronger for copper. On this substrate, the different experiments clearly show that the attractive interaction with the substrate dominates: the VB evidences the electronic coupling through the LUMO filling, the strong changes in the core-level spectra highlight the hybridization between the molecule orbitals and the substrate and the XSW measurements yield a short average carbon adsorption distance and a strong molecular distortion. Nonetheless, the same XSW measurements show that a repulsive behavior also exists but is confined to the fluorinated molecular edges that adsorb further away from the surface. Noteworthy, the high-quality XSW data together with the core-level fitting model enables an unprecedented degree of detail in the description of the adsorption distances within the molecule, thus highlighting the gentle curvature of the PEN-like carbon backbone and the sharp bending of the PFP-like fluorinated edges. On silver, where the substrate influence is much weaker, our results show a dominating intermolecular interaction, driven by the fluorinated edges and the C–H···F hydrogen bond formation, as inferred from the particular LEED pattern that correspond neither to the PEN case nor the PFP one. The electronic and chemical properties at the interface show no sign of electronic coupling with the substrate. Instead, dimerization-induced energy-level splitting of the HOMO is measured, further indicating the strong molecule-molecule electronic coupling, not just within the plane, but also between adjacent molecular planes. At higher coverages, intermolecular interactions also dominate on copper, where we see a different growth mode (Stranski-Krastanov) and electronic properties compared to PEN, further supporting the impact of the selective molecular fluorination. On the contrary, for silver no appreciable difference between the interface and the subsequent layers is observed, besides the energy-level splitting, further supporting the intermolecular-dominated interface. All in all, the selective fluorination of the short-molecular edges of PEN introduces significant changes in the intermolecular interactions. However, when the substrate interaction is dominating the interface properties, F4PEN behaves in all practical purposes like PEN.

8. Characterization of the ZnO polar surfaces

The experiments presented in this chapter were started as part of a project at Prof. Norbert Koch's group at Humboldt Universität zu Berlin. Owing to the success of the first XSW measurements on ZnO, further studies were planned to investigate the capabilities of ZnO as a suitable substrate for XSW experiments of organic overlayers. The measurements have been carried out with the collaboration of Dr. Jens Niederhausen, who has also been intensively involved in the discussion of the results. They are part of a larger, ongoing project that pursues an atomistic characterization of the ZnO polar surfaces, including also state-of-the-art DFT calculations (performed by Dr. Oliver T. Hofmann and Simon Erker, at Graz University of Technology).

As it has been pointed out in Sec. [4.2.2], the polar surfaces of ZnO are theoretically unstable due to the accumulating dipole stemming from the Zn–O layers along the c crystal direction. All the mechanisms proposed to explain their observed stability involve some sort of surface modification. It is therefore necessary to first study the surface previous to any experiments involving molecular overlayers. To this end, we devoted a significant effort to characterize the bare surfaces with a combination of photelectron spectroscoy techniques, LEED and, most remarkably, XSW. The results presented here aim at describing the polar surfaces of ZnO so that the effects and changes occurring at the interface with different π-conjugated molecules can be unambiguously explained and rationalized. Hence, this chapter can be considered a preface for Chap. [9]. However, the results obtained with the powerful HR-XPS–XSW combination are new and exciting enough so that they can stand on their own.

8.1. Preparation of the ZnO substrates

All the Zn- and O-terminated crystals employed in this thesis were acquired from Crystec GmbH, Berlin, with the following characteristics:

- Growth: hydrothermal [456–458].
- Size: 10 mm × 10 mm × 0.5 mm.
- Polishing: one side.
- Tolerance: $< 0.5°$ (typical $< 0.3°$).

According to the supplier, the crystals may contain alkali and alkaline atoms, such as Li, K, Na and Ca as impurities, all intrinsic to hydrothermal growth [457]. As it can be seen from Fig. [8.1], the substrates present different shades of yellow/green[1], most likely

[1] The origin of the yellowish/greenish color is still disputed. Ideally, ZnO should be transparent since the band gap is at the UV region.

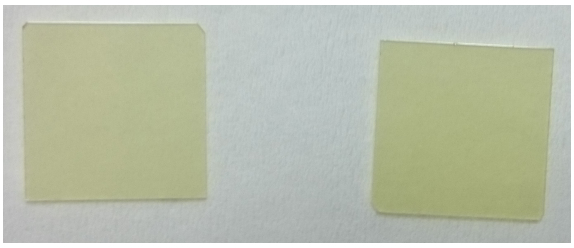

Figure 8.1: Photo of different ZnO crystals used during the experiments. Note the slight difference in the color.

due to the different impurities and concentrations thereof, which depend on the crystal badge[2]. Charge-carrier concentration and mobility measurements, performed by Dr. R. Loeffler from the *Forschungs- und Service-Einrichtung* LISA$^+$ using the Hall-effect and van-der-Pauw measurements [459], show an intrinsic n-type behavior of ZnO with a carrier concentration of $n_e = 1.51.10^{14}\,\mathrm{cm}^{-3}$ and a mobility of $\mu_e = 86.45\,\mathrm{cm}^2/\mathrm{Vs}$.

The substrate preparation, especially for metal single crystals, is typically done by several sputtering/annealing cycles to achieve a clean and homogeneous surface and, provided that the crystal quality is good enough (crucial for XSW experiments as discussed in Sec. [3.3]), no additional treatments such as annealing close to the crystal melting point are required. The preparation of the ZnO crystals is, however, more elaborate. Aiming at obtaining a very good crystal ordering in the bulk as well as a clean surface with the minimum damage, our collaborators in Berlin developed the following treatment, based on the procedure described by Götzen and Witte [460], that will be arbitrarily referred from now on as the **Standard Treatment**:

- Treatment in air: annealing in a quartz-tube furnace for 2 hours at 1000°C.
- Treatment in UHV:
  1. Annealing at 420°C (∼693 K) for 10 min.
  2. Sputtering for 15 min ($P_{\mathrm{Ar}} = 5.10^{-5}$ mbar, $E = 0.5$ keV).
  3. Annealing at 420°C (∼693 K) for 10 min.

The substrates were always let cool down inside the quartz tube before it was safe to remove them, taking the process a few hours. Then, they were mounted on an Omicron-type sample plate and inserted into the UHV chamber as soon as possible.

The substrates used for the main study with molecules were prepared following the **Standard Treatment**. Therefore, in the following section we will first characterize these surfaces. Then, the specific effect of the different steps of the treatment will be considered.

8.2. Characterization of the ZnO surfaces

The rocking scans shown in Fig. [8.2] were performed by Anton Zykov and Prof. Stefan Kowarik, from the Humboldt Universität zu Berlin. The UPS measurements presented in Fig. [8.4] were performed by Alessandro Grecco at Prof. Steffen Duhm's lab, at Soochow University.

The main limitation that was faced by our group in previous attempts to use ZnO in

[2] The particular effect of the bulk dopants and impurities is beyond reach at this point of the project.

XSW experiments was the poor crystal quality in the bulk, which hindered the creation of the XSW field. The furnace annealing overcomes this issue by yielding a highly-ordered crystal as it is drawn by the change in the reflectivity curve shown in the inset of Fig. [8.2]. Indeed, the single and narrow rocking curve around the (002) Bragg reflection is characteristic for high-quality crystals [456, 457]. The furnace annealing was applied to all the samples studied, regardless of posterior UHV treatment or deposition of molecules.

8.2.1. Surfaces prepared with the Standard Treatment

HR-XPS reveals the presence of surface contamination for the as-loaded sample. Certainly, the features appearing in the C 1*s* and N 1*s* region (not shown here) correspond to adsorbed hydrocarbons and other contaminants. The broad oxygen signal with a huge shoulder at the high BE side (Fig. [8.2a]) indicates the presence of inequivalent oxygen-containing species. The UHV part of the **Standard Treatment** seeks to remove these undesired adsorbates with the minimum damage to the surface. As it is clearly seen in Fig. [8.2a], the high BE shoulder mentioned above disappears from the O 1*s* spectrum, leaving a prominent sharp peak with a much smaller shoulder at the high BE side. The featureless carbon and nitrogen regions (not shown) provide additional evidence of the cleanliness of the surface.

The remaining oxygen core-level features, shown in Fig. [8.2a], have to be identified. Thus, we performed angle-dependent XPS measurements of the oxygen core-level signal, which is shown in Fig. [8.2b]. The change in the relative intensity between the main peak and the shoulder evidences the surface nature of the latter. Hence, the main peak is associated to the bulk-oxygen atoms, whereas the shoulder stems from the oxygen species on the surface. This labeling is in line with many other studies [310, 312, 322, 461]. We

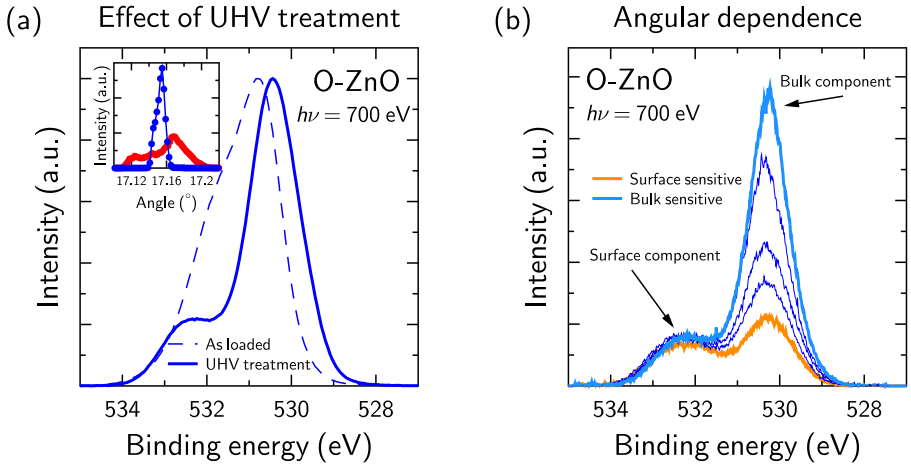

Figure 8.2.: Effect of the **Standard Treatment** on the samples: O 1*s* core-level spectra and X-ray reflectivity. (a) XP spectra corresponding to the O-ZnO substrate as loaded in the UHV chamber (dashed) and after the Standard treatment (solid). The UHV treatment removes the layer of adsorbates, yielding a clear main peak and a shoulder at higher BE. The inset shows a rocking scan around the (000–2) Bragg reflection before the furnace annealing (red) and afterwards (blue). The sharp peak of the annealed sample points out to a remarkable improvement of the crystal structure. (b) Angular-dependent XPS measurements, performed on an O-ZnO crystal, that highlight the surface-related origin of the side bump at high BE as opposed to the bulk origin of the main peak. The effect of the treatment renders the same results for the Zn-ZnO surface.

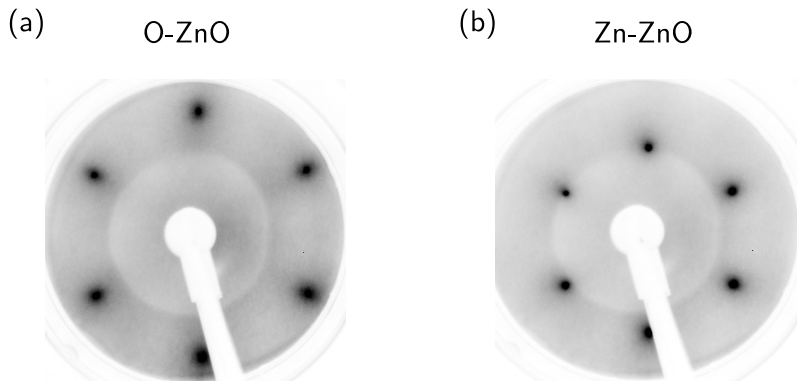

Figure 8.3.: Effect of the **Standard Treatment** on the samples: LEED. The diffraction patterns obtained for (a) the O-ZnO ($E = 88.5\,\text{eV}$) and (b) the Zn-ZnO ($E = 140\,\text{eV}$) surfaces. In both cases, the typical 6-spot pattern of the unreconstructed surface [460] appears. See Fig. [8.7] for more information on the LEED study.

note that, although Fig. [8.2] only displays data for the O-ZnO surface, the **Standard Treatment** has the same effects on the Zn-ZnO surface.

The intrinsic instability of the polar terminations also makes it necessary to inspect the in-plane geometry to track any possible reconstructions of the cleaned surfaces. Fig. [8.3] shows the LEED patterns of the **standard-treated** O-ZnO and Zn-ZnO crystals. The 6-fold spot pattern is typical for an unreconstructed surface [460]. They are observed for a very large electron-energy range and appear to be stable in time.

Next, the valence band (VB) features of the **standard-treated** substrates are inspected with UPS. Fig. [8.4] shows the region close to the band gap for both terminations. The colored area represents the gap states, which are clearly more prominent for the Zn-terminated case. The contribution from the gap states is typically obtained from the difference between the raw data and a Gaussian fit [199], i.e. the region that is not accounted for by the fit is assigned to them. Such differences in the electronic states agree with other studies that have reported a surface-dependent behavior for the VB features [462, 463]. The surface origin of the gap states will become important to rationalize, later on, possible charge transfer (CT) effects involving the adsorbed molecules.

Another intrinsic difference between the Zn- and the O-terminated surfaces is the BE shift between the main peak and the shoulder of the O $1s$ core-level signal. After many measurements of different samples, we concluded that, for the O-terminated case, the surface species appear at $\sim$1.9 eV above the main peak whereas, for the Zn-terminated one, it appears at $\sim$1.4 eV towards the high BE side, similar to previous reports [310,312,322,464]. The high reproducibility of these energy shifts, observed for different samples and preparation conditions, render two strong fitting constraints for the XSW and XPS data. Fig. [8.5a] displays the standard fitting model for the clean substrates used throughout this work. It is worth noting that these two models may be a simplification since they assume only two components to fit the spectra, one for the bulk and one for the surface species, neglecting possible contributions from vacancies and/or impurities [311]. However, as it will become more clear below, it renders very good XSW results. See Appendix [D] for a detailed discussion on the fitting model.

Previous to the discussion of the XSW measurements, it is worth explaining how to

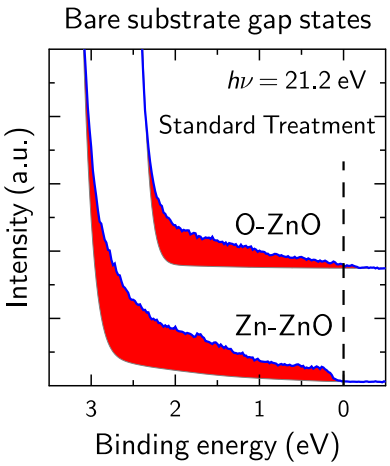

Figure 8.4: Effect of the **Standard Treatment** on the samples: UPS. The VB region close to the Fermi edge for the two bare polar standard-treated surfaces is shown. The red-colored region is the difference between the raw data and the fitted spectra with several Gaussian contributions, which corresponds to the gap states. These measurements, showing a major number of these for the Zn-ZnO, compared to the O-ZnO surface, are in line with previous studies [463]. As it is discussed in Ref. [465], the zinc vacancies seem to have a larger contribution to the band gap states than oxygen ones. We note that the Zn-ZnO spectrum has a Fermi-edge-like feature that may stem from the sample holder. A more advanced background subtraction method will be required, which in any case does not compromise our conclusion.

interpret the obtained information in the context of the ZnO crystal. Fig. [8.6] shows 2D sketches along the [00±2] directions with the zinc, the bulk- and surface-oxygen atoms distinctively colored and the distances of interest highlighted. Thus, one has to take into account that the XSW field is produced deep in the bulk of the crystal, away from the surface. However, the information obtained from the photoemitted electrons comes only from the first atomic layers[3]. Consequently, any changes to the vertical ordering (along c) of the first layers compared to the bulk, for instance due to an aggressive sputtering treatment or simply an intrinsic relaxation of the topmost layers, will appear as a mismatch between the measured XSW fitting parameters and those corresponding to the bulk crystal. For later comparisons, the ideal, or deep-bulk, coherent positions[4] for the O-ZnO crystal (shown in Fig. [8.6a]) are $P^{\text{bulk}}_{00\text{-}2}(\text{Zn}) = 0$ (or 1) for the zinc atoms and $P^{\text{bulk}}_{00\text{-}2}(\text{O}_{\text{bulk}}) \simeq 0.25$ for the bulk-oxygens atoms. For the Zn-ZnO (Fig. [8.6b]), these are $P^{\text{bulk}}_{002}(\text{Zn}) = 0$ (or 1) for the zinc and $P^{\text{bulk}}_{002}(\text{O}_{\text{bulk}}) \simeq 0.75$ for the bulk-oxygen atoms. In all cases the ideal coherent fraction is equal to 1, corresponding to a perfect vertical ordering. Given this context, the XSW results can be interpreted.

The XSW measurements performed along the [00±2] direction are shown in Fig. [8.5b], with the fitting parameters accompanying the photoelectron-yield curves. The core-level-fitting model of Fig. [8.5a] was used to evaluate the data for oxygen, which allows one to obtain separate information for the surface species and the bulk-oxygen atoms. We note that, for zinc, the weaker Zn $3s$ core-level signal was used instead of the usually reported Zn $2p$ to avoid possible non-dipole contributions from non-spherical orbitals to the photoemitted electrons (see. Sec. [3.3.2.3]). The XP spectrum of the Zn $3s$ signal

[3] The X-rays at ∼2.385 keV have an extintion length of ∼600 nm, whereas the O $1s$ and Zn $3s$ electrons have an inelastic mean free path of ∼32 Å and 36 Å, respectively.

[4] Note that the coherent position P_{H}, for a given species within the XSW field, is directly related to the average atomic position via $d_{\text{H}} = d_0(n + P_{\text{H}})$. For positions within the unit cell $n = 0$ and one can just express them, for instance along [00±2], as $d_{00\pm2} = P_{00\pm2} \cdot c_0/2$, where c_0 is the size of the unit cell (along the [00±1]). Therefore, knowing c_0 (e.g. from X-ray diffraction experiments), the XSW parameters corresponding to the bulk can be reversely calculated. For the Zn-ZnO, the oxygen atoms are sitting at $0.3748 \cdot c_0$ along the [002] direction. Consequently, $P^{\text{bulk}}_{002}(\text{O}_{\text{bulk}}) = 0.7496 \simeq 0.75$. For the O-ZnO case, $P^{\text{bulk}}_{00\text{-}2}(\text{O}_{\text{bulk}}) = 0.2504 \simeq 0.25$. The zinc layers are at the origin of the field, thus their coherent position is 0 (or equivalently 1).

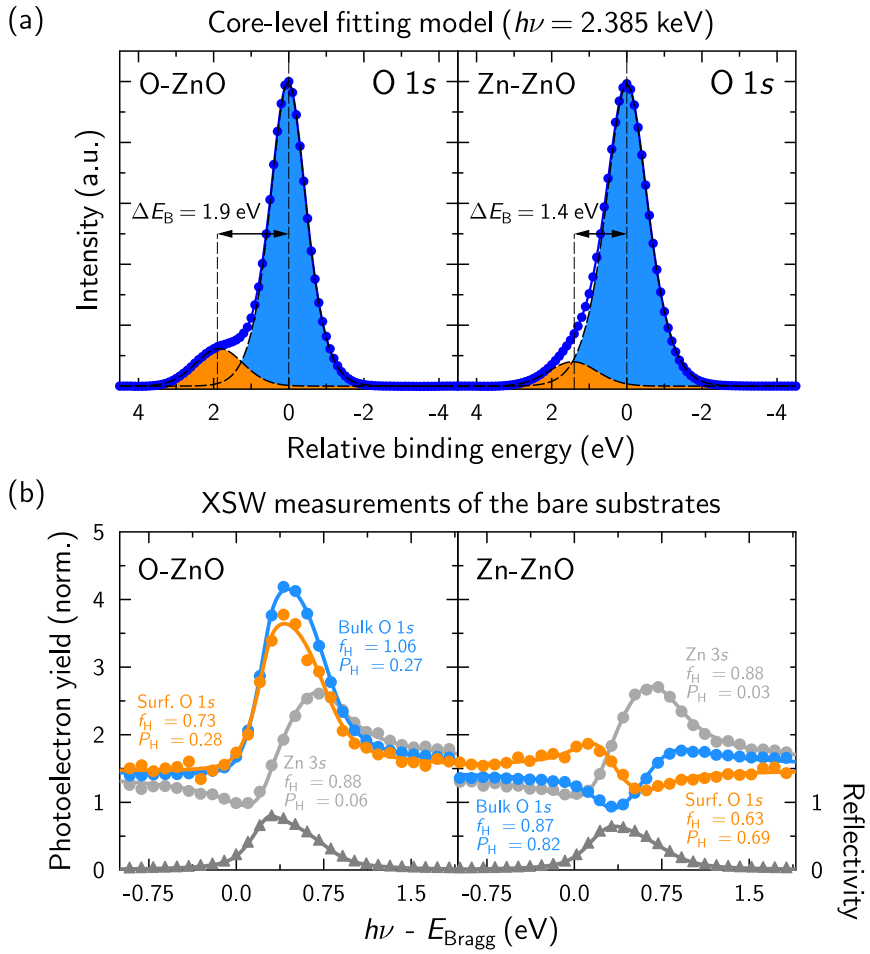

Figure 8.5.: Core-level model and characteristic XSW curves for the polar surface of ZnO after the **Standard Treatment**. (a) Two-component model employed to fit the O 1*s* core-level spectra of the bare substrates. The main peak stems from the bulk-oxygen atoms, whereas the side peak is attributed to surface species [461]. The most important parameter when fitting other spectra is the BE difference between the bulk component and the surface species, which is polarity-dependent. In addition, for the core-level model used to obtain the XSW fits shown in (b), a Lorentzian contribution of 60% is used for the bulk component and one of 20% for the surface contribution. Both values were experimentally assessed, as they rendered the highest coherent fractions when used to analyze the XSW data. A linear background was applied. In some cases the fitting routine and the posterior XSW analysis was repeated with a Shirley background and the output parameters of the XSW were unchanged. (b) Typical XSW measurements for the O- and Zn-terminated surfaces. The Zn 3*s* curves have the same modulation for both cases. The bulk and surface oxygens evolve differently around the Bragg energy, a fact that can be used as an unambiguous way to identify the surface termination.

(not shown) renders a symmetrical single peak, whose full area was used to evaluate the photoelectron yield. All the XSW parameters are summarized in Tab. [8.1]. Also, the relevant measurements for each surface treatment, discussed in the following sections, are displayed together in Figs. [8.11] for O-ZnO and [8.12] for Zn-ZnO.

Starting with the O-ZnO, the coherent position of Zn ($P_{00\text{-}2}(\mathrm{Zn}) = 0.06$) deviates slightly from the ideal value, which corresponds to an actual displacement of 0.14 Å above the ideal unit cell position. The bulk oxygen shows the same trend, with a coherent position ($P_{00\text{-}2}(\mathrm{O_{bulk}}) = 0.27$) 0.02 above the ideal value, corresponding to a vertical displacement

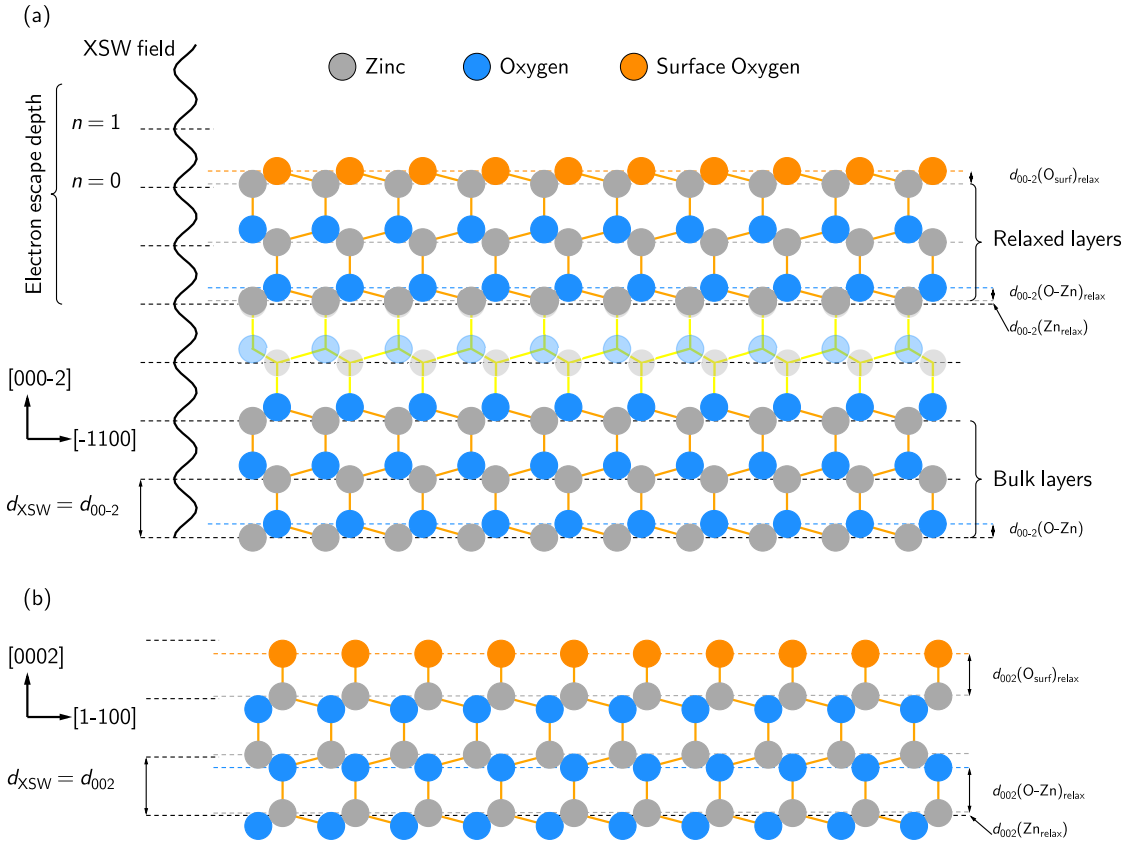

Figure 8.6.: 2D Projection of the O-ZnO (a) and Zn-ZnO (b) crystals along the [11$\bar{2}$0] direction. In (a), the XSW formation inside the ZnO crystal and the relevant magnitudes are highlighted, but they also apply to (b). In particular, the sketch points out that the generation of the XSW field is mostly happening deep in the bulk, away from the surface, although the actual information obtained from the XSW measurements is limited by the escape depth of the photoelectrons. Therefore, the periodicity of the field coincides with the lattice constant of the (000±2) planes in the bulk, but it may be the case that the information obtained stems from relaxed layers, i.e. the atoms are shifted in c with respect to the bulk. This can be identified if the fitting parameters differ from the ideal (bulk) ones. Of course, from the XSW measurements the position of the surface species with respect to the topmost zinc layer can also be obtained. It is worth noting that the positions obtained directly from the measurements are referred to the bulk zinc layers. Therefore, to obtain actual bonding distances within the relaxed layer, the shift of the zinc layer ($d_{00\pm2}(\mathrm{Zn_{relax}})$), if any, has to be accounted for.

of 0.08 Å. The surface species show almost the same coherent position as the bulk, denoting that a lower coordination of the surface atoms does not induce strong changes along the c direction. If we now look at the ordering, by considering the coherent fractions of zinc and the surface components, it is clear that a non-negligible degree of disorder is present. This will be later related to the sputtering procedure and the relatively low annealing temperature in UHV. Moving to Zn-ZnO, the XSW results for the zinc layers are virtually the same as those presented for the O-terminated surface. The coherent position of the bulk oxygens ($P_{002}(\mathrm{O_{bulk}}) = 0.82$), 0.07 higher than the one corresponding to the ideal structure, indicates a displacement of ∼0.18 Å with respect to the lattice positions. On the contrary, the surface species show a coherent position 0.06 lower than the bulk. Regarding the ordering, the coherent fractions for the zinc layers and the surface species are very similar to those of the O-ZnO. Also, the bulk oxygens show a similar ordering as the zinc

layers, indicating an homogeneous disorder.

Before concluding this subsection, it is worth commenting that the coherent fraction for the bulk oxygens of the O-ZnO sample, $f_{00\text{-}2}(O_{bulk}) = 1.06$, appears to be rather high compared to the value obtained for the zinc atoms ($f_{00\text{-}2}(Zn) = 0.88$) as well as to those of the bulk oxygens of Zn-ZnO. This trend is systematically observed, in some cases even rendering coherent fractions significantly higher than 1. Thus, as it will be discussed in Sec. [8.2.2.4], the measured values should be reduced by 15%.

8.2.2. Surfaces under different preparation conditions

Beyond our so-called **Standard Treatment**, it is interesting to know how the surface characteristics change when the following conditions are modified:

- Sputtering time.
- Annealing temperature: 420°C (∼693 K) vs. 700°C (∼973 K).
- Water dosing at RT and LT (∼150 K,∼-123°C).

For the sputtering, all the parameters but the time were kept unchanged with respect to the **Standard Treatment**. Different samples were investigated with increasing (intervals of 5 min) sputtering time. For the annealing and water dosing, the same sample was used for the whole treatment and then repeated on a new one for reproducibility. Measurements were performed at each step of the treatment. Thus, the samples were **standard-treated**, then the annealing at 700°C for 1 hour was performed. When the sample was thermalized, water was dosed into a chamber using a leak valve. After the measurements with water were performed at room temperature (RT), the sample was cooled down to ∼150 K (LT) and water was dosed again. The exposure, calculated in Langmuir (L)[5], was controlled through the water partial pressure inside the chamber and the dosing time. The water employed had been previously degassed with several freeze-pump-thaw cycles [466].

8.2.2.1. LEED characterization

References to different in-plane surface structures are abundant in the ZnO literature (summary in Sec. [4.2.2]). In order to better understand what are the changes happening during the surface treatment, LEED was recorded at different steps of the process. Interesting differences appear between the two terminations. For instance, the O-ZnO surface always displays the unreconstructed 6-fold pattern of Fig. [8.3]. However, as shown in Fig. [8.7], the as-loaded Zn-ZnO substrate shows a $(\sqrt{3} \times \sqrt{3})R30°$ reconstruction (red circles) coexisting with the (1×1) arrangement (square). Upon sputtering, the reconstruction is lifted and only the 6-fold spot pattern remains. Treating further the sample does not modify the in-plane arrangement. It has been reported that the $(\sqrt{3} \times \sqrt{3})R30°$ reconstruction appears on defect-free regions of the surface, thus the creation of these through sputtering may explain why this process lifts it [462].

[5] 1 Langmuir = 1 L corresponds to the exposure of 10^{-6} Torr of gas for 1 second.

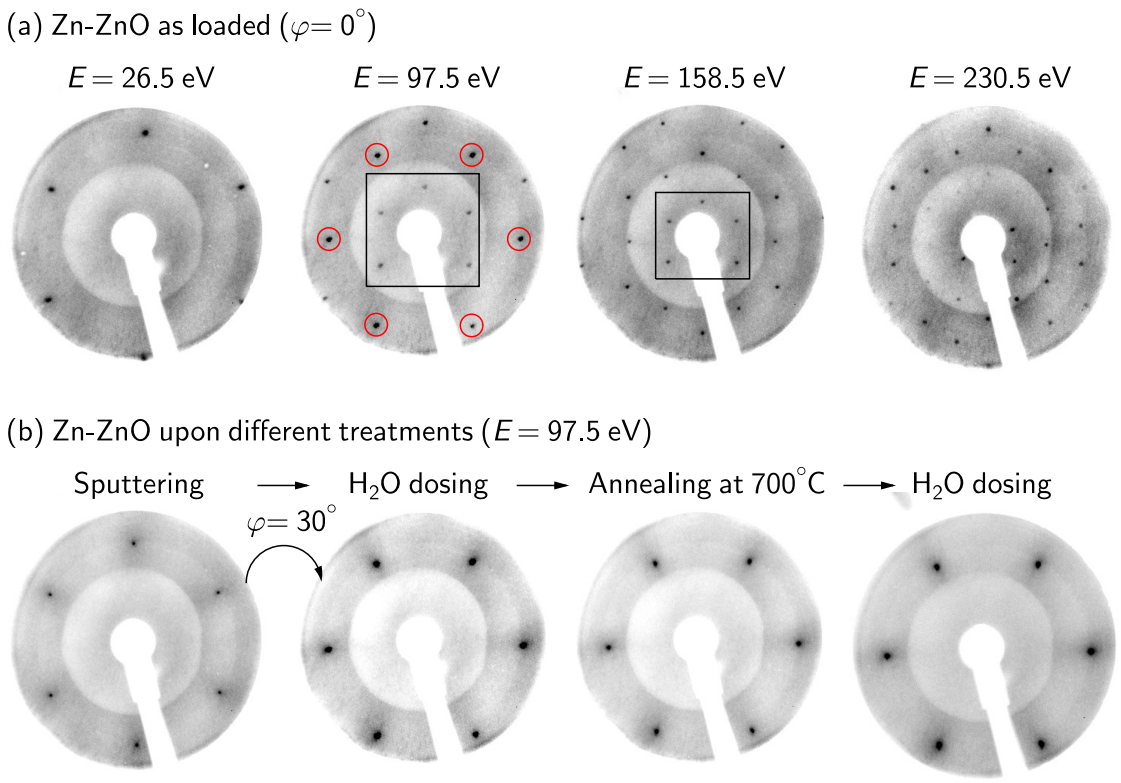

Figure 8.7.: LEED patterns corresponding to the Zn-ZnO surface under different treatments. (a) As-loaded sample measured at different electron energies (E) for a fixed azimuth of 0°. The diffraction pattern shows a $(\sqrt{3}\times\sqrt{3})R30°$ reconstruction (red circles) superimposed to the (1×1) spots (square). (b) The same substrate is measured after the different steps of the surface treatment (all taken at $E = 97.5$ eV). The most important change is the lifting of the $(\sqrt{3} \times \sqrt{3})R30°$ reconstruction upon sputtering, whereby only the unreconstructed (1×1) pattern remains. Further treatment such as annealing at high temperatures and subsequent water dosing do not produce any further changes. Note that the last three pictures of (b) have the azimuth rotated by 30° with respect to the first one and those of (a).

8.2.2.2. HR-XPS characterization

Besides the XPS characterization presented in the previous section, we monitored, in real-time, the evolution of the surface during the annealing up to 700°C (Fig. [8.8a]) and the subsequent thermalization (Fig. [8.8b]) of the sample. The set of normalized scans were recorded at different instants of the treatment with the objective of highlighting the spectral evolution of the O 1s core-level signal. For a better comparison of the relative intensity change, the spectra were artificially aligned so that the bulk peak is at 530.5 eV. The alignment, however, masks a trend seen for both terminations, namely, a binding-energy shift towards lower values coming along with the desorption of the surface species, which is then reversed with the thermalization of the sample. This may be explained by the changes in the work function as well as by band-bending contributions occurring upon desorption and readsorption of the surface species [312, 467]. Both terminations also show a broader bulk peak at high temperatures, which can be related to the higher thermal vibration of the atoms. An important difference between the two polar surfaces is the remaining shoulder at the high BE side of the bulk peak upon annealing at 700°C, only

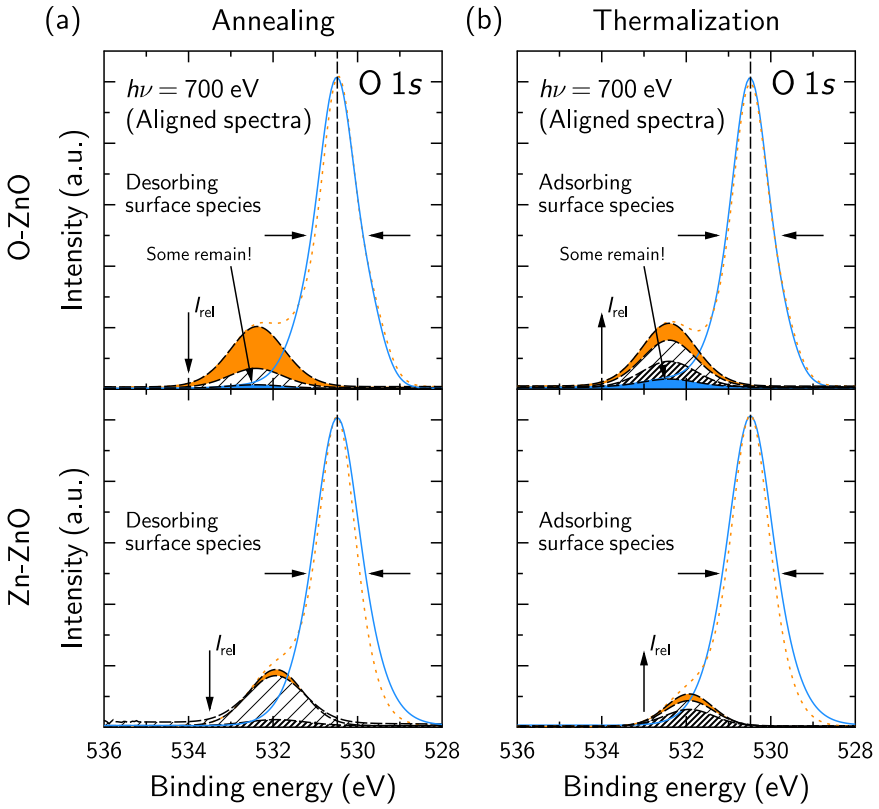

Figure 8.8.: Real-time evolution of the O 1*s* core-level signal during sample annealing (a) and its subsequent thermalization back to RT (b). The bulk peaks have been artificially aligned at 530.48 eV for a better comparison of the relative intensity change undergone by the surface species. The arrow of I_{rel} indicates the direction of the change, down for the decrease during annealing and up for the increase during thermalization. A common trend is that the line width of the bulk peak increases during annealing (see main text for the details). Noteworthy, for the O-ZnO surface a shoulder always remains, even upon annealing at 700°C, whereas for the Zn-ZnO, only the bulk peak is visible. Interestingly, as soon as the annealing is stopped and the sample starts to cool down, the shoulder immediately appears, meaning that the surface species readily adsorb again, being the readsorption faster in the O-ZnO. The intensity is normalized to the maximum value (bulk peak).

seen for O-ZnO substrates. The origin of this feature is not yet clear, it could be either species not removed by the annealing or bulk-oxygen atoms close to vacancies created upon annealing, which may have a slightly different chemical environment.

The dosing of water was also investigated with HR-XPS. The results show that, at RT, water does no seem to stick on the surface. Noteworthy, the core-level feature of the surface component appears sharper, a behavior that is observed for both terminations. For Zn-ZnO, Fig. [8.9a] shows the oxygen core-level signal recorded at different emission (take-off) angles with increasing surface sensitivity. Although the surface has been dosed with water, no H_2O-related features can be observed. The angular-dependent scans help to unambiguously resolve the binding energy difference between the surface and the bulk components for the Zn-terminated surface, which clearly agrees with the proposed ∼1.4 eV proposed in the previous section. In order to investigate a possible temperature-dependence on the water adsorption, the dosing was repeated at LT (∼150 K upon cooling with liquid nitrogen). The difference, as shown in Fig. [8.9b], is striking: a huge peak at ∼3.5 eV above the bulk component appears, clearly indicating the adsorption of several

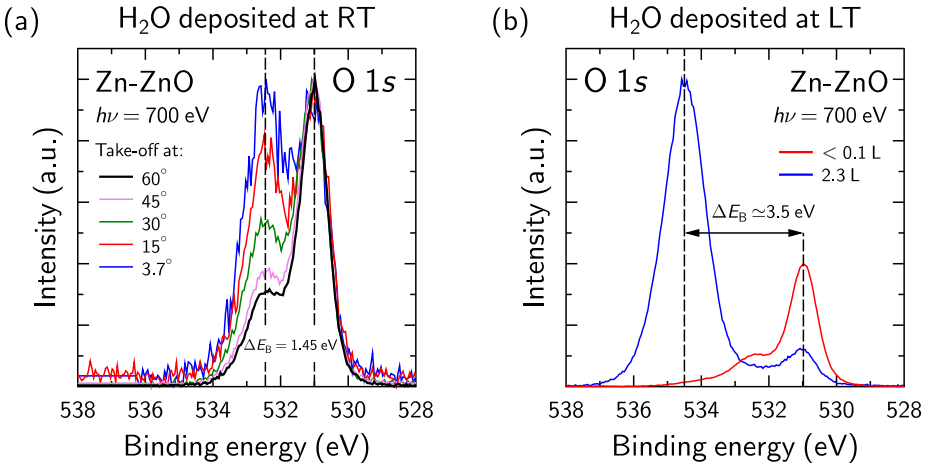

Figure 8.9.: HR-XPS ($h\nu = 700\,\text{eV}$) of water deposited on Zn-ZnO. (a) 2.3 L of water dosed at RT and measured at different emission (take-off) angles to increase the surface sensitivity. The intensity is normalized to the maximum of the bulk peak. Two important pieces of information can be extracted: first, the BE difference between the bulk and the surface components and secondly, that there is no spectral contribution evidencing the adsorption of water molecules at RT. (b) 2.3 L of water dosed at ∼150 K (sample cooled with liquid nitrogen). In this case, contrary to what is observed in (a), a significant peak corresponding to water can be clearly distinguished at $E_B = 534.5\,\text{eV}$, 3.5 eV above the bulk peak. For comparison, a spectrum of the surface, taken at LT, before the dosage is included. It is likely that at such low temperatures species readily start adsorbing.

water layers.

As mentioned, at RT the behavior is the same for the O-ZnO surface. The absence of new core-level features indicates that no water molecules are adsorbed. Interestingly, as shown in Fig. [8.10a], dosing water at LT introduces a large shoulder at the high BE side of the bulk peak, with a clear surface origin, as deduced from the angular-dependent measurement (Fig. [8.10b]). However, the bulk peak is clearly visible and more intense than the mentioned shoulder ruling out the presence of several adsorbed layers.

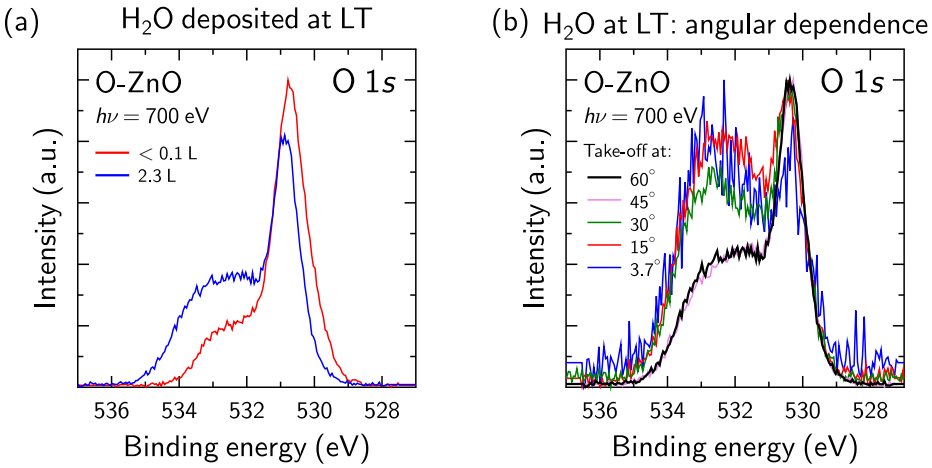

Figure 8.10.: HR-XPS ($h\nu = 700\,\text{eV}$) of water deposited on O-ZnO at LT (∼150 K). (a) Spectra, measured at LT, before (red) and after dosing 2.3 L of water into the chamber. The broad shoulder indicates the presence of several inequivalent oxygen species on the surface. Since the bulk peak is clearly visible, the presence of several water layers is discarded. (b) Spectra of 2.3 L adsorbed on the O-ZnO at LT measured at different take-off (emission) angles to enhance the surface sensitivity.

Finally, a common trend seen at RT for both surfaces is the faster recovery upon annealing of the core-level feature associated to the surface-oxygen component if water is dosed in the chamber. At this point, we cannot provide a quantitative description of it. However, it is plausible to think that the presence of water molecules that readily dissociate upon contact with the surface may recover the surface-oxygen species faster than just waiting for the residual gases to randomly impinge on the surface.

8.2.2.3. XSW characterization

The structural arrangement along the c-axis provided by the XSW technique presents very interesting results. Figures [8.11] and [8.12] summarize the XSW measurements, obtained from the O 1s core-level signal, for the O-ZnO and the Zn-ZnO surfaces, respectively, together with the corresponding core-level analysis and LEED images. The fitting parameters are included in Tab. [8.1]. Also, the reader can use Figs. [8.13] and [8.14] as a visual description of the trends explained next.

Starting with the O-ZnO, the as-loaded sample shows a prominent shoulder stemming from the surface contamination that, however, does not completely mask the bulk peak. It is worth mentioning that using just one fitting component to account for the surface/contaminant species may be rather simplistic but, without further characterization, adding additional components may be too speculative. In any case, using this 2-component model to fit the XSW data renders very good results. The bulk oxygens show a coherent position 0.02 below the ideal value ($P_{00\text{-}2}^{\text{bulk}}(\text{O}_{\text{bulk}}) \simeq 0.25$). This means, on the one hand, that the crystal ordering is very good (due to the furnace annealing) and, on the other hand, that the probed layers are slightly inwardly relaxed since the distance with respect to the zinc layer (origin of the XSW field) is smaller than in the ideal case. As it has been discussed above, the coherent fractions higher than 1 do not hold physical meaning. Therefore, the value of 1.27 should not be trusted and the actual coherent fraction should be close to 1. This will be explained, later, in Sec. [8.2.2.4]. Interestingly, the huge surface component also renders a coherent modulation of the photoelectron yield with a remarkably high coherent fraction, indicating a significant vertical ordering in the surface contaminants/species. This and the somewhat discordant coherent position ($P_{00\text{-}2}(\text{O}_{\text{surf}}) = 0.16$), compared to the clean surface (see Standard in Fig. [8.11]), may be explained by the fact that the contaminants adsorb on top of the surface oxygens. Indeed, the fact that one obtains, for the surface species, a coherent position that would correspond to a subsurface position does not make much sense for an O-terminated surface. Turning the coherent position to an actual adsorption distance renders a value of 3.02 Å with respect to the zinc layer, which is, assuming a bulk-like position for the topmost oxygen layer, ∼2.42 Å above the surface. We note that this is just a guiding distance. Certainly, the core-level feature used to account for the photoelectron yield does not only contain the adsorbed species but also the actual surface oxygens, which are located at a different position. Consequently, the values obtained stem from the most numerous species, the contaminants, but they are modified by the less abundant contributions.

Although it is not shown here, the first mild annealing (420°C) of the **Standard Treatment** procedure does not produce any changes to the XSW results and only a slight decrease on the surface/contamination component is evidenced in the XP spectrum (not shown). The real cleaning effect is performed by the sputtering, as it is readily evident by

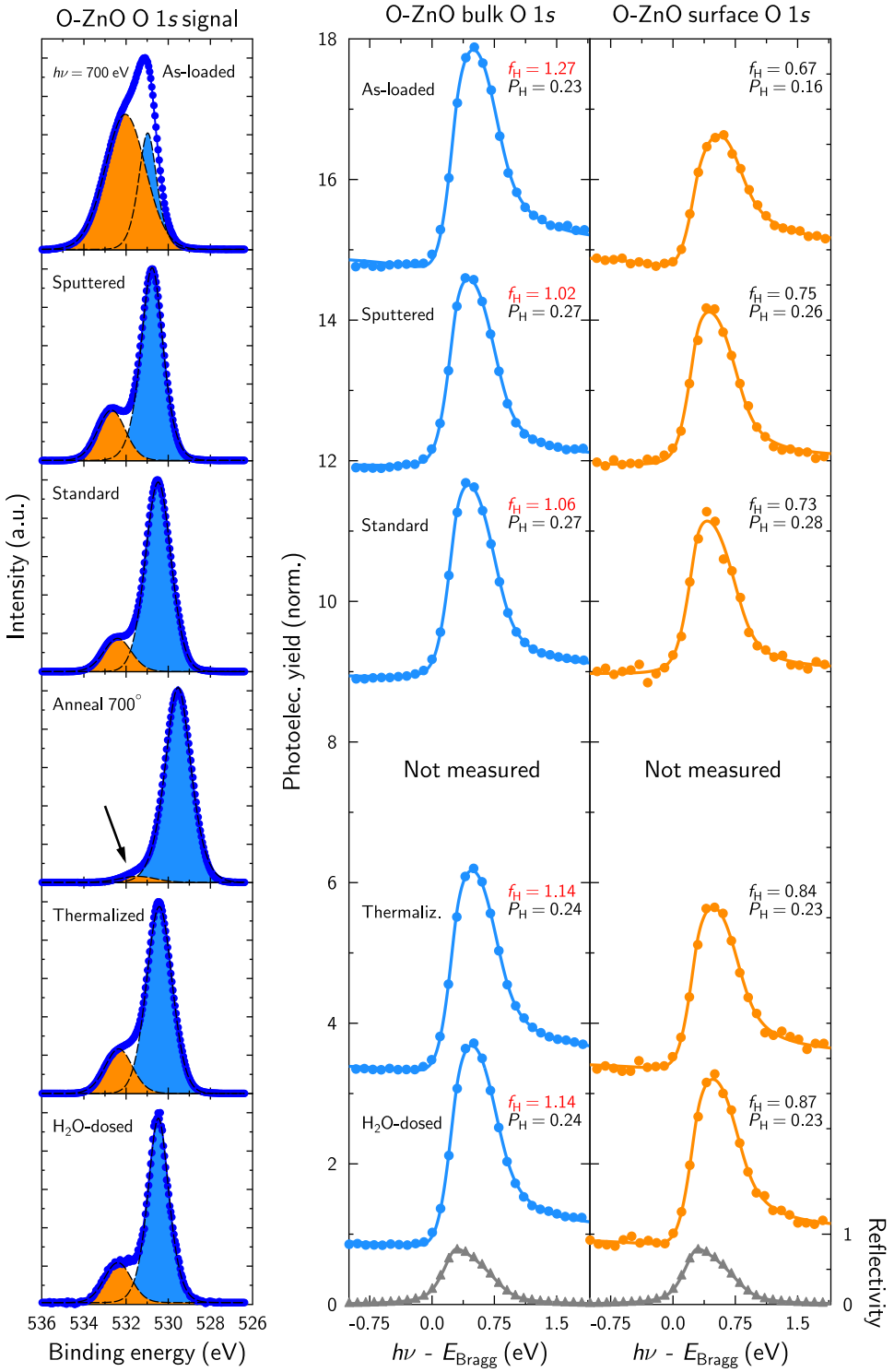

Figure 8.11.: Summary of the XPS and XSW measurements for the most relevant treatments performed on the O-terminated surface of ZnO. The treatments were carried out chronologically from top to bottom. In all the cases, the (1×1) LEED pattern was observed (identical to that of Fig. [8.3]). The coherent fractions higher than one (in red) are discussed in Sec. [8.2.2.4]. The fitting model for the core-level spectra and the XSW is the same as that described in Fig. [8.5].

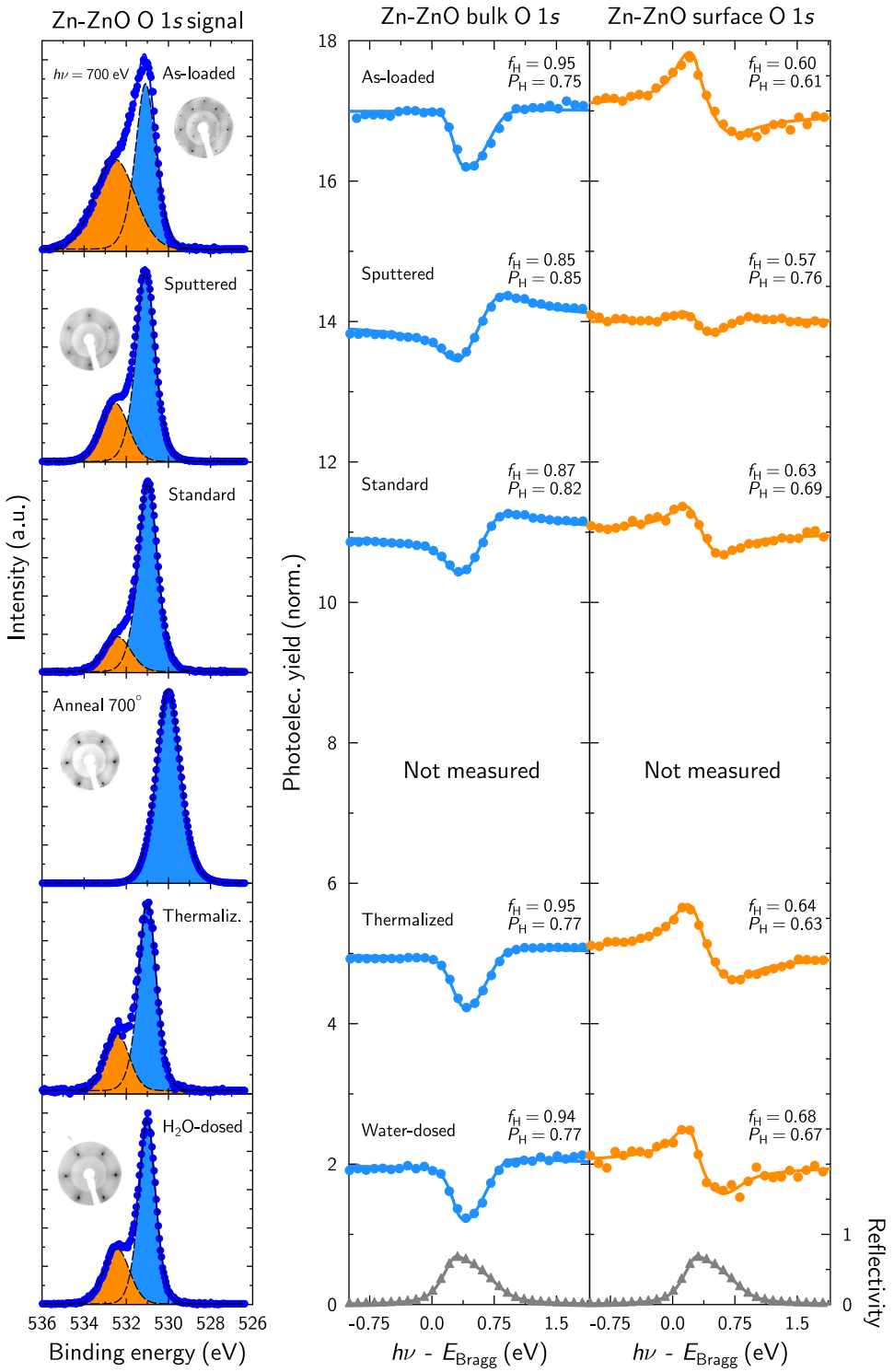

Figure 8.12.: Summary of the LEED, XPS and XSW measurements for the most relevant treatments performed on the Zn-terminated surface of ZnO. The treatments were carried out chronologically from top to bottom. The electron energy used in LEED is $E = 97.5\,\text{eV}$ in all cases. Note that the pattern corresponding to the sputtering treatment is rotated by 30°. Note the varying shapes of the photoelectron yield with the different treatments. The fitting model for the core-level spectra and the XSW is the same as that described in Fig. [8.5].

Substrate	Treatment	$f_{00\mp2}$	$P_{00\mp2}$	$d_{00\mp2}$ (Å)
O-ZnO	**Zn 3*s***			
	Bulk crystal	1.00	0 (or 1)	0 ($n=0$) 2.60 ($n=1$)
	As-loaded	1.04	0.01	0.03
	1st. annealing	Not measured		
	Sputtering	0.86	0.05	0.14
	Standard	0.88	0.06	0.14
	Annealing 700°C	0.97	0.02	0.06
	Water dosing	0.97	0.02	0.06
	Bulk O 1*s*			
	Bulk crystal	1.00	0.25	0.65
	As-loaded	1.27 (1.08)	0.23	0.60
	1st. annealing	Not measured		
	Sputtering	1.02 (0.83)	0.27	0.70
	Standard	1.06 (0.87)	0.27	0.70
	Annealing 700°C	1.14 (0.95)	0.24	0.62
	Water dosing	1.13 (0.94)	0.24	0.62
	Surface O 1*s*			
	Bulk crystal	–	–	–
	As-loaded	0.67	0.16	0.43 ($n=0$) 3.03 ($n=1$)
	1st. annealing	Not measured		
	Sputtering	0.75	0.26	0.68
	Standard	0.73	0.28	0.72
	Annealing 700°C	0.84	0.23	0.60
	Water dosing	0.84	0.23	0.60
Zn-ZnO	**Zn 3*s***			
	Bulk crystal	1	0 (or 1)	0 ($n=0$) 2.60 ($n=1$)
	As-loaded	1.00	0.99	2.57
	1st. annealing	1.00	0.99	2.57
	Sputtering	0.81	0.06	0.16
	Standard	0.88	0.03	0.08
	Annealing 700°C	0.97	1.00	2.58
	Water dosing	0.95	0.99	2.58
	Bulk O 1*s*			
	Bulk crystal	1	0.75	1.95
	As-loaded	0.95	0.75	1.95
	1st. annealing	0.94	0.75	1.95
	Sputtering	0.85	0.85	2.20
	Standard	0.87	0.82	2.14
	Annealing 700°C	0.95	0.77	2.00
	Water dosing	0.94	0.77	2.00
	Surface O 1*s*			
	Bulk crystal	–	–	–
	As-loaded	0.60	0.61	1.59
	1st. annealing	0.59	0.62	1.61
	Sputtering	0.57	0.76	1.97
	Standard	0.63	0.69	1.80
	Annealing 700°C	0.64	0.63	1.64
	Water dosing	0.67	0.67	1.75

Table 8.1.: Summary of the XSW fitting parameters and corresponding atomic positions for the different treatments applied to both polar surfaces. The zinc and bulk-oxygen positions are referred to the crystal structure along the [00±2] direction. Remember that the reference (origin of the XSW field) is the zinc layer. In red, the measured coherent fractions of the bulk-oxygen atoms of the O-ZnO crystals and in parenthesis the corrected values according to the discussion in Sec. [8.2.2.4]. For comparison, the ideal/deep-bulk positions are also included ("Bulk crystal").

the dramatic reduction of the surface component in the core-level spectrum of Fig. [8.11]. The 2-component model renders very good fits for the bulk as well as the surface species. Along with the cleaning of the substrate, the sputtering increases the disorder of the probed layers, as it can be seen by the reduced coherent fractions and, most remarkably, it increases the average position of the oxygen layer. This means that the sputtering re-

verses the initial inward relaxation. The completion of the **Standard Treatment** with the second mild annealing induces the desorption of the surface species, as evidenced by the lower intensity of the orange surface-related core-level component in Fig. [8.11]. The species readily adsorb upon turning off the heating and the coverage increases steadily with time. The XSW fitting parameters remain virtually unchanged, with only a slight increase of 0.02 of the surface coherent position. We note that any variations on the relative coverage of surface species, which relates to the intensity of the core-level component, does not influence the XSW results.

Contrary to the mild annealing, going to 700°C does produce notable changes. First, as it is seen with the corresponding core-level spectrum, the surface component is dramatically reduced although, surprisingly, a small tail remains. Although no XSW measurements were performed during the annealing, its effects can be observed in the measurements of the thermalized sample. The surface component has been readsorbed and the overall vertical ordering, as indicated by the coherent fractions, is improved. In addition, the coherent positions are also reduced, taking values very similar to the as-loaded sample. Thus, the high-temperature annealing reverses the damage introduced by the sputtering.

Finally, the dosing of water on the surface does not produce any significant change on the XSW measurements, which appear identical as before the dosing. This supports the detailed XPS analysis discussed in the previous section showing that, at RT, there is no molecular adsorption of water.

For the Zn-ZnO surface (Fig. [8.12]), the response to the different surface treatments is the same as for the O-ZnO. However, remarkable differences can be observed. Starting with the as-loaded sample, the core-level spectra for the O $1s$ signal shows a large shoulder at the high BE side, similarly to the other surface, but less intense. The LEED pattern corresponds to a $(1\times1)+(\sqrt{3}\times\sqrt{3})R30°$ reconstruction, whereas the XSW measurements show a nearly perfect vertical ordering of the bulk oxygens and no sign of relaxation, since the coherent position is equal to the ideal value ($P_{002}^{\mathrm{bulk}}(\mathrm{O_{bulk}}) \simeq 0.75$). As it happens with the O-terminated surface, the huge surface/contamination component renders a coherent modulation of the photoelectron yield with a remarkably high coherent fractions. Its coherent position, lower than the bulk value, renders an adsorption distance of $\sim$1.59 Å, which, according to the surface reconstruction, is the average over different adsorption sites. It is interesting to note, however, the lower adsorption distance, with respect to the topmost layer, compared to the O-ZnO case. This may be explained by the major reactivity of the zinc surface [318, 468].

The first mild annealing at 420°C (not shown) does not produce substantial changes besides the desorption of some of the adsorbed species. The sputtering, nonetheless, lifts the surface reconstruction and reduces significantly the amount of surface species. It also reduces the vertical ordering within the probed layers, most notably for the surface component, and induces an increase of 0.1 to the coherent positions of the bulk, which equals to an outward relaxation of $\sim$0.26 Å. The average adsorption distance of the surface species also increases by $\sim$0.39 Å with respect to the as-loaded values. Interestingly, for the Zn-ZnO surface, the second mild annealing does produce an appreciable change in the coherent positions, which are partially reduced, and the coherent fractions that are slightly increased.

The annealing at 700°C completely removes the surface species, which readily readsorb

when the heating is turned off and the sample starts to cool down (thermalize), but does not produce further changes in the in-plane arrangement. The XSW measurements performed upon thermalization reveal again the healing power of the high-temperature annealing: the bulk component shows a coherent fraction and position almost identical to those of the as-loaded sample. The same situation applies to the surface species.

The dosing of water only produces a slight increase of the coherent fraction and position of the surface species. The increase of 0.04 in the coherent position renders an average adsorption distance of 1.74 Å with respect to the zinc surface.

So far, we have only discussed the atomic position and its changes for the oxygen species. However, the same information is also available for the zinc atoms. The change in the coherent fractions and positions of the zinc layers for the different treatments is schematically displayed in Fig. [8.14]. The trend is exactly the same as the one reported for the oxygen bulk species (Fig. [8.13]). In this case, however, there is no fitting model applied, the photoelectron yield stemming from the zinc atoms is evaluated with the total area of the Zn 3*s* core-level signal (after a proper Shirley background subtraction). Thus, possible fitting-related artifacts are removed. In addition, the zinc layers are the origin of the XSW field and hence, deviations from the ideal values are readily seen. As a reminder for a perfectly ordered crystal the coherent fraction is 1 and atoms occupying positions at the origin of the field yield a coherent position of 0 or 1, which are equivalent. In Fig. [8.14] the destructive effect of the sputtering and the healing effect of the high-

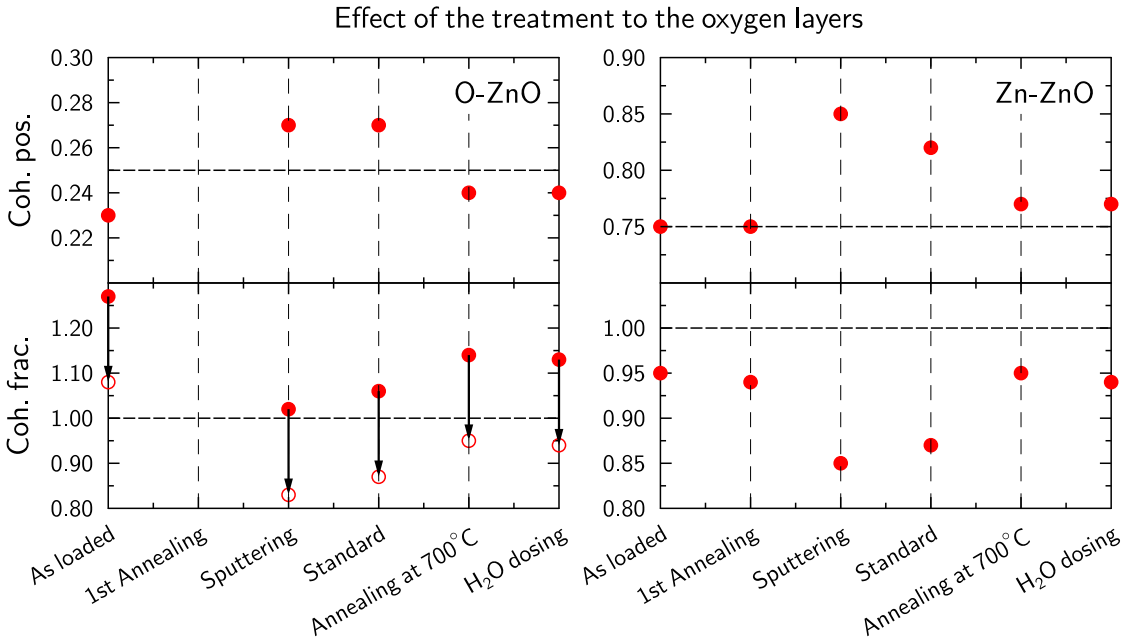

Figure 8.13.: Evolution of the XSW parameters along the $[00 \pm 2]$ direction corresponding to the topmost oxygen layers (extracted from the bulk component of the O 1*s* core-level signal) with the different surface treatments. The horizontal lines correspond to the ideal bulk crystal values (perfect ordering and no relaxation). Deviations from the ideal coherent positions indicate some sort of (inward/outward) surface relaxation, whereas deviations from the ideal coherent fraction indicate vertical disorder. The sputtering produces an outward relaxation of the topmost layers and increases the disorder. Conversely, the annealing at 700°C heals the surface and brings the parameters back to the bulk values. Note that the measured coherent fractions for the O-ZnO (filled circles) are physically impossible. As it will be discussed in Sec. [8.2.2.4], the values should be decreased by 15% (empty circles).

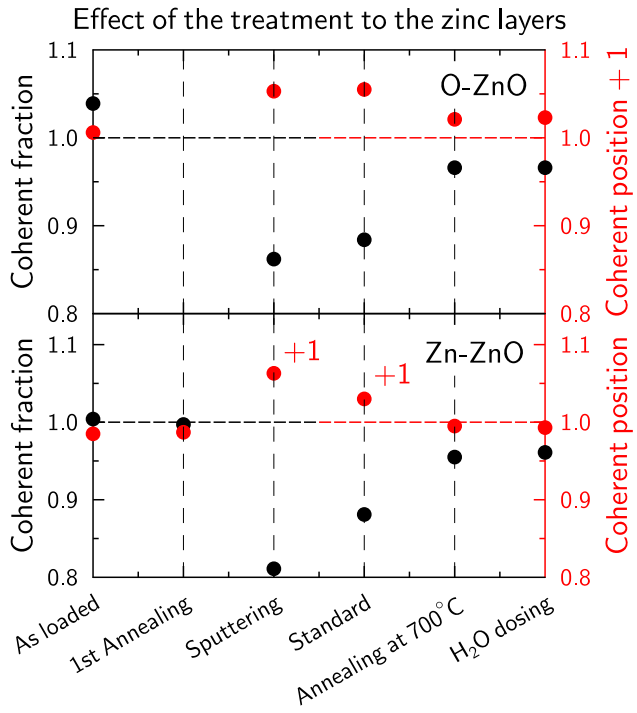

Figure 8.14: Evolution of the XSW parameters along the [00±2] direction corresponding to the topmost zinc layers (extracted from the Zn 3*s* core-level signal) with the different surface treatments. Note that, for the coherent position, 0 and 1 are equivalent. Deviations from the ideal values (horizontal lines) indicate, on the one hand, the presence of vertical disorder within the zinc atomic layers, and on the other, the existence of a layer displacement, either inward or outward. Thus, the sputtering produces an outward relaxation of the topmost layers and increases the disorder, whereas the annealing at 700°C heals the surface and brings the parameters back to the ideal-bulk values. For a more convenient depiction of the trend, some cases had 1 added to the P_H (cases labeled as +1). No measurements were performed for the first annealing of the O-ZnO.

temperature annealing are clearly shown.

As a concluding experiment for this section, we studied how the sputtering time affects the crystal structure. Different substrates were treated with increasing sputtering time (steps of 5 min). The results, presented in Fig. [8.15] for the zinc layers, clearly show that increasing the sputtering time reduces the vertical ordering and increases the average position of the atomic layers, which can be understood as an induced outward relaxation. The effect for the oxygen layers is qualitatively the same.

8.2.2.4. Comment on the coherent fractions

The coherent fractions are related to the distribution of positions along z, for a given species, within an XSW period. Therefore, values well above 1 are physically impossible and indicate that something is not correct. In some cases, the values are only slightly above 1, which can be attributed to the fitting routine. However, the systematically higher coherent fractions observed for the bulk-oxygen atoms of the O-ZnO case cannot be related to the fitting since they are only obtained for this particular case. Besides, this issue is most prominent when the crystal ordering is very good and less pronounced when disorder is introduced. Also, the fact that the coherent positions are unaffected and hold physical meaning (it suffices to compare them to the values obtained from XRD data) hints at a more physical, crystal-related origin. Comparing the different photoelectron yields in Fig. [8.11], one observes a clear amplitude increase of the photoelectron yield curve but not a change of the shape. This means that, around the Bragg condition, the photoelectron yield is greatly increased. The fact that this is only happening for a very specific case also excludes any experimental issues (e.g. some problems with the electron analyzer). A plausible explanation is the occurrence of photoelectron diffraction (PhD), i.e.

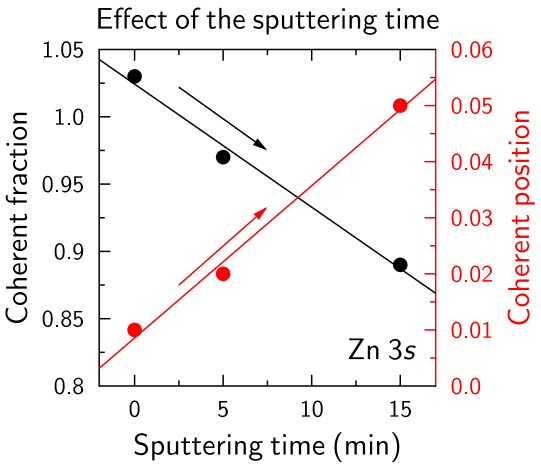

Figure 8.15: Evolution of the XSW parameters with the sputtering time obtained from the Zn 3*s* signal. The trend is clear: the longer the sputtering time the lower the crystal ordering and the higher the average zinc layer position. The displacement can be regarded as an induced outward relaxation. The other sputtering parameters were kept the same as in the **Standard Treatment** (Sec. [8.1]).

the constructive interference of the photoemitted electrons along certain directions, which has been reported to be the reason for some abnormal intensities measured in XPS [469]. Several PhD studies on the ZnO surfaces indicate intrinsic differences between the O- and Zn-ZnO angular-dependent intensity profile of the O 1*s* core-level signal [470–472], which would explain the dependence on the crystal quality and orientation. At this stage, however, this is just an hypothesis and further investigation is required. In order to provide more realistic values, one can take as a reference the coherent fractions of the zinc atoms as well as the difference between the values of the bulk oxygens and the zinc atoms for the Zn-ZnO case. Thus, one obtains that the values are ∼15% off. Nonetheless, a fair approximation would be just to consider that the coherent fractions are very similar to those of the zinc atoms. In any case, this particular issue does not compromise the phenomena and trends detailed in this chapter.

8.3. Discussion

In the following, the results presented above are discussed and the relevant findings for the subsequent interpretation of the ZnO-molecule interface are highlighted.

8.3.1. Influence of the termination on the bare surface properties

Let us start with the effect of the polarity on the structural, chemical and electronic properties of the surface, since they are the most relevant for the interface with COMs. The first particularity is the BE difference of the surface species with respect to the bulk. This indicates that the environment is different in both cases. Indeed, core-level spectra calculated for different surface structures render quantitatively different O 1*s* line shapes and BE differences between the bulk and the surface components [461]. Comparing our measured values (1.9 eV for the O-ZnO and 1.4 eV for the Zn-ZnO) and the peak profile to those from the calculations, for the O-ZnO, the best agreement corresponds to a bulk-like topmost oxygen layer with a (2×1)-H overlayer [461] and, for the Zn-ZnO, a bulk-like topmost layer with a (2×1)-OH overlayer [461]. This is supported by LEED (Fig. [8.3]) that shows a the 6-fold diffraction pattern, typical for unreconstructed surfaces.

A common assumption is that the stabilization of the polar surfaces is the balance between atomic rearrangements in the surface and the adsorption of foreign species (see Sec. [4.2.2.1]). From the results presented here, it seems evident that the adsorption of hydrogen and/or OH groups is the preferred mechanism for our conditions and preparation. From the XSW results, the surface-oxygen atoms of the clean O-ZnO are clearly at bulk-like positions, as demonstrated by the equal parameters obtained for the bulk and the surface species. Actually, just by considering the similar modulation of the photoelectron yield in Figs. [8.5] and [8.11] one can suspect a similar position. For the high-temperature annealed samples, which show an almost ideal crystal structure, it becomes clear that surface-oxygen atoms are at bulk-like positions. Interestingly, the XSW results for the Zn-ZnO surface show that the adsorbed species, most likely OH groups, are located below a bulk-like position (∼1.7 Å above the zinc topmost layer).

Although we cannot obtain direct information about the in-plane structure of the surface species, the higher coherent fractions obtained for the O-ZnO-surface component may be indicative of a more homogeneous arrangement compared to the Zn-terminated case. The clean Zn-ZnO surface is known to have triangular pits [294] that diffuse upon water dosing [303]. In this context, the lower coherent fractions could be explained by the presence of surface species on the flat terraces as well as at step edges of the triangular pits stemming from the adsorption of residual OH groups and/or water molecules that readily dissociate upon adsorption [473] (or hydrogen from the bulk that migrates to the surface [310]). In this case, time and/or water dosing may be important for the homogeneity of the surface. Vacancies created upon annealing may also originate favorable sites for the adsorbed species [474], which, as deduced from Fig. [8.4], are more abundant in Zn-ZnO.

As a final remark for the polarity-dependent stability of the surface [475], the unreconstructed surface observed for the as-loaded O-ZnO, as opposed to the (1×1)+$(\sqrt{3} \times \sqrt{3})R30°$ reconstructed Zn-ZnO, indicates that the stabilization of the former can be achieved solely by adsorption of foreign species, without requiring in-plane rearrangement.

8.3.2. Influence of the annealing and the sputtering to the surface

The sputtering is the main responsible for the surface cleanliness. It effectively removes the adsorbed contaminants, as shown in XPS (Figs. [8.11] and [8.12]) but, at the same time, it also damages the crystal structure of the first layers. As a rough approximation, Ar^+ ions with a kinetic energy of 100 eV (5 times lower than in our case) penetrate ∼20 Å into ZnO [476], which correspond to ∼8 ZnO bilayers[6]. Hypothetically, if one assumes a linear increase of the penetration depth with energy, an upper limit of 100 Å (∼38 ZnO bilayers) is reached for the energies used here.

Although the XSW field is generated deeper in the bulk[7] and is thus unaffected by the disorder, the collected photoelectrons entirely stem from the sputtered layers. Indeed, as shown in Appendix [F], 18 bilayers is the highest distance that electrons are able to travel to effectively escape the surface. This situation, as exemplified in the sketch of Fig. [8.6], allows one to identify variations of the atomic layers, along the [00±2] direction, with

[6] A ZnO bilayer comprises half of the unit cell along c, i.e. a zinc and oxygen paired atomic planes that correspond to 2.60 Å

[7] Calculations of the penetration of X-rays under Bragg reflection at 2.385 keV render a penetration of ∼3000 Å, which corresponds to roughly 600 ZnO unit cells.

respect to the deep bulk (undistorted values). Thus, our XSW results identify an increase in the average position of the atomic layers, both oxygen and zinc, upon sputtering. In addition, this upward displacement increases with the sputtering time (Fig. [8.15]). The upward displacement with respect to the deep-bulk positions comes along with an increase of the disorder as evidenced by a decrease of the coherent fractions.

Interestingly, annealing the sample produces the opposite trend, thus reversing the damage of the sputtering. Annealing at 420°C goes in this direction, but the temperature is too low to completely reverse it. Going to 700°C does markedly impact the XSW parameters, which almost restore the as-loaded values. Time seems to play a role as well, with annealing at 700°C for 1 h apparently being more effective than just 30 min (not shown).

These results may well explain why contradictory values for surface relaxations exist (see Sec. [4.2.2.1]). As we see, depending on the surface treatment, the amount and even the direction of the relaxation may change. Considering the values of the as-loaded samples for the O-ZnO, the bulk-oxygen atoms are contracted 0.05 Å from the ideal/deep-bulk position, whereas the zinc layer is 0.03 Å above the ideal value. Although this is very close to the precision of the technique, the results indicate the absence of a significant surface relaxation [313,316]. For comparison, the studies that have clearly measured a downward relaxation give contractions between the 16% [330] and 25% [329] with respect to the bulk spacing, clearly above the numbers reported here. For the Zn-ZnO, the situation is the same, i.e. the bulk-oxygen atoms are at bulk positions and the zinc layers 0.03 Å below. The bulk-like arrangement has been supported by other studies [309, 313, 314], although an outward relaxation of 7%, well above our values, has also been reported [315].

Since the XSW measurements shown here were obtained operating the electron analyzer in transmission mode, i.e. the electrons entering the analyzer were collected regardless of the incoming direction (see Sec. [3.3.2.3]), we are probing ∼18 ZnO bilayers (see Appendix [F]). Thus, the results are an average of those. One could argue that the reported values may well not be homogeneous for the different probed depths. Indeed, there are slight variations depending on the depth. Nonetheless, the coherent positions vary ±0.03 at most, which equals to ±0.08 Å (±0.03% of the [00±2] lattice spacing), well below the values reported for other studies. Therefore, we can safely conclude that the topmost layers of the as-loaded samples are bulk-like.

XPS measurements (not shown) at the Ar $2s$ core-level signal ($E_B = 326.3$ eV) indicate the presence of a significant amount of Ar embedded into the crystal. The XSW analysis (Fig. [8.16]) renders coherent positions quite close to the oxygen values. The low coherent fraction, however, does not support an exact ion substitution within the ZnO unit cell. It is thus reasonable to attribute the layer disorder to the argon implantation. Annealing at a high-enough temperature will remove the embedded argon ions and provide the thermal energy needed for the substrate atoms to recover the wurtzite positions.

Finally, the annealing also removes the surface species, which readily readsorb when the heating is turned off. This rapid recovery may well be attributed to residual hydrogen and OH present in the chamber. Interestingly, for in-situ cleaved ZnO crystals, the surface component is also visible [310], which the authors attribute to hydrogen impurities migrating from the bulk to the surface. Hydrogen interstitials and impurities are quite common in ZnO and have been discussed to be responsible for some of the optical properties of the material and even the intrinsic n-type behavior [478]. With our results, it

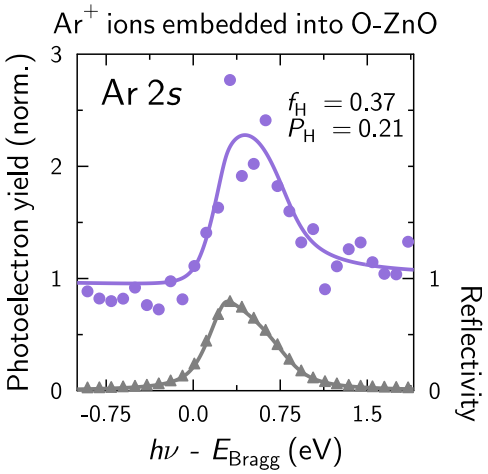

Figure 8.16: XSW measurements along the [00–2] direction for the Ar $2s$ core-level signal of the argon ions embedded in the O-ZnO substrate upon sputtering. The relatively low coherent fractions suggest a rather random distribution around oxygen-like sites, according to the coherent positions. As discussed in Ref. [477], it is unclear whether the zinc or the oxygen atoms are those most efficiently removed with the sputtering.

cannot be concluded which is the real origin, or at least, which is the largest contribution to the oxygen surface component. However, as discussed next, dosing water impacts the presence of surface species, thus hinting at a prominent external origin.

8.3.3. Influence of a water overlayer

In line with other reports [319, 321], XPS measurements rule out the adsorption of water molecules at RT. The measurements at angles that maximize the surface sensitivity (Fig. [8.9]) clearly discard the presence of core-level features related to H_2O molecules. Interestingly, the recovery of the surface component mentioned above seems to speed up in the presence of a water partial pressure in the chamber. But, at a certain point, dosing more water does not seem to produce further changes. This appears in line with a dissociative adsorption[8] of the water molecule [319, 321, 480] that goes on as long as the favorable adsorption sites on the surface are not occupied. Once the favorable sites are covered, the adsorption of water, either dissociative or molecular, stops. Therefore, from our XPS study at RT, the dosing of water only seems to saturate the surface component of the XP spectrum without further adsorption of molecular water.

The effect of water on the ZnO surfaces is still under debate. Early studies showed that dosing water on the O-ZnO surface favored the presence of the (1×1) unreconstructed surface [319, 321], which becomes completely covered with hydrogen. The fully hydrogenated surface seems to be rather inert and would hinder the adsorption of more water [319]. Later studies have shown that a half covered surface, H-(2×1), is energetically more favorable at RT [480]. In any case, the presence of vacancies seems to favor the dissociation behavior [473]. For Zn-ZnO, Önsten et al. studied the effect of water with STM and found that, with increasing dosage, the typical triangular islands and pits blur until completely vanishing. Furthermore, their XPS measurements showed how the O $1s$ signal grows a shoulder at the higher BE end of the bulk contribution, which was assigned

[8] Water dissociation on oxide surfaces requires a strong bonding between the water oxygen and a cation from the surface, as well as a short distance between the cation and anion sites of the substrate, which facilitates the bonding of hydrogen to the surface that will subsequently weaken the water O-H bond [479].

to OH groups [303]. The authors argue that the oxygen anions exposed at the edges of the islands contribute to the dissociation of water and the formation of OH on the surface that help to blur the triangular islands [303]. Ye et al. [481] studied this issue theoretically and found that for a monolayer coverage the adsorption is molecular, whereas for a critical coverage of 0.25 ML the adsorption happened to be dissociative. In between, molecular adsorption is theoretically plausible, however it depends much on the chemical conditions of the surface [481]. Most recently, a theoretical study found that oxygen adatoms on the Zn-ZnO surface, together with the presence of step edges, also trigger the dissociative behavior of water [482].

At LT, a clear multilayer contribution is only seen for the Zn-ZnO, whereas the O-ZnO only presents an extended shoulder. As discussed in Ref. [319], for the O-ZnO surface, the adsorption of a monolayer (at a substrate temperature of 160 K), a bilayer (135 K) and a multilayer (125 K) occurs at different temperatures, which may explain why the spectrum obtained in our case does not clearly show a multilayer contribution.

8.4. Conclusions

The data presented here yields a precise characterization of the polar surfaces of ZnO. Although a full discussion, involving theoretical input is not yet available, some conclusions can be readily obtained, namely, the adsorption distance of the surface species, the occurrence of surface relaxation and its direction, the surface disorder and reconstructions, as well as the VB fingerprint of each termination. Eventually, we will be able to describe, at the atomic scale, the surface and its evolution with varying preparation conditions. In the context of the ZnO-organic interface, however, the following conclusions can be drawn.

The most important finding is the adsorption position, along the [00±2] direction, of the surface species for both terminations. For the O-ZnO, the results clearly denote bulk-like surface, with the topmost oxygen layer at bulk-like positions and covered, most likely, by half a monolayer of hydrogen atoms [461]. If the hydrogen atoms are removed (with annealing at 700°C), the O 1*s* core-level spectrum still shows a small contribution besides the bulk signal, which is tentatively attributed to surface defects. Such a contribution will be masked by the readsorption of the surface species. The Zn-ZnO surface shows a bulk-like zinc top layer with OH groups adsorbed. The coverage depends on whether water is dosed or whether, upon annealing, enough time is left for the residual gases to readsorb. In any case, the surface species adsorb at ∼1.7 Å with respect to the zinc layer.

We have seen that the atomic ordering within the topmost layer is excellent thanks to the furnace annealing, but it decreases with the sputtering time. Interestingly, annealing at 700°C for one hour reverses the damage and disorder caused by the ion bombardment. Consequently, it is highly desirable to change, in the future, the current **Standard Treatment**. In particular, the last annealing should be performed at 700°C for 1 h, being 650°C probably more optimum to avoid possible crystal degradation [483]. This way, a clean as well as bulk-like structure at the surface can coexist. Also, it would be recommendable to dose a certain amount of water, or at least wait a few hours after the annealing, to make sure that the surface is homogeneously covered.

The results indicate that O-ZnO is more inert and homogeneous than Zn-ZnO. Thus, the first one is desirable for structural studies of the interface, i.e. as a substrate for XSW

studies, whereas the Zn-terminated seems to be more convenient for cases where electronic processes are favored. This will become even more clear in the following chapter when the response of the surface to the adsorption of a COM is investigated.

9. Perylene derivatives adsorbed on the polar surfaces of ZnO

In the last chapter of the results, we discuss the adsorption of different perylene derivatives on the polar surfaces of ZnO. We mainly focus on the HR-XPS and XSW measurements, although additional UPS and atomic force microscopy (AFM) experiments are included as well. In order to understand some of the findings regarding the COM-ZnO interface presented next, the characterization of the bare surfaces discussed in the previous chapter will become important. To the best of our knowledge, the XSW results presented here are the first involving large aromatic molecules adsorbed on a semiconductor surface.

9.1. Context

Owing to the relevant technological applications of hybrid inorganic-organic systems [484], their interface is attracting increasing interest. In particular, the need for a better understanding and control of the electronic processes happening when both materials are brought into contact, together with the necessary experimental validation of the theoretical calculations aiming at its modeling [485, 486], has made evident that an atomistic description of the interface between the π-conjugated materials and inorganic semiconductors is required. In recent years, surface-science techniques that have been successfully applied to study metal-organic interfaces have started to elucidate their electronic and chemical processes. However, the precise adsorption geometries and intramolecular distortions have not been experimentally accessed so far. As an illustrative example of the importance of obtaining such information, Schlesinger et al. [487] studied the ELA between the strong molecular acceptor F4TCNQ and the polar surfaces of ZnO. Without the adsorption geometry that accounts for possible adsorption-induced molecular distortions, the authors could just reproduce the observed trends, with a simple electrostatic model, but not the measured changes of the work function [487].

ZnO (together with TiO_2) has become a popular material to be combined with organic semiconductor materials. There are relevant examples of the combination of nanostructured ZnO with organic molecules that further exploit the nanoscale properties of the inorganic semiconductor [119, 281, 488, 489]. As our case study, however, we are going to focus on the interaction between the COMs and ZnO surfaces. In this context, surface-science studies performed on small molecules as well polymers are available, which have mainly focused on the electronic properties of these systems [35]. In general, a weak interaction with the bare ZnO surface has been reported [123, 292], although it depends on the substrate doping [490, 491], with some notable cases of dissociative adsorption [123, 492] and chemical-bond formation [493]. For low dopant concentrations, the coexistence of neutral and charged molecules has been observed, without signs of chemical interactions

or strong electronic coupling [492]. For weakly interacting systems, changes in the band bending upon adsorption have been reported as well [292, 487, 492]. For highly-doped conductive substrates, however, the presence of CT [377, 491], hybridization [491, 494] as well as bond formation [495] has been discussed too.

There is the agreement in the literature that the presence of vacancies at the (sub)surface affects the CT between ZnO and a molecular overlayer [277, 496], which also applies to deposited metals [497]. Indeed, this has been theoretically postulated [277, 377, 491] and experimentally verified with the adsorption of small molecules [498] as well as large adsorbates [277, 377, 468, 491]. Besides the presence of defects/vacancies, step edges may also be involved [498]. Regarding the polarity, there is also some consensus that the Zn-terminated surface is more reactive than the O-ZnO one [426, 468].

Finally, regarding the adsorption arrangement, a rather planar geometry has been extensively reported [377, 491, 493] although with a relative degree of distortion and/or tilting. Interestingly, cases of standing-up geometries, even at the first layer, have been reported [493, 499], although prone to change depending on the coverage [493] and the annealing treatment [499].

9.2. Results

In order to make direct comparisons easier, the results have been arranged as follows. First, different perylene derivatives, namely, perylene, PTCDA and PTCDI (see Sec. [4.1]) deposited on the **standard-treated**[1] O-ZnO surface are considered. This case highlights the role of the functional groups in the interaction with the surface. Secondly, to assess the impact of the surface polarity, PTCDI, used as the reference molecule, is deposited on a **standard-treated** Zn-ZnO surface. Finally, PTCDI is also deposited on several surfaces that underwent additional treatments, besides the standard, to further study the role of the surface on the different interaction channels between adsorbate and substrate.

9.2.1. Perylene derivatives adsorbed on the standard-treated O-ZnO surface

Perylene and its derivatives, PTCDA and PTCDI, render a smart selection to study how, in first place, the addition of acceptor functional groups affects the interface between the COM and ZnO and secondly, how small chemical modifications, in this case substituting an anhydride group for an imide one, impact the same interface properties. PTCDA has become a prototypical COM for the study of metal-organic interfaces whereas, as we have seen in Chap. [6], PTCDI holds similar chemical, geometrical and electronic properties as PTCDA although with a more versatile in-plane arrangement.

9.2.1.1. High-resolution XPS of (sub)monolayer coverages

The HR-XP spectra ($h\nu = 700\,\mathrm{eV}$) presented in Fig. [9.1] show the carbon C $1s$ and nitrogen N $1s$ (only present in PTCDI) core-level signals for the perylene derivatives deposited on the O-ZnO surface. For comparison, PTCDI deposited on the Zn-ZnO **standard-treated** surface is also included, although it will be discussed separately in Sec. [9.2.2].

[1] The treatment is described in Sec. [8.1].

Owing to the strong contributions of the bulk- and surface-ZnO components to the oxygen O 1*s* core-level signal, it is not straightforward to identify the molecular contribution to the spectrum, therefore it will be considered in Sec. [9.2.1.3] apart from the others.

Starting with perylene, the carbon spectrum presents a single prominent peak plus several much smaller features associated to shake-up satellites. Carbon atoms bound only to other carbon atoms (C-C) and carbon atoms bound also to hydrogen (C-H) contribute, with a proportion of 8:12, to the slightly asymmetric peak shape. The assignment of the components is done considering the aforementioned proportion. Thus, to account for the slight peak asymmetry, the C-H peak appears at the high BE side, with the smaller C-C contribution located at the low BE side. The spectrum shows no clear indication of substrate influence, in line with previous results [123]. We note that the peak shape is very similar to those measured for perylene adsorbed on Au(111) and Cu(111) (see Chap. [5]).

PTCDA, compared to perylene, has four hydrogen atoms removed to accommodate the four carboxylic groups, which are seen as a prominent feature at the high BE side of the C 1*s* spectrum. Interestingly, the perylene-core contribution does not seem affected by the functionalization as deduced from the same line shape and similar line width. However, the stoichiometry of the carbon atoms has changed compared to perylene: now there are four C-H atoms less and there are four C=O and 4 C-C-O atoms instead with ratio of C-C:C-H:C-C-O:C=O equal to 8:8:4:4. Considering that the line shape has not changed and that the C=O are clearly separated from the core core-level feature, the C-C-O feature has to be located very close in energy to the C-H contribution, otherwise the line shape is not reproduced. This situation is analogous to that discussed in Ref. [161] for a PTCDA multilayer deposited on Ag(111) and also for PTCDA on highly-conductive ZnO [491]. We note however, that our assignment of C-H and C-C is inverted compared to Ref. [491]. As we have stated in previous chapters, the peak assignment is not free from controversy, therefore we prioritize a consistent fit throughout the different experiments. In our case, we have the measurements of the unsubstituted perylene that can be used to highlight the specific core-level changes upon functionalization. Regarding the substrate influence, the unchanged line profile and the ∼3.5 eV difference between the core and the functional-group features, in line with the multilayer values (see Sec. [6.2.1]), indicates a rather weak interaction between the molecule and the substrate. Noteworthy, the chemical information of the oxygen atoms of PTCDA discussed in Sec. [9.2.1.3] indicates that a rather localized interaction may exist through the oxygen atoms.

For PTCDI, the carbon core-level signal is similar to that of PTCDA, although with some remarkable differences. First, the feature associated with the functional group appears closer to the core one (∼2.7 eV difference), similarly to that reported in Ref. [377]. Secondly, the feature in black, also highlighted with an arrow, appears more intense than for PTCDA and perylene. Finally, we note the low BE tail of the perylene-core feature shows a component that cannot be assigned, which could stem from spurious carbon or some local discrepancies with the fit. Turning to the nitrogen N 1*s* core-level spectrum, two prominent features separated by ∼1.6 eV are revealed. Since the two nitrogen atoms of PTCDI are chemically equivalent, the presence of two distinguishable components have an origin external to the molecule. According to the literature, such double peaks are associated to the charging of some of the species [249, 254]. In this case, the loss of the hydrogen due to charge transfer (CT) could also induce this shift [127, 172]. Similarly to

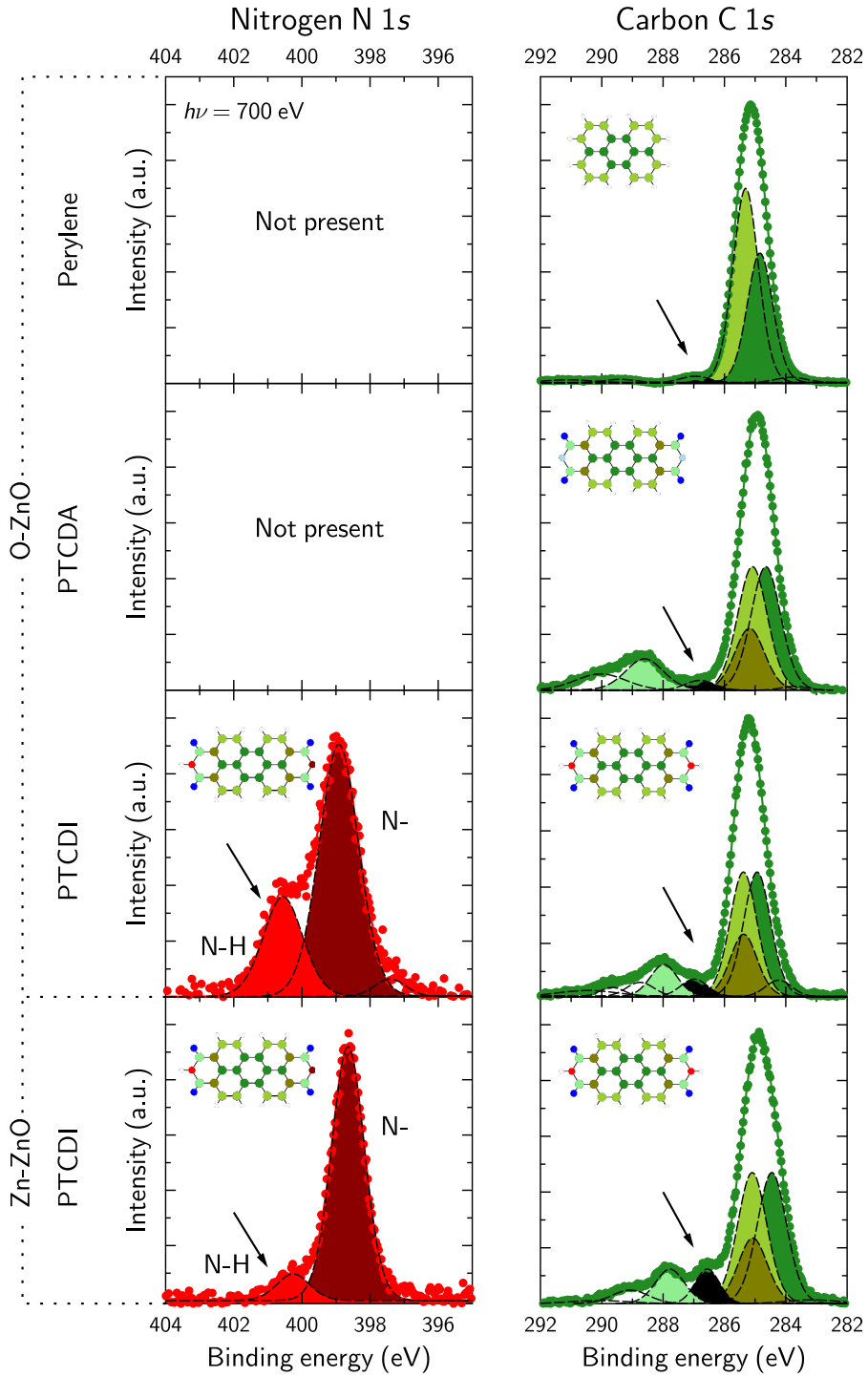

Figure 9.1.: HR-XPS ($h\nu = 700\,\text{eV}$) for perylene, PTCDA and PTCDI adsorbed on the **standard-treated** O-ZnO surface. For comparison PTCDI adsorbed on the equally treated Zn-ZnO is included. See the inset molecule for the color code of the different components. We note the black component of the C 1*s* spectra, which changes in intensity, depending on the molecule and also on the substrate termination. The fitting model was done similarly to those explained in Sec. [6.2.2].

the case of PTCDI adsorbed on TiO_2 [127], our collaborators performed calculations (not shown) for the charged vs. the deprotonated species and resolved that the deprotonation of nitrogen explains better the energy shift. Hence, the high BE peak is associated to neutral protonated species (N-H), whereas the low BE peak is related to the deprotonated nitrogen species (N-). Noteworthy, this effect also leaves a fingerprint in the carbon spectra. Indeed, the black feature is attributed to the carbon atoms of the functional groups that have received the additional charge of the substrate. This has been also reported for other molecules and oxide surfaces and is constrained to the molecules at the interface [127,377,491]. From a pure core-level perspective, one may think that the CT received from the substrate only affects the functional groups since the perylene-core feature appears unaffected.

As a final remark, we note that, in our case, the BE position of the carbon spectra for PTCDA and PTCDI, compared to those of Ref. [491] and [377], respectively, is at much lower values. We attribute this discrepancy to the different synthesis of ZnO, doping concentration and surface preparation employed.

9.2.1.2. XSW results: adsorption heights and molecular distortion

Based on the core-level fitting models shown in the previous section, the XSW data for perylene, PTCDA and PTCDI was evaluated. The results obtained are presented in Fig. [9.2]. The different components within the core could not be decoupled, therefore only the average perylene core distance is reported. Remarkably, the positions of the functional carbon atoms as well as the inequivalent nitrogen species could be analyzed separately. Before starting with the discussion of the data, we remind the reader that the coherent positions are obtained with respect to the virtual bulk-like position of the topmost zinc layer (see Fig. [8.6]). As discussed in Sec. [8.2.1], the distance between maxima (and minima) of the XSW field is the same as the lattice spacing of the *bulk* ZnO along the [00±2] direction. Therefore, regardless of any relaxation of the top layers, the XSW output parameters are referenced to the same layer. Of course, possible changes in the lattice spacing of the topmost layers will have to be considered to obtain the actual adsorption distance with respect to the surface. Both the measured and the corrected distance to the topmost layer are summarized in Tab. [9.1]. We note that, although the obtained coherent positions are referred to a bulk-like layer, independent of the surface changes, the molecules and their coherent fractions and positions are influenced by what is happening at the surface (morphology, ordering, presence of OH/H or not). As we will see in Sec. [9.2.3], modifying the surface conditions renders different output parameters in the XSW. The adsorption distances and intramolecular distortions of the different perylene derivatives deposited on the **standard-treated** O-ZnO surface, referred to the surface topmost species, are shown in Fig. [9.3a].

Quite surprisingly, for the three cases, the perylene core renders (virtually) the same coherent positions[2], thus yielding equal adsorption distances with respect to the reference layer. This appears in stark contrast to the adsorption behavior of the three molecules on other substrates, where they show different adsorption distances (see discussion in Chaps. [5] and [6] or a visual summary in Fig. [10.1]). The real adsorption distance with

[2] Note also that the modulation of the photoelectron yield has the same shape too.

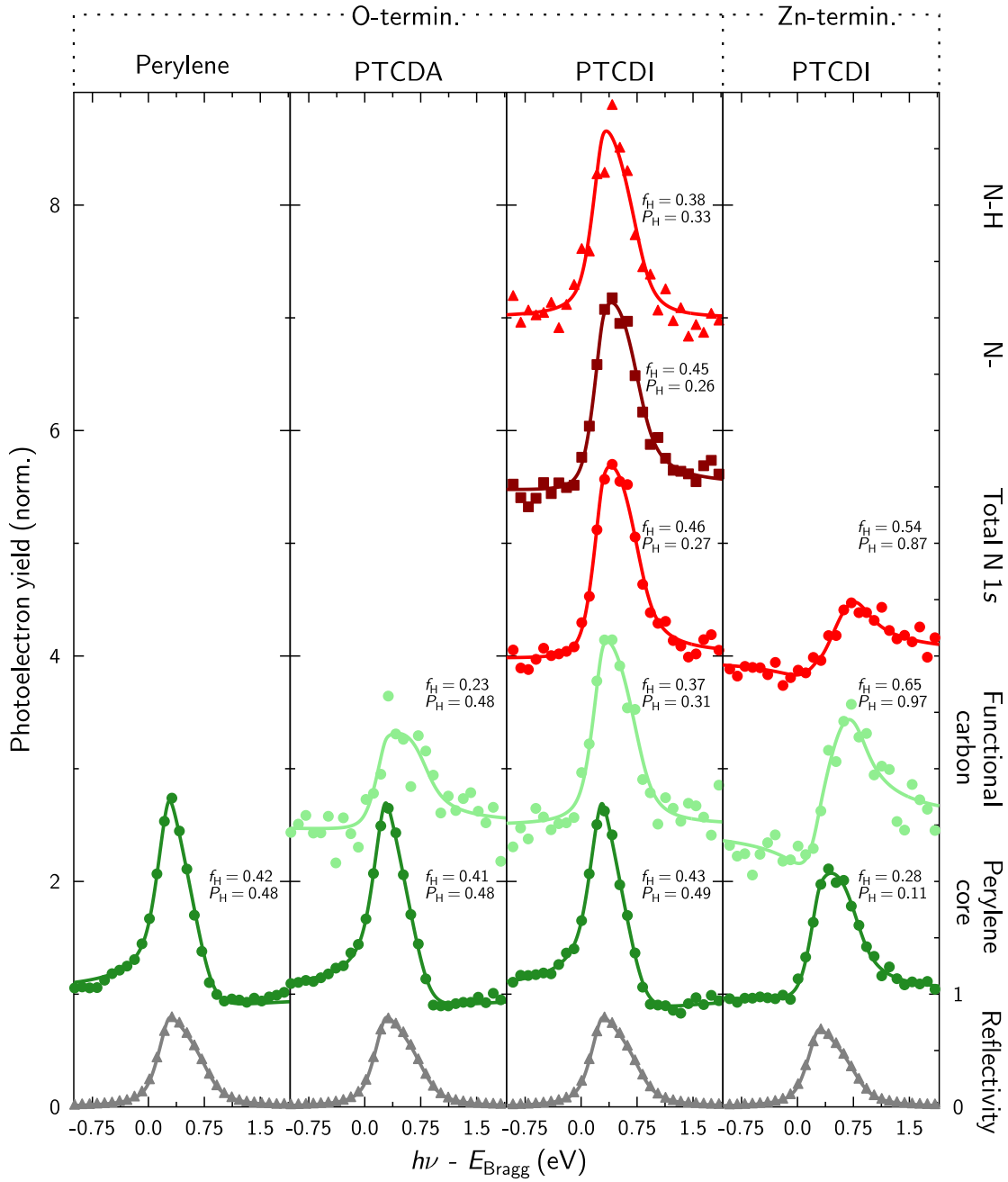

Figure 9.2.: XSW measurements along **H** = [00∓2] for the different perylene derivatives deposited on the **standard-treated** O-ZnO. For comparsion, PTCDI adsorbed on the equally treated Zn-ZnO surface is included. The evaluation of the photoelectron yield was carried out using a fitting model shown in Fig. [9.1]. We highlight the fact that the functional carbon as well as the inequivalent nitrogen species could be successfully decoupled and analyzed. The extracted adsorption distances are displayed in Fig. [9.3].

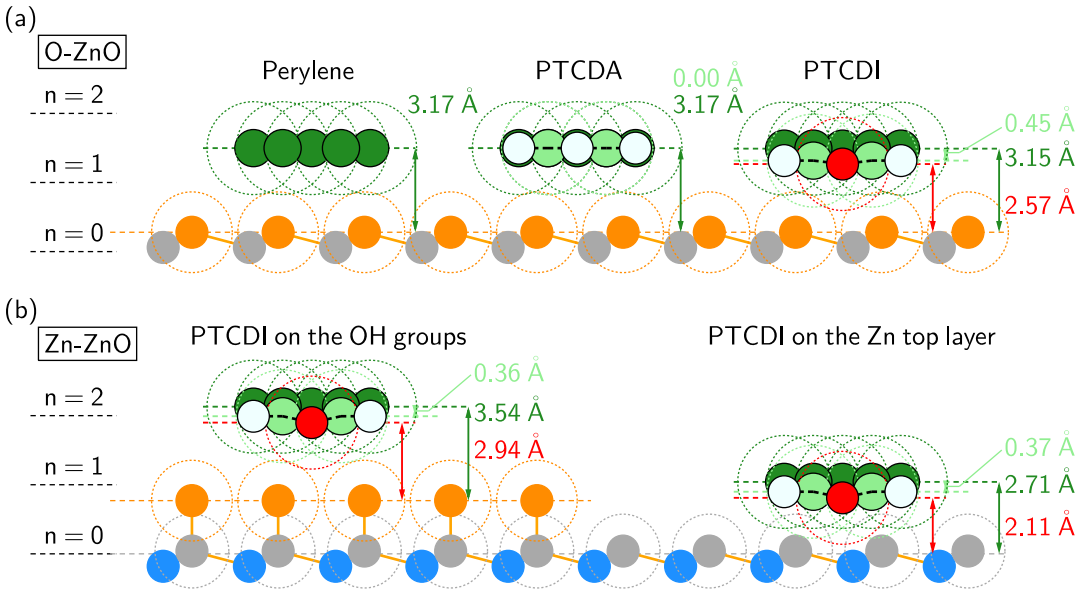

Figure 9.3.: Adsorption geometry corresponding to different perylene derivatives deposited on the **standard-treated** polar surfaces of ZnO. Note that the surface follows the color code introduced in Chap. [8]: in gray zinc, blue the bulk-oxygen and orange the surface-oxygen species. Hydrogen belonging to OH groups is not depicted. Color code for the molecules in the insets of Fig. [9.1]. The dashed circles represent the van-der-Waals radii. The information of the oxygen species could not be obtained (carboxylic species) or it is discussed separately (anhydride oxygens of PTCDA). Note that, for simplicity, only the average nitrogen adsorption distance is reported. (a) Adsorption distances for perylene, PTCDA and PTCDI on O-ZnO. (b) Adsorption distance for PTCDI adsorbed on Zn-ZnO with two possible configurations, adsorbing on top of the surface OH groups or directly onto the topmost zinc layer. Comparing the adsoprtion distances for both cases and the sum of vdW radii, it is likely that PTCDI adsorbs directly onto the zinc layer (see Sec. [9.2.2] for the discussion).

respect to the topmost layer obtained after accounting for the sputtering-induced outward relaxation turns out to be 0.04 Å shorter for PTCDI than for PTCDA and perylene. The coherent fractions are also very similar, indicating the same degree of ordering for the three cases.

For PTCDA, the carbon atoms of the functional groups render the same coherent position as the perylene core, hinting at a rather planar carbon structure. Nonetheless, as it will be shown in Sec. [9.2.1.3], the oxygen atoms do not seem to align with the core, but rather bend towards the surface. The lower coherent fractions of the functional carbon atoms may be in part due to the rather scattered photoelectron yield or it could also be that the position changes from molecule to molecule, with functional groups bending differently depending on the local surface morphology.

PTCDI appears as a more interesting case owing to the chemically inequivalent nitrogen atoms. The XSW analysis reveals that they also have different adsorption distances, being the deprotonated nitrogen (N-) closer to the surface than the N-H species. This is in line with the previous assumption that the substrate is the responsible for the deprotonation reaction of some of the imide groups. The preferential interaction of these with the substrate is further supported by the bending towards the surface of the functional carbon atoms. The different coherent fractions of PTCDI are very close to each other, indicating a rather homogeneous vertical ordering within the molecule. Interestingly, theoretical calculations of the adsorption of PTCDI on the $(10\bar{1}0)$ surface of ZnO show a slightly tilted

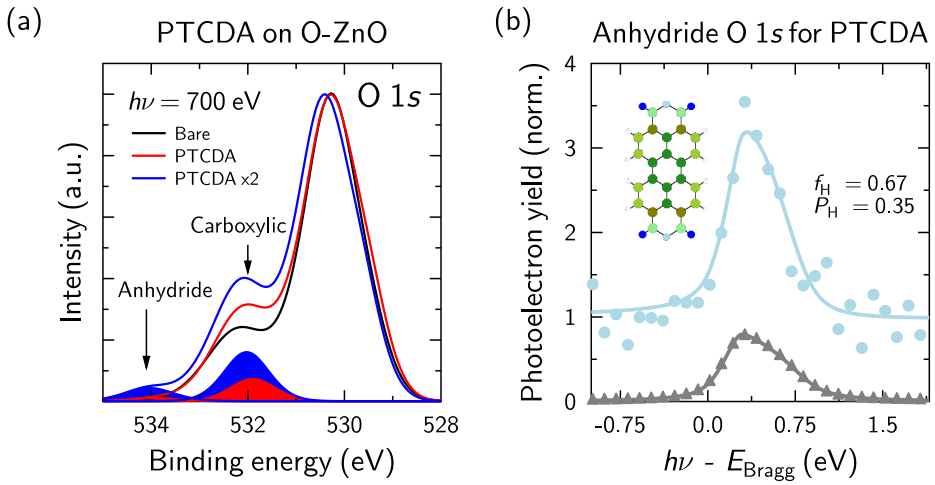

Figure 9.4.: Chemical and structural information corresponding to the carboxylic and anhydride oxygen species of PTCDA deposited on a **standard-treated** O-ZnO surface. (a) HR-XPS ($h\nu = 700\,\text{eV}$) scans for two different coverages (nominally 2 and 4 Å) of PTCDA. Two molecule contributions can be observed, one belonging to the four carboxylic atoms ($E_\text{B} \sim 532\,\text{eV}$) and another one for the two anhydride ($E_\text{B} \sim 534\,\text{eV}$) oxygen atoms. (b) XSW measurements along the **H** = [00–2] direction corresponding to the O 1*s* anhydride component with the related fitting parameters.

geometry, with one long molecular edge closer to the surface than the other and an overall downward bending of the functional groups. If this situation is also applicable to the O-ZnO surface, this may explain the rather low coherent fraction for a planar adsorption. We note that the same situation may apply to PTCDA and perylene as well.

9.2.1.3. Comment on the molecular-oxygens species

The photoelectrons stemming from the ZnO substrate outnumber those belonging to the molecular overlayer. Therefore, the contribution of the latter to the O 1*s* core-level spectrum is difficult to decouple. For the case of PTCDA, however, we were able to identify the spectral features related to the anhydride- as well as the carboxylic-oxygen atoms. Quite remarkably, the XSW measurements using the anhydride components also rendered good results. Fig. [9.4] includes the HR-XP spectra for two different PTCDA coverages (nominal coverages of 2 and 4 Å) together with the XSW analysis of the anhydride component for the highest coverage deposited (4 Å). The core-level features are 2 eV apart, which corresponds to the separation between the carboxylic and the anhydride oxygen signals reported for a PTCDA multilayer deposited on Ag(111) [152].

Regarding the XSW measurement, although the photoelectron yield is rather noisy, it renders a clear modulation. The results of the fit, however, have to be taken with caution. On the one hand, the equal coherent positions for the core and the functional carbons ($P_\text{H} = 0.48$) indicate that there is no strong bending of the functional group. On the other hand, the coherent position obtained for the anhydride oxygen ($P_\text{H} = 0.35$) indicates that these atoms are adsorbing ∼0.34 Å below the carbon structure. A reasonable way that could explain this apparent discrepancy, namely, the undistorted position of the C=O carbon atoms of the functional group with respect to the core and the significant bending of the anhydride-oxygen atoms towards the surface, is that the carboxylic-oxygen

atoms are bending upwards and thus pull up the C=O atoms counteracting the push-down of the anhydride species. Although the situation where carboxylic-oxygen atoms bend differently from the anhydride ones has been reported before [66, 258, 405], the fact that it is the anhydride-oxygen atoms those doing it downwards has not been found so far. Despite the remarkable fact of identifying and decoupling the molecular components from the substrate signal, there might still be some contribution from the ZnO species to the photoelectron yield of the anhydride-oxygen signal. Therefore, we advice not to take the XSW parameters as completely certain but rather as an indication of the possible bending of the oxygen atoms with respect to the carbon structure.

9.2.1.4. Coverage-dependent UPS

Having characterized the chemical properties as well as the vertical geometry of the different COM-ZnO interfaces, we turn our attention to the electronic properties. Although they are not the main focus of this work and therefore, we refrain from a deeper discussion, a qualitative interpretation of the data readily provides important information about the interface as well as the subsequent thin-film growth. The UPS measurements were performed by Dr. Jens Niederhausen at Humboldt University, Berlin, using a commercially available setup (Omicron), consisting of preparation chamber (base pressure $< 3 \cdot 10^{-9}$ mbar) separated from the analysis chamber (base pressure $< 10^{-10}$ mbar). UPS measurements were performed with He I radiation. Spectra were collected in normal emission and with 45° take-off angle with SPECS PHOIBOS 100 hemispherical energy analyzer. The UV light intensity was attenuated to minimize UV light-induced film degradation and sample charging. The AFM[3] measurements were performed by Thorsten Schultz at Humboldt University, Berlin.

Figure [9.5] summarizes the valence band (VB) characteristics of the different COM-O-ZnO interfaces. Starting with the survey scans (Fig. [9.5a]), the increasing coverage of perylene attenuates the substrate spectral features, but even for a nominal coverage of 100 Å (∼25 ML) they are still clearly visible. This is indicative of a strong island growth. The maximum deposition for PTCDA was ∼4 ML. At this coverage the substrate features are still visible. Within this coverage range it becomes speculative whether a wetting layer has been created already or not, therefore the growth mode remains inconclusive. Nonetheless, from optical measurements of PTCDA on a polycristalline ZnO surface, the formation of 3D clusters was reported, requiring the deposition of several monolayers to obtain a molecule-only signal [491]. In contrast, for ∼5 ML nominal monolayers of PTCDI, the substrate VB features disappear almost completely, hinting at a more homogeneous layer-by-layer growth. To support the assumption for the two extreme scenarios, AFM measurements of the thickest coverages of perylene and PTCDI on the O-ZnO surface are shown in Fig. [9.6], where it is clearly visible that perylene forms huge islands, as opposed to PTCDI, which covers the surface much more homogeneously. From our measurements we cannot resolve whether perylene may form a wetting layer.

The region close to the Fermi edge (Fig. [9.5b]) reveals the presence of the relaxed

[3] Atomic force microscopy is a scanning-probe technique that is used to obtain information about the surface morphology. Shortly, it consists of a nanostructured tip that oscillates over the surface. Depending on the attraction/repulsion with the surface, the oscillation will change, which is used to map the surface morphology.

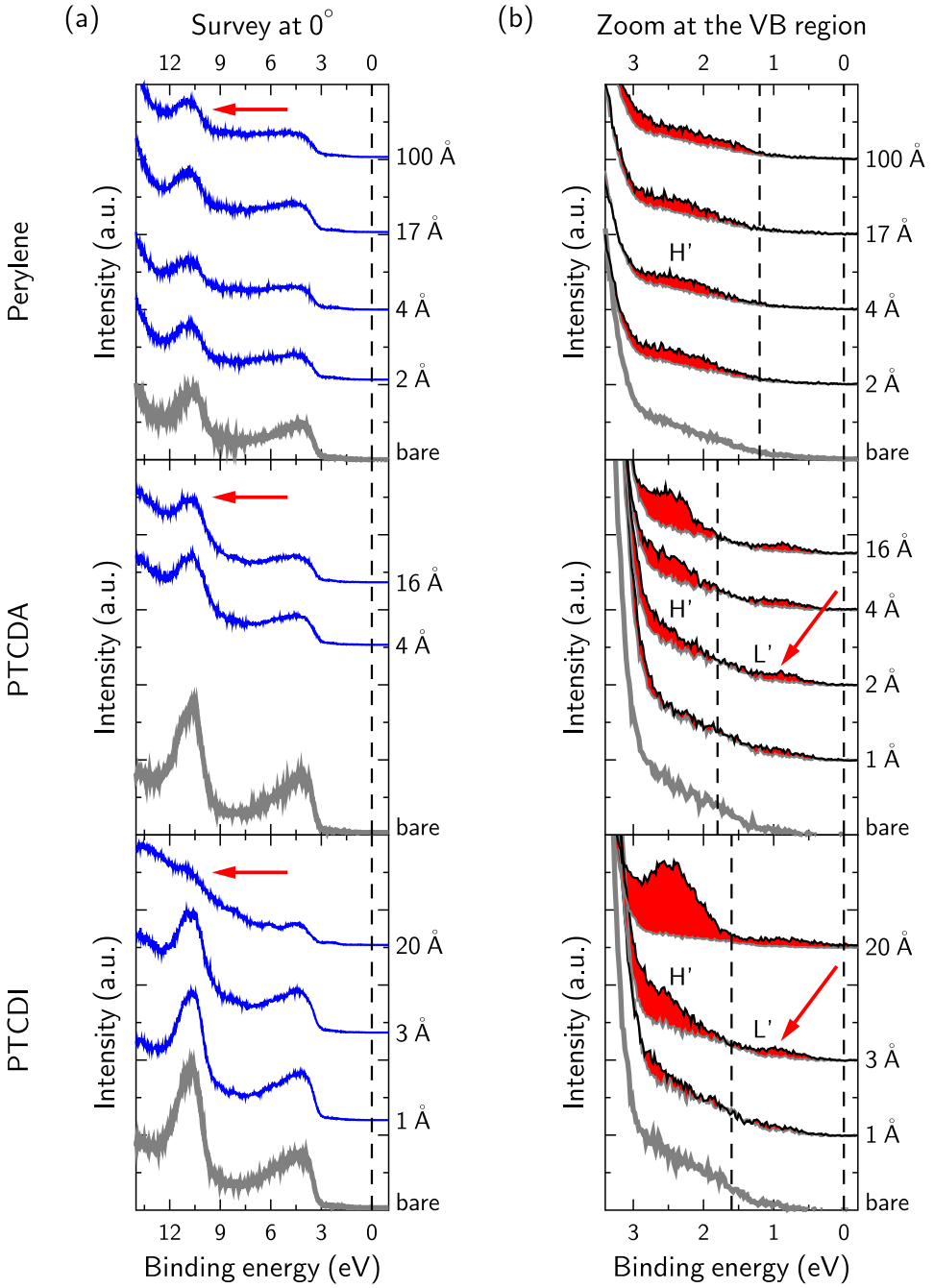

Figure 9.5.: UPS measurements performed for different coverages of perylene, PTCDA and PTCDI deposited on the **standard-treated** O-ZnO surface. (a) Survey scans of the VB where the intensity change of the substrate peaks upon molecular deposition can be used as an indication of the molecular growth. For instance, the complete disappearance of these upon PTCDI deposition of a thin film indicates that the molecules have, at least, several layers that uniformly cover the surface. In contrast, perylene forms islands since even at a nominal coverage of 100 Å the substrate features are still visible. (b) Zoom at the region close to the Fermi edge, where the frontier orbitals, namely the HOMO and the LUMO, may be observed. We highlight the presence of a partially-filled LUMO (L') for PTCDA and PTCDI, but not for perylene.

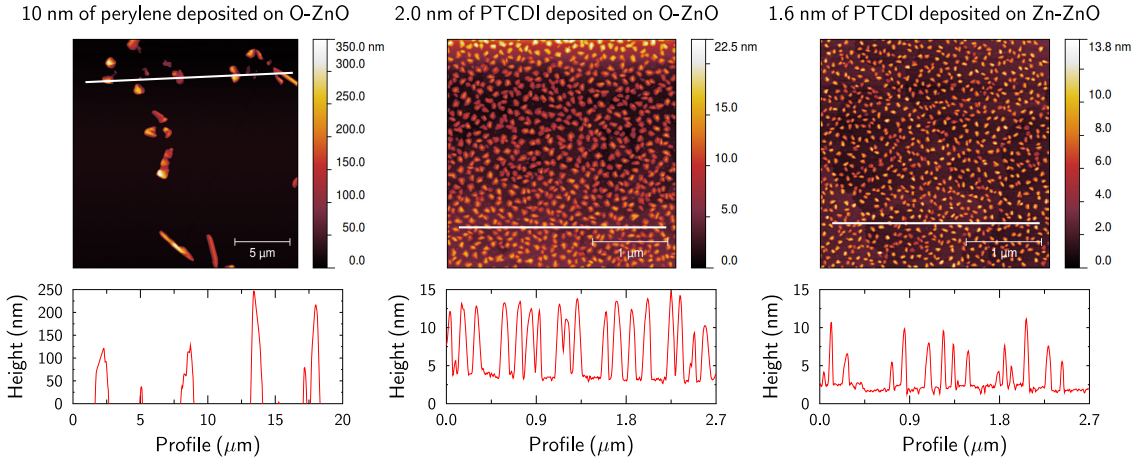

Figure 9.6.: AFM images for perylene adsorbed on O-ZnO (nominal coverage of 100 Å), PTCDI adsorbed on O-ZnO (nominal coverage of 20 Å) and Zn-ZnO (nominal coverage of 16 Å). This measurements, far from complete, highlight the strong island formation of perylene compared to the more homogeneous growth of PTCDI, which seems to grow similarly regardless of the surface termination.

HOMO (H') in all three cases. The most prominent intensity corresponds to PTCDI, which appears in line with a more homogeneously covered surface. In contrast, perylene shows a rather weak intensity, which could be explained by the fact that the molecules pile up in the big islands, hence mainly electrons from the top layers reach the analyzer. This seems to be the case, although less pronounced, for PTCDA. More interestingly, an additional feature in the PTCDA and PTCDI case appears close to the band gap, which is tentatively associated to the filling of the molecular LUMO (L'). The absence of similar features for perylene indicates that, similarly to the case of metals, the presence of functional groups facilitate the CT from the substrate.

9.2.1.5. Comment on the in-plane arrangement within the first monolayer

The same (sub)monolayers that were studied with HR-XPS and XSW were also characterized with LEED. Surprisingly, for all the cases, diffraction patterns related to the molecular overlayers were absent (measurements not included) and only the 6-fold diffraction patterns of unreconstructed ZnO could be observed. This would mean that the molecules lack a long-range in-plane ordering.

In another set of experiments, a PTCDI multilayer was deposited on a **standard-treated** O-ZnO substrate. The multilayer contribution was annealed at 240°C to leave only one full monolayer on the surface. No LEED patterns besides those for the unreconstructed surface could be observed (not included). The same procedure with the same results was performed with a DIP multilayer.

9.2.2. PTCDI adsorbed on the standard-treated Zn-ZnO surface

As the next step in our investigation, PTCDI was deposited on a **standard-treated** Zn-ZnO surface under the same conditions as those reported above. The HR-XPS measurements are included in Fig. [9.1]. There are several interesting differences compared

to the O-ZnO case. First, the carbon C 1*s* spectrum appears broader. This could happen, either because the molecules adsorb closer to the substrate [166], or because they occupy rather inhomogeneous adsorption cites [168], or because of both. Secondly, the black feature that is associated with CT to the functional group is much more intense, which goes hand in hand with the spectral changes in the nitrogen N 1*s* core-level. Indeed, the intensity ratio between the protonated nitrogen species (N-H) and the deprotonated ones (N-) is favored towards the latter, being the protonated contribution only a small shoulder. Hence, from a purely core-level perspective, it seems that the Zn-terminated surface favors CT.

Moving to the XSW results (Fig. [9.2]), at first glance, the shape of the photoeletron yield modulation readily indicates a different position within the XSW field. For this case, however, the adsorption position on the surface is not so evident. Owing to the surface termination, namely, with the bare zinc topmost layer or with hydroxyl (OH) species covering the surface, PTCDI may have two possible adsorption configurations (see Fig. [9.3b]). Before going into more detail, let us discuss first the relative position of the different chemical species within the molecule, i.e. the intramolecular distortions. Thus, the nitrogen atoms, being almost completely deprotonated, adsorb ∼0.6 Å below the perylene carbon core. Such a remarkable bending seems to pull the whole functional group towards the surface, as deduced from the lower coherent position of the C=O carbon with respect to the core (∼0.36 Å below). The distortion of the core is supported by the low coherent fraction of the perylene core compared to that of the functional group. This can be explained by considering that functional group anchor to the surface with the core bending in a strong bridge shape. This effect may be more pronounced than for the O-ZnO case.

Going back to the question of the actual adsorption location of PTCDI on the Zn-ZnO surface, as shown in Fig. [9.3b], depending on the ambiguity n when converting coherent positions to actual adsorption distances (see Eq. [3.10]), one obtains two sets of values that fit both the adsorption on top of the OH species as well as the adsorption directly on the Zn topmost layer. From a strictly geometrical perspective, both scenarios are possible. Nonetheless, the strong broadening of the C 1*s* core-level spectra and the amount of deprotonated nitrogen atoms, suggests a closer adsorption to the zinc layers. In any case, this will become more clear when the adsorption of PTCDI on Zn-ZnO is discussed under other surface preparation conditions (Sec. [9.2.3.3]).

Regarding the UPS measurements for this case (Fig. [9.7]), the situation is very similar to PTCDI adsorbing on O-ZnO. The final nominal coverage of ∼30 ML, provides additional support for some of the assumption made for the other polar termination. First the molecular features are properly assigned, namely, the relaxed HOMO (H'), the HOMO of the multilayer (away from the substrate influence) and, most importantly, the spectral features in the band gap region that are purely an interface phenomenon (L'). Fig. [9.6] also includes an AFM image of a similar coverage as that measured for the O-ZnO substrate. Thus, comparing both polar terminations, one can conclude that, at least for the coverages studied here, the surface polaritiy does not seem to affect the growth mode of PTCDI.

Finally, LEED measurements performed on the same coverages used in the HR-XPS and XSW measurements reveal no in-plane ordering, similarly to what was found for the O-ZnO surface. A possible explanation could be that the coverage is not enough to

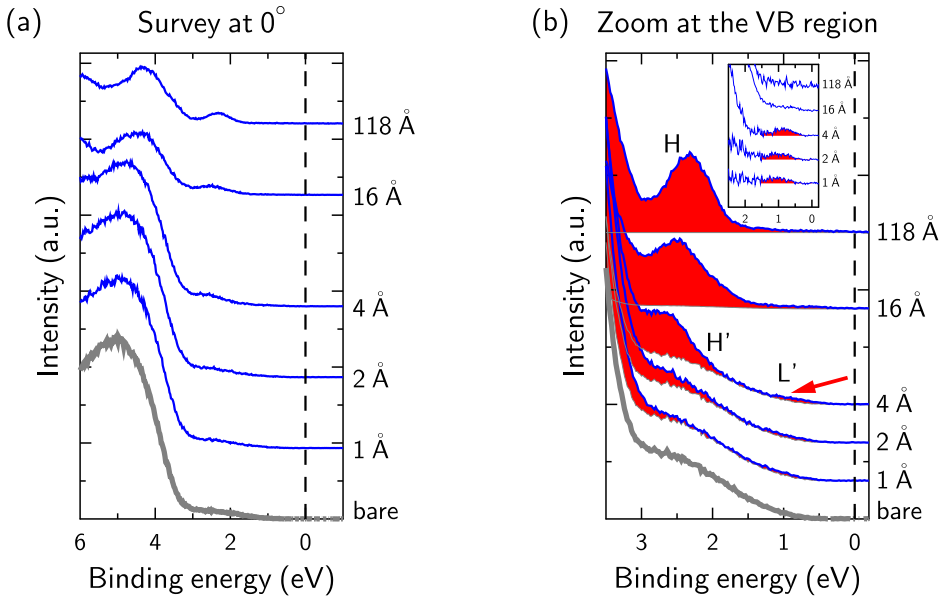

Figure 9.7.: UPS measurements performed for different coverages of PTCDI deposited on the **standard-treated** Zn-ZnO surface. (a) Survey of the VB. (b) Zoom at the region close to the Fermi edge, where the frontier orbitals, namely, the HOMO and the LUMO may be observed. We highlight the presence of a partially filled LUMO (L').

induce a long-range ordering, or most likely that the strong surface interaction hinders the rearrangement of the molecules over the surface. In any case, the possible surface disorder may also have an influence.

9.2.3. Adsorption of PTCDI under different substrate conditions

The measurements performed on the **standard-treated** surfaces left some open questions regarding the actual adsorption position with respect to the surface. An approach that may shed some light upon them is to slightly vary the surface conditions to see how the molecular adsorption changes. Actually, the results obtained are twofold: on the one hand, it gives information about the interaction of the molecule with the substrate and on the other hand, the molecule can be regarded as a probe for the actual surface morphology. The idea of using molecules to inspect the ZnO surface is not new [318, 474], but it has not been used in the context of COMs and XSW so far. Next, we are going to present the HR-XPS and XSW results obtained when PTCDI is deposited on surfaces that underwent different treatments besides the standard one. These include water dosing, hight-temperature annealing and even deposition on a warm substrate.

9.2.3.1. O-ZnO: annealing at 700°C and water dosing at RT

As it has been discussed in Chap. [8], sputtering the surface creates disorder and induces an effective outward relaxation of the topmost layers. Annealing at 700°C reverses these effects almost completely. Also, it has been shown that water dosing at RT does not stick to the surface, but rather tops up the core-level feature related to the surface-oxygen species, indicating a dissociative adsorption as long as favorable sites are available for this to happen. Consequently, the surface that has been annealed at HT and water-dosed will

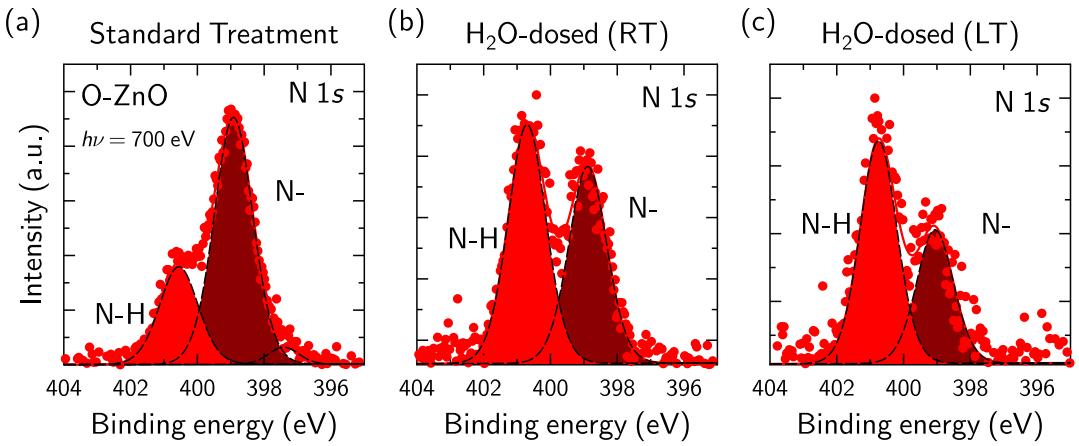

Figure 9.8.: HR-XPS ($h\nu = 700$ eV) comparison of the nitrogen N 1*s* core-level signal of PTCDI adsorbed on the differently-treated O-ZnO surfaces. (a) **Standard-treated** surface, added for comparsion. (b) Surface that had been additionally annealed at 700°C and then dosed with ∼2.3 L of water at RT. (c) Surface dosed with ∼2.3 L of H_2O dosed at ∼150 K. The relative-intensity change between the protonated- and the deprotonated-nitrogen components can be regarded as a direct measurement of the amount of molecules undergoing CT from the substrate.

be clean, ordered, and homogeneously covered with surface species, which is most likely to be decorated by H in a (2×1)-H arrangement, i.e. 50% of the surface is covered by OH groups, comparing our data to available calculations [461] and similar experimental conditions [480].

Upon deposition of PTCDI on this surface, the HR-XPS measurements of the C 1*s* (not shown) do not display any remarkable change compared to those of the **standard-treated** surface. Interestingly, the nitrogen signal (Fig. [9.8]b) also displays the 2 features associated to the intact nitrogen (N-H) and the deprotonated species (N-). However, the intensity ratio has changed, being in this case almost 1:1. This indicates that the degree of deprotonation has been reduced.

The XSW results (Fig. [9.9]) show a similar trend, namely, the functional-carbon atoms adsorb below the perylene backbone, the nitrogen atoms even further down, being the deprotonated ones the closest to the surface. However, the coherent positions have substantially changed. For instance, that of the perylene core has been reduced by 0.14, whereas those of N-H and N-, have done it by 0.08 and 0.11, respectively. Overall, the coherent fractions have also increased, being around 0.65 for the perylene core and the nitrogen species. The C=O carbon of the functional groups show lower coherent fractions and a slight decrease of 0.05 in the coherent position. This difference between the perylene core and the functional carbon may be explained by a decrease of the tilting and/or bending of the backbone structure upon homogenization of the surface or by the fact that the functional groups have different adsorption heights depending on the molecule.

At this point, we recall that the annealing at 700°C decreases the surface coherent position by 0.04. Although the reduction of the values related to PTCDI decrease slightly more, the change may be explained by the reduction of the outward relaxation as well as by the improvement of the surface ordering and homogeneity.

In this case, the spectral feature corresponding to the carboxylic oxygen of PTCDI could be clearly resolved and the results obtained from the XSW analysis render a coherent

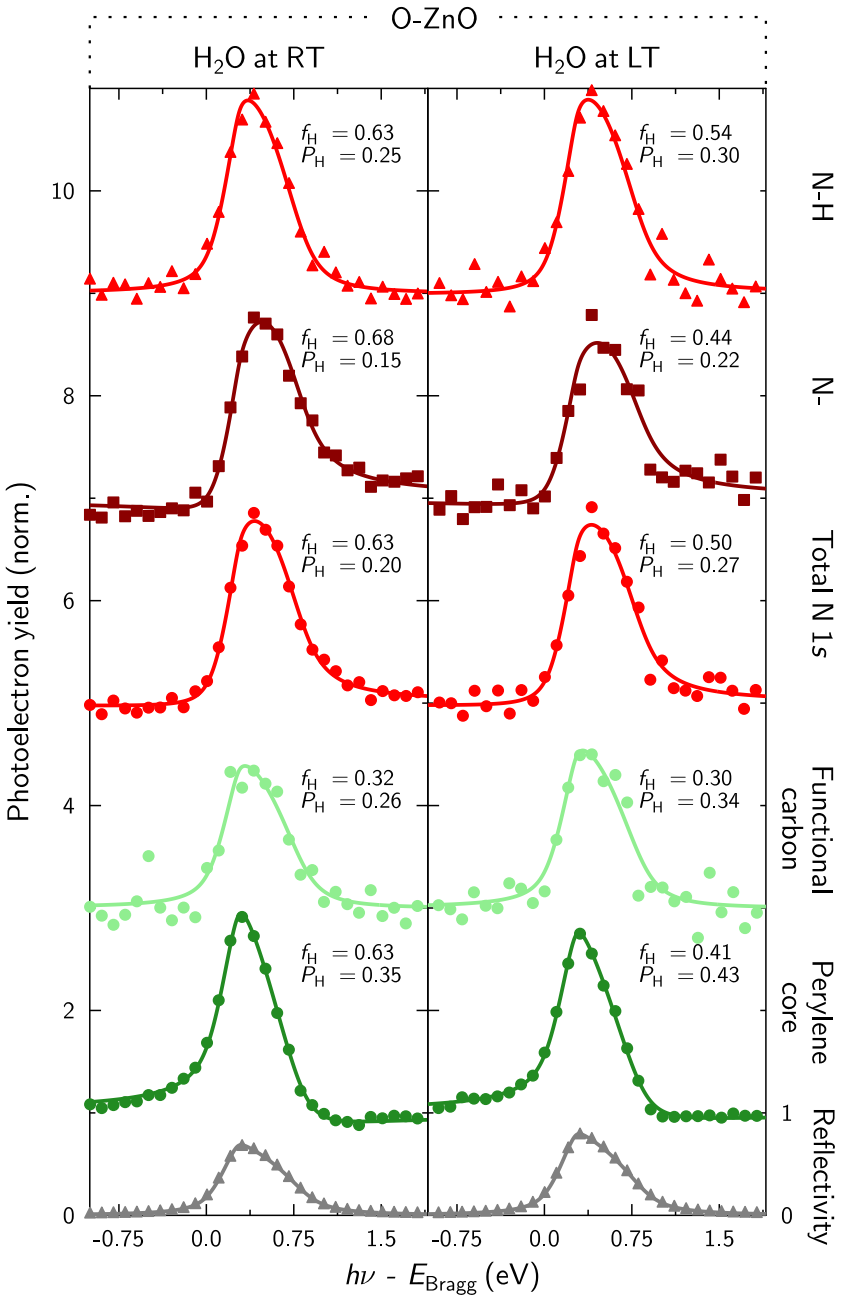

Figure 9.9.: XSW measurements along the **H** = [00–2] direction for PTCDI adsorbed on water-dosed O-ZnO surfaces (H_2O coverage 2.3 L) at RT and LT (∼150 K). The fitting parameters are included.

modulation, clearly differentiated from those of the bulk and the surface-oxygen species, which is a sign that the component stems from another position within the XSW field. The HR-XP spectra, together with the XSW analysis are reported in Fig. [9.10]. The XSW results yield a remarkably different adsorption distance. As it has been advised when discussing the information of the oxygen species for PTCDA (Sec. [9.2.1.3]), the trend is to be trusted more than the actual fitting parameters. In any case, the adsorption

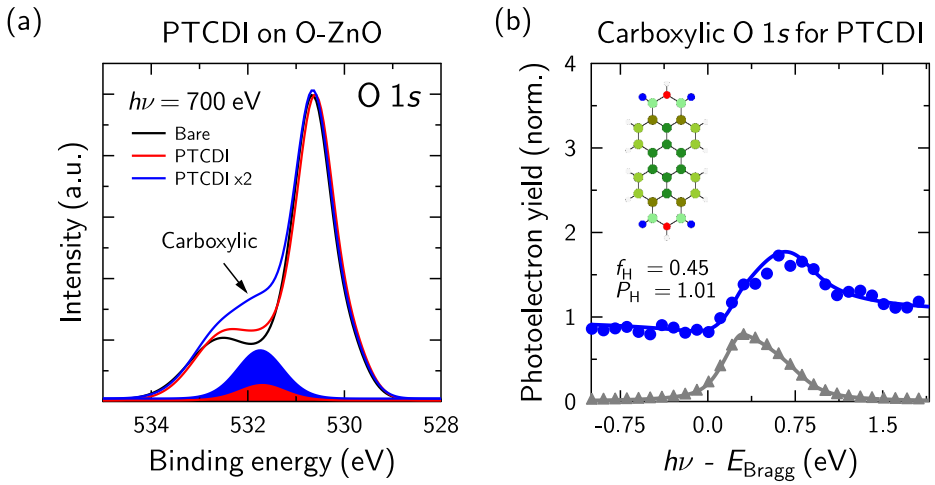

Figure 9.10.: Chemical and structural information corresponding to the carboxylic-oxygen species of PTCDI deposited on a **standard-treated** O-ZnO surface that was subsequently annealed at 700°C for 1 h and then dosed with water at RT. (a) HR-XPS ($h\nu = 700$ eV) scans for two different coverages (nominally 1.5 and 4 Å) of PTCDI. The increased coverage unambiguously reveals the presence of the spectral feature at $E_B \sim 530.6$ eV. (b) XSW measurements along the **H** = [00–2] direction corresponding to the O 1*s* carboxylic-oxygen component with the corresponding fitting parameters.

position would correspond to a strong bending towards the surface.

9.2.3.2. O-ZnO: water dosing at LT

Contrary to what is observed at RT, dosing water at LT (∼150 K in our case) leads to the molecular adsorption of this on the surface (see Sec. [8.2.2]). It is thus interesting to see how the molecules will arrange in this case. To test it, PTCDI was deposited on the H_2O-covered O-ZnO. The surface, previous to the dosing, had been cleaned with the **Standard Treatment** and then was also annealed at 700°C. The core-level analysis of the carbon C 1*s* signal (not shown) does not reveal any particular changes. However, for nitrogen, the intensity ratio of the double peak now favors the protonated species (Fig. [9.8c]), indicating that the amount of nitrogen atoms that loose the attached hydrogen has been further reduced compared to the dosing at RT (Fig. [9.8b]). Interestingly, the oxygen O 1*s* signal (Fig. [9.11a]) seems to indicate that some of the H_2O molecules have been desorbed upon deposition of the PTCDI. This could be either by the heat stemming from the effusion cells during film deposition or induced by PTCDI reaching the surface. Unfortunately, fitting the core-level spectrum is too speculative at this point, restricting the information that we can obtain.

The XSW measurements (Fig. [9.9]) reveal very similar photoelectron yield modulations compared to the two previous cases, namely, PTCDI adsorbed on the **standard-treated** surface and on the HT-annealed and water-dosed one. However, the coherent fractions have decreased, which indicates that the PTCDI layer is more disordered than in the other two cases, and also the coherent positions are much higher than for the dosing at RT. In this case, such an increase is not related to the outward relaxation of the first layers, but rather to the surface morphology. At this point, not having specific information about the surface-oxygen atoms, nor the adsorbed water molecules on the surface makes

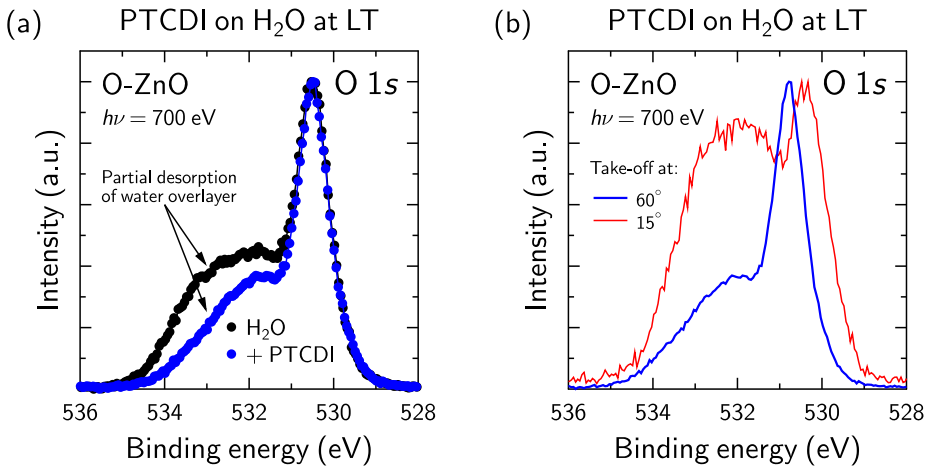

Figure 9.11.: HR-XPS ($h\nu = 700\,\text{eV}$) for the oxygen O $1s$ core-level signal corresponding to PTCDI deposited on a water-dosed surface at LT ($\sim$150 K). (a) Oxygen core-level signal before the PTCDI deposition and afterwards. The comparison of the two normalized spectra indicates that, upon deposition of PTCDI, some species desorb, most likely water molecules. Scans artificially aligned. (b) Angular-dependent scans of PTCDI deposited on the water-dosed O-ZnO at LT that highlight the surface component.

the following statement rather speculative. However, the fact that, upon adsorption of PTCDI, the shoulder of the oxygen core-level decreases (Fig. [9.11a]) and the fact that the nitrogen signal still shows the existence of deprotonated species (Fig. [9.8c]), which require the substrate intervention for the reaction to take place, indicates that either the presence of water molecules is residual or that PTCDI has moved to be in direct contact with the surface. Actually, this can be regarded as an argument in favor of the existence of a dissociated first water layer even at low temperatures [319]. Indeed, the presence of a fully covered OH surface may explain the increased surface component of the oxygen core-level spectrum (Fig. [9.11a]) as well as the adsorption distance within a similar range as before the dosing at LT. The higher coherent position, together with the lowered coherent fractions may be indicative of a rather inhomogeneous adsorption position, depending on the surface morphology underneath, similarly to the **standard-treated** case discussed in Sec. [9.2.1.2].

9.2.3.3. Zn-ZnO: adsorption of PTCDI on a warm substrate

As we have mentioned for the adsorption of PTCDI on the **standard-treated** Zn-ZnO surface (Sec. [9.2.2]), it is unclear whether the molecules adsorb on top of OH groups or directly in contact with the zinc topmost layer. In order to elucidate this, PTCDI was deposited on a warm substrate, which had been previously **standard-treated** and HT-annealed, so that the amount of OH groups on the surface is significantly reduced. The substrate was annealed at 500°C to remove the hydroxyl groups, as it is shown in Fig. [9.12a], the oxygen core-level signal displays a single symmetric peak without any surface contribution. The deposition of PTCDI was performed roughly $\sim$30 min after the heating was turned off. The time delay between the end of the annealing process and the deposition of the molecules was not enough to let foreign species cover the surfaces. Indeed, as it is shown in Fig. [9.12b], the O $1s$ core-level spectrum shows only a small contribution

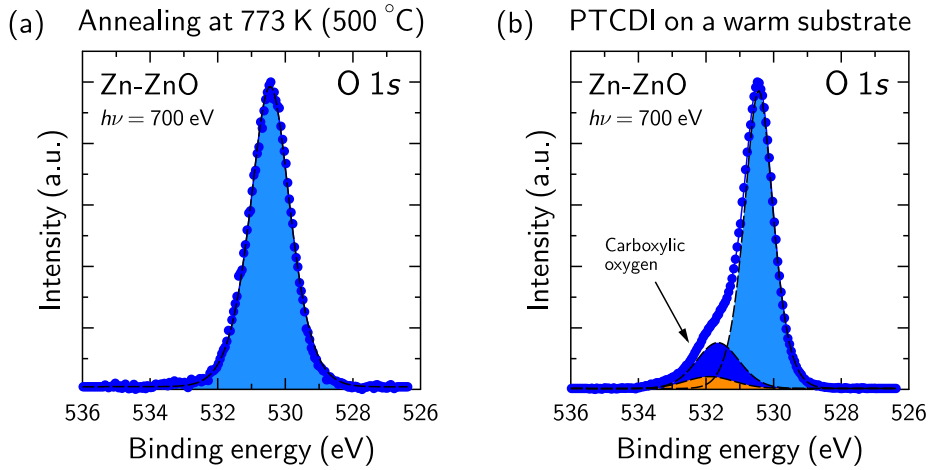

Figure 9.12.: HR-XPS ($h\nu = 700\,\text{eV}$) for the oxygen O 1*s* core-level signal corresponding to PTCDI adsorbed on a warm Zn-ZnO substrate. (a) Scan of the O 1*s* signal during the annealing of the substrate at 500°C that shows a single symmetric peak indicating the complete desorption of the surface species. (b) Scan of the O 1*s* signal for the same sample upon deposition of a PTCDI (sub)monolayer. The deposition was done 30 min after the annealing was stopped, although the substrate was still warm, a small portion of surface species had already adsorbed (orange component).

belonging to OH groups compared to the carboxylic-oxygen one. The comparison of the N 1*s* core-level between th **standard-treated** sample and the warm one (Fig. [9.12]) does not show major differences rather a higher background for the latter. Thus, one cannot deduce any changes to the degree of deprotonation, athough they are not expected either.

The XSW measurements presented in Fig. [9.14] are significantly different from those shown for PTCDI adsorbed on the **standard-treated** Zn-terminated surface (see Fig. [9.2]). The most remarkable change is the increased coherent fractions, which double for the perylene core and also slightly increase for the functional-carbon atoms and the deprotonated nitrogen atoms. The coherent positions, on the contrary, decrease. The perylene core, for instance, is reduced by 0.14 (∼0.36 Å), the same as for the functional-carbon atoms, whereas for the deprotonated nitrogen decreases by 0.07(∼0.18 Å). This reduction, on the one hand, can be attributed to the lifting of the relaxation upon annealing at 700°C. On the other hand, the smaller amount of surface species may allow the molecules to more homogeneously organize on the surface, especially the perylene core. The fact that the nitrogen species, once the surface relaxation is accounted for, have an almost negligible change compared to the core may be explained by the fact that the molecule just becomes flatter on the surface or, as we have just mentioned, have a lower distribution of positions along z. As we have concluded above, the interaction with the substrates is mostly happening through the functional groups, therefore, the fact that the position of the atoms does not change is indicative that PTCDI adsorbs directly on the zinc layer, regardless of whether there are hydroxyl groups or not, which, in any case, just hinder a flatter, more homogeneous adsorption.

For this case, no LEED was recorded. Therefore, we cannot unambiguously conclude whether such a surface preparation treatment renders a long-range in-plane ordering of PTCDI. This will be elucidated in future experiments.

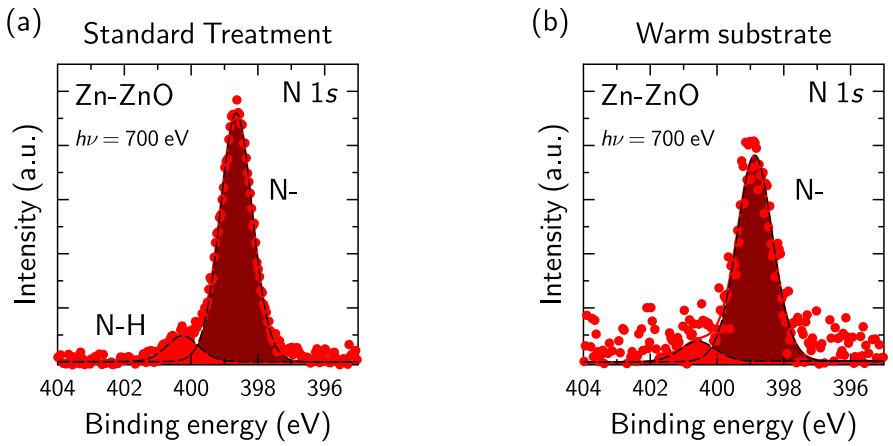

Figure 9.13.: $h\nu = 700\,\mathrm{eV}$) comparison of the nitrogen N 1*s* core-level signal of PTCDI adsorbed on the differently treated Zn-ZnO surfaces. (a) **Standard-treated** surface, added for comparison. (b) Scan performed on a PTCDI (sub)monolayer adsorbed on a warm substrate, i.e., the deposition was performed shortly (30 min) after the annealing was stopped. Although the scan is rather noisy, a prominent, single peak is still visible.

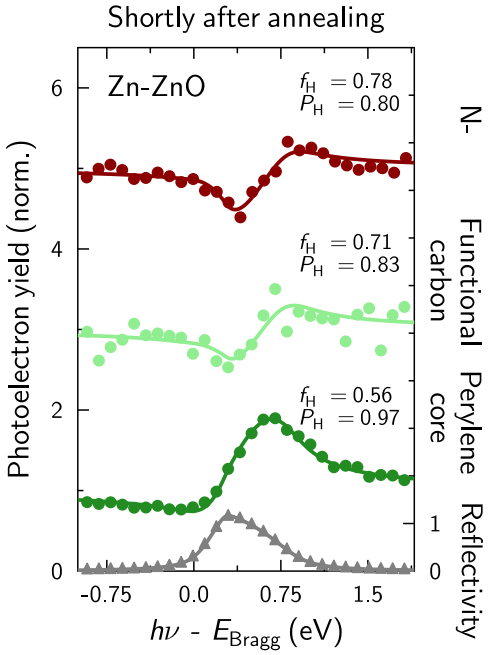

Figure 9.14: XSW measurements along the **H** = [002] direction corresponding to PTCDI deposited on a warm Zn-ZnO substrate. The deposition of PTCDI was performed 30 min after the substrate annealing at 500°C had been stopped. The same substrate had been previously annealed at 700°C, therefore the surface relaxation had been lifted. We note the increased coherent fraction compared to the measurements in Fig. [9.2].

9.3. Discussion

The set of experiments presented above yield a comprehensive, although not complete, set of measurements that allows one to bring together the electronic, chemical and structural properties of the COM-ZnO interface. In the following, we discuss them having two goals in mind, the first one is to rationalize some ways to improve the CT between the COM layers and the ZnO substrates, the second one is to better understand the polar surfaces using the information obtained from the COM-ZnO interface, i.e. using the molecule as a surface probe.

Substrate	Treatment	Comp.	$f_{00\mp2}$	$P_{00\mp2}$	$d_{00\mp2}$ (Å)	dist. to surf. (Å)
O-ZnO	**Perylene**					
	Standard	Total C 1*s*	0.42	0.48	3.85	3.17
	PTCDA					
	Standard	Anh. O 1*s*	0.67	0.35	3.52	2.85
		C=O	0.23	0.48	3.86	3.17
		Core	0.41	0.48	3.84	3.17
	PTCDI					
	Standard	N-H	0.38	0.33	3.47	2.73
		N-	0.45	0.26	3.28	2.54
		Total N 1*s*	0.46	0.27	3.31	2.57
		C=O	0.37	0.31	3.42	2.68
		Core	0.43	0.49	3.87	3.13
	Annealing+Water	Total O 1*s*	0.45	1.01	2.63	2.05
		N-H	0.63	0.25	3.26	2.67
		N-	0.68	0.15	3.00	2.42
		Total N 1*s*	0.63	0.20	3.13	2.55
		C=O	0.32	0.26	3.29	2.71
		Core	0.63	0.35	3.50	2.93
	Water at LT	N-H	0.54	0.30	3.38	
		N-	0.44	0.22	3.17	
		Total N 1*s*	0.50	0.27	3.30	
		C=O	0.30	0.34	3.48	
		Core	0.41	0.43	3.72	
Zn-ZnO	**PTCDI**					
	Standard	N-	0.54	0.87	2.28 (*) / 4.88 (#)	2.11 (*) / 2.94 (#)
		C=O	0.65	0.97	2.51 (*) / 5.12 (#)	2.34 (*) / 3.18 (#)
		Core	0.28	0.11	2.88 (*) / 5.48 (#)	2.71 (*) / 3.54 (#)
	Annealed (warm)	N-	0.78	0.80	2.08 (*) / – (%)	2.09 (*) / – (%)
		C=O	0.71	0.83	2.15 (*) / – (%)	2.16 (*) / – (%)
		Core	0.56	0.97	2.52 (*) / – (%)	2.53 (*) / – (%)

Table 9.1.: Summary of the XSW fitting parameters and related adsorption distances for the perylene derivatives adsorbed on the polar surfaces of ZnO prepared with different treatments. $d_{00\pm2}$ is the value obtained applying $d_{00\pm2} = d_0(P_{00\pm2} + n)$ and is referred to the topmost bulk-like zinc layer. Consequently, to obtain the actual distance to the surface, $d_{00\pm2}$ has to be corrected considering the position of the surface oxygen or any possible relaxation of the topmost zinc layer. For instance, (*) are obtained assuming that PTCDI is directly adsorbed on the topmost-zinc layer (applying $n = 0$) and the actual adsorption distance is obtained by subtracting the layer relaxation. On the contrary, (#) (applying $n = 1$) the adsorption is considered to take place on top of the surface species, therefore the actual adsorption distance is obtained by subtracting the position of the surface-oxygen atoms. In (%), no surface species could be measured with XPS, hence we consider that, indeed, the only option is that PTCDI adsorbs directly on the topmost Zn layers.

9.3.1. Influence of the functional groups

As we have discussed in Chap. [5] and [6], the presence of functional groups facilitates the electronic coupling between the substrate and the molecule. In this context, it seems that ZnO is another clear example of it. Indeed, the combination of UPS and XPS reveals the chemical and electronic fingerprints of a charge donation from the substrate to the molecule that induces, on the one hand, the partial filling of the LUMO of PTCDA and PTCDI and, on the other hand, the (partial) deprotonation of the nitrogen atoms of PTCDI.

Our findings appear in line with other results reported in the literature. For instance, Winget et al. [377] studied the interface properties of PTCDI on a (highly doped) conductive Zn-ZnO substrate and identified the presence of near-surface zinc vacancies as those responsible for the CT to the molecule. The role of the defects is also behind the CT effects observed for this molecule on TiO_2 [127]. Similarly to PTCDI, PTCDA has been shown

to be involved in integer CT from the ZnO substrate [491]. Unfortunately, one cannot evidence the integer CT for PTCDA from our set of measurements. However, for PTCDI the integer CT can be associated to the presence of protonated and deprotonated nitrogen species. Indeed, as it is discussed for PTCDI on TiO_2, such a double peak is related to the presence of defect states and the ratio between the protonated and the deprotonated peaks is balanced in favor of the N- component when the defect states are higher. In our case, the same effect is obtained by changing the surface preparation methods (see Figs. [9.8] and [9.13]).

Very interestingly, for F4TCNQ and F6TCNNQ, two strong molecular acceptors that are invovled in CT processes when deposited on other substrates [50, 254], there is no evidence of CT, nor chemical interactions between them and ZnO [292, 487]. Noteworthy, they modify strongly the ZnO WF, although mostly through changes of the surface band bending [292, 487] and also adsorption-induced intramolecular dipoles, as we show in Appendix [E].

Considering now the role of the functional groups on the vertical geometry, it is quite surprising to see that regardless of the functional group, the three perylene derivatives have their carbon backbones at virtually the same adsorption distance on the O-ZnO substrate. One could speculate that this is determined by the perylene core. However, F6TCNNQ also adsorbs at the same distance (Appendix [E]). Even the nitrogen atoms, comparing PTCDI and F6TCNNQ, are at very similar vertical positions. This finding goes in line with the studies that report a rather weak interaction between the adsorbed molecules and the ZnO substrates [292, 487, 490]. In this case, it was also reported that the adsorption geometry of F4TCNQ is insensitive to the dopant concentration of the ZnO [490].

As a final remark for this part, the absence of in-plane ordering is striking. PTCDA and most prominently PTCDI are known to form well ordered layers on a large variety of substrates, even on metal-oxide surface [124, 125, 127]. Although our results indicate that closed layers are formed for PTCDI and PTCDA, in contrast to perylene that forms big islands, the lack of in-plane ordering may be regarded as a drawback for the formation of buffer layers on contacts. As we will discuss in the following section, the surface morphology may be responsible, but we already anticipate that this issue requires further investigation.

9.3.2. Influence of the surface termination and preparation

Besides the chemical tuning of the molecules, the other way to affect and control the interface properties is by modifying the surface, e.g. by introducing dopant species through ion implantation [110]. For ZnO, it has been reported that depending on the sputtering strength, one favors the introduction of more surface defects, which are primarily involved in CT effects with the COM overlayers [277]. In our case, we used the annealing time and water dosing to see how the chemical and structural properties of the interface with PTCDI are changed. From the structural point of view, the effect of the annealing on the molecular overlayer and subsequent water dosing cannot be unambiguously decoupled because the deposition was performed on substrates that had undergone both treatments.

Starting with the annealing at 700°C, we have seen that it reverses the disorder and the outward relaxation introduced by the sputtering process, also rendering a more homogeneous and ordered surface, as it is seen by the higher coherent fractions and the reduced

measured adsorption distance. Interestingly, the perylene core of PTCDI is the most affected by the surface treatment, with the nitrogen atoms only adsorbing at slightly lower positions. This points out towards a reduction of the static disorder within the different molecules depending on the morphology underneath rather than an actual systematic decrease of the overall adsorption distance.

As we have discussed in Chap. [8], the dosing of water at RT likely contributes to the homogenous decoration of the surface with H and/or OH groups. This effect can be inferred from the overall higher coherent fractions, although the precise contribution cannot be decoupled from the effect of the annealing. More evident is the ratio between the protonated and deprotonated nitrogen species of PTCDI. According to the literature [127,377], the surface defects (vacancies) are responsible for such effect and, as it is seen for the water-dosed surface at RT, and more pronounced at LT, the amount of deprotonated species decreases (Fig. [9.8]) for the water-dosed substrates. This supports the idea that the dissociated water molecules occupy vacancy positions.

Finally, regardless of the treatment, the polarity also plays a very important role. From the N 1*s* core-level measurements and the XSW results, it can be concluded that the interaction strength with the Zn-terminated surface is stronger. Indeed, the adsorption distance are much lower, the C 1*s* core-level is broader and the nitrogen atoms are mostly deprotonated. This behavior is analogous to what we have also measured for F6TCNNQ but excluding the presence of charged nitrogen atoms (Appendix [E]). Actually, when considering F6TCNNQ, the degree of defluorination is much higher for this termination than for the O-terminated one (Appendix [E]). This would support the role of the vacancies and, in particular, the zinc vacancies in the CT effects with the substrate. Finally, it is also interesting to see that the molecules adsorb directly on the Zn-ZnO surface and not on top of the OH groups.

9.4. Conclusions

In recent years, more and more studies are systematically applying surface-science techniques to infer the interface between π-conjugated molecules and metal-oxide substrates. As it became clear when trying to rationalize the metal-organic interface, the precise knowledge of adsorption distances and intramolecular distortions is key to achieve a complete picture of the processes undergone upon adsorption of the organic compounds. So far, this structural information has been absent for the inorganic-organic semiconductor interface. Consequently, the results presented here fill an important gap in this context. Furthermore, they show that, with the right crystal preparation, the XSW method can be extended also to other materials besides the prototypical metal single crystals. The results presented here are part of an ongoing project, which also involves theoretical calculations. Consequently, the interpretation and implications derived from them are still being matured. However, at this point some safe conclusions can be outlined.

The adsorption distance of perylene and its derivatives PTCDA and PTCDI on the O-ZnO surface render almost equally planar adsorption distances for the carbon core. The presence of functional groups, however, introduces intramolecular distortions, clearly resolved for PTCDI and most likely also present in PTCDA. From the HR-XP spectra, no sign of hybridization or strong coupling with the substrate can be deduced. For PTCDA

and more strongly for PTCDI, there are indications of a partial charging of the functional groups. This charge transfer from the substrate to the functional group also induces the loss of the hydrogen in some of the PTCDI imide groups, as it is clearly seen in the N $1s$ core-level spectra, with the presence of two peaks. The two nitrogen species adsorb at different adsorption distances, being the deprotonated nitrogen closer to the surface, hinting at a substrate-induced origin for such a hydrogen loss. The additional UPS measurements indicate the presence of new states upon deposition of PTCDA and PTCDI, which are assigned to be charges that go to the LUMO. The findings regarding the vertical geometry apply not only to perylene derivatives but also to F6TCNNQ, as shown in Appendix [E].

Taking PTCDI as the reference molecule, we have observed that the surface polarity has a significant impact on the chemical properties of the molecule since the nitrogen species are almost completely deprotonated, indicating that the occurrence of CT is more pronounced in this case. The broader C $1s$ core-level and the XSW results indicate that PTCDI adsorbs closer to the surface, most likely in direct contact with the zinc topmost layer.

The surface treatment, besides the polarity difference, can also be used to modify the interface properties. The high-temperature annealing at 700°C heals the damage induced by the sputtering and renders a more ordered surface. This is seen by the fact that the coherent fractions have an overall increase. Dosing water at RT also helps to have a homogeneously saturated coverage of OH groups, which may also help to increase the order of the molecular overlayer. Interestingly, upon water dosing, the ratio between protonated and deprotonated nitrogen species changes. For the water-dosed samples, less species are deprotonated. In the literature, the occurrence of CT is linked to the presence of near-surface vacancies (either zinc or oxygen). It is plausible to assume that the migration of H and OH towards vacancy sites upon dissociative adsorption of H_2O may help to reduce their impact on the COM overlayer.

Although the measurements presented here render a comprehensive characterization of the structural and chemical properties of the different ZnO-COM, more effort has to be devoted to provide a more detailed framework for the electronic changes in the frontier orbitals of the different COMs. In particular, possible modifications in the band bending will have to be investigated. In addition, the issue with the long-range order at the (sub)monolayer regime has to be elucidated. By studying whether COMs deposited on a warm substrate (i.e. shortly after the annealing) form a supramolecular arrangement may give a hint on whether the adsorbed surface species (OH/H) hinder a suitable molecule-molecule interaction.

Part III.

Summary and outlook

10. Summary

The need to undestand and control the interface properties at the atomic scale, as a way to obtain efficient organic-based optoelectronic devices, requires, in many cases, the rationalization of the effects produced by minute chemical modifications. In this work, we have focused on perylene and pentacene derivatives that present a partial nitrogen or fluorine substitution in their chemical structure. We shall summarize the main findings of this thesis in the following.

As a first step, we investigated the unsubstituted perylene molecule, a simple hydrocarbon structure that can be funcitonalized by the addition of several functional groups. Despite its core role in many well-studied derivatives, such as PTCDA and DIP, some basic information was missing, namely, the adsorption geometry when deposited on the coinage metals. To fill this gap, we measured the adsorption distance of perylene on the (111) surfaces of gold and copper with the XSW technique. The results, presented in **Chap. [5]**, are quite unexpected: perylene adsorbs closer to the surface than its derivatives (see Fig. [10.1]), although there is no sign of strong electronic coupling with the surface nor charge transfer (CT) [334, 335].

Next, we investigated PTCDI, a perylene derivative very similar to the well-studied PTCDA, where only the anhydride oxygen is substituted by a N-H group. From the chemical perspective, this simple change significantly increases the tunability of the molecule since the hydrogen atom of the imide group can be further substituted by many different chain groups [353]. So far, information regarding the interface of PTCDI with the coinage metals has been scarce. Therefore, we devoted ourselves to the thorough characterization of these systems. The results presented in **Chap. [6]** describe the electronic, chemical and structural properties of the different interfaces. Overall, the characterization of the frontier orbitals via UPS and the adsorption distances via XSW renders a behavior very similar to PTCDA. Nonetheless, the intramolecular distortions differ substantially (see Fig. [10.1]), which is indicative for the presence of different, local substrate-molecule interactions, definitely requiring theoretical input to be understood properly. In addition, the shape and broadening of the core-level spectra change remarkably depending on the substrate underneath, a sign of the varying nature of the metal-molecule interaction. Interestingly, when comparing copper and gold, which are two extreme cases since PTCDI is chemisorbed on the first and physisorbed on the second, the core-level spectra do not seem to follow the trend for the lifetime broadening. This should be higher for copper than for gold, as expected for the stronger substrate interaction of the former [165]. We tentatively attribute this discrepancy to intermolecular interactions, which are quite strong on gold, owing to the hydrogen-bond formation between adjacent molecules. On the contrary, our measurements indicate the absence of long-range order on copper. Finally, the comparison of different derivatives with the unsubstituted perylene molecule reveals that a short adsorption distance does not necessarily imply the existence of strong electronic coupling

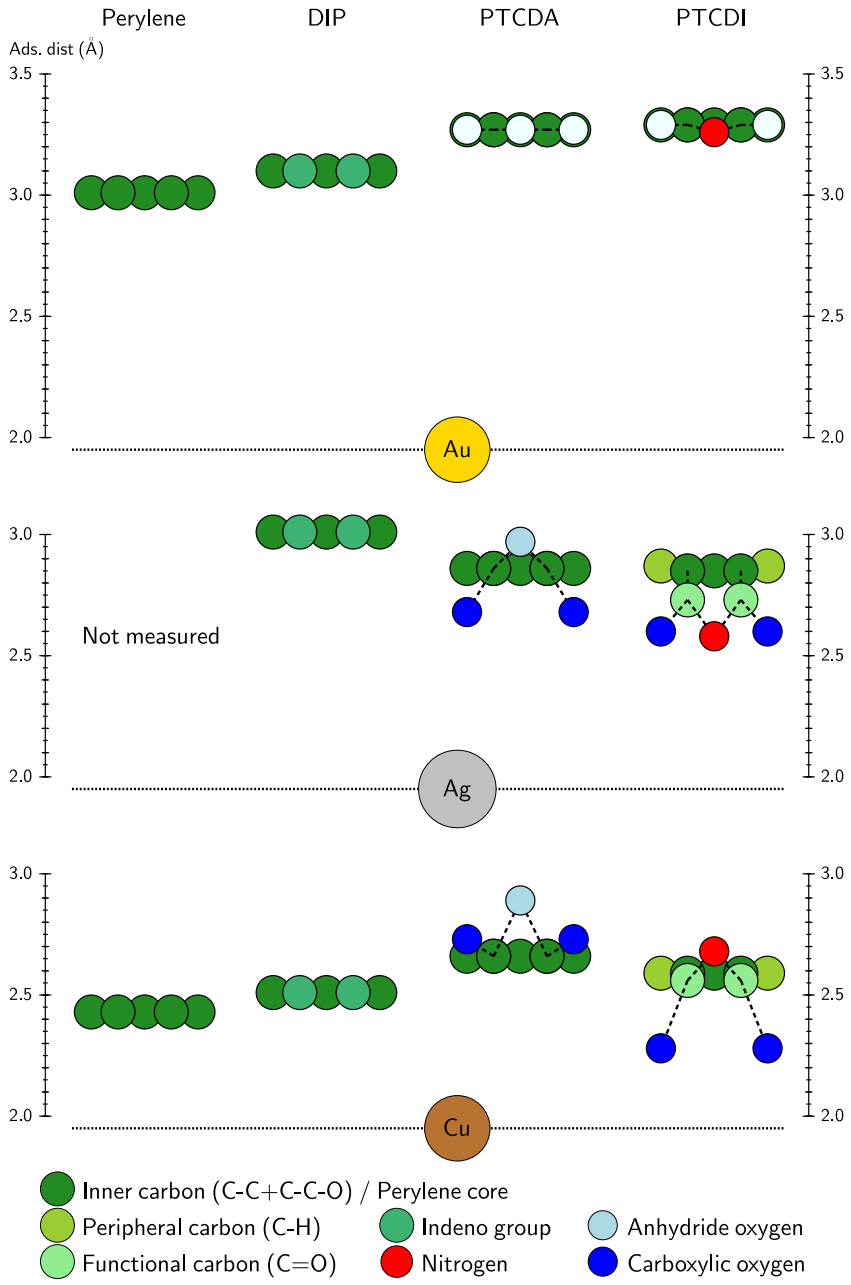

Figure 10.1.: Comparison of different perylene derivatives adsorbed on the three coinage metals. The adsorption distances are extracted from XSW measurements. The values for DIP on Au(111), Ag(111) and Cu(111) are extracted from Ref. [58], for PTCDA on Au(111) from Ref. [70], on Ag(111) from Ref. [217] and on Cu(111) from Ref. [65]. Figure taken from Ref [69].

with the substrate and/or CT. Consequently, in the case of perylene and its derivatives, the functional groups favor the CT with the substrate but are not directly responsible for the short adsorption distance of the molecule.

The fluorination of COMs, i.e. the substitution of hydrogen by fluorine, has been explored as a mechanism to increase stability against oxidation as well as a way to modify the electronic properties of the π-conjugated molecules. In **Chap. [7]**, we investigated the changes at the interface when the short edges of pentacene are fluorinated, rendering a strong intramolecular dipole and fostering molecule-molecule interactions through the C-F$\cdots$H bond formation. Using the recently synthesized F4PEN, we deposited it on Cu(111) and Ag(111). As schematically summarized in Fig. [10.2], with the combination of HR-XPS and XSW, we developed a fitting model that allows one to obtain information from three inequivalent carbon atoms within the molecular core. Together with the position of the fluorine atoms, we were able to draw a very detailed picture of the vertical adsorption geometry. In particular, a remarkable difference of 0.9 Å between the fluorinated-carbon atoms of the short molecular edges and the central benzene ring was reported. Nonetheless, the average adsorption distance of the carbon atoms indicates that the backbone is gently bending, hence only the fluorinated edges account for the substantial carbon spread. Comparing our additional UPS and LEED measurements with those available for PEN, we found that the electronic properties and in-plane arrangement are identical. This allowed us to conclude that such a selective chemical modification only produces a local, upward bending of the short fluorinated edges owing to the higher steric repulsion of the fluorine atoms. This leaves the strong electronic coupling between the substrate and the carbon backbone undistorted. Noteworthy, in the thin-film regime, the electronic and chemical properties change compared to those of the first layer thus exhibiting a behavior different than that of PEN. When F4PEN is deposited on silver, the results can neither be fully ascribed to PEN nor PFP (the fully fluorinated PEN). Although the adsorption distance is similar to that of PEN, the in-plane ordering is different from both cases and the UPS measurements indicate the presence of stronger coupling with the adjacent molecular layers rather than with the substrate. The results show that partial fluorination is an effective way to tune the interface properties as long as the coupling with the substrate is weak (on silver) or inexistent (in the thin-film regime). In these cases, the hydrogen-bond formation between fluorine and hydrogen atoms of adjacent molecules enables new configurations absent in PEN and PFP.

In **Chap. [8]**, we demonstrated that the combination of HR-XPS and XSW can be used successfully to characterize the complex polar surfaces of ZnO, a necessary precondition to study the technologically-relevant ZnO-organic interface. With the proper fitting model we measured the position along the [00$\pm$2] direction of the surface species, which were also monitored in real-time XPS under different annealing and water-dosing processes. Most remarkably, we elucidated the precise effect of sputtering and annealing on the topmost ZnO layers. In particular, we measured the degree of surface relaxation induced by the sputtering, its dependence with time and how annealing at high temperature can completely heal the surface. Thus, we demonstrated that depending on the sputtering time, annealing time and temperature, different degrees of relaxation can be obtained. These results may help to explain why one can find different and even contradictory values for the surface relaxation of ZnO in the literature.

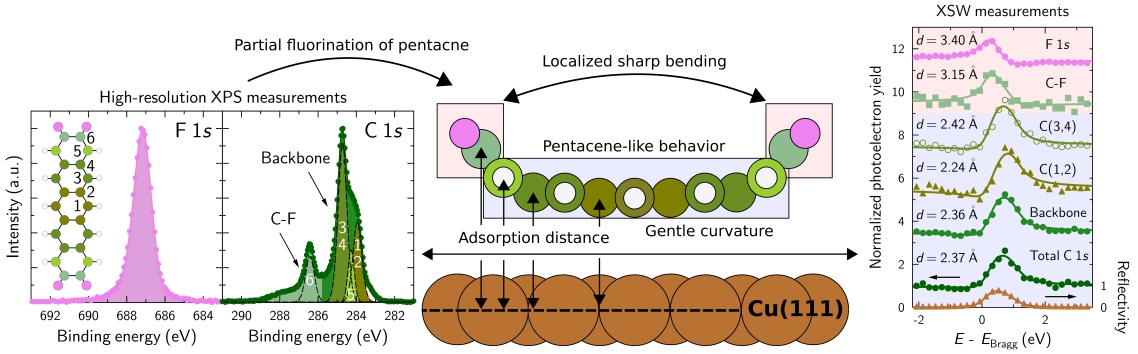

Figure 10.2.: This figure summarizes the most relevant finding of Chap. [7] as well as it exemplifies the spirit of this work: using HR-XPS to obtain a core-level fitting model that is then used in the XSW analysis to resolve the adsorption distance for as many inequivalent species as possible.

In the last part, we investigated the adsorption characteristics of three perylene derivatives, namely, the unsubstituted perylene, PTCDA and PTCDI on the polar surfaces of ZnO. The results presented in **Chap. [9]** indicate a strong dependence on the polarity, either zinc- or oxygen-terminated surfaces. On the O-ZnO surface, the three molecules adsorb at almost the same distance, indicating that the physisorbed perylene core does not have a specific interaction with the substrate. Nonetheless, the XSW measurements show a remarakble molecular distortion, with the functional groups of PTCDA and PTCDI bending towards the surface. This goes along with the fingerprints of CT to the molecular groups. In particular, the nitrogen core-level signal of PTCDI shows the presence of two different species, which are attributed to the existence of protonated (N-H) and deprotonated (N-) species. Using the intensity ratio between both nitrogen species, we monitored the degree of "reactivity" between PTCDI and the differently treated surfaces. Zn-ZnO appears as the most reactive surface. In this case, it seems that the molecule adsorbs in direct contact with the zinc topmost layer, instead of doing it on top of the OH species. For the O-ZnO surface, dosing water at room temperature minimizes the deprotonation of nitrogen, which is tentatively explained by the fact that the dissociated molecules occupy the vacancy positions thereby reducing the active sites whereby surface and adsorbates interact. Our results highlight the importance of the polarity and the presence of functional groups for the existence of CT between the molecular overlayer and the ZnO surface. Also, the impact of dosing water on the occurrence of CT indicates that the surface defects play a major role in this process.

As a final and general remark for this work, we demonstrated the advantages of systematically combining HR-XPS and XSW measurements. The information obtained from XSW measurements is limited by the quality of the data as well as the fitting model that may allow one to distinguish between inequivalent species. Since nowadays the dedicated beamlines offer excellent signal-to-nosie ratios, even for low coverages and weak core-level signals, the main limiting factor is finding a suitable model to fit the data. Therefore, using HR-XPS to obtain a valid fitting model is key to exploit the chemical resolution of the XSW. We hope that these results will encourage others to combine both systematically.

11. Outlook

The concluding chapter of this work aims at providing some guidelines and recommendations for future projects based on the findings presented here. We are confident that our results together with the comprehensive literature review will facilitate further investigations.

The synergy between theory and experiments pushes the understanding of nature forward. Theory needs experiments to validate its assumptions whereas experiments need theory to rationalize and generalize their findings. In the particular context of this thesis, the resolved adsorption distances for inequivalent carbon species within a given molecule is an ideal case to further test available state-of-the-art density-functional theory calculations with van-der-Waals corrections that so far have provided the most accurate description of adsorption geometries of COMs on coinage metals. In this direction, F4PEN represents a very suitable case since different positions within the molecular structure are provided. In addition, the remarkable difference between the core and the fluorinated edges renders a nice case to investigate the interplay between attractive an repulsive forces in the overall adsorption geometry.

Continuing with the context of theoretical calculations, PTCDI (and also PTCDA) render very puzzling substrate-dependent distortions. The different configuration of the heteroatoms (nitrogen and oxygen) depending on the substrate underneath indicates very subtle interactions between molecule and surface that cannot be understood without the help of theoretical input. The connection between the conformational changes observed here and the electronic coupling with the substrate certainly requires a more systematic approach, which we hope will be encouraged by our experimental data.

We have stressed the need to combine a precise core-level fitting model with XSW measurements to further exploit its chemical sensitivity. However, the core-level assignment is a controversial topic since one can find different models that fit the same spectrum. Although in our work we have used the XSW measurements to independently validate the fitting model, there is the need for more core-level spectra calculations, which provide independent input for the proper XPS fitting.

From the experimental perspective, our results have lead to further questions that should be addressed. Starting with perylene and PTCDI, we have found that perylene adsorbs at significantly lower adsorption distances on gold than its derivatives. Very interestingly, it has been reported that the adsorption of perylene (but not PTCDA) perturbs the surface reconstruction of Au(111) [264]. It would thus be interesting to further investigate this system. A priori, perylene is expected to have a phsisorptive behavior on gold, hence the fact that it may influence the surface reconstruction is rather surprising. Similarly, there are reports that PTCDI has coverage-dependent behavior on gold [389], which, however, could not be evidenced from our results. In order to clarify this, a more precise coverage-dependent, XPS and XSW study should be performed.

The substrate-dependent vacuum-level shift observed upon increasing coverage is something not yet well-understood. For instance, PTCDA thin films present the same vacuum-level shift regardless of the substrate underneath [67]. However, PTCDI renders different values depending on the substrate. This shows how strong the impact is of changing an oxygen atom for a N-H group. This substrate-dependent evolution of the vacuum-level shift has been observed for some systems, but not for others.

The measurements obtained for F4PEN have allowed one to distinguish two opposing behaviors within the same molecule, namely, repulsive vs. attractive. In order to test the adsorption geometry of longer acenes obtained in theoretical calculations, it would be interesting to perform XSW measurements on e.g. heptacene [500] deposited on copper where a significant, upward bending of the short molecular edges is observed without the need of fluorination [430]. If the chemical environment between the central rings and the outer carbon atoms differs enough, the bending could also be resolved.

For ZnO, the XSW measurement that have located the position of the adsorbed species along the surface perpendicular direction is a significant achievement. As a further refinement, measuring XSW along other crystal directions will enable the triangulation of the exact position of these species, allowing one to clearly identify whether the bulk-like position is also found in the in-plane direction. For the bare substrates, implications on the electronic properties such as band bending and occurrence of gap states, under the different preparation conditions reported here, will need further investigation. This way, the structural changes will be connected unambiguously to the electronic properties exhibited by the substrate. As a final step, a suitable theoretical model shall be able to reproduce the experimental findings.

For the adsorbed π-conjugated systems on ZnO, the absence of long-range order is still puzzling. In order to elucidate whether the presence of the adsorbed surface species hinder the molecular rearrangement, the experiments should be repeated for overlayers that have been deposited on a freshly annealed sample, so that the adsorbed OH groups are in the lowest number possible. Finally, the adsorption geometry of molecules other than perylene derivatives should be further investigated, for instance by using phthalocyanines.

Part IV.

Appendix

A. XSW study of TAT deposited on the coinage metals

The results presented here were published in Ref. [249] as a part of a broader multitechnique study of TAT (see Sec. [4.1]) deposited on Au(111), Ag(111) and Cu(111). Next, a short motivation to the project is given and is followed by the discussion of the XSW results. The details can be found in the aforementioned reference.

In the context of metal-organic interfaces, despite the remarkable progress achieved in the last 20 years, open questions still remain. Having systematic data for different systems and substrates helps to rationalize the different observed phenomena. TAT is a promising COM in the context of OPV devices. It has a strong acceptor character and has been reported to grow forming π-stacked layers. The interface with metal electrodes, however, was still unexplored and a multitechnique study of TAT adsorbed on (111) surface of the coinage metals was performed.

Figure [A.1] shows the XSW data evaluated for the carbon and nitrogen signals of TAT adsorbed on the coinage metals. The fitting parameters are included in the plot. The presence of the nitrogen atoms embedded in the molecular backbone, instead of being present as side groups, limits its freedom to bend towards the surface. As it can be seen from the coherent positions, these are very similar to those of the carbon atoms, meaning that the overall molecular distortion is limited. On silver, the nitrogen atoms are $\sim$0.1 Å below the carbon backbone, the biggest difference within the three cases, which may be due to the major hybridization of the molecular frontier orbitals with the substrate atoms as well as to a major presence of charged molecules, as seen by XPS, compared to the copper case [249].

The adsorption distances, summarized in Fig. [A.2], are a clear example of the typical behavior observed when the same molecule is adsorbed on the coinage metals, namely, the lower the substrate nobility, the shorter the adsorption distance. The overall adsorption distances are, interestingly, very similar to those of perylene (see Chap. [5]) and close to those of DIP [58]. However, especially on gold and copper, the results vary substantially from those of PTCDA and PTCDI (see Fig. [10.1]). On silver, the LUMO is partially filled [249], similarly to PTCDA [67, 396], PTCDI (Chap. [6]) and DIP [351]. In addition, on Cu(111), TAT shows a totally filled LUMO [249], again similarly to PTCDA [67], PTCDI (Chap. [6]) and DIP [75, 351]. Therefore, despite the similar electronic characteristics of the interface of TAT with those of DIP, PTCDA and PTCDI, the adsorption distances vary substantially. This small, but representative, differences are not yet well understood. A possible factor that may play a role is the presence of functional groups. TAT, DIP and perylene have a rather planar and rigid structure, whereas PTCDA and PTCDI have the functional groups that bend towards the surface, which may facilitate the CT but also may cause some steric repulsion. More systematic calculations are required in this direction.

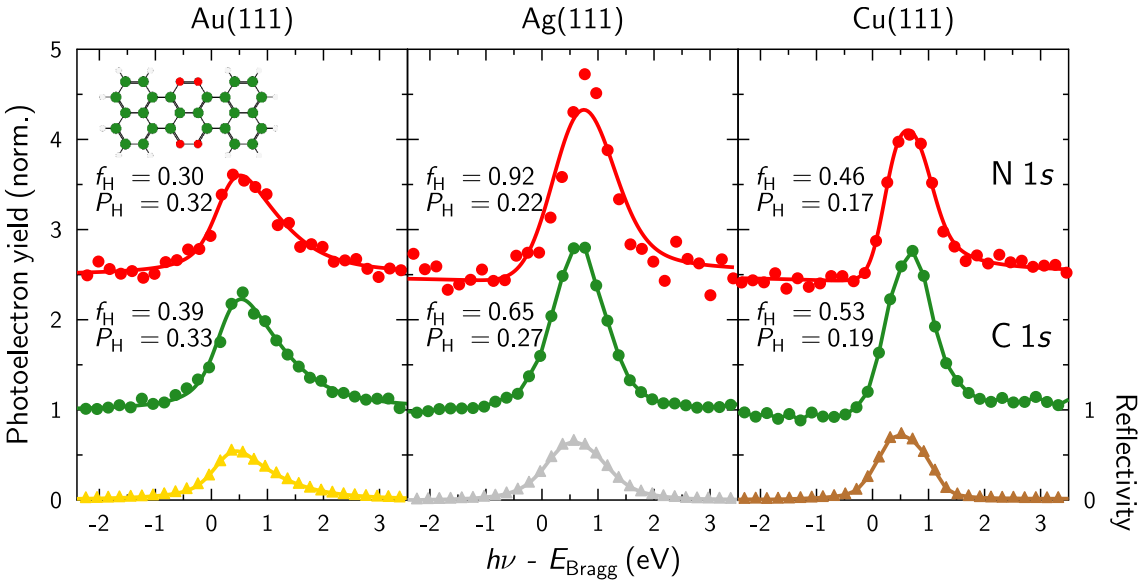

Figure A.1.: XSW measurements along **H** = [111] for the carbon and nitrogen atoms of TAT adsorbed on the coinage metals. The total area for each core-level signal [249] was used to evaluate the photoelectron yield.

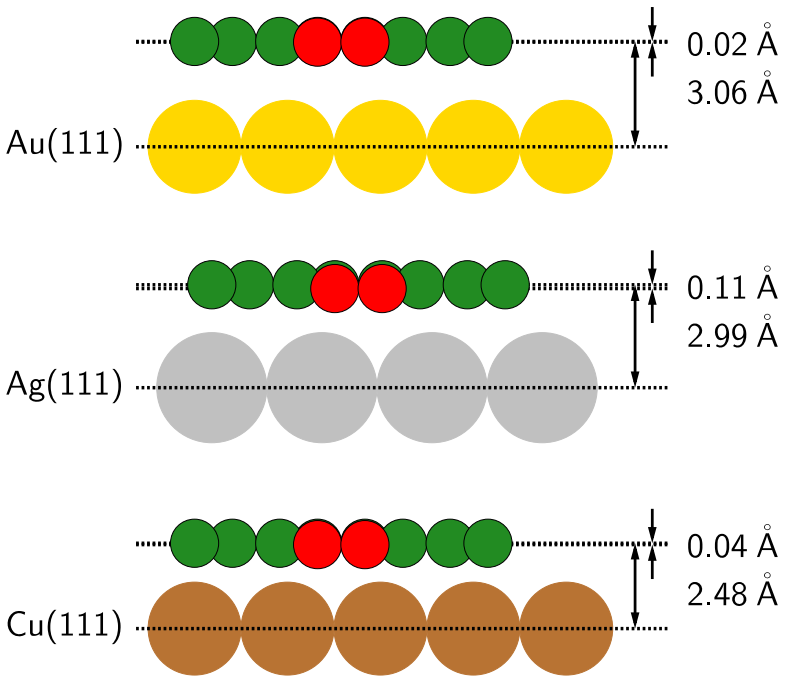

Figure A.2.: Sketch of TAT adsorbed on the coinage metals. The adsorption distances are obtained form the XSW measurements of Fig. [A.1].

B. F4PEN: beam-damage tests and additional measurements

This appendix chapter contains additional measurements and considerations regarding the adsorption behavior of F4PEN on Ag(111) and Cu(111) that were not included in Chap. [7]. In particular, beam-damage tests for the soft-XPS and XSW measurements are reported, the measured bending of the PEN core is reviewed in detail and the low BE shoulder shown in the C 1*s* core-level spectra is carefully analyzed in order to proof that it corresponds to carbon species directly bonding to substrate atoms.

XSW: Influence of the beam-damage and reproducibility

It has been reported that acenes, in particular pentacene (PEN), are prone to oxidation [501, 502], being 6,13-pentacenequinone (P2O) one of the most common byproducts [501]. Furthermore, C–F bonds are also likely to break under long X-ray exposure, such as that encountered during XSW experiments. Consequently, especial care was devoted to make sure that the data presented in Chap. [7] was not compromised by these undesired effects.

Of particular interest are the XSW measurements of the F 1*s* core-level signal corresponding to the case of F4PEN on Cu(111). The remarkable and unexpected distance of ∼1 Å between the average carbon (2.36 Å) and fluorine (3.40 Å) adsorption distances requires a closer look at the data to make sure that what it is actually measured are fluorine atoms belonging to F4PEN and not free fluorine atoms attached to the surface or step edges. For that purpose, we are going to consider two different aspects: first, the results obtained on different spots of the sample and secondly, changes occurring during the XSW scan. Fig. [B.1] contains XSW results obtained from two different sample spots. By checking the fitting parameters, the reproducibility within the sample is demonstrated and besides, it is shown that taking the average of different spots is a valid way to improve statistics without compromising the fit analysis.

In order to rule out other possible adsorption distances stemming from the ambiguity given by n in the equation used to calculate them, Fig. [B.2] shows different results obtained for different values of n applied to the equation $d_H = d_0(n + P_H)$ (see Sec. [3.3]). The one given by $n = 0$ is not physically possible because the adsorption distance is smaller than the sum of the fluorine and copper atomic radii. On the other extreme, $n = 2$ renders an adsorption distance that it is too high since it renders a difference of more than 3 Å between the fluorine and the carbon backbone, which could only be given by an extreme bending of the molecule. Therefore, the only reasonable value is the one obtain by $n = 1$. It is worth noting that the coherent fractions are high enough to discard the case for standing-up molecules. Indeed, the spread of inequivalent adsorption distances

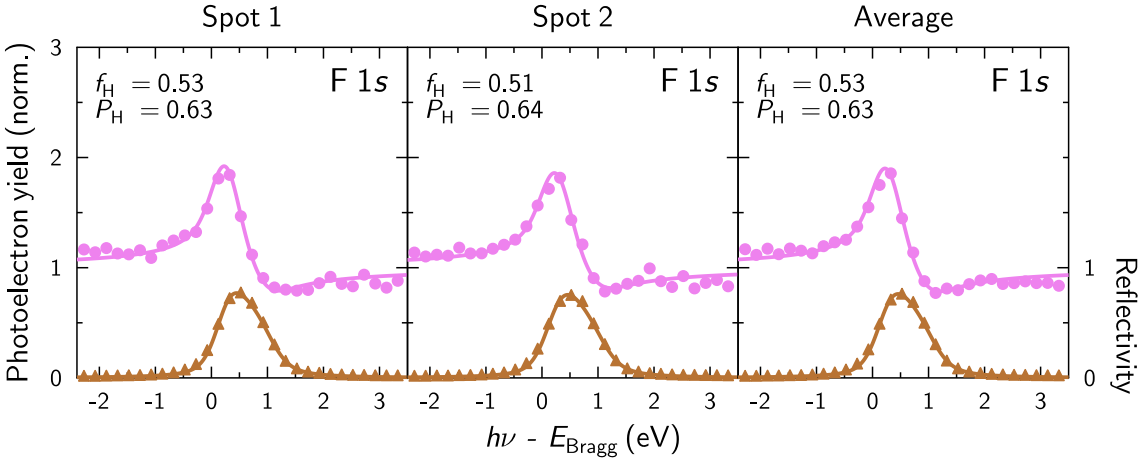

Figure B.1.: XSW measurements along **H** = [111], using the F 1*s* signal, on different spots of a F4PEN (sub)monolayer adsorbed on Cu(111). Left: Spot 1. Center: Spot 2. Right: Average of the two spots. The fitting parameters obtained from the analysis show that the results are reproducible within the film and that taking the average of two spots improves the statistics without affecting the analysis.

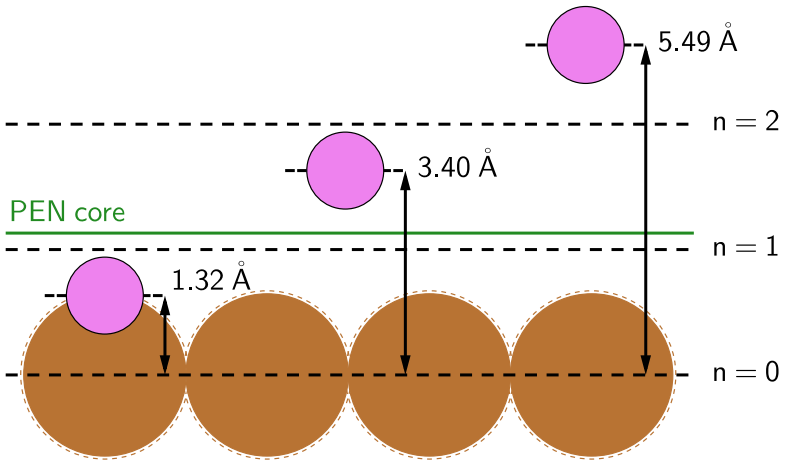

Figure B.2.: Adsorption distances of the fluorine atoms calculated for different values of n in equation $d_H = d_0(n + P_H)$. As a reference, the average adsorption distance of the F4PEN carbon backbone (noted as PEN core) is indicated with a green line.

along ∼17 Å (long axis of the molecule) could be considered as a random distribution of atoms, yielding a coherent fraction equal or very close to 0.

Finally, Fig. [B.3] shows the first and the last scans of the XSW series, together with the superposition of all 31 scans, for the two measured spots as well as their average. Comparing the first scan (Scan 1) with the last one (Scan 31), there are, indeed, differences. For instance, as marked with an arrow, a small peak appears at the low BE side; the main peak becomes broader and slightly shifts towards lower BE energies. However, the impact of these changes is very small as it can be inferred by checking the scan add-up (right plots in Fig. [B.3]) since the weight of the beam damage peak is very small.

In conclusion, the small beam damage appearing during the XSW scans has a negligible impact on the measured adsorption distances since its effect on the different XPS

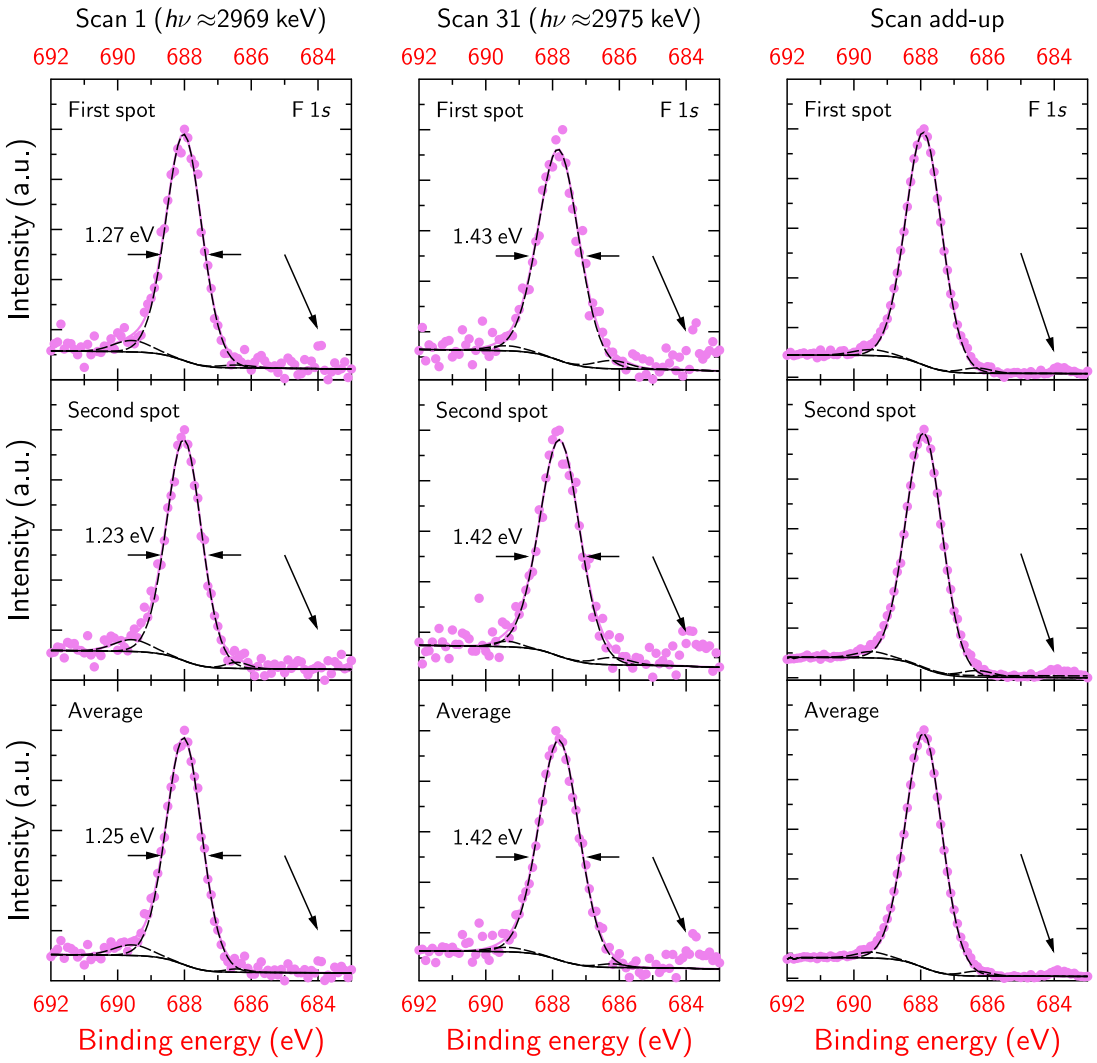

Figure B.3.: F 1*s* XP spectra extracted from the XSW measurements taken for different spots on a F4PEN (sub)monolayer adsorbed on Cu(111). In particular, the first scan (left) and the last scan (center) are plotted to identify any possible beam-induced spectral changes. Specifically, peak broadening and new peaks are highlighted (with an arrow). The right plots show the XSW-scan series added up to show the relative impact of the beam-induced low-BE component. Binding energy not calibrated.

scans is rather limited and, consequently, the photoelectron yield evaluation remains virtually unaffected. Also, within the deposited F4PEN layer on Cu(111), the results are reproducible.

HR-XPS: carbon-fluorine vs. carbon-substrate core-level components

Owing to the higher cross-section of the soft X-rays for light elements, such as carbon and fluorine, it is important to consider the effect of beam damage on their corresponding core-level spectra. Fig. [B.4] shows the particular effects of the beam on them. Starting

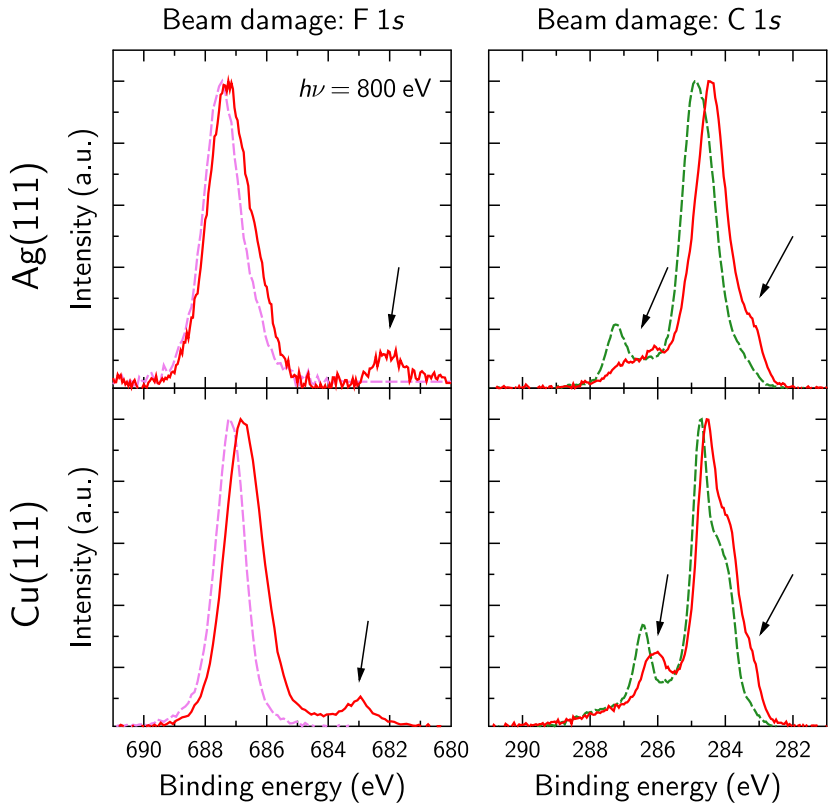

Figure B.4.: Effect of the soft-X-ray beam (800 eV) on the F 1*s* and C 1*s* core-level spectra measured for F4PEN adsorbed on Ag(111) and Cu(111). The violet (fluorine) and green (carbon) dashed lines report the intact spectra, whereas the damaged ones are shown in red for both core-level signals. The arrows highlight the main spectral changes induced by the beam. Besides, a shift towards lower BE is observed accompanied with a broadening of the main line. Of special interest is the decrease of the C–F feature and the concomitant intensity increase of the shoulder at the low BE side of the main peak, which is associated with carbon bound to substrate atoms. This effect is more prominent for silver than copper.

with fluorine, which is the most sensitive to beam damage, one can observe a broadening of the main line and a shift towards lower BE energies. Most importantly, a peak around 682 eV appears. The same trends appear regardless of the substrate underneath. The effects of the soft X-rays on the carbon spectra also include a BE shift towards lower energies and a broadening, although less pronounced. However, the most drastic effect is the intensity decrease observed for the C–F component, also accompanied by a pronounced shift towards lower BE. This is clearly seen for the carbon spectra on silver, where a bump appears at 286 eV, tentatively ascribed to the damaged C–F bonds. Indeed, a weaken bond may well reduce the electron-withdrawing effect of fluorine allowing the bonding carbon to screen better the core-hole.

Along with the decrease of the C–F component, one can observe an intensity increase of the low BE shoulder, observed on both substrates and also reported for PFP deposited on Cu(111) [57,417] and other acenes with C–Br bonds [451,503,504]. Koch et al. [57] related the low BE component observed for PFP adsorbed on Cu(111) to molecules adsorbing close to step edges. This hypothesis is further corroborated by Glowatzki et al. [417], who also related it to decomposed molecules. For dibromotetracene adsorbed on different

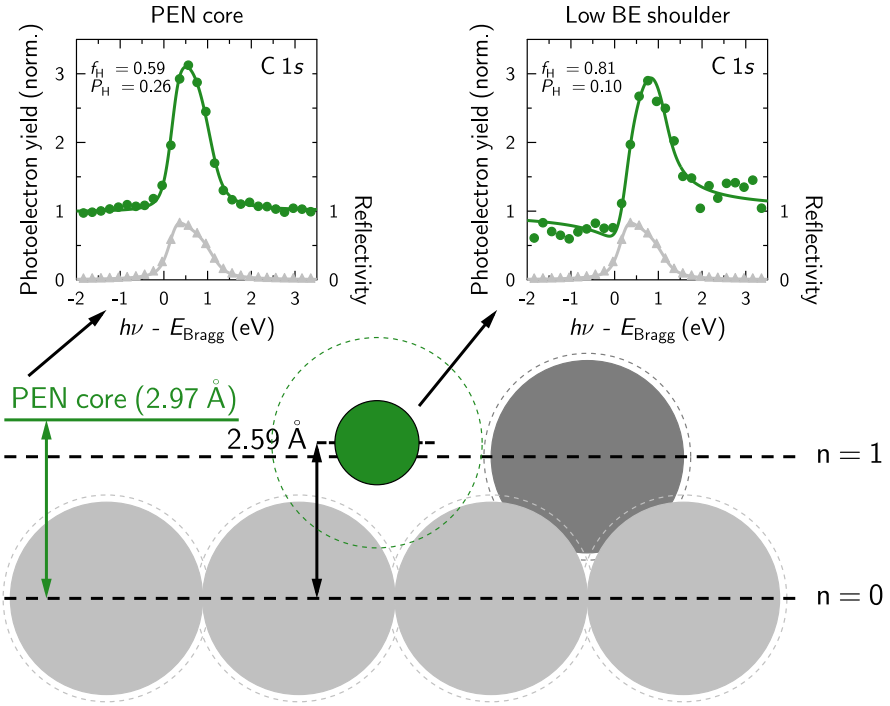

Figure B.5.: Comparison of the XSW measurements along the **H** = [111] direction corresponding to the PEN core and the C 1*s* low BE shoulder of F4PEN adsorbed on Ag(111). The mentioned shoulder renders a coherent modulation of the photoelectron yield corresponding to an adsorption distance of 2.59 Å, which is ∼ 0.4Å below the average carbon distance of F4PEN adsorbed on the said substrate. The coherent fit and the closer adsorption distance to the substrate supports the assumption that the spectral shoulder is originated by carbon atoms bound the surface at the surface and/or to step edges (both cases possible from a purely XSW perspective).

silver and copper surfaces [451,503,504], a low BE shoulder appears in the C 1*s* spectrum, which is assigned to carbon atoms that have lost the bromine and bound to substrate atoms instead [451,503,504]. In addition, the bromine core-level signal shows two sets of Br 3*d* doublets, shifted in energy from each other, which are assigned to bromine atoms attached to carbon and bromine atoms bonding directly to the substrate [451,503,504]. From our measurements, as mentioned above, an intensity decrease of the C–F component is followed by an increase of the low BE shoulder. As shown in Fig. [B.5], the photoelectron yield of this component ("low BE shoulder") renders a coherent modulation with a shape clearly different from that of the PEN core, which readily indicates that they are at different positions. The fitting of the curve provides an adsorption distance much closer to the surface, ∼0.4 eV below the carbon backbone. This appears in full agreement with the hypothesis that the low BE component originates from carbon atoms bound to the surface. The sketch in Fig. [B.5] displays two possible scenarios: either the carbon atoms bound to surface atoms or to substrate atoms in the vicinity of step edges. Unfortunately, only from the XSW side, one cannot tell which one dominates.

Finally, for copper, one expects a similar effect, considering the presence of a shoulder at the low BE side of the main core-level peak, although no coherent XSW fits could be extracted.

C. XSW study of PTCDA adsorbed on PbS

The results presented here are part of a broader study dealing with the atomistic description of the interaction between different molecular ligands and lead sulfide (PbS).

COMs have started to be systematically studied in the context of colloidal quantum dots (CQDs) since they render a way to improve the properties of the latter. The new systems, called coupled organic-inorganic nanostructures (COINs) [505], consist of arrays of CQDs interconnected via organic molecules (linkers). These systems take advantage of the COM π-states to improve and/or modify the optoelectronic properties of the system. The success of these systems relies on the proper understanding of the interface between the CQD surface and the organic molecule. An atomistic description is eventually required. So far, they have been investigated computationally and the experimental characterization is missing.

Within the available materials, lead sulfide (PbS) is a prominent material in the context of CQDs. Typical PbS CQDs have eight well-passivated (111) surfaces and six (001) reactive facets, whereby the interaction with the molecular ligands is happening. Therefore, in order to see how the molecules interact with them, we studied, with XSW, the adsorption of several molecules deposited on the (001) reactive surface of PbS. The particular aim was to identify possible molecular distortions which reveal preferential interaction channels with the substrate.

In these experiments, instead of a commercially-available single crystal, we took a piece of galena (natural form of PbS) [506–510] and cleaved it in situ under UHV conditions. This was performed attaching a cleavage caliper into the UHV chamber. Noticeably, the first Bragg reflection that can be used for the XSW experiments is the (002). Being its energy for the NI geometry 2.088 keV, it is too low to be accessed with the current double-crystal monochromator at beamline I09. Instead, the (004) reflection, with a corresponding Bragg energy of 4.180 keV, was used. The inconvenient is that the cross-section is rather low for such high energies and the recorded XP spectra is pretty noisy and the resolution is bad. The results of the bare PbS surface (not shown here) are very similar to those reported before [511]. An additional problem that we faced during the experiments is the rather inhomogeneous crystal quality. Consequently, finding spots with a decent reflectivity was challenging.

Several molecules were deposited, but here only PTCDA will be presented, which is the most relevant molecule in the context of this work. The XP spectra recorded during the XSW scans did not allow to differentiate the carboxylic and the anhydride oxygens. Although it is pretty likely that both oxygen species have different adsorption distance, here we only report the average of the two. Also, only the average carbon distance is reported. This means that, for both core-level signals, the total area was taken to evaluate the XSW results presented in Fig. (C.1).

Despite the lack of chemical resolution, which does not allow to differentiate the in-

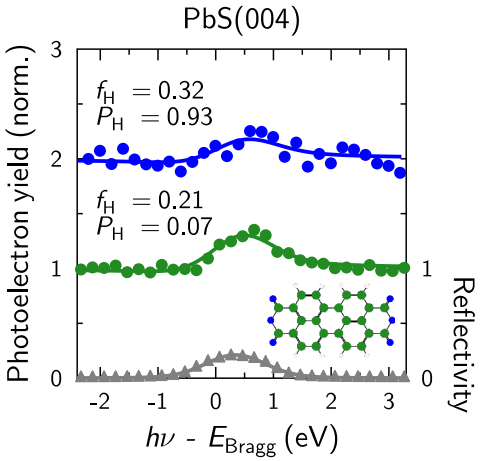

Figure C.1: XSW measurements along the **H** = [004] direction ($(E_{Bragg} \sim 4.18\,\text{keV}$) obtained for the carbon and oxygen atoms of PTCDA adsorbed on PbS. The total area of each core-level signal was used to evaluate the photoelectron yield. The carboxylic- and anhydride-oxygen species could not be distinguished.

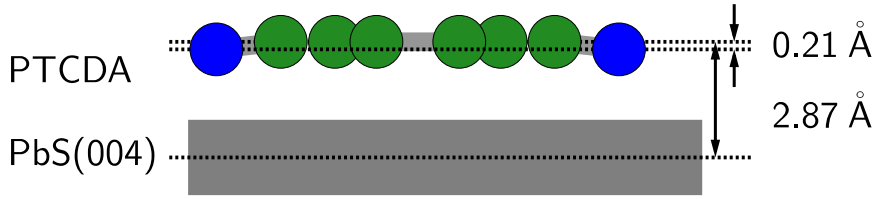

Figure C.2.: Sketch of the adsorption geometry of PTCDA on PbS.

equivalent species within a chemical signal, the results yield some interesting conclusions. The first one is that the molecules adsorb rather flat on the surface, although the vertical ordering is not very high[1]. The second is that the oxygen atoms are adsorbing at a lower position than the carbon backbone. Consequently, one deduces that they are the main channel whereby the interaction with the substrate occurs, similarly to what we have seen on ZnO and what it happens for the coinage metals. Fig. [C.2] shows a sketch of the measured adsorption geometry. The average distance of the carbon core, 2.87 Å, is similar to that found for PTCDA [217] on silver and much lower than that measured on O-ZnO (Chap. [9]). Such a relatively low adsorption distance may be explained by the absence of contaminants (thanks to the in-situ cleavage) or adsorbed species (such as OH groups in the case of ZnO), which may render the reactive surfaces of PbS more exposed.

[1] This is also because the periodicity of the XSW field, given by the lattice spacing along the [004] direction, is very small. Therefore, the thermal vibrations and statical disorder have a major impact on the coherent fraction.

D. Refinement of the O 1s core-level fitting model of O-ZnO

In the literature, the vast majority of core-level spectroscopy studies of bare, UHV-cleaned, ZnO surfaces use a two-component model to fit the oxygen O 1*s* spectra: one component is used to fit the bulk species, which are associated to the most intense feature, whereas the second one is attributed to the surface species that appear at the high-energy side of the bulk contribution. Basically, the same has been used in this work (see Sec. [8.2.1]) and additional species have been introduced only when water and/or molecules were deposited on the surface. It is a simple model that renders very good results, as we have seen in chapters [8] and [9]. However, there have been some studies, supported by theoretical calculations, that consider additional contributions, mostly involving uncoordinated oxygen atoms close to vacancies [311, 495]. In light of the present study, we raise the question on whether the amount of these species is enough to have a detectable fingerprint within the core-level signal and, if so, whether these contributions can be used to obtain structural information about the surface and sub-surface. In any case, this possible refinement of the fitting model does not have a major impact on the results, discussion and conclusions presented in the aforementioned chapters. Most importantly, the adsorption distances and intramolecular distortions of the studied COMs are not compromised since they are always referred to the topmost species and these are virtually unaffected by the fitting model.

The more components one uses, the better the fit obtained for a given core-level signal. Therefore, we used the quality of the XSW analysis as an independent criterion to validate whether the XPS fit would hold physical (or at least structural) meaning. Fig. [D.1] compares the 2-component model with the model that gave a quantitative improvement of the overall XSW analysis. The 2-component model overlooks the presence of defects on the surface, which is masked by the larger FWHM of the fitting components. Following the reasoning presented in Ref. [311] and references therein, we included two new components: one ∼0.8 eV below the bulk peak, corresponding to oxygen species close to zinc vacancies, and another one ∼0.8 eV above it, corresponding to surface species occupying another adsorption site. The binding energy position of the 2-component surface species with respect to the bulk is kept fixed in the refined model. The additional change introduced is that the Lorentzian contribution of all 4 peaks is set to be 30%.

With the new model, the coherent fractions obtained for the bulk and the initial surface component increase, which is always regarded as a sign for a good fitting model. The variation of the coherent positions lay within ±0.02, thus within the error bars. The new components show lower coherent positions, meaning that they occupy sub-surface sites, thus not influencing the discussion of the molecular adsorption geometries. Interestingly, these two components render values that significantly vary from sample to sample and treatment to treatment, as opposed to the high reproducibility of the values obtained for the bulk and surface species in the 2-component model. For instance, P_{H} within a 0.1–0.2

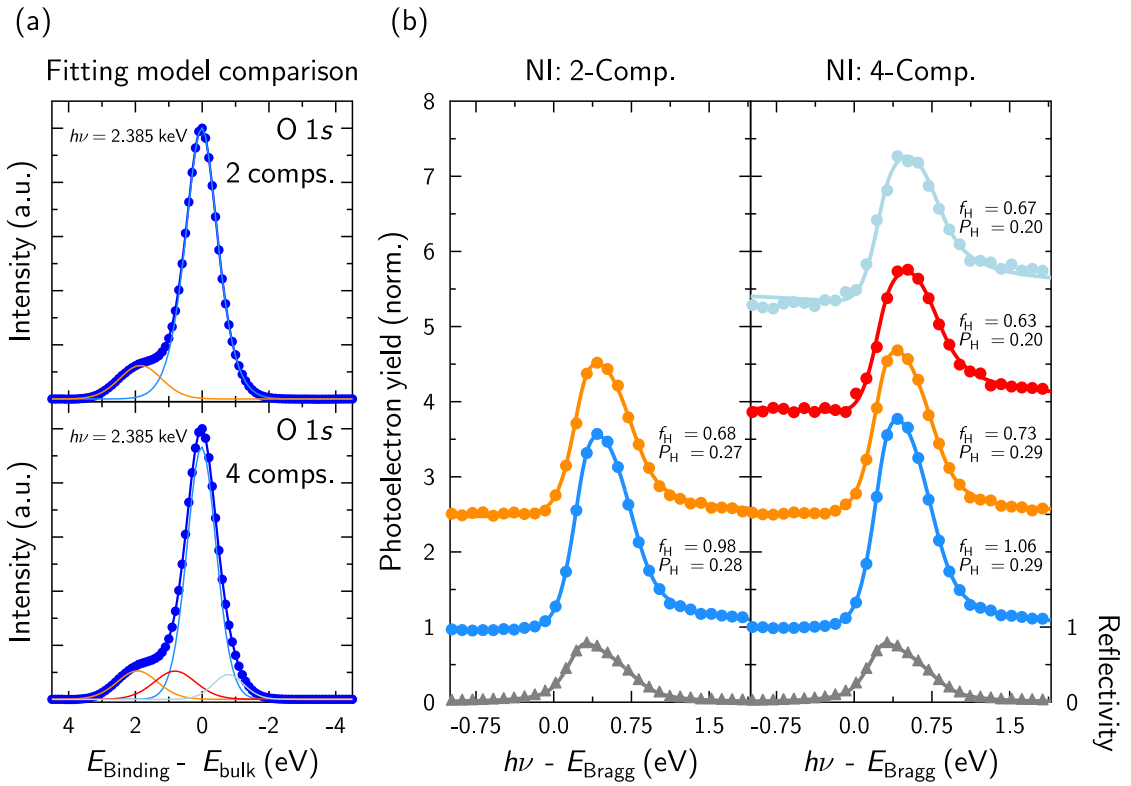

Figure D.1.: Comparison between the 2-component model used through this work and a plausible refinement, labeled as 4-component model, for the fitting of the O 1*s* core-level corresponding to the bare 0-ZnO. (a) The two core-level fitting models are compared. (b) XSW measured along the **H** = [00-2] direction, normal to the surface, obtained with the two core-level models from (a). The fitting parameters are included for comparison. Besides the blue component for the bulk atoms and the orange for the surface species, the 4-component model includes additional components for oxygen atoms close to zinc vacancies, in red, and for surface species occupying a different position, most likely close to surface defects (see text for the details).

interval have been obtained. This is unfortunate since it does not allow to obtain conclusive information about the location of these species within the crystal. Nonetheless, its slight random character, linked to the treatment procedure, agrees with the assumption that they are defect- or vacancy-related. This would explain why the coherent fractions are much lower and why the coherent positions change so much (vacancies and defects are expected to be more or less randomly created). It is worth noting that the comparatively different shape of the photoelectron yield and the remarkably different coherent positions rule out that these two new components might just be reminiscences from the bulk and/or surface components, but rather that they have a distinctive position within the XSW field.

All in all, this section does not pretend to draw solid and complete conclusions out of the refinement of the model. For that, it should be applied in XSW measurements using other reflections, so that the position can be triangulated. Furthermore, support from theory and additional experiments, for instance photoelectron diffraction, would be very helpful. Nonetheless, the results presented here serve the purpose of showing how, with the new dedicated beamlines, the fitting model has become a key factor limiting/increasing the information that can be obtained from XSW experiments. Also, it is a very good example of the power of the technique and its chemical sensitivity.

E. F6TCNNQ adsorbed on the polar surfaces of ZnO

Context

F6TCNNQ (see Sec. [4.1]) is a strong molecular acceptor similar in electronic properties to the well studied F4TCNQ [33, 34, 50, 512–514], but with the advantage that it has a higher molecular weight, making it less volatile and thus more stable for OMBD growth [515]. Both have been recurrently employed as interlayer materials to tune the (electrode) substrate work function (WF) [50, 254, 487, 512] or as molecular dopants in heteromolecular films [33, 514, 516]. Recently, Schlesinger et al. employed F4TCNQ [487] and F6TCNNQ [292] to tune the ZnO WF with very similar results, an increase of 2.8 eV for both molecules. The qualitative trend could be explained just considering electrostatic reasons [487], with the doping concentration of ZnO being the dominating parameter [487, 490]. However, a quantitative description is beyond reach without taking into account possible adsorption-induced distortion changes that may contribute to the formation of intramolecular dipoles [487]. It is clear that the precise structural information of the organic/ZnO interface is important if one wants to correctly predict the WF change. With this in mind, we performed XSW measurements of F6TCNNQ (sub)monolayers deposited on the two ZnO polar surfaces.

Results and discussion

The F6TCNNQ (sub)monolayers were prepared similarly to those of the perylene derivatives reported in Chap. [9]. Fig. [E.1] shows representative XPS measurements of the deposited layers on both surfaces. In this case, only hard X-rays were employed (a few eV off-Bragg), therefore the resolution is worse than the scans shown for the perylene derivatives. Nonetheless, different inequivalent carbon atoms could be resolved, namely, C–F and C–C + C–N. Not so positive is the presence of beam damage seen for the fluorine core-level signal that appears as a bump at the low BE side of the main line, similarly to what has been discussed in the appendix chapter [B] for F4PEN. Also at the low BE side of the carbon C 1*s* spectra, one can identify a shoulder that is related to carbon atoms bound to the substrate, again similarly to what it has been discussed for F4PEN (see Chap. [7] and appendix [B]). Interestingly, no relative BE shifts can be observed between both surfaces, but rather a broader (∼0.1 eV for fluorine and nitrogen, ∼0.2 eV for carbon) line shape for the case of Zn-ZnO. The higher intensities associated to the spectral features related to possible defluorination for Zn- compared to O-ZnO appear in line with the higher reactivity of the first compared to the latter surface termination. As it is discussed in Ref. [292], no traces of chemical bonding between the molecule and the substrate can be

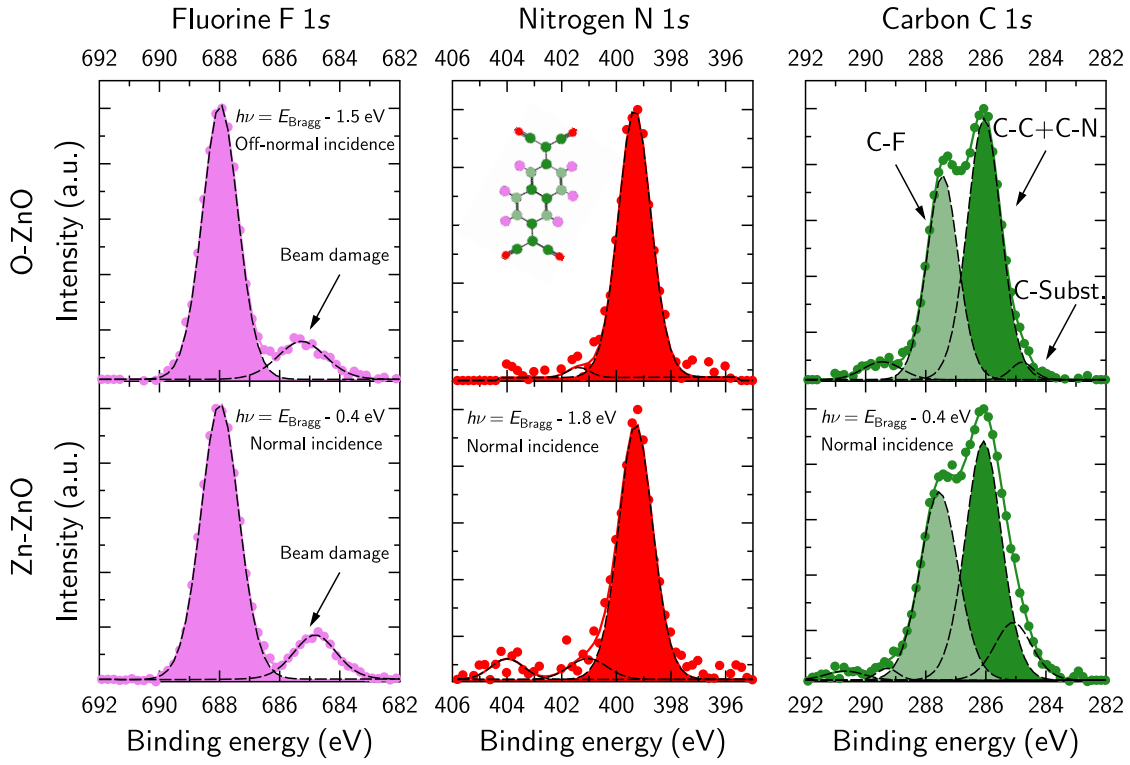

Figure E.1.: Hard-XPS measurements of F6TCNNQ adsorbed on the polar surfaces of ZnO. A very similar fitting model is used to account for the photoelectron yield in the XSW measurements shown in Fig. [E.2].

identified, nor evidences of integer CT, since the N 1*s* core-level peak only shows a single peak, as opposed to PTCDI (see Sec. [9.2.1.1]) and HATCN [292].

The XSW data was evaluated using the fitting model of Fig. [E.1], which allowed to obtain structural information from the two inequivalent carbon species considered as well as the fluorine and nitrogen atoms. The results are presented in Fig. [E.2] and the fitting parameters f_H and P_H included in Tab. [E.1]. Overall the trends are very similar to what has been observed for the perylene derivatives adsorbed on the standard-treated surfaces (see Sec. [8.1] for the procedure) studied in Chap. [9]. Especially on O-ZnO, the values obtained are almost the same as those for perylene, PTCDA and PTCDI, supporting the finding that this substrate has no specific interaction with the molecular carbon backbone. Also, one can observe that the coherent fractions are very similar, although the perylene derivatives and the F6TCNNQ were measured on different substrates and beamtimes, thus pointing out that the standard treatment yields very reproducible, although slightly disordered, surface conditions.

The XSW results also corroborate that the Zn-terminated surface is more prone to become disordered, as shown by the much lower coherent fractions of F6TCNNQ. For this case, the results leave some room for the interpretation of the real adsorption position of the adsorbate, either on top of the oxygen surface species or directly on the topmost zinc layer. For PTCDI, it is more clear that the right scenario is adsorption directly on the zinc layer, since the reported adsorption distances appear too far away from the oxygen species if this situation is considered. Nonetheless, for F6TCNNQ the situation is not so evident.

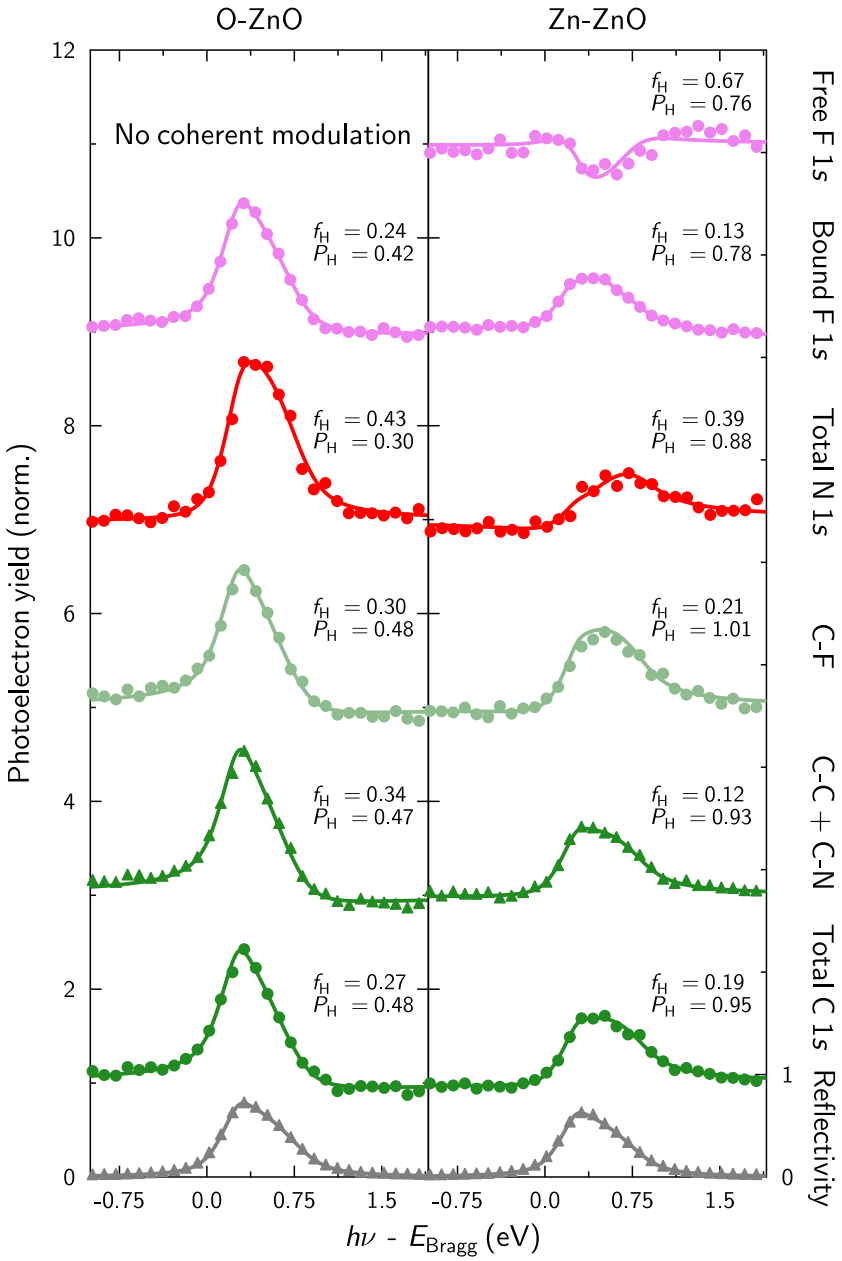

Figure E.2.: XSW measurements of F6TCNNQ adsorbed on the polar surfaces of ZnO. **H** = [00-2] for the O-ZnO and **H** = [002] for the Zn-ZnO surface.

Indeed, the adsorption distances for the on-top-of-zinc case are very short as shown in Fig. [E.3]. However, such a short adsorption can be associated with the higher broadening of the core-level spectra [166] and the higher reactivity of the Zn-terminated surface. Last but not least, the free fluorine atoms yield a very similar photoelectron modulation as the surface oxygen species. The fitting parameters are very similar as well, meaning that, upon detaching from the molecule, they may occupy surface-oxygen-like positions directly bonding to zinc atoms. Actually, even the fluorine atoms of the molecule seem to be

Substrate	Component	$f_{00\mp2}$	$P_{00\mp2}$	$d_{00\mp2}$ (Å)	
O-ZnO	F 1*s* free	–	–	–	
	F 1*s* molecule	0.24	0.42	2.97	
	N 1*s* total	0.43	0.30	2.66	
	C–F	0.30	0.48	3.12	
	C–C + C–N	0.34	0.47	3.10	
	C 1*s* total	0.27	0.48	3.12	
Zn-ZnO				On top of OH	On top of Zn
	F 1*s* free	0.67	0.76	2.60	1.75
	F 1*s* molecule	0.13	0.78	2.66	1.80
	N 1*s* total	0.39	0.88	2.92	2.06
	C–F	0.21	1.01	3.25	2.40
	C–C + C–N	0.12	0.93	3.05	2.19
	C 1*s* total	0.19	0.95	3.10	2.24

Table E.1.: Fitting parameters extracted from the XSW measurements presented in Fig. [E.2] corresponding to (sub)monolayer coverages of F6TCNNQ adsorbed on the polar surfaces of ZnO. For the O-ZnO surface, the adsorption distances are given with respect to the surface oxygens. For the Zn-terminated surface, however, two hypothesis are given: one corresponding to the case where F6TCNNQ adsorbs on top of OH groups, the other one being the case where it adsorbs directly on the topmost zinc layer. For the adsorption of F6TCNNQ directly on the zinc layer, the provided distances take into account the outward relaxation (∼0.16 Å) of the topmost layer.

adsorbing at similar positions.

It is worth noting that the coherent fractions are low, especially for the Zn-terminated surface. As mentioned, the surface standard treatment without high-temperature annealing leaves the surface with a certain degree of disorder. However, this alone does not account for such a low coherent fractions. A plausible explanation is that F6TCNNQ adsorbs with a remarkable tilt of the central rings. This would explain on the one hand, why the nitrogens have a higher coherent fraction, all are similarly bending towards the surface, and on the other, why the two carbon components have such a dissimilar adsorption distances.

Finally, considering that the F4TCNQ and F6TCNNQ render very similar interface properties [292], one could compare the measurements presented here with the adsorption geometry for F4TCNQ on O-ZnO obtained from DFT calculations [490]. Thus, Xu et al. report an adsorption distance of 2.1 Å above the hydrogen atoms decorating the oxygen topmost layer. Considering that the O–H bond is ~ 1 Å, the results are virtually the same as the distance obtained from XSW. Besides, they obtain a difference of 0.4 Å between the nitrogen and the fluorine atoms, being the former the closest to the surface. Again, their calculations are in very good agreement with the values reported here.

Conclusions

In conclusion, the XSW results for the strong acceptor F6TCNNQ deposited on the O-ZnO surface show a very similar adsorption geometry as the perylene derivatives, with the same trend for the nitrogen atoms bending towards the surface and a virtually equal adsorption distance for the carbon core. On Zn-ZnO, however, F6TCNNQ adsorbs much closer to the surface than PTCDI with a significant degree of disorder, typical for molecules with a remarkable tilting, which may add up to the intrinsic surface disorder remaining from the sputtering. The results point out to a higher reactivity of the Zn-terminated surface, compared to O-ZnO, as deduced from the higher degree of defluorination and the lower

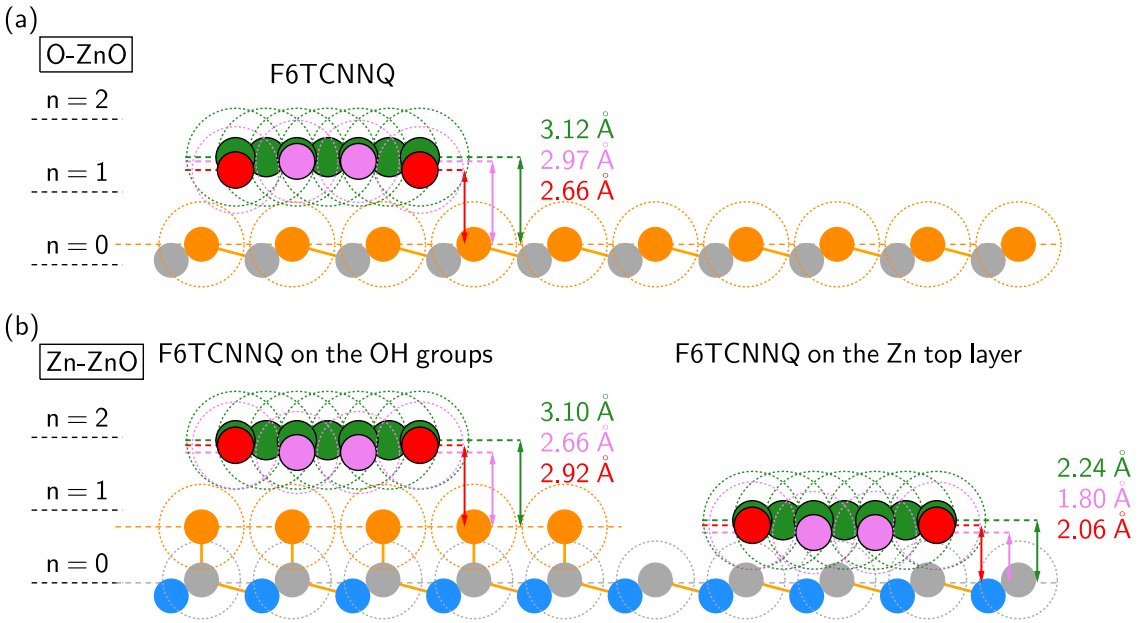

Figure E.3.: Adsorption of F6TCNNQ on the (a) O-ZnO and (b) Zn-ZnO polar surfaces. Note that the surface follows the color code introduced in Chap. [8]: in gray zinc, blue the bulk-oxygen and orange the surface-oxygen species. Hydrogen belonging to OH groups is not depicted. The values are extracted from the XSW measurements reported in Fig. [E.2] and summarized in Tab. [E.1]. As discussed in the main text, the two cases considered for the adsorption of the Zn-terminated surface are depicted, namely, the molecules adsorb on top of the OH groups or directly onto the topmost zinc layer. Note that, for simplicity, only the average carbon distance (Total C $1s$) is displayed. The dashed circles represent the vdW radii.

adsorption distance of the molecule. In both surfaces, however, the same trend for the adsorption geometry appears, namely, the nitrogen and fluorine atoms adsorbing closer to the surface.

F. Angular-dependent XSW analysis. Probing different depths

The electron analyzer available at beamline I09 (see Sec. [3.5.1]), where the XSW experiments presented here were performed, has a relatively large acceptance angle of ±30°. This may pose some inconvenience, e.g., photoelectrons are collected far away from the geometry where the non-dipole approximation holds (see Sec. [3.3.2.3]). Nonetheless, it also entails some advantages. For instance, more electrons can be collected thus increasing the signal-to-noise ratio, which makes information from weaker core-level features accessible. Also, the fact that the measured electrons can be separately analyzed in angular mode, depending on their emission (take-off) angle, enables one to exploit the information depth coming along with the different angles. This is particularly interesting when studying possible surface relaxation of the ZnO.

The angular mode allows one to select how many intervals or slices should be considered when collecting the photoelectrons. In our case, the 60° were divided in 24 slices, each recorded electrons coming from a 2.5° arc. Since in normal-incidence geometry (Sec. [3.3.2.2]) the sample blocks half of the analyzer aperture, only 12 of the 24 slices are actually collecting electrons. In practice, however, the first two (slice 12 and 13) and the last (slice 24) are not usable because of a very weak signal. In Fig. [F.1], the slices have been converted to actual angles. The 90° correspond to the electrons that are emitted perpendicular to the X-ray incident beam. The coherent fractions and positions are obtained using the signal for each separate slice to account for the photoelectron yield. Non-dipole corrections [47] for each separate angle are also applied. For the particular case of ZnO shown here, each emission angle is associated to a certain penetration depth, which is expressed in terms of ZnO layers, being one layer ∼2.6 Å (lattice spacing along [00±2] direction). The depth is calculated using the inelastic mean free path (λ) of the O $1s$ and Zn $3s$ electrons, ∼32 Å and ∼36 Å respectively, and the corresponding emission angle. More precisely, it is considered that 95% of the electrons originate within an interval of 3λ, which then travel a distance $d = 3\lambda\cos(\theta)$ through the sample, where θ is the emission angle.

The angle-dependent XSW results shown in Fig. [F.1] correspond to **standard-treated** (see Sec. [8.1] for the details of the treatment) O-ZnO and Zn-ZnO samples. For clarity, we only plot results for one case, however, the trends were found to be identical across other samples and beamtimes. Considering the value range, it is readily seen that the coherent fractions change substantially more compared to the coherent positions. Besides the extreme case of the O $1s$ signal stemming from the O-ZnO, which has been discussed in Sec. [8.2.2.4], the other coherent fractions vary within a range of ∼0.1, whereas the coherent positions only change within ∼ 0.03. The literature contains only a few references that report angular-dependent XSW results [66, 228, 517] and only Ref. [517] provides information for the coherent fractions and positions. There, it is shown the major impact on

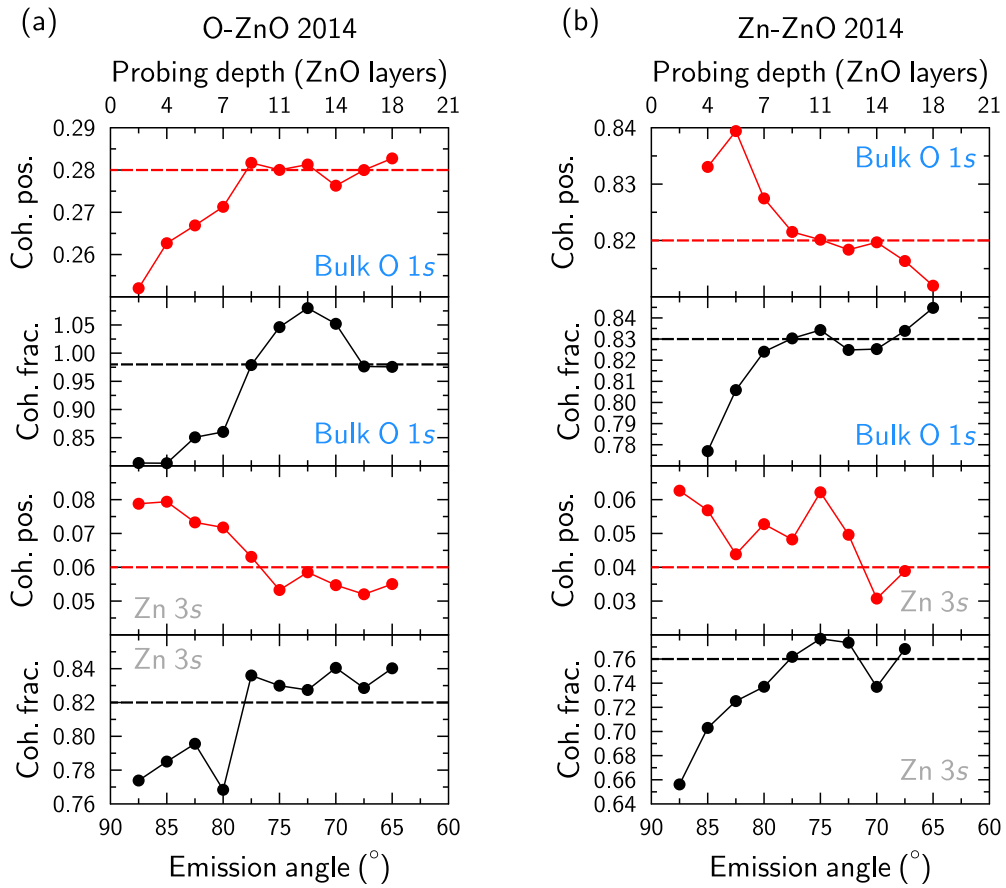

Figure F.1.: Coherent fractions and positions obtained from XSW measurements recorded in angular mode for the zinc Zn 3*s* and the oxygen O 1*s* core-level signals stemming from the two polar surfaces of ZnO. Each emission angle is associated to a certain depth (see text for the details). The dashed lines correspond to the values obtained in transmission mode.

the coherent fractions, in agreement with our findings. As it is discussed in Ref. [518], the analyzer may introduce some non-linear dependence to the electron collection that mostly affects the coherent fractions. In any case, it is not yet well understood why this happens.

For the discussion of the depth-dependent data in Fig. [F.1], one can roughly distinguish between the first ∼9 layers and the last 9 to 18 layers. The topmost ones seem to change significantly the values, whereas the last 9 render more stable results. This would go in line with a major impact of the sputtering on the first layers, which is in any case expected. The major discrepancy between the angle-resolved results and those obtained in transmission mode (i.e. integrating over all the angles), the latter indicated with a dashed line in Fig. [F.1], still lays within the experimental uncertainty as well as the statistical variation observed among different samples and measurements. Therefore, the discussion and the conclusions described in Chap. [8] are not compromised. In any case, a more systematic analysis of the angle-resolved data will be required to provide a final solid number for the surface relaxation, if there is any at all.

Finally, the results presented above give an idea of the uncertainty that may be introduced to the measurements if they are recorded with the analyzer operated in transmission

mode. In our case, the difference is shown to be 0.03 at most. In this direction, recent publications have started to consider how XSW measurements of COM adsorbates are affected by the large acceptance angle of the analyzer [66, 228, 517]. The angular spread of the coherent positions is also relatively small compared to that of the coherent fractions, although it depends on the core-level signal being considered [228]. While the discussion of relative adsorption distances and intramolecular distortions obtained in transmission mode still holds, it may be recommendable in the future to systematically consider the angular dependence of the coherent positions, especially if the values are to be used as benchmark for theoretical calculations.

G. Molecular bilayers and heterostructures investigated with XSW

This chapter contains the XSW analysis of different heteromolecular structures. They are part of a broader project that includes multiple characterization techniques, namely, STM, LEED, XPS and UPS. They were published in Ref. [519].

Context

A proper energy-level alignment between an organic active material and the metal electrode is of paramount importance to obtain an efficient charge transport through the metal-organic interface. Being able to tune at will the energy barriers for charge injection/withdrawal is an important step towards feasible, efficient organic optoelectronic devices. To this end, depositing a template layer of another organic compound between the metal contact and the active material has been proven an effective way to achieve it. However, new fundamental questions arise for these systems, where one is interested to see how the metal contact affects the heteromolecular interface. Does the substrate affect the electronic and conformational properties of the second layer? How is the interaction between the different organic layers? Do the molecules mix, form domains or keep a bilayer arrangement instead? If the latter is the case, does the second layer randomly arrange or follows some sort of ordering? Besides the remarkable fundamental interest of these questions, they also help to address design issues such as diffusion of the top layers towards the contacts or the stability of the template layers, all hampering the effective role of the template layer and eventually the device performance.

In recent years, (sub)monolayer as well as bilayer systems made of two different molecules have started to be systematically studied with the same set of techniques that have been successfully used to correlate conformational and electronic properties at the metal-organic interface. Starting with the case of heteromolecular (sub)monolayers, the mixing of molecules with opposite character, namely, donor and acceptor, has been shown to effectively tune the electrode work function (see Ref. [30] and references therein). In this context, different studies have investigated how the concentration of each molecule and the strength of the donor/acceptor character modify the interface properties [30, 31, 115]. In the precise context of vertical adsorption geometries, two independent groups have reported an unexpected behavior [345, 346]. More precisely, in a donor-acceptor heteromolecular (sub)monolayer, the molecule with the strongest acceptor character attracts the metal-electron cloud towards itself, which is further promoted by the fact that the nearby donor (or weakest acceptor) molecule repeals it. As a consequence, although the LUMO of the acceptor might get filled, the significant electron cloud below the molecule increases the Pauli repulsion and thus the molecule adsorption distance [346]. This leads to coun-

terintuitive situation such as in the case of PTCDA-CuPc on Ag(111), where the LUMO of PTCDA gets totally filled (indicating a major electronic coupling with the substrate), but its adsorption distance increases [345].

In the case of bilayer structures, the system PTCDA-CuPc on Ag(111) has emerged as the prototypical case. Stadtmüller et al. [116] first reported on the commensurate chemisorption of a CuPc monolayer deposited on a closed monolayer of PTCDA adsorbed on Ag(111). Later studies [520, 521] demonstrated that there is no evidence for the electronic coupling between PTCDA and CuPc, thus being the latter actually physisorbed on PTCDA. Thus, the UPS features appearing upon CuPc adsorption corresponded solely to PTCDA [520]. It was shown that charge transfer from silver to PTCDA increases with increasing CuPc coverage, which is explained by the screening effect that enables a further filling of the PTCDA LUMO [520]. Stadtmüller et al. also reported results of the inverse system, i.e. PTCDA adsorbed on a closed layer of CuPc on Ag(111) [522]. Interestingly, this system seems to be not favorable and what happens is that some CuPc molecules are moved to the second layer by the PTCDA molecules adsorbing directly on the silver surface.

The mechanism behind the molecular exchange, i.e. molecules of the second layer moving to the first and those initially in direct contact with the substrate being displaced up, is not yet clearly understood. In order to shed light upon this issue, we investigated two different systems, namely, CuPc deposited on a close layer of P4O on Ag(111) and CuPc deposited on a closed layer of P2O on Ag(111). It is well known that the small chemical difference between P2O and P4O has a strong impact on the interface properties with silver [71]. In particular, the interaction strength with the substrate (derived from the degree of LUMO filling, bending of the oxygen atoms and the average adsorption distance) is much higher for P4O than P2O, being the first chemisorbed whereas the latter is physisorbed on Ag(111). In a multitechnique study, we have identified that the interaction strength with the substrate is the key factor that decides which molecule will occupy the first layer regardless of the deposition sequence. By considering different measurable parameters for the separate monolayers adsorbed on the substrate of interest, as a way to characterize the interaction strength, one can predict the actual arrangement in the bilayer case [519]. Here, however, we will just focus on the XSW results and the subsequent problems encountered analyzing these systems.

Results and discussion

The first layer of PxO (x = 2,4) was prepared by depositing a thick film and annealing out the multilayer contribution (the process was monitored with XPS). This method ensures the presence of a closely-packed template layer. The CuPc layer was deposited afterwards and the nominal coverage, always being below a full monolayer, was calibrated with a QCM.

The problems found when analyzing the XSW data for these systems are manifold. First, the carbon signal stems from the first and the second layer. Secondly, if molecular exchange happens, it can be the case that the initial molecule is occupying positions in both layers. Therefore, one has to precisely know the deposited coverages and be able to decouple the core-level contributions of the first and second layer. The latter may

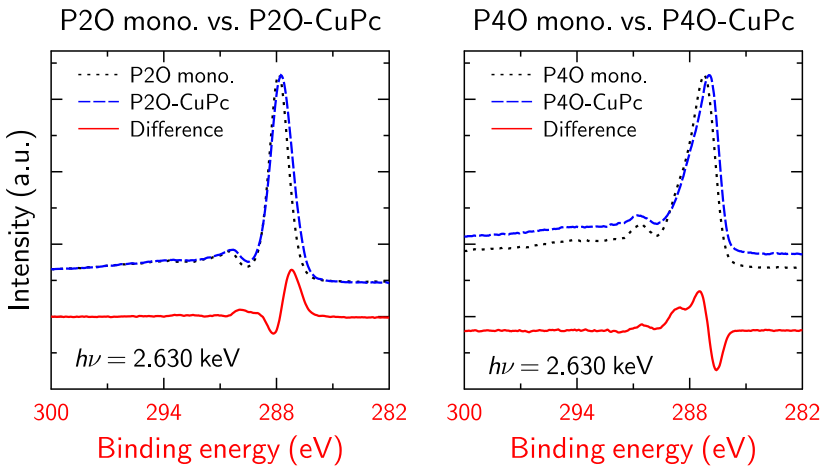

Figure G.1.: HR-XPS measurements ($h\nu = 700\,\text{eV}$) of the C 1s core-level signal corresponding to a closed monolayer of P2O (left) and P4O (right) deposited on Ag(111) with and without the subsequent CuPc deposition. The subtraction of the single PxO layer to the CuPc-PxO spectrum does not allow one to clearly identify the CuPc core-level features.

be easily solved if the two molecules used have clearly distinctive features that can be readily assigned to each case [114, 346, 523]. Otherwise a careful fit of the data needs to be done [345, 520, 524]. In our case, since PxO contain only carbon and oxygen and CuPc contain carbon, nitrogen and copper, the problem is to decouple the carbon contribution from each molecule. Figure [G.1] shows the C 1s signal for the PxO layer with and without the deposition of the CuPc layer. In both cases, it is very difficult to assign unambiguous components to each molecule, thus making this method inviable.

A careful core-level fit of the spectra was also carried out (not shown here), but the subsequent analysis of the XSW did not yield positive results. Consequently, Fig. [G.2] shows the successfully-analyzed XSW signals with all the values summarized in Tab. [G.1]. In the case of CuPc-P2O, however, the O 1s signal corresponds to molecules in the first and second layer, which we did not decouple. Nonetheless, the results provide interesting information. Starting with the CuPc-P2O case, the deposition of the CuPc layer induces an increase of 0.13 in the coherent position of oxygen (likely to stem from the average of both layers), whereas the coherent fraction remains relatively unchanged. Interesting enough, the coherent fractions of the copper and nitrogen signals of CuPc are much higher than those of P2O, which appears suspicious, since this would correspond to a highly ordered layer on top of a rather disordered one. Actually, by comparing the results with those of CuPc directly adsorbed on Ag(111) [525, 526], it is plausible to assume that CuPc diffuses towards the substrate surface and displaces the P2O to the second layer[1]. The situation appears similar to the molecular exchange reported in Ref. [522]. The molecular exchange of P2O by CuPc was later verified [519].

The CuPc-P4O, on the contrary, seems to follow the deposition order. P4O is forming a highly ordered layer on Ag(111) with high coherent fractions[2]. Upon deposition of

[1] The small discrepancy between the adsorption distance reported here for CuPc and those of the monolayer [525, 526] may well be due to the rearrangement of the adsorption distances in the heteromolecular monolayer, similarly to what it has been reported for other systems [345, 346].

[2] Recent reports have found that the coherent fractions may be influenced by some artifacts stemming

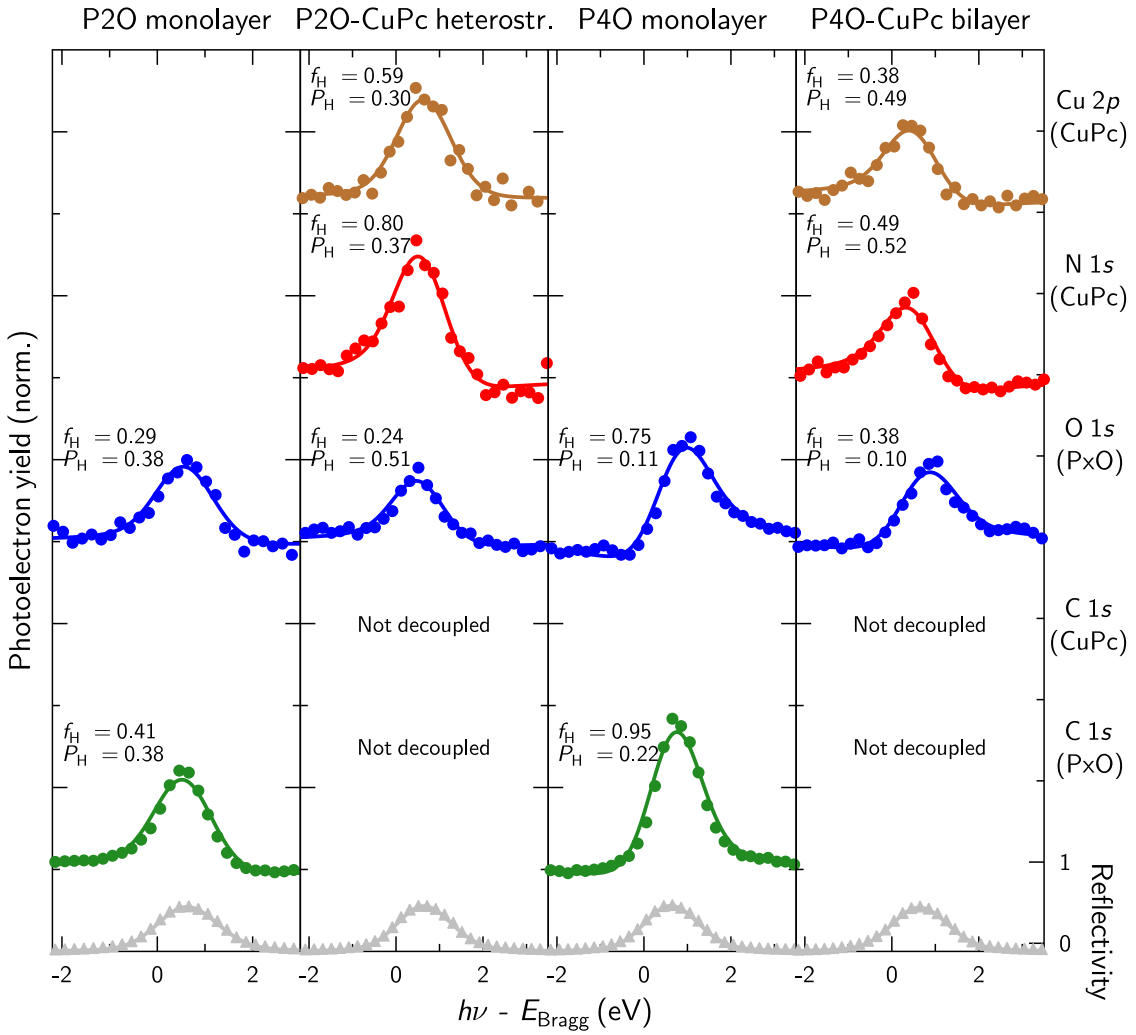

Figure G.2.: XSW measurements along **H** = [111] for the core-level signals that could be unambiguously assigned to the different CuPc-PxO systems deposited on Ag(111). The total area for each XP signal was used to evaluate the photoelectron yield. The oxygen signal of the P2O-CuPc case stems from P2O molecules in both layers.

the CuPc, the oxygen remains virtually at the same position, but the coherent fraction decreases substantially, which is tentatively attributed to some statistical perturbations introduced when depositing the CuPc. Nevertheless, the XSW results proof the bilayer formation arrangement, which is also supported by STM measurements [519].

Figure [G.3] summarizes the reported adsoprtion distances for the CuPc-P2O and the CuPc-P4O systems.

from the electron analyzer [518], especially on Ag(111), values above 0.9 are highly unrealistic (because of the thermal vibrations set an upper limit). As it is suggested in the supporting information of Ref. [518], the values should be decreased by 10%.

Monolayer							
	P2O		CuPc			P4O	
	C 1s	O 1s	C 1s	N 1s	Cu 2p	C 1s	O 1s
f_{111}	0.41	0.29	0.63 (*)	0.64 (*)	0.77 (*)	0.95	0.75
P_{111}	0.38	0.38	0.31 (*)	0.27 (*)	0.28 (*)	0.22	0.11
d_{111} (Å)	3.25	3.25	3.09 (*)	3.00 (*)	3.02 (*)	2.88	2.62
CuPc-P2O heterostructure							
f_{111}	n. d.	0.24 (#)	n. d.	0.80	0.59	–	–
P_{111}	n. d.	0.51 (#)	n. d.	0.37	0.30	–	–
d_{111} (Å)		3.56 (#)	n. d.	3.23	3.06	–	–
CuPc-P4O bilayer							
f_{111}	–	–	n. d.	0.49	0.38	n. d.	0.38
P_{111}	–	–	n. d.	0.52	0.49	n. d.	0.10
d_{111} (Å)	–	–	n. d.	5.94	5.87	n. d.	2.59

Table G.1.: Summary of the values extracted from the XSW measurements that could be unambiguously analyzed. (*) Values of the CuPc (sub)monolayer adsorbed on Ag(111) are taken from Ref. [526]. (#) The high adsorption distance, bigger than the sum of the substrate–oxygen vdW radii, suggests that this value is an average of P2O molecules in the first and second layer (later corroborated with STM [519]).

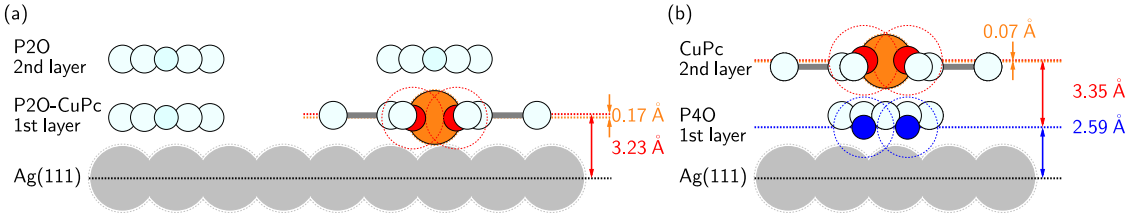

Figure G.3.: Sketch of the systems investigated as obtained from XSW. Only the unambiguously resolved adsorption distances are colored. (a) CuPc-P2O heterestructure adsorbed on Ag(111). Although CuPc is deposited on top of a closed layer of P2O, it diffuses towards the surface and displaces the P2O molecules to the top. Thus, the first layer is populated by CuPc as well as P2O molecules, whereas the second layer is only occupied by P2O molecules. (b) Bilayer arrangement formed upon deposition of CuPc on top of a closed layer of P4O.

H. XSW measurements at KMC-1 beamline (BESSY II). Test beamtime

The specific requirements of the XSW technique (see the details in Sec. [3.3]) make it difficult to find suitable beamlines that are able to allocate these kind of experiments. Due to the energy range employed (a few keV at least), it seems obvious that HAXPS beamlines may be the first option. In this context, one of the possible candidates is the KMC-1 beamline [527, 528] at BESSY II, in Berlin. Next, we present our XSW measurements of PTCDA adsorbed on Cu(111) performed at the HIKE end-station [529, 530] of the KMC-1 beamline. We discuss the improvements required to allocated XSW experiments with similar standards as those found in especially dedicated XSW beamlines.

The first problem faced during the experiments was the relatively bad UHV conditions. This is because HAXPS is commonly used to study bulk properties, thus making the surface preparation less demanding or even inexistent. This implies that many samples do not require any in-situ treatment and are loaded directly to the chamber. Consequently, the vacuum at the preparation chamber was at the 10^{-8} mbar regime and the analysis chamber at the high 10^{-10} mbar. Both ranges are suboptimal for surface-science experiments.

During the measurements, we found that the following important requirements were fulfilled:

- Optimum stability of the beam position.
- Optimum beam divergence from the Si(111) reflection of the monocrhomator.
- No appreciable contribution from higher harmonics of the beam.

However, some important issues were spotted:

- Beam current not recorded for all scans.
- No fluorescent screen available to record the reflectivity.
- Setup not optimum for NI-XSW experiments.
- Beam flux that compensate the defocussing of the beam was suboptimal.

The beam current is used to normalize the beam intensity, this way, possible beam fluctuations from measurement to measurement are removed. Most importantly, the reflectivity is at the core of the XSW analysis. Hence, not being able to measure it makes a proper data analysis impossible. In addition, the reflectivity is used as a reference to optimize the experiment geometry and is also used to find good spots (optimal crystallinity) on the sample. Although the detector is placed at 90° with respect to the incoming beam, which is optimum for NI-XSW experiments, the acceptance angle (±16°) of the analyzer limits

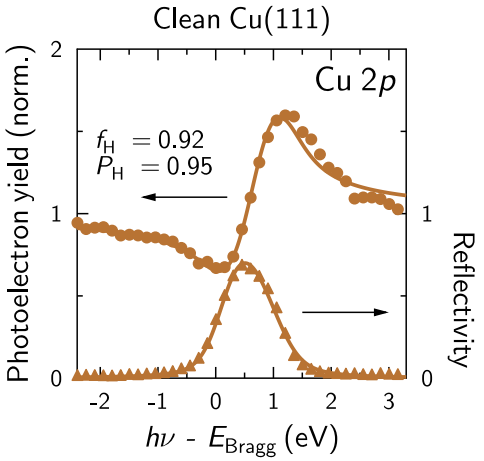

Figure H.1: Photoeletron yield modulation obtained from the Cu $2p$ core-level signal measured along **H** = [111] of a clean Cu(111) surface. The reflectivity curve employed to fit the data was obtained in another beamtime at the DLS. The creation of the XSW field can be deduced from the nicely modulated yield, comparable to that shown in Fig. [4.2].

the amount of electrons entering the analyzer, which has to be compensated with a higher flux in a fully defocused beam (to avoid beam damage and still having a good signal-to-noise ratio). Despite these drawbacks we were able to record some measurements of the clean crystal as well as the C $1s$ and O $1s$ for PTCDA. Fig. [H.1] contains an example of photoelectron yield modulation corresponding to the Cu $2p$ core-level signal of the clean copper substrate. It shows that the XSW field could be created. In order to provide a first fit to the data, the rocking curve from another experiment, at a dedicated bealmine, was used.

The preliminary XSW measurements of the copper substrate using the (111) reflection show that, indeed, a XSW field in back-reflection can be generated, as can be seen from the beam-energy dependent modulation of the Cu $2p$ photoelectron yield. Further analysis of the C $1s$ and O $1s$ core-levels will reveal whether the photoelectron signal stemming from the adsorbate layer is strong enough to be analyzed or, on the contrary, higher beam flux is needed for the purpose. In this direction, a first estimate of the (sub)monolayer data shows that the signal-to-background ratio is at the limit of what could be used and besides, the carboxylic contribution to the C $1s$ spectra cannot be resolved. Additionally, other issues were already spotted, which prevent the beamline to be properly used for this kind of experiments. These are: suboptimal vacuum conditions for measuring and depositing (sub)monolayer coverages, lack of a reflectivity screen and systematic recording of the beam current for each scan. Further analysis of the adsorbate data is required, but it appears that XSW experiments may be possible after a modification of the end-station, preferably with a suitable insertion device [226].

I. Improvements of the triple-cell evaporator

During this thesis some modifications were done to the evaporation cell, which was initially designed by Dr. Takuya Hosokai and later modified by Dr. Christoph Bürker. In particular, the electrical connections were improved and the material of some parts was changed from ceramics to stainless steel. Also, the pieces that were close to the heating wires were changed from stainless steel to molybdenum. The improvements were thought and designed together with Dr. Alexander Gerlach and Bernd Hofferberth, the latter being who prepared the blueprints attached next and dealt with the mechanical workshop. Following this improvements, a duplicate of the cell was also built.

The initial design, shown in Fig. [I.1] and described in more detail in Ref. [47], consists of three thermally-insulated evaporation cells that are resistively heated using a tantalum wire. A thermocouple allows one to monitor the temperature for the separate cells. The compounds are placed inside quartz-glass crucibles that are held with a stainless-steel structure. The parts used for the construction are the following:

- Multi-port flange (1 CF-40 + 5 CF-16) MDC 409014 (MDC Vacuum).
- z-axis linear transfer (100 mm) ZLTM100 (VACGEN) with two CF-40 flanges.
- Rotary-motion feedthrough MDC 670000 (MDC Vacuum).
- Multi-pin electrical feedthrough MDC 9132000 (MDC Vacuum)
- Thermocouple feedtrough MDC 9332014 (MDC Vacuum).
- T-piece to be attached between the cell (CF-40 flange) and the chamber (CF-40 flange) allowing a simultaneous pumping (CF-16 flange).

With time and use the ceramic parts (made of Macor®) that were embedded into of the structure started to get damaged (extreme case seen in Fig. [I.1c]). Also, the electrical connections and some of the insulating elements were not optimal. Therefore, modifications of the initial design were made towards correcting these issues:

- Solid pieces of ceramics were used to cover the supporting rods and the rotary feedthrough (see Fig. [I.2a]).
- The support structure was made entirely of stainless steel, including the bottom ring (Fig. [I.2b and c] and blueprint [I.3])
- Copper cables with Kapton® insulation were used.
- Electrical contacts for the heating wire were improved (Fig. [I.2c]).
- Thermal shielding for the crucibles improved (blueprints [I.4] and [I.5]).
- A shutter for the coevaporation of molecules was designed (see blueprint [I.6]).

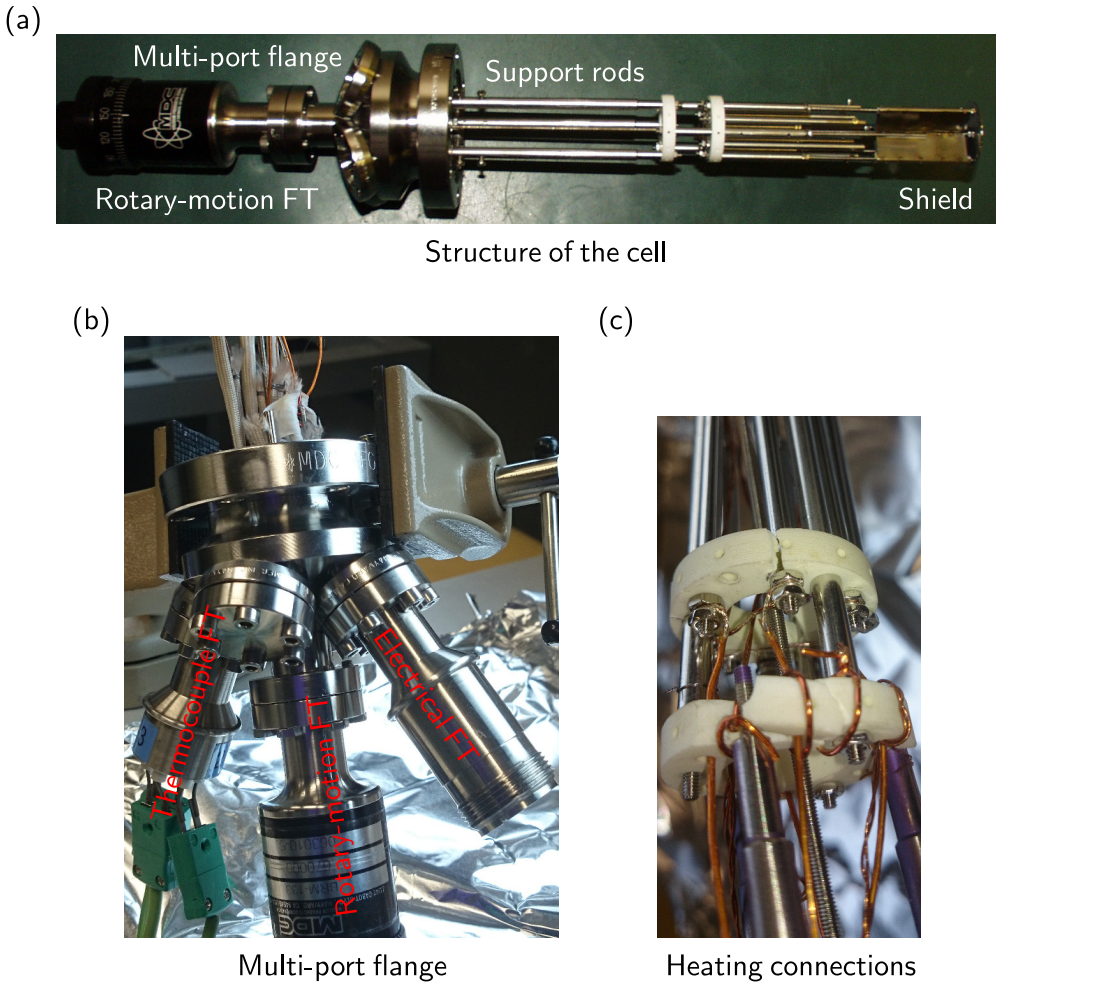

Figure I.1.: Photos of the initial design. FT stand for feedthrough. (a) Structure of the cells without the feedthroughs and without the z-axis transfer. (b) Detail of the multi-port flange with the different feedthroughs. Note the insulating fabric used for the bottom connections inside the cell. (c) Detail of the broken ceramic disks that kept the structure solid. The structure rods of the bottom are placed such that there is no electric contact with the bottom rods used for the heating of the crucibles.

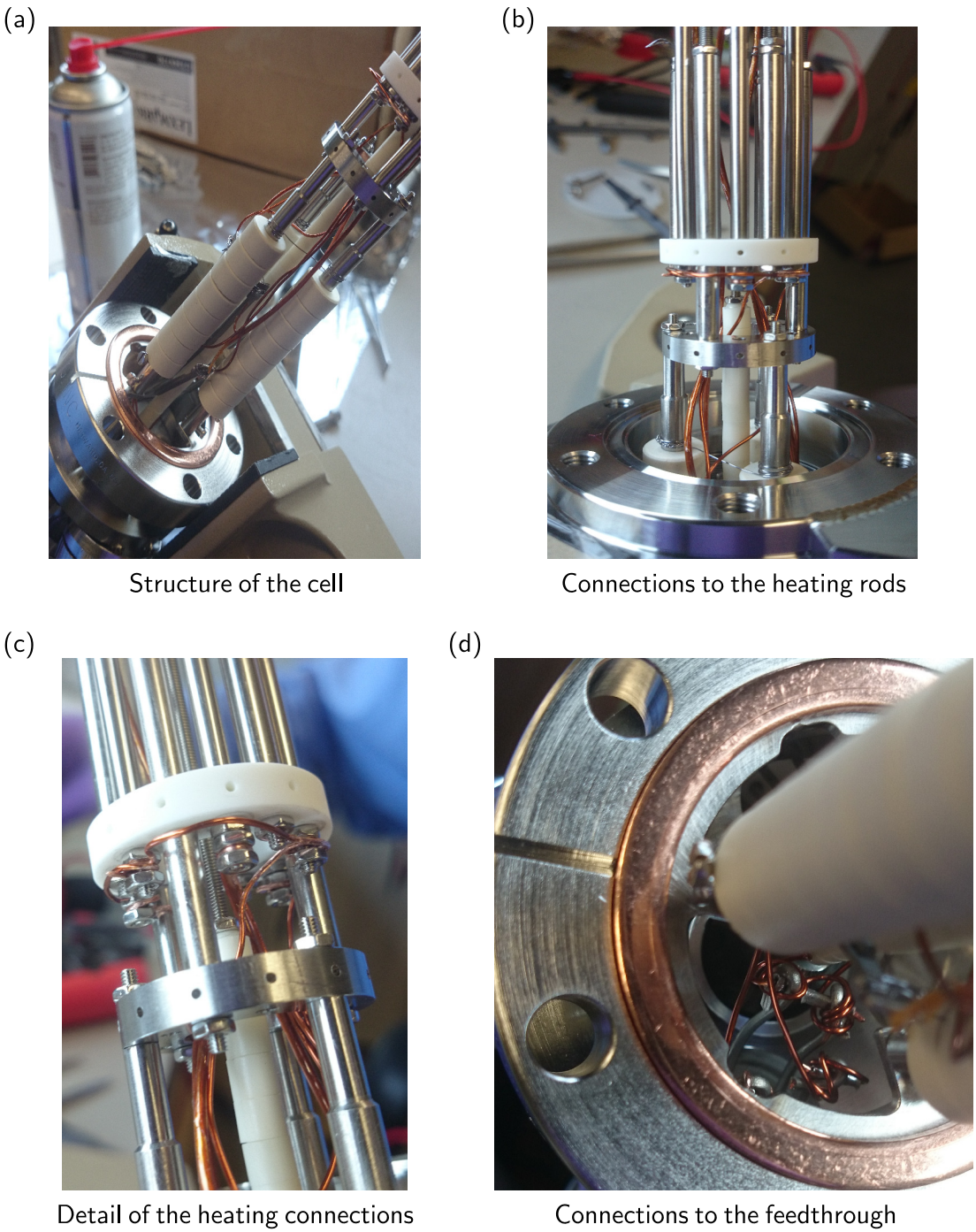

Figure I.2.: Photos showing the improvements applied to the evaporation cell. (a) Detail of the structure rods and the new stainless-steel ring that holds the upper part. Note the ceramic insulation. (b) Detail of the improved support section of the cell. The bottom ring now is made of stainless steel. The connections have been newly made and improved, as in can be seen in more detail in (c). The cables are covered with Kapton® to avoid shortcuts. (d) Close view of the bottom connections to the feedthroughs. It was made sure that no undesired contact exists.

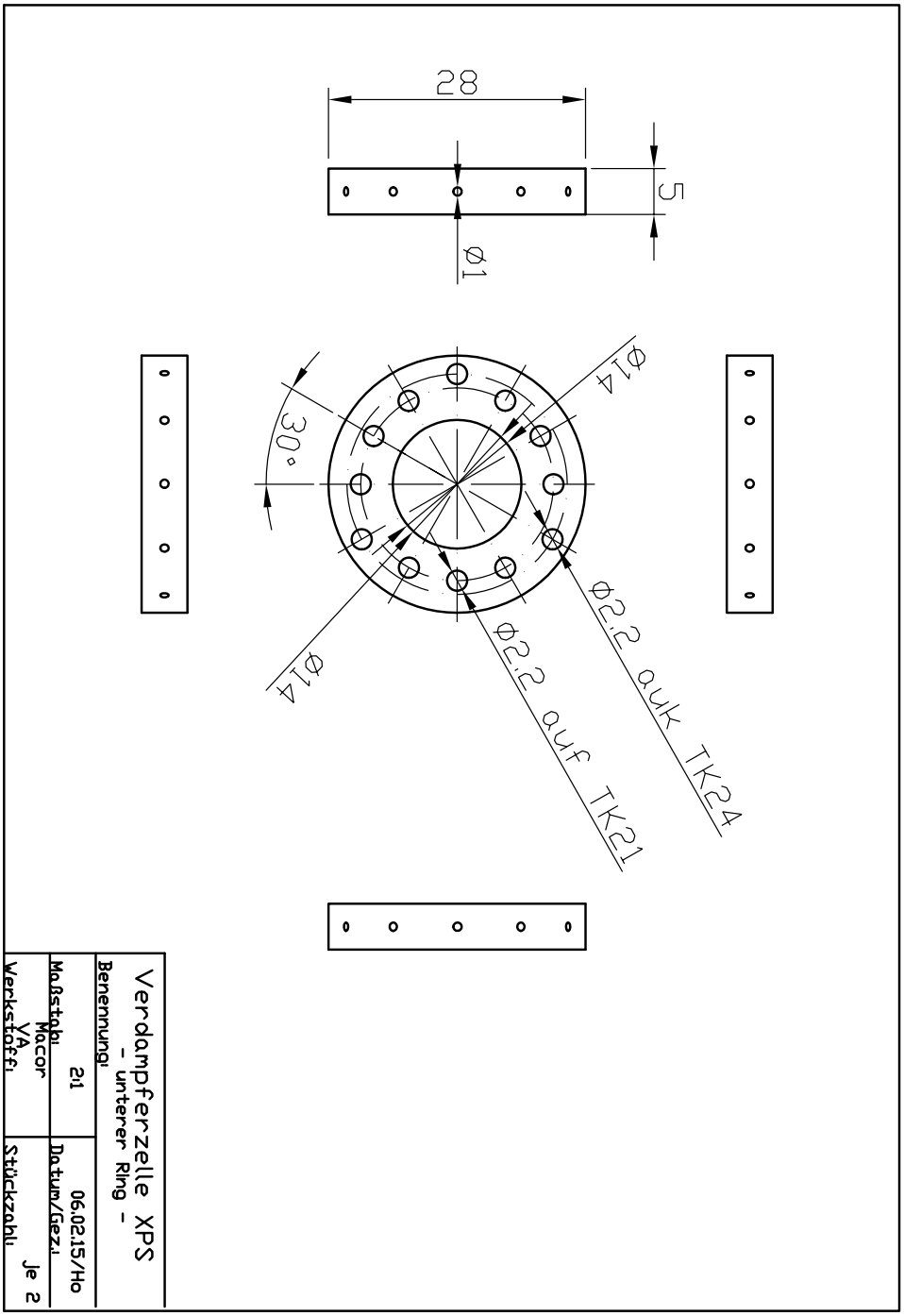

Figure I.3.: Stainless-steel ring that is used to hold the structure.

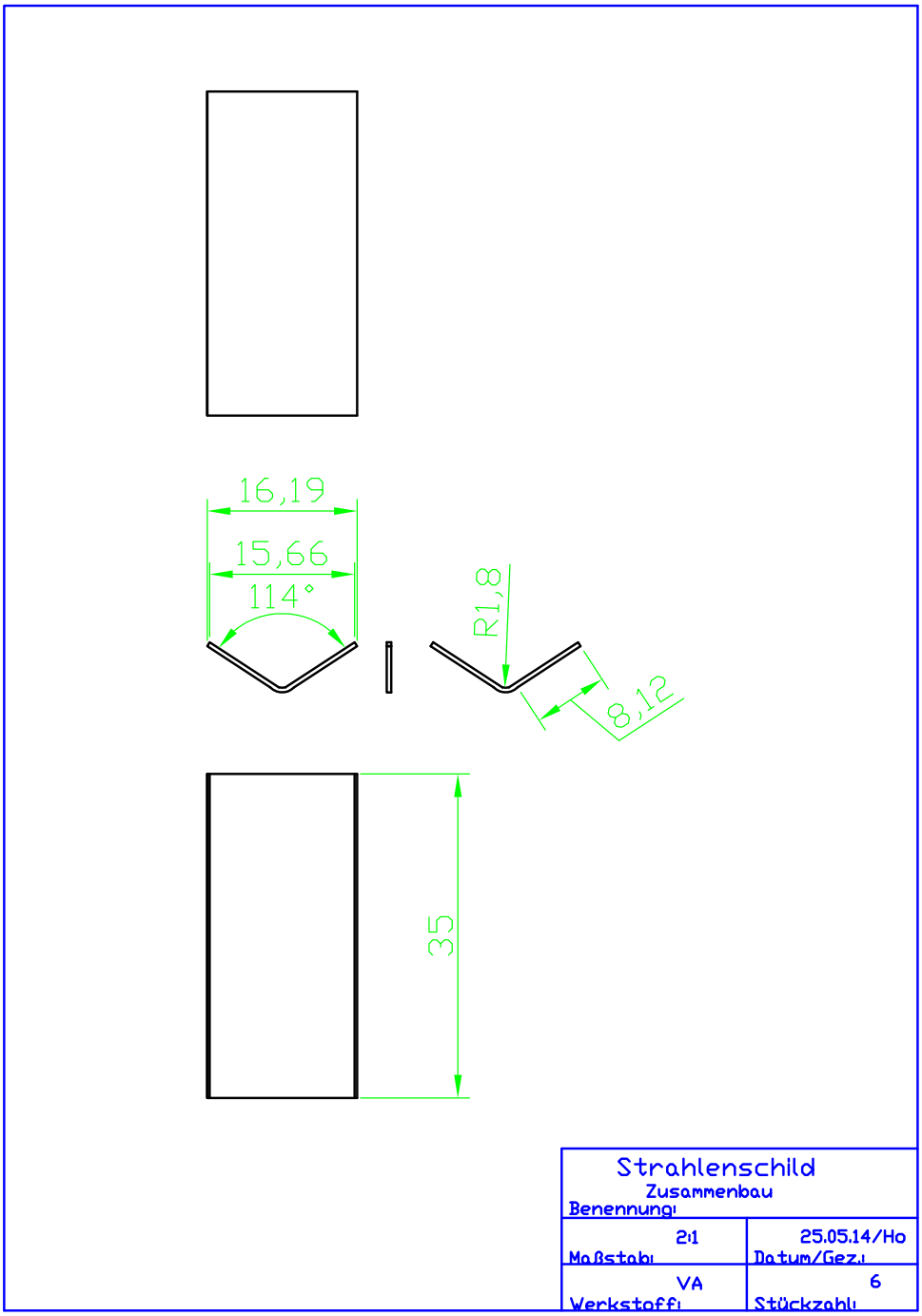

Figure I.4.: Thermal-insulating structure that separates the three crucibles (1).

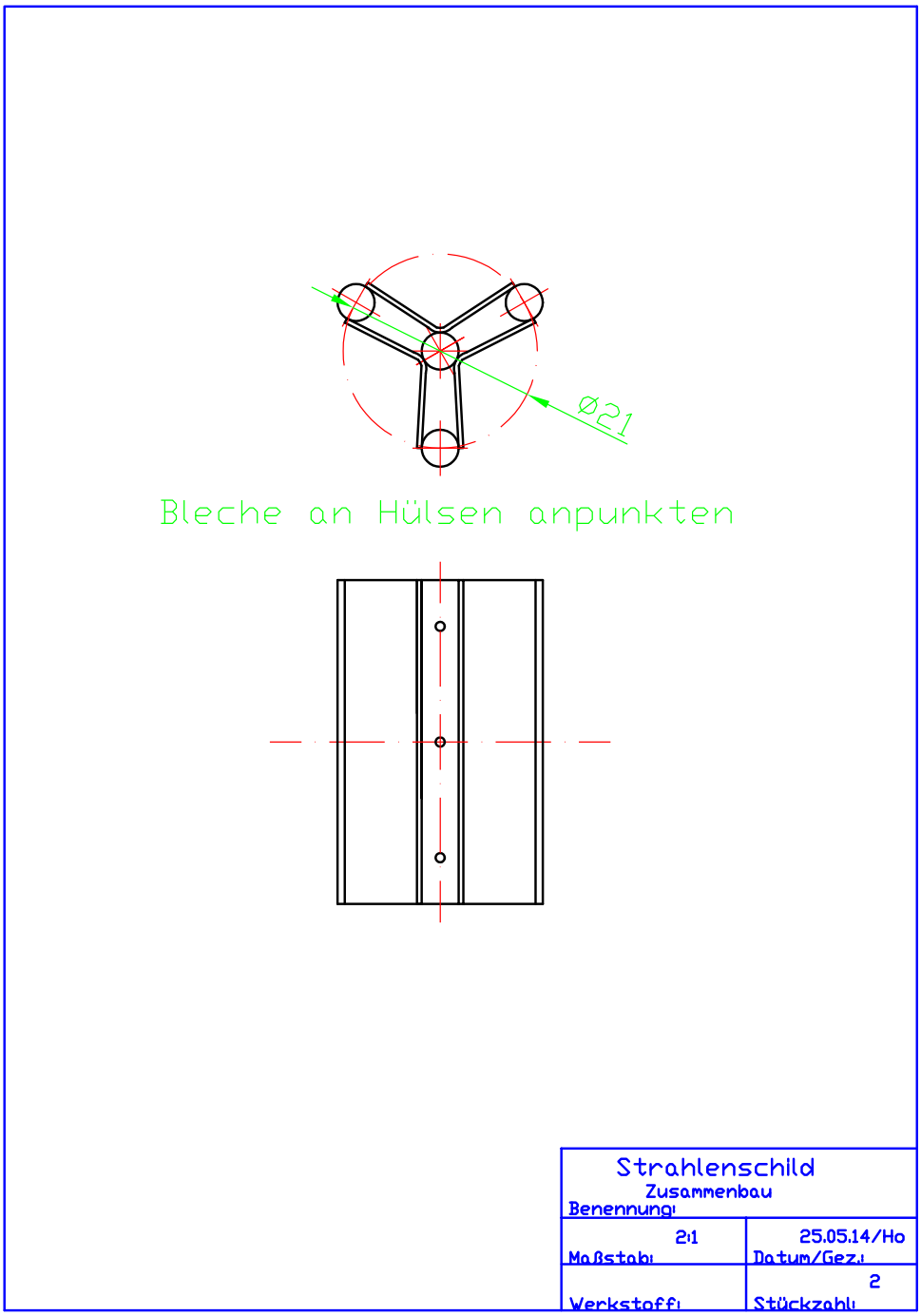

Figure I.5.: Thermal-insulating structure that separates the three crucibles (2).

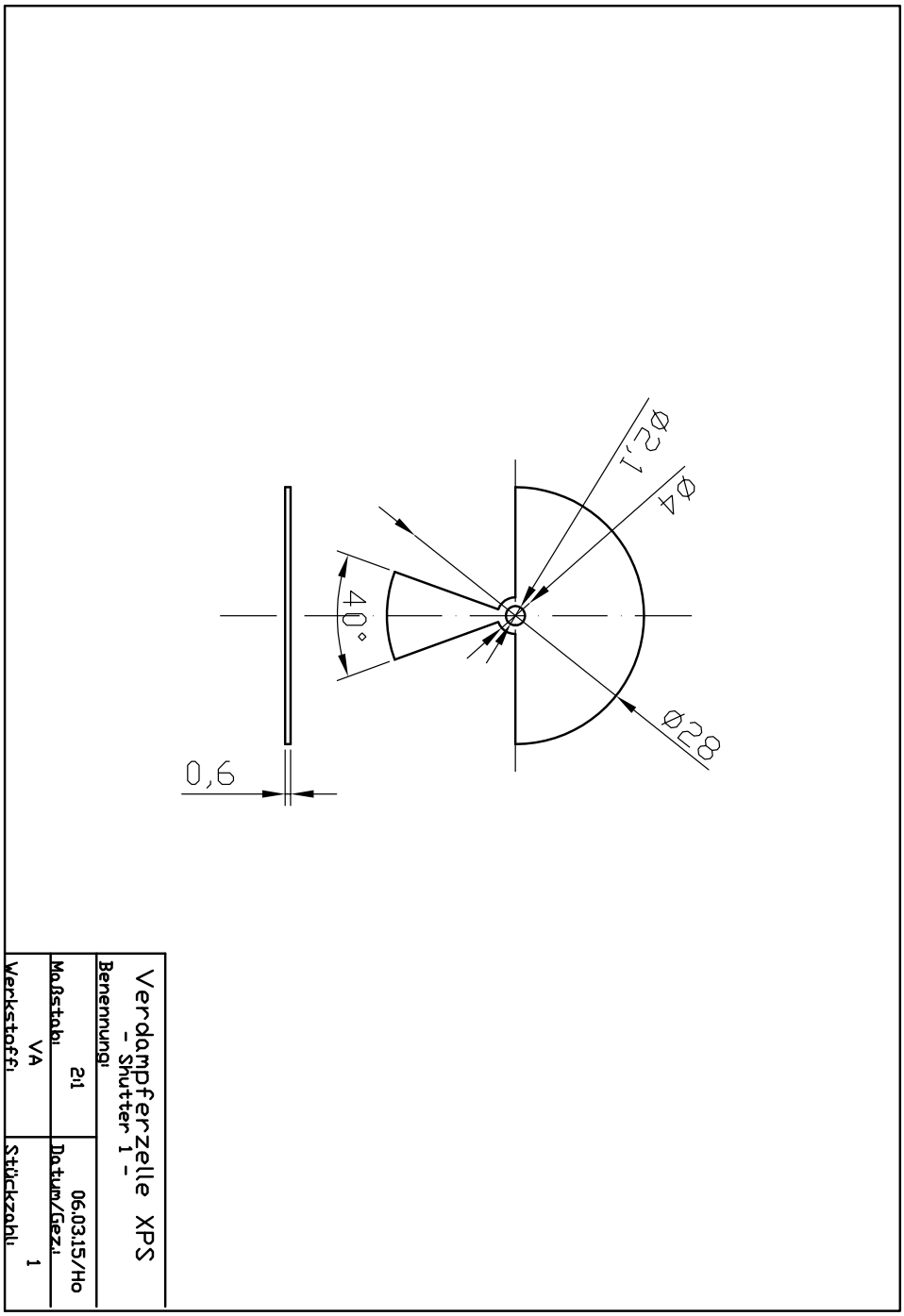

Figure I.6.: Stainless-steel shutter for coevaporation of two compounds.

Bibliography

[1] M. Castells, The rise of the Network Society: The Information Age: Economy, society, and culture, volume I of *Information Age* (Wiley-Blackwell, 2009), 2nd edition.

[2] S. C. Cowley, The quest for fusion power, *Nat. Phys.* **12**(5), 384, doi:10.1038/nphys3719 (2016).

[3] D. Mamaluy and X. Gao, The fundamental downscaling limit of field effect transistors, *Appl. Phys. Lett.* **106**(19), 193503, doi:10.1063/1.4919871 (2015).

[4] E. Gibney, Nobel for blue LED that revolutionized lighting, *Nature* **514**(7521), 152, doi:10.1038/514152a (2014).

[5] S. Günes, H. Neugebauer, and N. S. Sariciftci, Conjugated polymer-based organic solar cells, *Chem. Rev.* **107**(4), 1324, doi:10.1021/cr050149z (2007).

[6] A. Mishra and P. Bäuerle, Small molecule organic semiconductors on the move: Promises for future solar energy technology, *Angew. Chem. Int. Ed.* **51**(9), 2020, doi:10.1002/anie.201102326 (2012).

[7] R. M. Metzger, Unimolecular electronics, *Chem. Rev.* **115**(11), 5056, doi:10.1021/cr500459d (2015).

[8] A. Vilan, D. Aswal, and D. Cahen, Large-area, ensemble molecular electronics: Motivation and challenges, *Chem Rev.* **117**(5), 4248, doi:10.1021/acs.chemrev.6b00595 (2017).

[9] P. M. Beaujuge and J. M. J. Fréchet, Molecular design and ordering effects in π-functional materials for transistor and solar cell applications, *J. Am. Chem. Soc.* **133**(50), 20009, doi:10.1021/ja2073643 (2011).

[10] H. Sirringhaus, 25th anniversary article: Organic field-effect transistors: The path beyond amorphous silicon, *Adv. Mater.* **26**(9), 1319, doi:10.1002/adma.201304346 (2014).

[11] C. Liu, Y. Xu, and Y.-Y. Noh, Contact engineering in organic field-effect transistors, *Mater. Today* **18**(2), 79, doi:10.1016/j.mattod.2014.08.037 (2015).

[12] Y. Lin, Y. Li, and X. Zhan, Small molecule semiconductors for high-efficiency organic photovoltaics, *Chem. Soc. Rev.* **41**(11), 4245, doi:10.1039/c2cs15313k (2012).

[13] J. Roncali, P. Leriche, and A. Cravino, From one- to three-dimensional organic semiconductors: In search of the organic silicon?, *Adv. Mater.* **19**(16), 2045, doi:10.1002/adma.200700135 (2007).

[14] A. Moliton and R. C. Hiorns, The origin and development of (plastic) organic electronics, *Polym. Int.* **61**(3), 337, doi:10.1002/pi.4173 (2012).

[15] S. R. Forrest, The path to ubiquitous and low-cost organic electronic appliances on plastic, *Nature* **428**, 911, doi:10.1038/nature02498 (2004).

[16] Y. Qian, X. Zhang, L. Xie, D. Qi, B. K. Chandran, X. Chen, and W. Huang, Stretchable organic semiconductor devices, *Adv. Mater.* **28**(42), 9243, doi:10.1002/adma.201601278 (2016).

[17] Y. Nakayama, Y. Mizuno, T. Hosokai, T. Koganezawa, R. Tsuruta, A. Hinderhofer, A. Gerlach, K. Broch, V. Belova, H. Frank, M. Yamamoto, J. Niederhausen, H. Glowatzki, J. P. Rabe, N. Koch, H. Ishii, F. Schreiber, and N. Ueno, Epitaxial growth of an organic p–n heterojunction: C_{60} on single-crystal pentacene, *ACS Appl. Mater. Interfaces* **8**(21), 13499, doi:10.1021/acsami.6b02744 (2016).

[18] F. Anger, T. Breuer, A. Ruff, M. Klues, A. Gerlach, R. Scholz, S. Ludwigs, G. Witte, and F. Schreiber, Enhanced stability of rubrene against oxidation by partial and complete fluorination, *J. Phys. Chem. C* **120**(10), 5515, doi:10.1021/acs.jpcc.5b12293 (2016).

[19] M. Nam, M. Cha, H. H. Lee, K. Hur, K.-T. Lee, J. Yoo, I. K. Han, S. J. Kwon, and D.-H. Ko, Long-term efficient organic photovoltaics based on quaternary bulk heterojunctions, *Nat. Comms.* **8**, 14068, doi:10.1038/ncomms14068 (2017).

[20] H. Ishii, K. Sugiyama, E. Ito, and K. Seki, Energy level alignment and interfacial electronic structures at organic/metal and organic/organic interfaces, *Adv. Mater.* **11**(8), 605, doi:10.1002/(SICI)1521-4095(199906)11:8<605::AID-ADMA605>3.0.CO;2-Q (1999).

[21] F. Flores, J. Ortega, and H. Vázquez, Modelling energy level alignment at organic interfaces and density functional theory, *Phys. Chem. Chem. Phys.* **11**, 8658, doi:10.1039/B902492C (2009).

[22] Y. Zhou, C. Fuentes-Hernandez, J. Shim, J. Meyer, A. J. Giordano, H. Li, P. Winget, T. Papadopoulos, H. Cheun, J. Kim, M. Fenoll, A. Dindar, W. Haske, E. Najafabadi, T. M. Khan, H. Sojoudi, S. Barlow, S. Graham, J.-L. Brédas, S. R. Marder, A. Kahn, and B. Kippelen, A universal method to produce low-work function electrodes for organic electronics, *Science* **336**(6079), 327, doi:10.1126/science.1218829 (2012).

[23] M. Oehzelt, N. Koch, and G. Heimel, Organic semiconductor density of states controls the energy level alignment at electrode interfaces, *Nat. Commun.* **5**, 4174, doi:10.1038/ncomms5174 (2014).

[24] M. Oehzelt, K. Akaike, N. Koch, and G. Heimel, Energy-level alignment at organic heterointerfaces, *Sci. Adv.* **1**(10), e1501127, doi:10.1126/sciadv.1501127 (2015).

[25] N. Koch, Energy levels at interfaces between metals and conjugated organic molecules, *J. Phys.: Condens. Matter* **20**(18), 184008, doi:10.1088/0953-8984/20/18/184008 (2008).

[26] S.-M. Lee, J. H. Kwon, S. Kwon, and K. C. Choi, A review of flexible OLEDs toward highly durable unusual displays, *IEEE Trans. Electron Devices* **64**(5), 1922, doi:10.1109/TED.2017.2647964 (2017).

[27] J.-F. Tremblay, The rise of OLED displays, *C&EN* **94**(28), 30 (2016).

[28] H. Kroemer, Nobel Lecture: Quasielectric fields and band offsets: teaching electrons new tricks, *Rev. Mod. Phys.* **73**, 783, doi:10.1103/RevModPhys.73.783 (2001).

[29] M. Schwarze, W. Tress, B. Beyer, F. Gao, R. Scholz, C. Poelking, K. Ortstein, A. A. Gunther, D. Kasemann, D. Andrienko, and K. Leo, Band structure engineering in organic semiconductors, *Science* **352**(6292), 1446, doi:10.1126/science.aaf0590 (2016).

[30] E. Goiri, P. Borghetti, A. El-Sayed, J. E. Ortega, and D. G. de Oteyza, Multi-component organic layers on metal substrates, *Adv. Mater.* **28**(7), 1340, doi:10.1002/adma.201503570 (2016).

[31] B. Stadtmüller, S. Schröder, and C. Kumpf, Heteromolecular metal-organic interfaces: Electronic and structural fingerprints of chemical bonding, *J. Electron. Spectrosc. Relat. Phenom.* **204**, 80, doi:10.1016/j.elspec.2015.03.003 (2015).

[32] A. Hinderhofer and F. Schreiber, Organic-organic heterostructures: Concepts and applications, *ChemPhysChem* **13**(3), 628, doi:10.1002/cphc.201100737 (2012).

[33] I. Salzmann and G. Heimel, Toward a comprehensive understanding of molecular doping organic semiconductors (review), *J. Electron Spectrosc. Relat. Phenom.* **204**, 208, doi:10.1016/j.elspec.2015.05.001 (2015).

[34] I. Salzmann, G. Heimel, M. Oehzelt, S. Winkler, and N. Koch, Molecular electrical doping of organic semiconductors: Fundamental mechanisms and emerging dopant design rules, *Acc. Chem. Res.* **49**(3), 370, doi:10.1021/acs.accounts.5b00438 (2016).

[35] R. M. Hewlett and M. A. McLachlan, Surface structure modification of ZnO and the impact on electronic properties, *Adv. Mater.* **28**(20), 3893, doi:10.1002/adma.201503404 (2016).

[36] A. Kumatani, Y. Li, P. Darmawan, T. Minari, and K. Tsukagoshi, On practical charge injection at the metal/organic semiconductor interface, *Sci. Rep.* **3**(1), 1026, doi:10.1038/srep01026 (2013).

[37] A. Opitz, J. Wagner, W. Brütting, I. Salzmann, N. Koch, J. Manara, J. Pflaum, A. Hinderhofer, and F. Schreiber, Charge separation at molecular donor-acceptor interfaces: Correlation between morphology and solar cell performance, *IEEE J. Sel. Top. Quant.* **16**, 1707, doi:10.1109/JSTQE.2010.2048096 (2010).

[38] N. Koch, Organic electronic devices and their functional interfaces, *ChemPhysChem* **8**(10), 1438, doi:10.1002/cphc.200700177 (2007).

[39] S. Braun, W. R. Salaneck, and M. Fahlman, Energy-level alignment at organic/metal and organic/organic interfaces, *Adv. Mater.* **21**(14–15), 1450, doi:10.1002/adma.200802893 (2009).

[40] N. Koch, N. Ueno, and A. T. S. Wee (Editors), The molecule-metal interface (Wiley VCH-Verlag, Weinheim, 2013), doi:10.1002/9783527653171.

[41] A. Kahn, N. Koch, and W. Gao, Electronic structure and electrical properties of interfaces between metals and π-conjugated molecular films, *J. Polym. Sci. B Polym. Phys.* **41**(21), 2529, doi:10.1002/polb.10642 (2003).

[42] J.-L. Bredas, Mind the gap!, *Mater. Horiz.* **1**(1), 17, doi:10.1039/C3MH00098B (2014).

[43] A. Kahn, Fermi level, work function and vacuum level, *Mater. Horiz.* **3**(1), 7, doi:10.1039/C5MH00160A (2016).

[44] M. Schwoerer and H. C. Wolf, Organic molecular solids (Wiley-VCH Verlag GmbH & Co., Weinheim, 2007), doi:10.1002/9783527618651.

[45] A. Köhler and B. Heinz, Electronic processes in organic semiconductors, an introduction (Wiley-VCH Verlag GmbH, 2015), doi:10.1002/9783527685172.

[46] N. Ueno and S. Kera, Electron spectroscopy of functional organic thin films: Deep insights into valence electronic structure in relation to charge transport property, *Prog. Surf. Sci.* **83**(10–12), 490, doi:10.1016/j.progsurf.2008.10.002 (2008).

[47] C. Bürker, Adsorption geometry of π-conjugated organic molecules on metal surfaces studied with the X-ray standing wave technique, Ph.D. thesis, Eberhard Karls Universität Tübingen (2014).

[48] Z. Zhang and J. T. Yates, Band bending in semiconductors: Chemical and physical consequences at surfaces and interfaces, *Chem. Rev.* **112**(10), 5520, doi:10.1021/cr3000626 (2012).

[49] D. Cahen and A. Kahn, Electron energetics at surfaces and interfaces: Concepts and experiments, *Adv. Mater.* **15**(4), 271, doi:10.1002/adma.200390065 (2003).

[50] L. Romaner, G. Heimel, J. L. Brédas, A. Gerlach, F. Schreiber, R. L. Johnson, J. Zegenhagen, S. Duhm, N. Koch, and E. Zojer, Impact of bidirectional charge transfer and molecular distortions on the electronic structure of a metal-organic interface, *Phys. Rev. Lett.* **99**, 256801, doi:10.1103/PhysRevLett.99.256801 (2007).

[51] O. T. Hofmann, P. Rinke, M. Scheffler, and G. Heimel, Integer versus fractional charge transfer at metal(/insulator)/organic interfaces: Cu(/NaCl)/TCNE, *ACS Nano* **9**(5), 5391, doi:10.1021/acsnano.5b01164 (2015).

[52] G. Witte, S. Lukas, P. S. Bagus, and C. Wöll, Vacuum level alignment at organic/metal junctions: ´´Cushion´´ effect and the interface dipole, *Appl. Phys. Lett.* **87**(26), 263502, doi:10.1063/1.2151253 (2005).

[53] P. S. Bagus, V. Staemmler, and C. Wöll, Exchangelike effects for closed-shell adsorbates: Interface dipole and work function, *Phys. Rev. Lett.* **89**(9), 096104, doi:10.1103/PhysRevLett.89.096104 (2002).

[54] A. Opitz, A. Wilke, P. Amsalem, M. Oehzelt, R.-P. Blum, J. P. Rabe, T. Mizokuro, U. Hörmann, R. Hansson, E. Moons, and N. Koch, Organic heterojunctions: Contact-induced molecular reorientation, interface states, and charge re-distribution, *Sci. Rep.* **6**, 21291, doi:10.1038/srep21291 (2016).

[55] M. Samadi Khoshkhoo, H. Peisert, T. Chassé, and M. Scheele, The role of the density of interface states in interfacial energy level alignment of PTCDA, *Org. Elec.* **49**, 249, doi:10.1016/j.orgel.2017.06.065 (2017).

[56] N. Armbrust, F. Schiller, J. Güdde, and U. Höfer, Model potential for the description of metal/organic interface states, *Sci. Rep.* **7**, 46561, doi:10.1038/srep46561 (2017).

[57] N. Koch, A. Gerlach, S. Duhm, H. Glowatzki, G. Heimel, A. Vollmer, Y. Sakamoto, T. Suzuki, J. Zegenhagen, J. P. Rabe, and F. Schreiber., Adsorption induced intramolecular dipole: Correlating molecular conformation and interface electronic structure, *J. Am. Chem. Soc.* **130**(23), 7300, doi:10.1021/ja800286k (2008).

[58] C. Bürker, N. Ferri, A. Tkatchenko, A. Gerlach, J. Niederhausen, T. Hosokai, S. Duhm, J. Zegenhagen, N. Koch, and F. Schreiber, Exploring the bonding of large hydrocarbons on noble metals: Diindoperylene on Cu(111), Ag(111), and Au(111), *Phys. Rev. B* **87**(16), 165443, doi:10.1103/PhysRevB.87.165443 (2013).

[59] W. Liu, F. Maaß, M. Willenbockel, C. Bronner, M. Schulze, S. Soubatch, F. S. Tautz, P. Tegeder, and A. Tkatchenko, Quantitative prediction of molecular adsorption: Structure and binding of benzene on coinage metals, *Phys. Rev. Lett.* **115**(3), 036104, doi:10.1103/PhysRevLett.115.036104 (2015).

[60] A. Tkatchenko, L. Romaner, O. T. Hofmann, E. Zojer, C. Ambrosch-Draxl, and M. Scheffler, Van der Waals interactions between organic adsorbates and at organic/inorganic interfaces, *MRS Bull.* **35**(06), 435, doi:10.1557/mrs2010.581 (2010).

[61] R. J. Maurer, V. G. Ruiz, J. Camarillo-Cisneros, W. Liu, N. Ferri, K. Reuter, and A. Tkatchenko, Adsorption structures and energetics of molecules on metal surfaces: Bridging experiment and theory, *Prog. Surf. Sci.* **91**(2), 72, doi:10.1016/j.progsurf.2016.05.001 (2016).

[62] A. Tkatchenko and M. Scheffler, Accurate molecular van der Waals interactions from ground-state electron density and free-atom reference data, *Phys. Rev. Lett.* **102**(7), 073005, doi:10.1103/PhysRevLett.102.073005 (2009).

[63] V. Ruiz, W. Liu, E. Zojer, M. Scheffler, and A. Tkatchenko, Density-functional theory with screened van der Waals interactions for the modeling of hybrid inorganic-organic systems, *Phys. Rev. Lett.* **108**(14), 146103, doi:10.1103/PhysRevLett.108.146103 (2012).

[64] N. Ferri, R. A. DiStasio, A. Ambrosetti, R. Car, and A. Tkatchenko, Electronic properties of molecules and surfaces with a self-consistent interatomic van der Waals density functional, *Phys. Rev. Lett.* **114**(17), 176802, doi:10.1103/PhysRevLett.114.176802 (2015).

[65] A. Gerlach, S. Sellner, F. Schreiber, N. Koch, and J. Zegenhagen, Substrate dependent bonding distances of PTCDA - A comparative X-ray standing wave study on Cu(111) and Ag(111), *Phys. Rev. B* **75**(4), 045401, doi:10.1103/PhysRevB.75.045401 (2007).

[66] S. Weiß, I. Krieger, T. Heepenstrick, S. Soubatch, M. Sokolowski, and F. S. Tautz, Determination of the adsorption geometry of PTCDA on the Cu(100) surface, *Phys. Rev. B* **96**(7), 075414, doi:10.1103/PhysRevB.96.075414 (2017).

[67] S. Duhm, A. Gerlach, I. Salzmann, B. Bröcker, R. Johnson, F. Schreiber, and N. Koch, PTCDA on Au(111), Ag(111) and Cu(111): Correlating bonding distance and interfacial charge transfer, *Org. Electron.* **9**(1), 111, doi:10.1016/j.orgel.2007.10.004 (2008).

[68] M. Willenbockel, D. Lüftner, B. Stadtmüller, G. Koller, C. Kumpf, S. Soubatch, P. Puschnig, M. G. Ramsey, and F. S. Tautz, The interplay between interface structure, energy level alignment and chemical bonding strength at organic-metal interfaces, *Phys. Chem. Chem. Phys.* **17**(3), 1530, doi:10.1039/C4CP04595E (2014).

[69] A. Franco-Cañellas, Q. Wang, K. Broch, D. A. Duncan, P. K. Thakur, L. Liu, S. Kera, A. Gerlach, S. Duhm, and F. Schreiber, Metal-organic interface functionalization via acceptor end groups: PTCDI on coinage metals, *Phys. Rev. Materials* **1**(1), 013001(R), doi:10.1103/PhysRevMaterials.1.013001 (2017).

[70] S. K. M. Henze, O. Bauer, T.-L. Lee, M. Sokolowski, and F. S. Tautz, Vertical bonding distances of PTCDA on Au(111) and Ag(111): Relation to the bonding type, *Surf. Sci.* **601**(6), 1566, doi:10.1016/j.susc.2007.01.020 (2007).

[71] G. Heimel, S. Duhm, I. Salzmann, A. Gerlach, A. Strozecka, J. Niederhausen, C. Bürker, T. Hosokai, I. Fernandez-Torrente, G. Schulze, S. Winkler, A. Wilke, R. Schlesinger, J. Frisch, B. Bröker, A. Vollmer, B. Detlefs, J. Pflaum, S. Kera, K. J. Franke, N. Ueno, J. I. Pascual, F. Schreiber, and N. Koch, Charged and metallic molecular monolayers through surface-induced aromatic stabilization, *Nature Chem.* **5**(3), 187, doi:10.1038/nchem.1572 (2013).

[72] L. Kilian, A. Hauschild, R. Temirov, S. Soubatch, A. Schöll, A. Bendounan, F. Reinert, T.-L. Lee, F. S. Tautz, M. Sokolowski, and E. Umbach, Role of intermolecular interactions on the electronic and geometric structure of a large π-conjugated molecule adsorbed on a metal surface, *Phys. Rev. Lett.* **100**(13), 136103, doi:10.1103/PhysRevLett.100.136103 (2008).

[73] O. T. Hofmann, H. Glowatzki, C. Bürker, G. M. Rangger, B. Bröker, J. Niederhausen, T. Hosokai, I. Salzmann, R.-P. Blum, R. Rieger, A. Vollmer, P. Rajput,

A. Gerlach, K. Müllen, F. Schreiber, E. Zojer, N. Koch, and S. Duhm, Orientation-dependent work-function modification using substituted pyrene-based acceptors, *J. Phys. Chem. C* **121**(44), 24657–, doi:10.1021/acs.jpcc.7b08451 (2017).

[74] T. Hosokai, K. Yonezawa, K. Kato, R. Makino, J. Yang, K. R. Koswattage, A. Gerlach, F. Schreiber, N. Ueno, and S. Kera, Structural requirements for surface-induced aromatic stabilization, *MRS Proc.* **1647**, doi:10.1557/opl.2014.348 (2014).

[75] K. Yonezawa, Y. Suda, S. Yanagisawa, T. Hosokai, K. Kato, T. Yamaguchi, H. Yoshida, N. Ueno, and S. Kera, Charge transfer states appear in the π-conjugated pure hydrocarbon molecule on Cu(111), *Appl. Phys. Express* **9**(4), 045201, doi:10.7567/APEX.9.045201 (2016).

[76] H. Yamane, K. Kanai, Y. Ouchi, N. Ueno, and K. Seki, Impact of interface geometric structure on organic-metal interface energetics and subsequent films electronic structure, *J. Electron. Spectrosc. Relat. Phenom.* **174**(1–3), 28, doi:10.1016/j.elspec.2009.03.002 (2009).

[77] M.-C. Lu, R.-B. Wang, A. Yang, and S. Duhm, Pentacene on Au(111), Ag(111) and Cu(111): From physisorption to chemisorption, *J. Phys.: Condens. Matter* **28**(9), 094005, doi:10.1088/0953-8984/28/9/094005 (2016).

[78] X. Bouju, C. Mattioli, G. Franc, A. Pujol, and A. Gourdon, Bicomponent supramolecular architectures at the vacuum–solid interface, *Chem. Rev.* **117**(3), 1407, doi:10.1021/acs.chemrev.6b00389 (2017).

[79] J. A. Venables, G. D. T. Spiller, and M. Hanbücken, Nucleation and growth of thin films, *Rep. Prog. Phys.* **47**(4), 399, doi:10.1088/0034-4885/47/4/002 (1984).

[80] M. Einax, W. Dieterich, and P. Maass, Colloquium: Cluster growth on surfaces: Densities, size distributions, and morphologies, *Rev. Mod. Phys.* **85**(3), 921, doi:10.1103/RevModPhys.85.921 (2013).

[81] G. Hlawacek, P. Puschnig, P. Frank, A. Winkler, C. Ambrosch-Draxl, and C. Teichert, Characterization of step-edge barriers in organic thin-film growth, *Science* **321**(5885), 108, doi:10.1126/science.1159455 (2008).

[82] S. Bommel, N. Kleppmann, C. Weber, H. Spranger, P. Schäfer, J. Novák, S. Roth, F. Schreiber, S. Klapp, and S. Kowarik, Unravelling the multilayer growth of the fullerene C_{60} in real time, *Nat. Comm.* **5**, 5388, doi:10.1038/ncomms6388 (2014).

[83] S. Kowarik, A. Gerlach, and F. Schreiber, Organic molecular beam deposition: Fundamentals, growth dynamics, and *in-situ* studies, *J. Phys.: Condens. Matter* **20**, 184005, doi:10.1088/0953-8984/20/18/184005 (2008).

[84] U. Heinemeyer, K. Broch, A. Hinderhofer, M. Kytka, R. Scholz, A. Gerlach, and F. Schreiber, Real-time changes in the optical spectrum of organic semiconducting films and their thickness regimes during growth, *Phys. Rev. Lett.* **104**(25), 257401, doi:10.1103/PhysRevLett.104.257401 (2010).

[85] M. Oettel, M. Klopotek, M. Dixit, E. Empting, T. Schilling, and H. Hansen–Goos, Monolayers of hard rods on planar substrates. I. Equilibrium, *J. Chem. Phys.* **145**(7), 074902, doi:10.1063/1.4960618 (2016).

[86] M. Klopotek, H. Hansen-Goos, M. Dixit, T. Schilling, F. Schreiber, and M. Oettel, Monolayers of hard rods on planar substrates. II. Growth, *J. Chem. Phys.* **146**(8), 084903, doi:10.1063/1.4976308 (2017).

[87] J. Slaughter, W. Weber, G. Güntherodt, and C. M. Falco, Quantitative Auger and XPS analysis of thin films, *MRS Bull.* **17**(12), 39, doi:10.1557/S0883769400046947 (2013).

[88] P. L. Lévesque, H. Marchetto, T. Schmidt, F. C. Maier, H.-J. Freund, and E. Umbach, Correlation Between Substrate Morphology and the Initial Stages of Epitaxial Organic Growth: PTCDA/Ag(111), *J. Phys. Chem. C* **120**(34), 19271, doi:10.1021/acs.jpcc.6b06781 (2016).

[89] W. Brütting and C. Adachi (Editors), Physics of organic semiconductors (Wiley VCH-Verlag, Weinheim, Weinheim, 2012), 2nd edition, doi:10.1002/3527606637.

[90] S. Kowarik, A. Gerlach, S. Sellner, F. Schreiber, L. Cavalcanti, and O. Konovalov, Real-time observation of structural and orientational transitions during growth of organic thin films, *Phys. Rev. Lett.* **96**(12), 125504, doi:10.1103/PhysRevLett.96.125504 (2006).

[91] V. Coropceanu, J. Cornil, D. A. da Silva Filho, Y. Olivier, R. Silbey, and J.-L. Brédas, Charge transport in organic semiconductors, *Chem. Rev.* **107**(4), 926, doi:10.1021/cr050140x (2007).

[92] J. Hermann, R. A. DiStasio, and A. Tkatchenko, First-principles models for van der Waals interactions in molecules and materials: Concepts, theory, and applications, *Chem. Rev.* **117**(6), 4714, doi:10.1021/acs.chemrev.6b00446 (2017).

[93] L. Woods, D. Dalvit, A. Tkatchenko, P. Rodriguez-Lopez, A. Rodriguez, and R. Podgornik, Materials perspective on Casimir and van der Waals interactions, *Rev. Mod. Phys.* **88**(4), 045003, doi:10.1103/RevModPhys.88.045003 (2016).

[94] M. Sadhukhan and A. Tkatchenko, Long-range repulsion between spatially confined van der Waals dimers, *Phys. Rev. Lett.* **118**(21), 210402, doi:10.1103/PhysRevLett.118.210402 (2017).

[95] T. Steiner, The hydrogen bond in the solid state, *Angew. Chem. Int. Ed.* **41**(1), 48, doi:10.1002/1521-3773(20020104)41:1<48::AID-ANIE48>3.0.CO;2-U (2002).

[96] G. R. Desiraju, Hydrogen bridges in crystal engineering: Interactions without borders, *Acc. Chem. Res.* **35**(7), 565, doi:10.1021/ar010054t (2002).

[97] R. Madueno, M. T. Räisänen, C. Silien, and M. Buck, Functionalizing hydrogen-bonded surface networks with self-assembled monolayers, *Nature* **454**, 618, doi:10.1038/nature07096 (2008).

[98] P. Han and P. S. Weiss, Electronic substrate-mediated interactions, *Surf. Sci. Rep.* **67**(2), 19, doi:10.1016/j.surfrep.2011.11.001 (2012).

[99] E. C. H. Sykes, B. A. Mantooth, P. Han, Z. J. Donhauser, and P. S. Weiss, Substrate-mediated intermolecular interactions: A quantitative single molecule analysis, *J. Am. Chem. Soc.* **127**(19), 7255, doi:10.1021/ja0472331 (2005).

[100] E. Goiri, J. M. García-Lastra, M. Corso, Z. M. Adb El-Fattah, J. E. Ortega, and D. G. de Oteyza, Understanding periodic dislocations in 2D supramolecular crystals: The PFP/Ag(111) interface, *J. Phys. Chem. Lett.* **3**(7), 848, doi:10.1021/jz300051d (2012).

[101] J. N. O'Shea, J. Schnadt, P. A. Brühwiler, H. Hillesheimer, N. Mårtensson, L. Patthey, J. Krempasky, C. Wang, Y. Luo, and H. Ågren, Hydrogen-bond induced surface core-level shift in isonicotinic acid, *J. Phys. Chem. B* **105**(10), 1917, doi:10.1021/jp003675x (2001).

[102] J. O'Shea, Y. Luo, J. Schnadt, L. Patthey, H. Hillesheimer, J. Krempasky, D. Nordlund, M. Nagasono, P. Brühwiler, and N. Mårtensson, Hydrogen-bond induced surface core-level shift in pyridine carboxylic acids, *Surf. Sci.* **486**(3), 157, doi:10.1016/S0039-6028(01)01058-5 (2001).

[103] N. Gonzalez-Lakunza, M. E. Cañas-Ventura, P. Ruffieux, R. Rieger, K. Müllen, R. Fasel, and A. Arnau, Hydrogen-bonding fingerprints in electronic states of two-dimensional supramolecular assemblies, *ChemPhysChem* **10**(17), 2943, doi:10.1002/cphc.200900722 (2009).

[104] M. Ruiz-Osés, D. G. de Oteyza, I. Fernández-Torrente, N. Gonzalez-Lakunza, P. M. Schmidt-Weber, T. Kampen, K. Horn, A. Gourdon, A. Arnau, and J. E. Ortega, Non-covalent interactions in supramolecular assemblies investigated with electron spectroscopies, *ChemPhysChem* **10**(6), 896, doi:10.1002/cphc.200800828 (2009).

[105] M. Willenbockel, B. Stadtmüller, K. Schönauer, F. C. Bocquet, D. Lüftner, E. M. Reinisch, T. Ules, G. Koller, C. Kumpf, S. Soubatch, P. Puschnig, M. G. Ramsey, and F. S. Tautz, Energy offsets within a molecular monolayer: the influence of the molecular environment, *New J. Phys.* **15**(3), 033017, doi:10.1088/1367-2630/15/3/033017 (2013).

[106] R. C. Haddon, Electronic structure, conductivity and superconductivity of alkali metal doped C_{60}, *Acc. Chem. Res.* **25**(3), 127, doi:10.1021/ar00015a005 (1992).

[107] B. Stadtmüller, J. Seidel, N. Haag, L. Grad, C. Tusche, G. van Straaten, M. Franke, J. Kirschner, C. Kumpf, M. Cinchetti, and M. Aeschlimann, Modifying the surface of a rashba-split Pb-Ag alloy using tailored metal-organic bonds, *Phys. Rev. Lett.* **117**(9), 096805, doi:10.1103/PhysRevLett.117.096805 (2016).

[108] C. Zwick, A. Baby, M. Gruenewald, E. Verwüster, O. T. Hofmann, R. Forker, G. Fratesi, G. P. Brivio, E. Zojer, and T. Fritz, Complex stoichiometry-dependent reordering of 3,4,9,10-perylenetetracarboxylic dianhydride on Ag(111) upon K intercalation, *ACS Nano* **10**(2), 2365, doi:10.1021/acsnano.5b07145 (2016).

[109] B. Stadtmüller, N. Haag, J. Seidel, G. van Straaten, M. Franke, C. Kumpf, M. Cinchetti, and M. Aeschlimann, Adsorption heights and bonding strength of organic molecules on a Pb–Ag surface alloy, *Phys. Rev. B* **94**(23), 235436, doi:10.1103/PhysRevB.94.235436 (2016).

[110] A. Baby, M. Gruenewald, C. Zwick, F. Otto, R. Forker, G. van Straaten, M. Franke, B. Stadtmüller, C. Kumpf, G. P. Brivio, G. Fratesi, T. Fritz, and E. Zojer, Fully atomistic understanding of the electronic and optical properties of a prototypical doped charge-transfer interface, *ACS Nano* **11**(10), 10495, doi:10.1021/acsnano.7b05828 (2017).

[111] G. Mercurio, O. Bauer, M. Willenbockel, B. Fiedler, T. Sueyoshi, C. Weiss, R. Temirov, S. Soubatch, M. Sokolowski, and F. S. Tautz, Tuning and probing interfacial bonding channels for a functionalized organic molecule by surface modification, *Phys. Rev. B* **87**, 121409(R), doi:10.1103/PhysRevB.87.121409 (2013).

[112] M. Cinchetti, S. Neuschwander, A. Fischer, A. Ruffing, S. Mathias, J.-P. Wüstenberg, and M. Aeschlimann, Tailoring the spin functionality of a hybrid metal-organic interface by means of alkali-metal doping, *Phys. Rev. Lett.* **104**(21), 217602, doi:10.1103/PhysRevLett.104.217602 (2010).

[113] T. Ules, D. Lüftner, E. M. Reinisch, G. Koller, P. Puschnig, and M. G. Ramsey, Continuous or discrete: Tuning the energy level alignment of organic layers with alkali dopants, *Phys. Rev. B* **94**(20), 205405, doi:10.1103/PhysRevB.94.205405 (2016).

[114] A. El-Sayed, P. Borghetti, E. Goiri, C. Rogero, L. Floreano, G. Lovat, D. J. Mowbray, J. L. Cabellos, Y. Wakayama, A. Rubio, J. E. Ortega, and D. G. de Oteyza, Understanding energy-level alignment in donor-acceptor/metal interfaces from core-level shifts, *ACS Nano* **7**(8), 6914, doi:10.1021/nn4020888 (2013).

[115] C. Henneke, J. Felter, D. Schwarz, F. Stefan Tautz, and C. Kumpf, Controlling the growth of multiple ordered heteromolecular phases by utilizing intermolecular repulsion, *Nat. Mater.* **16**, 628–, doi:10.1038/nmat4858 (2017).

[116] B. Stadtmüller, T. Sueyoshi, G. Kichin, I. Kröger, S. Soubatch, R. Temirov, F. S. Tautz, and C. Kumpf, Commensurate registry and chemisorption at a hetero-organic interface, *Phys. Rev. Lett.* **108**, 106103, doi:10.1103/PhysRevLett.108.106103 (2012).

[117] C. R. Kagan, D. B. Mitzi, and C. D. Dimitrakopoulos, Organic-inorganic hybrid materials as semiconducting channels in thin-film field-effect transistors, *Science* **286**(5441), 945, doi:10.1126/science.286.5441.945 (1999).

[118] S. Coe, W.-K. Woo, M. Bawendi, and V. Bulović, Electroluminescence from single monolayers of nanocrystals in molecular organic devices, *Nature* **420**(6917), 800, doi:10.1038/nature01217 (2002).

[119] M. Law, L. E. Greene, J. C. Johnson, R. Saykally, and P. Yang, Nanowire dye-sensitized solar cells, *Nat. Mater.* **4**(6), 455, doi:10.1038/nmat1387 (2005).

[120] S. Blumstengel, S. Sadofev, C. Xu, J. Puls, and F. Henneberger, Converting Wannier into Frenkel excitons in an inorganic/organic hybrid semiconductor nanostructure, *Phys. Rev. Lett.* **97**(23), 237401, doi:10.1103/PhysRevLett.97.237401 (2006).

[121] D. P. Woodruff, Normal incidence X-ray standing wave determination of adsorbate structures, *Prog. Surf. Sci.* **57**(1), 1, doi:10.1016/S0079-6816(98)00012-4 (1998).

[122] S. F. Bent, Organic functionalization of group IV semiconductor surfaces: principles, examples, applications, and prospects, *Surf. Sci.* **500**(1–3), 879, doi:10.1016/S0039-6028(01)01553-9 (2002).

[123] A. Komolov, P. Møller, J. Mortensen, S. Komolov, and E. Lazneva, Electronic properties of a zinc oxide surface modified by ultra-thin layers of conjugated organic molecules, *Surf. Sci.* **586**(1-3), 129, doi:10.1016/j.susc.2005.05.006 (2005).

[124] S. Godlewski, A. Tekiel, W. Piskorz, F. Zasada, J. S. Prauzner-Bechcicki, Z. Sojka, and M. Szymonski, Supramolecular ordering of PTCDA molecules: The key role of dispersion forces in an unusual transition from physisorbed into chemisorbed state, *ACS Nano* **6**(10), 8536, doi:10.1021/nn303546m (2012).

[125] V. Lanzilotto, G. Lovat, G. Otero, L. Sanchez, M. F. López, J. Méndez, J. A. Martín-Gago, G. Bavdek, and L. Floreano, Commensurate growth of densely packed PTCDI islands on the rutile TiO_2(110) surface, *J. Phys. Chem. C* **117**(24), 12639, doi:10.1021/jp402852u (2013).

[126] G. Fratesi, V. Lanzilotto, S. Stranges, M. Alagia, G. P. Brivio, and L. Floreano, High resolution NEXAFS of perylene and PTCDI: a surface science approach to molecular orbital analysis, *Phys. Chem. Chem. Phys.* **16**(28), 14834, doi:10.1039/c4cp01625d (2014).

[127] V. Lanzilotto, G. Lovat, G. Fratesi, G. Bavdek, G. P. Brivio, and L. Floreano, TiO_2(110) charge donation to an extended π-conjugated molecule, *J. Phys. Chem. Lett.* **6**(2), 308, doi:10.1021/jz502523u (2015).

[128] G. Otero-Irurueta, J. I. Martínez, G. Lovat, V. Lanzilotto, J. Méndez, M. F. López, L. Floreano, and J. A. Martín-Gago, Densely Packed Perylene Layers on the Rutile TiO_2(110)-(1 $\times$ 1) Surface, *J. Phys. Chem. C* **119**(14), 7809, doi:10.1021/acs.jpcc.5b00851 (2015).

[129] Y. Cai and Y. P. Feng, Review on charge transfer and chemical activity of TiO_2: Mechanism and applications, *Prog. Surf. Sci.* **91**(4), 183, doi:10.1016/j.progsurf.2016.11.001 (2016).

[130] S. Rangan, C. Ruggieri, R. Bartynski, J. I. Martínez, F. Flores, and J. Ortega, Adsorption geometry and energy level alignment at the PTCDA/TiO_2(110) interface, *J. Phys. Chem. B* **122**(2), 534, doi:10.1021/acs.jpcb.7b04227 (2018).

[131] T. Schultz, R. Schlesinger, J. Niederhausen, F. Henneberger, S. Sadofev, S. Blumstengel, A. Vollmer, F. Bussolotti, J.-P. Yang, S. Kera, K. Parvez, N. Ueno,

K. Müllen, and N. Koch, Tuning the work function of GaN with organic molecular acceptors, *Phys. Rev. B* **93**(12), 125309, doi:10.1103/PhysRevB.93.125309 (2016).

[132] B. Saparov and D. B. Mitzi, Organic–inorganic perovskites: Structural versatility for functional materials design, *Chem. Rev.* **116**(7), 4558, doi:10.1021/acs.chemrev.5b00715 (2016).

[133] N. Arora, M. I. Dar, A. Hinderhofer, N. Pellet, F. Schreiber, S. M. Zakeeruddin, and M. Grätzel, Perovskite solar cells with CuSCN hole extraction layers yield stabilized efficiencies greater than 20%, *Science* **358**(6364), 768, doi:10.1126/science.aam5655 (2017).

[134] P. Hofmann, Surface physics: An introduction (Self-published, 2012).

[135] D. P. Woodruff and T. A. Delchar, Modern techniques of surface science (Cambrdige University Press, 1994), 2nd edition, doi:10.1017/CBO9780511623172.

[136] J. T. Yates Jr., Experimental innovations in surface science (Springer International Publishing, 2015), 2nd edition, doi:10.1007/978-3-319-17668-0.

[137] A. Schöll and F. Schreiber, Chapter 26 - Thin films of organic molecules: Interfaces and epitaxial growth, in M. Henini (Editor), Molecular Beam Epitaxy, pages 591–609 (Elsevier, Oxford, 2013), doi:10.1016/B978-0-12-387839-7.00026-9.

[138] F. Schreiber, Organic molecular beam deposition, pages 15–40 (Wiley-VCH Verlag GmbH & Co. KGaA, Weinheim, 2012), 2nd edition, doi:10.1002/3527606637.ch1.

[139] S. R. Forrest, Ultrathin organic films grown by organic molecular beam deposition and related techniques, *Chem. Rev.* **97**(6), 1793, doi:10.1021/cr941014o (1997).

[140] H. P. Bonzel and C. Kleint, On the history of photoemission, *Prog. Surf. Sci.* **49**, 107, doi:10.1016/0079-6816(95)00035-W (1995).

[141] S. Suga and A. Sekiyama, Photoelectron spectroscopy (Springer, Berlin, Heidelberg, 2014), doi:10.1007/978-3-642-37530-9.

[142] M. Salmeron and R. Schlögl, Ambient pressure photoelectron spectroscopy: A new tool for surface science and nanotechnology, *Surf. Sci. Rep.* **63**(4), 169, doi:10.1016/j.surfrep.2008.01.001 (2008).

[143] J. A. Colón Santana, Quantitative core level photoelectron spectroscopy (Morgan & Claypool Publishers, 2015), doi:10.1088/978-1-6270-5306-8.

[144] S. Hüfner, Photoelectron spectroscopy (Springer, Berlin Heidelberg, 2003), doi:10.1007%2F978-3-662-03209-1.

[145] F. Reinert and S. Hüfner, Photoemission spectroscopy – from early days to recent applications, *New J. Phys.* **7**(1), 97, doi:10.1088/1367-2630/7/1/097 (2005).

[146] F. Schreiber, A. Gerlach, N. Koch, E. Zojer, M. Sokolowski, F. S. Tautz, M. Rohlfing, and E. Umbach, Comment on "Electron core-hole interaction and its induced ionic structural relaxation in molecular systems under X-ray irradiation", *Phys. Rev. Lett.* **99**, 059601, doi:10.1103/PhysRevLett.99.059601 (2007).

[147] A. Jablonski and C. J. Powell, Practical expressions for the mean escape depth, the information depth, and the effective attenuation length in Auger-electron spectroscopy and X-ray photoelectron spectroscopy, *J. Vac. Sci. Technol. A* **27**(2), 253, doi:10.1116/1.3071947 (2009).

[148] C. Fadley, X-ray photoelectron spectroscopy: Progress and perspectives, *J. Electron Spectrosc. Relat. Phenom.* **178–179**, 2, doi:10.1016/j.elspec.2010.01.006 (2010).

[149] K. Siegbahn, Electron spectroscopy for atoms, molecules, and condensed matter, *Rev. Mod. Phys.* **54**(3), 709, doi:10.1103/RevModPhys.54.709 (1982).

[150] G. P. Williams, Electron binding energies, in X-ray Data Booklet, chapter 1 (Lawrence Berkeley National Laboratory, 2009), 2nd edition.

[151] J. J. Mudd, T.-L. Lee, V. Muñoz-Sanjosé, J. Zúñiga-Pérez, D. Hesp, J. M. Kahk, D. J. Payne, R. G. Egdell, and C. F. McConville, Hard X-ray photoelectron spectroscopy as a probe of the intrinsic electronic properties of CdO, *Phys. Rev. B* **89**(3), 035203, doi:10.1103/PhysRevB.89.035203 (2014).

[152] M. Häming, A. Schöll, E. Umbach, and F. Reinert, Adsorbate-substrate charge transfer and electron-hole correlation at adsorbate/metal interfaces, *Phys. Rev. B* **85**(23), 235132, doi:10.1103/PhysRevB.85.235132 (2012).

[153] A. Baby, H. Lin, G. P. Brivio, L. Floreano, and G. Fratesi, Core-level spectra and molecular deformation in adsorption: V-shaped pentacene on Al(001), *Beilstein J. Nanotechnol.* **6**, 2242, doi:10.3762/bjnano.6.230 (2015).

[154] M. Smith, L. Scudiero, J. Espinal, J.-S. McEwen, and M. Garcia-Perez, Improving the deconvolution and interpretation of XPS spectra from chars by ab initio calculations, *Carbon* **110**, 155, doi:10.1016/j.carbon.2016.09.012 (2016).

[155] K. Diller, R. J. Maurer, M. Müller, and K. Reuter, Interpretation of X-ray absorption spectroscopy in the presence of surface hybridization, *J. Chem. Phys.* **146**(21), 214701, doi:10.1063/1.4984072 (2017).

[156] N. Mårtensson and A. Nilsson, Core-Level line shapes of adsorbates: effects of electronic and vibrational excitations, *J. Electron Spectrosc. Relat. Phenom.* **52**, 1, doi:10.1016/0368-2048(90)85001-P (1990).

[157] P. S. Bagus, F. Illas, G. Pacchioni, and F. Parmigiani, Mechanisms responsible for chemical shifts of core-level binding energies and their relationship to chemical bonding, *J. Electron Spectrosc. Relat. Phenom.* **100**(1–3), 215, doi:10.1016/S0368-2048(99)00048-1 (1999).

[158] P. S. Bagus, E. S. Ilton, and C. J. Nelin, The interpretation of XPS spectra: Insights into materials properties, *Surf. Sci. Rep.* **68**(2), 273, doi:10.1016/j.surfrep.2013.03.001 (2013).

[159] A. Schöll, Y. Zou, T. Schmidt, R. Fink, and E. Umbach, High-resolution photoemission study of different NTCDA Monolayers on Ag(111): Bonding and screening influences on the line shapes, *J. Phys. Chem. B* **108**(38), 14741, doi:10.1021/jp049005z (2004).

[160] H.-J. Freund and R. W. Bigelow, Dynamic effects in VUV- and XUV-spectroscopy of organic molecular solids, *Phys. Scr.* **T17**, 50, doi:10.1088/0031-8949/1987/T17/006 (1987).

[161] A. Schöll, Y. Zou, M. Jung, T. Schmidt, R. Fink, and E. Umbach, Line shapes and satellites in high-resolution X-ray photoemission spectra of large π-conjugated molecules, *J. Chem. Phys.* **121**, 10260, doi:10.1063/1.1807812 (2004).

[162] M. L. M. Rocco, M. Haeming, D. R. Batchelor, R. F. andA. Schöll, and E. Umbach, Electronic relaxation effects in condensed polyacenes: A high-resolutionphotoemission study, *J. Chem. Phys.* **129**, 074702, doi:10.1063/1.2966356 (2008).

[163] A. E. Ellis, M. Feher, and T. G. Wright, Electronic and photoelectron spectroscopy (Cambridge University Press, 2005), doi:10.1017/CBO9781139165037.

[164] F. Sette, G. K. Wertheim, Y. Ma, G. Meigs, S. Modesti, and C. T. Chen, Lifetime and screening of the C 1*s* photoemission in graphite, *Phys. Rev. B* **41**(14), 9766, doi:10.1103/PhysRevB.41.9766 (1990).

[165] D. G. de Oteyza, I. Silanes, M. Ruiz-Osés, E. Barrena, B. P. Doyle, A. Arnau, H. Dosch, Y. Wakayama, and J. E. Ortega, Balancing intermolecular and molecule-substrate interactions in supramolecular assemblies, *Adv. Funct. Mater.* **19**(2), 259, doi:10.1002/adfm.200801453 (2009).

[166] P. Borghetti, A. El-Sayed, E. Goiri, C. Rogero, J. Lobo-Checa, L. Floreano, J. E. Ortega, and D. G. de Oteyza, Spectroscopic fingerprints of work-function-controlled phthalocyanine charging on metal surfaces, *ACS Nano* **8**(12), 12786, doi:10.1021/nn5060333 (2014).

[167] A. Nilsson and N. Mårtensson, Vibrational broadening in core-level spectra from adsorbates: C, N and O on Ni(100), *Phys. Rev. Lett.* **63**(14), 1483, doi:10.1103/PhysRevLett.63.1483 (1989).

[168] M. B. Casu, B.-E. Schuster, I. Biswas, C. Raisch, H. Marchetto, T. Schmidt, and T. Chassé, Locally resolved core-hole screening, molecular orientation, and morphology in thin films of diindenoperylene deposited on Au(111) single crystals, *Adv. Mater.* **22**, 3740, doi:10.1002/adma.201001265 (2010).

[169] W. Egelhoff, Core-level binding-energy shifts at surfaces and in solids, *Surf. Sci. Rep.* **6**(6–8), 253, doi:10.1016/0167-5729(87)90007-0 (1987).

[170] G. Tu, Y. Tu, O. Vahtras, and H. Ågren, Core electron chemical shifts of hydrogen-bonded structures, *Chem. Phys. Lett.* **468**(4-6), 294, doi:10.1016/j.cplett.2008.12.023 (2009).

[171] F. Bisti, A. Stroppa, F. Perrozzi, M. Donarelli, S. Picozzi, M. Coreno, M. de Simone, K. C. Prince, and L. Ottaviano, The electronic structure of gas phase croconic acid compared to the condensed phase: More insight into the hydrogen bond interaction, *J. Chem. Phys.* **138**(1), 014308, doi:10.1063/1.4773059 (2013).

[172] J. S. Stevens, S. J. Byard, C. C. Seaton, G. Sadiq, R. J. Davey, and S. L. M. Schroeder, Crystallography aided by atomic core-level binding energies: Proton transfer versus hydrogen bonding in organic crystal structures, *Angew. Chem. Int. Ed.* **50**(42), 9916, doi:10.1002/anie.201103981 (2011).

[173] S. Garcia-Gil, A. Arnau, and A. Garcia-Lekue, Exploring large O 1s and N 1s core level shifts due to intermolecular hydrogen bond formation in organic molecules, *Surf. Sci.* **613**, 102, doi:10.1016/j.susc.2013.03.017 (2013).

[174] H. Sezen and S. Suzer, XPS for chemical- and charge-sensitive analyses, *Thin Solid Films* **534**, 1, doi:10.1016/j.tsf.2013.02.002 (2013).

[175] C. Papp and H.-P. Steinrück, In situ high-resolution X-ray photoelectron spectroscopy – Fundamental insights in surface reactions, *Surf. Sci. Rep.* **68**(3–4), 446, doi:10.1016/j.surfrep.2013.10.003 (2013).

[176] H. Yoshida, E. Ito, M. Hara, and N. Sato, Core level energy differences between the surface and bulk of organic semiconductor films: The effect of electrostatic polarization energy, *Synth. Met.* **161**(23-24), 2549, doi:10.1016/j.synthmet.2011.09.015 (2012).

[177] H. Yoshida and N. Sato, A precise analysis of the core-level energy difference between the surface and bulk region of organic semiconductor thin films, *J. Phys. Chem. C* **116**(18), 10033, doi:10.1021/jp3009404 (2012).

[178] M. B. Casu, Evidence for efficient screening in organic materials, *phys. stat. sol. (RRL)* **2**(1), 40, doi:10.1002/pssr.200701270 (2008).

[179] V. Nilsson, M. Van den Bossche, A. Hellman, and H. Grönbeck, Trends in adsorbate induced core level shifts, *Surf. Sci.* **640**, 59, doi:10.1016/j.susc.2015.03.019 (2015).

[180] T. C. Taucher, I. Hehn, O. T. Hofmann, M. Zharnikov, and E. Zojer, Understanding chemical versus electrostatic shifts in X-ray photoelectron spectra of organic self-assembled monolayers, *J. Phys. Chem. C* **120**(6), 3428, doi:10.1021/acs.jpcc.5b12387 (2016).

[181] F. Himpsel, Angle-resolved measurements of the photoemission of electrons in the study of solids, *Adv. Phys.* **32**(1), 1, doi:10.1080/00018738300101521 (1983).

[182] J. Braun, The theory of angle-resolved ultraviolet photoemission and its applications to ordered materials, *Rep. Prog. Phys.* **59**(10), 1267, doi:10.1088/0034-4885/59/10/002 (1996).

[183] H. Offenbacher, D. Lüftner, T. Ules, E. M. Reinisch, G. Koller, P. Puschnig, and M. G. Ramsey, Orbital tomography: Molecular band maps, momentum maps and the imaging of real space orbitals of adsorbed molecules, *J. Electron Spectrosc. Relat. Phenom.* **204**, 92, doi:10.1016/j.elspec.2015.04.023 (2015).

[184] P. Puschnig, S. Berkebile, A. J. Fleming, G. Koller, K. Emtsev, T. Seyller, J. D. Riley, C. Ambrosch-Draxl, F. P. Netzer, and M. G. Ramsey, Reconstruction of molecular orbital densities from photoemission data, *Science* **326**(5953), 702, doi:10.1126/science.1176105 (2009).

[185] P. Puschnig, E.-M. Reinisch, T. Ules, G. Koller, S. Soubatch, M. Ostler, L. Romaner, F. S. Tautz, C. Ambrosch-Draxl, and M. G. Ramsey, Orbital tomography: Deconvoluting photoemission spectra of organic molecules, *Phys. Rev. B* **84**, 235427, doi:10.1103/PhysRevB.84.235427 (2011).

[186] D. Lüftner, T. Ules, E. M. Reinisch, G. Koller, S. Soubatch, F. S. Tautz, M. G. Ramsey, and P. Puschnig, Imaging the wave functions of adsorbed molecules, *PNAS* **111**(2), 605, doi:10.1073/pnas.1315716110 (2013).

[187] M. Hollerer, D. Lüftner, P. Hurdax, T. Ules, S. Soubatch, F. S. Tautz, G. Koller, P. Puschnig, M. Sterrer, and M. G. Ramsey, Charge transfer and orbital level alignment at inorganic/organic interfaces: The role of dielectric interlayers, *ACS Nano* **11**(6), 6252, doi:10.1021/acsnano.7b02449 (2017).

[188] D. Lüftner, S. Weiß, X. Yang, P. Hurdax, V. Feyer, A. Gottwald, G. Koller, S. Soubatch, P. Puschnig, M. G. Ramsey, and F. S. Tautz, Understanding the photoemission distribution of strongly interacting two-dimensional overlayers, *Phys. Rev. B* **96**(12), 125402, doi:10.1103/PhysRevB.96.125402 (2017).

[189] D. R. Zahn, G. N. Gavrila, and M. Gorgoi, The transport gap of organic semiconductors studied using the combination of direct and inverse photoemission, *Chem. Phys.* **325**(1), 99, doi:10.1016/j.chemphys.2006.02.003 (2006).

[190] S. Krause, M. B. Casu, A. Schöll, and E. Umbach, Determination of transport levels of organic semiconductors by UPS and IPS, *New J. Phys.* **10**(8), 085001, doi:10.1088/1367-2630/10/8/085001 (2008).

[191] T. Schultz, T. Lenz, N. Kotadiya, G. Heimel, G. Glasser, R. Berger, P. W. M. Blom, P. Amsalem, D. M. de Leeuw, and N. Koch, Reliable work function determination of multicomponent surfaces and interfaces: The role of electrostatic potentials in ultraviolet photoelectron spectroscopy, *Adv. Mater. Interfaces* **4**(19), 1700324, doi:10.1002/admi.201700324 (2017).

[192] J.-L. Brédas, D. Beljonne, V. Coropceanu, and J. Cornil, Charge-transfer and energy-transfer processes in π-conjugated oligomers and polymers: A molecular picture, *Chem. Rev.* **104**(11), 4971, doi:10.1021/cr040084k (2004).

[193] S. Kera, H. Yamane, and N. Ueno, First-principles measurements of charge mobility in organic semiconductors: Valence hole–vibration coupling in organic ultrathin films, *Prog. Surf. Sci.* **84**(5-6), 135, doi:10.1016/j.progsurf.2009.03.002 (2009).

[194] M. Graus, M. Grimm, C. Metzger, M. Dauth, C. Tusche, J. Kirschner, S. Kümmel, A. Schöll, and F. Reinert, Electron-vibration coupling in molecular materials: Assignment of vibronic modes from photoelectron momentum mapping, *Phys. Rev. Lett.* **116**(14), 147601, doi:10.1103/PhysRevLett.116.147601 (2016).

[195] S. Duhm, G. Heimel, I. Salzmann, H. Glowatzki, R. L. Johnson, A. Vollmer, J. P. Rabe, and N. Koch, Orientation-dependent ionization energies and interface dipoles in ordered molecular assemblies, *Nat. Mater.* **7**(4), 326, doi:10.1038/nmat2119 (2008).

[196] S. Zhong, J. Q. Zhong, A. T. Wee, and W. Chen, Molecular orientation and electronic structure at organic heterojunction interfaces, *J. Electron Spectrosc. Relat. Phenom.* **204**, 12, doi:10.1016/j.elspec.2015.02.014 (2015).

[197] P. Nagpal and V. I. Klimov, Role of mid-gap states in charge transport and photoconductivity in semiconductor nanocrystal films, *Nat. Comms.* **2**(486), doi:10.1038/ncomms1492 (2011).

[198] S. Zhong, J. Q. Zhong, H. Y. Mao, J. L. Zhang, J. D. Lin, and W. Chen, The role of gap states in the energy level alignment at the organic–organic heterojunction interfaces, *Phys. Chem. Chem. Phys.* **14**(41), 14127, doi:10.1039/c2cp41107e (2012).

[199] J.-P. Yang, F. Bussolotti, S. Kera, and N. Ueno, Origin and role of gap states in organic semiconductor studied by UPS: As the nature of organic molecular crystals, *J. Phys. D: Appl. Phys.* **50**(42), 423002, doi:10.1088/1361-6463/aa840f (2017).

[200] J. Zegenhagen and A. Kazimirov (Editors), The X-ray standing wave technique. Principles and applications (World Scientific Publishing, Singapore, 2013).

[201] B. W. Batterman, Effect of dynamical diffraction in X-ray fluorescence scattering, *Phys. Rev.* **133**, A759, doi:10.1103/PhysRev.133.A759 (1964).

[202] J. W. Knowles, Anomalous absorption of slow neutrons and X-rays in nearly perfect single crystals, *Acta. Cryst.* **9**(1), 61, doi:10.1107/S0365110X56000115 (1956).

[203] B. W. Batterman, Detection of foreign atom sites by their X-ray fluorescence scattering, *Phys. Rev. Lett.* **22**, 703, doi:10.1103/PhysRevLett.22.703 (1969).

[204] S. K. Andersen, J. A. Golovchenko, and G. Mair, New applications of X-ray standing-wave fields to solid state physics, *Phys. Rev. Lett.* **37**, 1141, doi:10.1103/PhysRevLett.37.1141 (1976).

[205] J. Zegenhagen, Surface structure determination with X-ray standing waves, *Surf. Sci. Rep.* **18**(7–8), 202, doi:10.1016/0167-5729(93)90025-K (1993).

[206] M. Bedzyk, D. Bilderback, G. Bommarito, M. Caffrey, and J. Schildkraut, X-ray standing waves: a molecular yardstick for biological membranes, *Science* **241**(4874), 1788, doi:10.1126/science.3175619 (1988).

[207] T. L. Lee, Y. Qian, P. F. Lyman, J. C. Woicik, J. G. Pellegrino, and M. J. Bedzyk, The use of X-ray standing waves and evanescent-wave emission to study buried strained-layer heterostructures, *Physica B* **221**(1-4), 437, doi:10.1016/0921-4526(95)00964-7 (1996).

[208] E. Schneck and B. Demé, Structural characterization of soft interfaces by standing-wave fluorescence with X-rays and neutrons, *Curr. Opin. Colloid Interface Sci.* **20**(4), 244, doi:10.1016/j.cocis.2015.06.001 (2015).

[209] P. L. Cowan, J. A. Golovchenko, and M. F. Robbins, X-ray standing waves at crystal surfaces, *Phys. Rev. Lett.* **44**, 1680, doi:10.1103/PhysRevLett.44.1680 (1980).

[210] M. J. Bedzyk and G. Materlik, Determination of the position and vibrational amplitude of an adsorbate by means of multiple-of X-ray standing-wave measurements, *Phys. Rev. B* **31**, 4110, doi:10.1103/PhysRevB.31.4110 (1985).

[211] T. Nakagiri, K. Sakai, A. Iida, T. Ishikawa, and T. Matsushita, X-ray standing wave method applied to the structural study of Langmuir-Blodgett-films, *Thin Solid Films* **133**(1-4), 219, doi:10.1016/0040-6090(85)90443-2 (1985).

[212] M. J. Bedzyk, G. M. Bommarito, and J. S. Schildkraut, X-ray standing waves at a reflecting mirror surface, *Phys. Rev. Lett.* **62**(12), 1376, doi:10.1103/PhysRevLett.62.1376 (1989).

[213] M. Sugiyama, S. Maeyama, S. Heun, and M. Oshima, Chemical-state-resolved X-ray standing-wave analysis using chemical-shift in photoelectron-spectra, *Phys. Rev. B* **51**(20), 14778, doi:10.1103/PhysRevB.51.14778 (1995).

[214] P. Fenter, F. Schreiber, L. Berman, G. Scoles, P. Eisenberger, and M. J. Bedzyk, On the structure and evolution of the buried S/Au interface in self-assembled monolayers: X-ray standing wave results, *Surf. Sci.* **412**, 213, doi:10.1016/S0039-6028(98)00428-2 (1998).

[215] L. Kilian, W. Weigang, E. Umbach, A. Langner, M. Sokolowski, H. L. Meyerheim, H. Maltor, B. C. C. Cowie, T. Lee, and P. Bäuerle, Adsorption site determination of a large π-conjugated molecule by normal incidence X-ray standing waves: end-capped quaterthiophene on Ag(111), *Phys. Rev. B* **66**(7), 075412, doi:10.1103/PhysRevB.66.075412 (2002).

[216] J. Stanzel, W. Weigand, L. Kilian, H. L. Meyerheim, C. Kumpf, and E. Umbach, Chemisorption of NTCDA on Ag(111): A NIXSW study including non-dipolar and electron-stimulated effects, *Surf. Sci.* **571**(1–3), L311, doi:10.1016/j.susc.2004.07.048 (2004).

[217] A. Hauschild, K. Karki, B. C. C. Cowie, M. Rohlfing, F. S. Tautz, and M. Sokolowski, Molecular distortions and chemical bonding of a large π-conjugated molecule on a metal surface, *Phys. Rev. Lett.* **94**(3), 036106, doi:10.1103/PhysRevLett.94.036106 (2005).

[218] A. Gerlach, F. Schreiber, S. Sellner, H. Dosch, I. A. Vartanyants, B. C. C. Cowie, T.-L. Lee, and J. Zegenhagen, Adsorption-induced distortion of F_{16}CuPc on Cu(111) and Ag(111): An X-ray standing wave study, *Phys. Rev. B* **71**(20), 205425, doi:10.1103/PhysRevB.71.205425 (2005).

[219] I. A. Vartanyants and M. V. Kovalchuk, Theory and applications of X-ray standing waves in real crystals, *Rep. Prog. Phys.* **64**(9), 1009, doi:10.1088/0034-4885/64/9/201 (2001).

[220] A. Gerlach, C. Bürker, T. Hosokai, and F. Schreiber, X-ray standing waves and surfaces X-ray scattering studies of molecule-metal interfaces (WILEY-VCH Verlag, 2013), doi:10.1002/9783527653171.ch6.

[221] A. Authier, Dynamical theory of X-ray diffraction (Oxford University Press, Oxford, 2003).

[222] R. A. J. Wooley, C. P. Martin, G. Miller, V. R. Dhanak, and P. J. Moriarty, Adsorbed molecular shuttlecocks: An NIXSW study of Sn phthalocyanine on Ag(111) using Auger electron detection, *Surf. Sci.* **601**(5), 1231, doi:10.1016/j.susc.2006.12.030 (2007).

[223] L. Cheng, P. Fenter, M. J. Bedzyk, and N. C. Sturchio, Fourier-expansion solution of atom distributions in a crystal using X-ray standing waves, *Phys. Rev. Lett.* **90**(25), 255503, doi:10.1103/PhysRevLett.90.255503 (2003).

[224] J. Zegenhagen, B. Detlefs, T.-L. Lee, S. Thiess, H. Isern, L. Petit, L. André, J. Roy, Y. Mi, and I. Joumard, X-ray standing waves and hard X-ray photoelectron spectroscopy at the insertion device beamline ID32, *J. Electron Spectrosc. Relat. Phenom.* **178–179**(0), 258, doi:10.1016/j.elspec.2009.09.008 (2010).

[225] T.-L. Lee, C. Bihler, W. Schoch, W. Limmer, J. Daeubler, S. Thieß, M. S. Brandt, and J. Zegenhagen, Fourier transform imaging of impurities in the unit cells of crystals: Mn in GaAs, *Phys. Rev. B* **81**(23), 235207, doi:10.1103/PhysRevB.81.235207 (2010).

[226] J.-E. Rubensson, Synchrotron radiation (Morgan & Claypool Publishers, 2016), doi:10.1088/978-1-6817-4115-4.

[227] D. P. Woodruff, D. L. Seymour, C. F. McConville, C. E. Riley, M. D. Crapper, N. P. Prince, and R. G. Jones, A simple X-ray standing wave technique for surface structure determination - theory and an application, *Surf. Sci.* **195**(1–2), 237, doi:10.1016/0039-6028(88)90794-7 (1988).

[228] G. van Straaten, M. Franke, F. C. Bocquet, F. S. Tautz, and C. Kumpf, Non-dipolar effects in photoelectron-based normal incidence X-ray standing wave experiments, *J. Electron Spectrosc. Relat. Phenom.* **222**, 106, doi:10.1016/j.elspec.2017.07.007 (2018).

[229] Casa Software Ltd, Bay House, 5 Grosvenor Terrace, Teigmnmouth, Devon, TQ14 8NE, UK (2017).

[230] Scilab Enterprises, Scilab: Free and open source software for numerical computation, Scilab Enterprises, Orsay, France (2012).

[231] M. A. VanHove, W. H. Weinberg, and C.-M. Chan, Low-energy electron diffraction (Springer, Berlin Heidelberg, 1986), doi:10.1007/978-3-642-82721-1.

[232] U. Scheithauer, G. Meyer, and M. Henzler, A new LEED instrument for quantitative spot profile analysis, *Surf. Sci.* **178**(1-3), 441, doi:10.1016/0039-6028(86)90321-3 (1986).

[233] L. Kilian, E. Umbach, and M. Sokolowski, Molecular beam epitaxy of organic films investigated by high resolution low energy electron diffraction (SPA-LEED): 3,4,9,10-perylenetetracarboxylicacid-dianhydride (PTCDA) on Ag(111), *Surf. Sci.* **573**(3), 359, doi:10.1016/j.susc.2004.10.004 (2004).

[234] C. Stellwag, G. Held, and D. Menzel, The geometry of ordered benzene layers on Ru(001), *Surf. Sci.* **325**(1-2), L379, doi:10.1016/0039-6028(94)00842-6 (1995).

[235] Z. V. Zheleva, T. Eralp, and G. Held, Complete experimental structure determination of the p$(3 \times 2)pg$ phase of glycine on Cu{110}, *J. Phys. Chem. C* **116**(1), 618, doi:10.1021/jp2057282 (2012).

[236] T. Sirtl, J. Jelic, J. Meyer, K. Das, W. M. Heckl, W. Moritz, J. Rundgren, M. Schmittel, K. Reuter, and M. Lackinger, Adsorption structure determination of a large polyaromatic trithiolate on Cu(111): Combination of LEED-I(V) and DFT-vdW, *Phys. Chem. Chem. Phys.* **15**, 11054, doi:10.1039/C3CP50752A (2013).

[237] K. Heinz, LEED and DLEED as modern tools for quantitative surface structure determination, *Rep. Prog. Phys.* **58**(6), 637, doi:10.1088/0034-4885/58/6/003 (1995).

[238] E. Bauer, Low energy electron microscopy, *Rep. Prog. Phys.* **57**(9), 895, doi:10.1088/0034-4885/57/9/002 (1994).

[239] E. Bauer, LEEM basics, *Surf. Rev. Lett.* **5**(6), 1275, doi:10.1142/S0218625X98001614 (1998).

[240] H. Marchetto, T. Schmidt, U. Groh, F. C. Maier, P. L. Lévesque, R. H. Fink, H.-J. Freund, and E. Umbach, Direct observation of epitaxial organic film growth: Temperature-dependent growth mechanisms and metastability, *Phys. Chem. Chem. Phys.* **17**(43), 29150, doi:10.1039/C5CP05124J (2015).

[241] G. Held, Low-energy electron diffraction crystallography of surfaces and interfaces, *Bunsen-Magazin* (12), 124 (2010).

[242] R. Forker, M. Meissner, and T. Fritz, Classification of epitaxy in reciprocal and real space: rigid versus flexible lattices, *Soft Matter* **13**(9), 1748, doi:10.1039/C6SM02688E (2017).

[243] D. E. Hooks, T. Fritz, and M. D. Ward, Epitaxy and molecular organization on solid substrates, *Adv. Mater.* **13**, 227, doi:10.1002/1521-4095(200102)13:4<227::AID-ADMA227>3.0.CO;2-P (2001).

[244] S. C. B. Mannsfeld and T. Fritz, Advanced modelling of epitaxial ordering of organic layers on crystalline surfaces, *Mod. Phys. Lett. B* **20**(11), 585, doi:10.1142/S0217984906011189 (2006).

[245] C. Bürker, A. Franco-Cañellas, K. Broch, T.-L. Lee, A. Gerlach, and F. Schreiber, Self-metalation of 2*H*-tetraphenylporphyrin on Cu(111) studied with XSW: Influence of the central metal atom on the adsorption distance, *J. Phys. Chem. C* **118**(25), 13659, doi:10.1021/jp503046w (2014).

[246] http://www.opengda.org/ (2017).

[247] M. Basham, J. Filik, M. T. Wharmby, P. C. Y. Chang, B. El Kassaby, M. Gerring, J. Aishima, K. Levik, B. C. A. Pulford, I. Sikharulidze, D. Sneddon, M. Webber, S. S. Dhesi, F. Maccherozzi, O. Svensson, S. Brockhauser, G. Náray, and A. W. Ashton, Data Analysis WorkbeNch (DAWN), *J. Synchrotron Rad.* **22**(3), 853, doi:10.1107/S1600577515002283 (2015).

[248] Diamond Light Source, web page (2017).

[249] A. Yang, A. Franco-Cañellas, M. Sato, B. Wang, R.-B. Wang, H. Koike, I. Salzmann, P. K. Thakur, T.-L. Lee, L. Liu, S. Kera, A. Gerlach, K. Kanai, J. Fan, F. Schreiber, and S. Duhm, Nitrogen substitution impacts organic-metal interface energetics, *Phys. Rev. B* **94**(15), 155426, doi:10.1103/PhysRevB.94.155426 (2016).

[250] C. Wang, H. Dong, W. Hu, Y. Liu, and D. Zhu, Semiconducting π-conjugated systems in field-effect transistors: A material odyssey of organic electronics, *Chem. Rev.* **112**(4), 2208, doi:10.1021/cr100380z (2012).

[251] P. I. Djurovich, E. I. Mayo, S. R. Forrest, and M. E. Thompson, Measurement of the lowest unoccupied molecular orbital energies of molecular organic semiconductors, *Org. Elec.* **10**(3), 515, doi:10.1016/j.orgel.2008.12.011 (2009).

[252] J. T. Markiewicz and F. Wudl, Perylene, oligorylenes, and aza-analogs, *ACS Appl. Mater. Interfaces* **7**(51), 28063, doi:10.1021/acsami.5b02243 (2015).

[253] I. Salzmann, R. Opitz, S. Rogaschewski, J. P. Rabe, N. Koch, and B. Nickel, Phase separation in vacuum codeposited pentacene/6,13-pentacenequinone thin films, *Phys. Rev. B* **75**(17), 174108, doi:10.1103/PhysRevB.75.174108 (2007).

[254] C. Christodoulou, A. Giannakopoulos, G. Ligorio, M. Oehzelt, M. Timpel, J. Niederhausen, L. Pasquali, A. Giglia, K. Parvez, K. Müllen, D. Beljonne, N. Koch, and M. V. Nardi, Tuning the electronic structure of graphene by molecular dopants: impact of the substrate, *ACS Appl. Mater. Interfaces* **7**(34), 19134, doi:10.1021/acsami.5b04777 (2015).

[255] F. Zhang and A. Kahn, Investigation of the high electron affinity molecular dopant F6-TCNNQ for hole-transport materials, *Adv. Funct. Mater.* **28**(1), 1703780, doi:10.1002/adfm.201703780 (2018).

[256] J. Fan, L. Zhang, A. L. Briseno, and F. Wudl, Synthesis and characterization of 7,8,15,16-tetraazaterrylene, *Org. Lett.* **14**(4), 1024, doi:10.1021/ol203285n (2012).

[257] A. Zangwill, Physics at surfaces (Cambridge University Press, 1988), doi:10.1017/CBO9780511622564.

[258] O. Bauer, G. Mercurio, M. Willenbockel, W. Reckien, C. Heinrich Schmitz, B. Fiedler, S. Soubatch, T. Bredow, F. S. Tautz, and M. Sokolowski, Role of functional groups in surface bonding of planar π-conjugated molecules, *Phys. Rev. B* **86**, 235431, doi:10.1103/PhysRevB.86.235431 (2012).

[259] G. Mercurio, O. Bauer, M. Willenbockel, N. Fairley, W. Reckien, C. H. Schmitz, B. Fiedler, S. Soubatch, T. Bredow, M. Sokolowski, and F. S. Tautz, Adsorption height determination of nonequivalent C and O species of PTCDA on Ag(110) using X-ray standing waves, *Phys. Rev. B* **87**(4), 045421, doi:10.1103/PhysRevB.87.045421 (2013).

[260] B. Hammer and J. K. Nørskov, Why gold is the noblest of all the metals, *Nature* **376**(6537), 238, doi:10.1038/376238a0 (1995).

[261] C. Wöll, S. Chiang, R. J. Wilson, and P. H. Lippel, Determination of atom positions at stacking-fault dislocations on Au(111) by scanning tunneling microscopy, *Phys. Rev. B* **39**, 7988, doi:10.1103/PhysRevB.39.7988 (1989).

[262] J. V. Barth, H. Brune, G. Ertl, and R. J. Behm, Scanning tunneling microscopy observations on the reconstructed Au(111) surface: Atomic structure, long-range superstructure, rotational domains, and surface defects, *Phys. Rev. B* **42**(15), 9307, doi:10.1103/PhysRevB.42.9307 (1990).

[263] A. R. Sandy, S. G. J. Mochrie, D. M. Zehner, K. G. Huang, and D. Gibbs, Structure and phases of the Au(111) surface: X-ray-scattering measurements, *Phys. Rev. B* **43**, 4667, doi:10.1103/PhysRevB.43.4667 (1991).

[264] J. T. Sun, L. Gao, X. B. He, Z. H. Cheng, Z. T. Deng, X. Lin, H. Hu, S. X. Du, F. Liu, and H.-J. Gao, Surface reconstruction transition of metals induced by molecular adsorption, *Phys. Rev. B* **83**(11), 115419, doi:10.1103/PhysRevB.83.115419 (2011).

[265] H. B. Michaelson, The work function of the elements and its periodicity, *J. Appl. Phys.* **48**(11), 4729, doi:10.1063/1.323539 (1977).

[266] C. Klingshirn, ZnO: Material, physics and applications, *ChemPhysChem* **8**(6), 782, doi:10.1002/cphc.200700002 (2007).

[267] V. Srikant and D. R. Clarke, On the optical band gap of zinc oxide, *J. Appl. Phys.* **83**(10), 5447, doi:10.1063/1.367375 (1998).

[268] M. D. McCluskey and S. J. Jokela, Defects in ZnO, *J. App. Phys.* **106**(7), 071101, doi:10.1063/1.3216464 (2009).

[269] M. D. McCluskey, C. D. Corolewski, J. Lv, M. C. Tarun, S. T. Teklemichael, E. D. Walter, M. G. Norton, K. W. Harrison, and S. Ha, Acceptors in ZnO, *J. App. Phys.* **117**(11), 112802, doi:10.1063/1.4913827 (2015).

[270] Z. L. Wang, Zinc oxide nanostructures: Growth, properties and applications, *J. Phys.: Condens. Matter* **16**(25), R829, doi:10.1088/0953-8984/16/25/R01 (2004).

[271] Ü. Özgür, Y. I. Alivov, C. Liu, A. Teke, M. A. Reshchikov, S. Doğan, V. Avrutin, S.-J. Cho, and H. Morkoç, A comprehensive review of ZnO materials and devices, *J. Appl. Phys.* **98**(4), 041301, doi:10.1063/1.1992666 (2005).

[272] A. Janotti and C. G. Van de Walle, Fundamentals of zinc oxide as a semiconductor, *Rep. Prog. Phys.* **72**(12), 126501, doi:10.1088/0034-4885/72/12/126501 (2009).

[273] K. Ellmer, A. Klein, and B. Rech (Editors), Transparent conductive zinc oxide: Basics and applications in thin film solar cells, volume 104 of *Springer Series in Materials Science* (Springer, Berlin, 2008), doi:10.1007/978-3-540-73612-7.

[274] H. Morkoç and Ü. Özgür, Zinc oxide: Fundamentals, materials and device technology (Wiley-VCH Verlag GmbH & Co. KGaA, Darmstadt, 2009), doi:10.1002/9783527623945.

[275] D. Norton, Y. Heo, M. Ivill, K. Ip, S. Pearton, M. Chisholm, and T. Steiner, ZnO: Growth, doping & processing, *Mater. Today* **7**(6), 34, doi:10.1016/S1369-7021(04)00287-1 (2004).

[276] A. Djurišić, A. Ng, and X. Chen, ZnO nanostructures for optoelectronics: Material properties and device applications, *Prog. Quant. Electron.* **34**(4), 191, doi:10.1016/j.pquantelec.2010.04.001 (2010).

[277] P. Schulz, L. L. Kelly, P. Winget, H. Li, H. Kim, P. F. Ndione, A. K. Sigdel, J. J. Berry, S. Graham, J.-L. Brédas, A. Kahn, and O. L. A. Monti, Tailoring electron-transfer barriers for zinc oxide/C_{60} fullerene interfaces, *Adv. Funct. Mater.* **24**(46), 7381, doi:10.1002/adfm.201401794 (2014).

[278] J. Lee, D. C. Sorescu, and X. Deng, Tunable lattice constant and band gap of single- and few-layer ZnO, *J. Phys. Chem. Lett.* **7**(7), 1335, doi:10.1021/acs.jpclett.6b00432 (2016).

[279] C. H. Swartz, Transport and surface conductivity in ZnO, *J. Mater. Res.* **27**(17), 2205, doi:10.1557/jmr.2012.133 (2012).

[280] Z. L. Wang, Nanostructures of zinc oxide, *Mater. Today* **7**(6), 26, doi:10.1016/S1369-7021(04)00286-X (2004).

[281] M. Laurenti, S. Stassi, G. Canavese, and V. Cauda, Surface engineering of nanostructured ZnO surfaces, *Adv. Mater. Interfaces* **4**(2), 1600758, doi:10.1002/admi.201600758 (2017).

[282] C. Wöll, The chemistry and physics of zinc oxide surfaces, *Prog. Surf. Sci.* **82**(2–3), 55, doi:10.1016/j.progsurf.2006.12.002 (2007).

[283] P. W. Tasker, The stability of ionic crystal surfaces, *J. Phys. C: Solid State Phys.* **12**(22), 4977, doi:10.1088/0022-3719/12/22/036 (1979).

[284] J. Goniakowski, F. Finocchi, and C. Noguera, Polarity of oxide surfaces and nanostructures, *Rep. Prog. Phys.* **71**(1), 016501, doi:10.1088/0034-4885/71/1/016501 (2008).

[285] J. Zúñiga-Pérez, V. Consonni, L. Lymperakis, X. Kong, A. Trampert, S. Fernández-Garrido, O. Brandt, H. Renevier, S. Keller, K. Hestroffer, M. R. Wagner, J. S. Reparaz, F. Akyol, S. Rajan, S. Rennesson, T. Palacios, and G. Feuillet, Polarity in GaN and ZnO: Theory, measurement, growth, and devices, *App. Phys. Rev.* **3**(4), 041303, doi:10.1063/1.4963919 (2016).

[286] D. Mora-Fonz, T. Lazauskas, M. R. Farrow, C. R. A. Catlow, S. M. Woodley, and A. A. Sokol, Why are polar surfaces of ZnO stable?, *Chem. Mater.* **29**(12), 5306, doi:10.1021/acs.chemmater.7b01487 (2017).

[287] C. Noguera, Polar oxide surfaces, *J. Phys.: Condens. Matter* **12**(31), R367, doi:10.1088/0953-8984/12/31/201 (2000).

[288] R. Gu, K. Tang, S. Gu, J. Ye, S. Huang, Z. Yao, S. Zhu, and Y. Zheng, Substrate polarity and surface pretreatment temperature dependence of ZnO homoepitaxy, *Appl. Surf. Sci.* **361**, 33, doi:10.1016/j.apsusc.2015.11.131 (2016).

[289] S. A. Chevtchenko, J. C. Moore, Ü. Özgür, X. Gu, A. A. Baski, H. Morkoç, B. Nemeth, and J. E. Nause, Comparative study of the (0001) and (000$\bar{1}$) surfaces of ZnO, *Appl. Phys. Lett.* **89**(18), 182111, doi:10.1063/1.2378589 (2006).

[290] M. W. Allen, R. Heinhold, P. Miller, M. J. H. Henseler, R. J. Mendelsberg, S. M. Durbin, and R. J. Reeves, Polarity effects in the optical properties of hydrothermal ZnO, *Appl. Phys. Lett.* **103**(23), 231109, doi:10.1063/1.4837219 (2013).

[291] Y. Sun, L. Chen, Y. Bao, Y. Zhang, J. Wang, M. Fu, J. Wu, and D. Ye, The applications of morphology controlled zno in catalysis, *Catalysts* **6**(12), 188, doi:10.3390/catal6120188 (2016).

[292] R. Schlesinger, Energy-level control at hybrid inorganic/organic semiconductor interfaces, Phd thesis, Humboldt-Universität zu Berlin, Berlin (2016), doi:10.1007/978-3-319-46624-8.

[293] K. Oura, V. G. Lifshits, A. Saranin, A. V. Zotov, and M. Katayama, Surface science (Springer-Verlag, Berlin Heidelberg, 2003), doi:10.1007/978-3-662-05179-5.

[294] O. Dulub, L. A. Boatner, and U. Diebold, STM study of the geometric and electronic structure of ZnO(0001)-Zn, (000$\bar{1}$)-O, (10$\bar{1}$0), and (11$\bar{2}$0) surfaces, *Surf. Sci.* **519**(3), 201, doi:10.1016/S0039-6028(02)02211-2 (2002).

[295] O. Dulub, U. Diebold, and G. Kresse, Novel stabilization mechanism on polar surfaces: ZnO(0001)-Zn, *Phys. Rev. Lett.* **90**(1), 016102, doi:10.1103/PhysRevLett.90.016102 (2003).

[296] G. Kresse, O. Dulub, and U. Diebold, Competing stabilization mechanism for the polar ZnO(0001)-Zn surface, *Phys. Rev. B* **68**(24), 245409, doi:10.1103/PhysRevB.68.245409 (2003).

[297] N. Jedrecy, M. Sauvage-Simkin, and R. Pinchaux, The hexagonal polar ZnO(0001)-(1×1) surfaces: structural features as stemming from X-ray diffraction, *Appl. Surf. Sci.* **162–163**, 69, doi:10.1016/S0169-4332(00)00172-0 (2000).

[298] S. Torbrügge, F. Ostendorf, and M. Reichling, Stabilization of zinc-terminated ZnO(0001) by a modified surface stoichiometry, *J. Phys. Chem. C* **113**(12), 4909, doi:10.1021/jp804026v (2009).

[299] M. Valtiner, M. Todorova, G. Grundmeier, and J. Neugebauer, Temperature stabilized surface reconstructions at polar ZnO(0001), *Phys. Rev. Lett.* **103**(6), 065502, doi:10.1103/PhysRevLett.103.065502 (2009).

[300] M. Valtiner, M. Todorova, and J. Neugebauer, Hydrogen adsorption on polar ZnO(0001)-Zn: Extending equilibrium surface phase diagrams to kinetically stabilized structures, *Phys. Rev. B* **82**(16), 165418, doi:10.1103/PhysRevB.82.165418 (2010).

[301] S.-C. Chang and P. Mark, The crystallography of the polar (0001) Zn and (000$\bar{1}$)O surfaces of zinc oxide, *Surf. Sci.* **46**(1), 293, doi:10.1016/0039-6028(74)90256-8 (1974).

[302] T. Becker, S. Hövel, M. Kunat, C. Boas, U. Burghaus, and C. Wöll, Interaction of hydrogen with metal oxides: The case of the polar ZnO(0001) surface, *Surf. Sci.* **486**(3), L502, doi:10.1016/S0039-6028(01)01120-7 (2001).

[303] A. Önsten, D. Stoltz, P. Palmgren, S. Yu, M. Göthelid, and U. O. Karlsson, Water adsorption on ZnO(0001): Transition from triangular surface structures to a disordered hydroxyl terminated phase, *J. Phys. Chem. C* **114**(25), 11157, doi:10.1021/jp1004677 (2010).

[304] M. Hellström, I. Beinik, P. Broqvist, J. V. Lauritsen, and K. Hermansson, Subsurface hydrogen bonds at the polar Zn-terminated ZnO(0001) surface, *Phys. Rev. B* **94**(24), 245433, doi:10.1103/PhysRevB.94.245433 (2016).

[305] F. Ostendorf, S. Torbrügge, and M. Reichling, Atomic scale evidence for faceting stabilization of a polar oxide surface, *Phys. Rev. B* **77**(4), 041405(R), doi:10.1103/PhysRevB.77.041405 (2008).

[306] H. Zheng, M. Gruyters, E. Pehlke, and R. Berndt, "Magic" vicinal zinc oxide surfaces, *Phys. Rev. Lett.* **111**(8), 086101, doi:10.1103/PhysRevLett.111.086101 (2013).

[307] A. Wander, F. Schedin, P. Steadman, A. Norris, R. McGrath, T. S. Turner, G. Thornton, and N. M. Harrison, Stability of polar oxide surfaces, *Phys. Rev. Lett.* **86**(17), 3811, doi:10.1103/PhysRevLett.86.3811 (2001).

[308] K. Ozawa and K. Mase, Comparison of the surface electronic structures of H-adsorbed ZnO surfaces: An angle-resolved photoelectron spectroscopy study, *Phys. Rev. B* **83**(12), 125406, doi:10.1103/PhysRevB.83.125406 (2011).

[309] C. M. Schlepütz, Y. Yang, N. S. Husseini, R. Heinhold, H.-S. Kim, M. W. Allen, S. M. Durbin, and R. Clarke, The presence of a (1×1) oxygen overlayer on ZnO(0001) surfaces and at Schottky interfaces, *J. Phys.: Condens. Matter* **24**(9), 095007, doi:10.1088/0953-8984/24/9/095007 (2012).

[310] R. Heinhold and M. W. Allen, Polarity-dependent photoemission of in situ cleaved zinc oxide single crystals, *J. Mater. Res.* **27**(17), 2214, doi:10.1557/jmr.2012.181 (2012).

[311] H. Li, L. K. Schirra, J. Shim, H. Cheun, B. Kippelen, O. L. A. Monti, and J.-L. Bredas, Zinc oxide as a model transparent conducting oxide: A theoretical and experimental study of the impact of hydroxylation, vacancies, interstitials, and extrinsic doping on the electronic properties of the polar ZnO(0002) surface, *Chem. Mater.* **24**(15), 3044, doi:10.1021/cm301596x (2012).

[312] R. Heinhold, G. T. Williams, S. P. Cooil, D. A. Evans, and M. W. Allen, Influence of polarity and hydroxyl termination on the band bending at ZnO surfaces, *Phys. Rev. B* **88**(23), 235315, doi:10.1103/PhysRevB.88.235315 (2013).

[313] S. Overbury, P. Radulovic, S. Thevuthasan, G. Herman, M. Henderson, and C. Peden, Ion scattering study of the Zn and oxygen-terminated basal plane surfaces of ZnO, *Surf. Sci.* **410**(1), 106, doi:10.1016/S0039-6028(98)00307-0 (1998).

[314] M. Sambi, G. Granozzi, G. A. Rizzi, M. Casarin, and E. Tondello, An angle-scanned photoelectron diffraction study on the surface relaxation of ZnO(0001), *Surf. Sci.* **319**(1–2), 149, doi:10.1016/0039-6028(94)90577-0 (1994).

[315] H. Maki, N. Ichinose, N. Ohashi, H. Haneda, and J. Tanaka, The lattice relaxation of ZnO single crystal (0001) surface, *Surf. Sci.* **457**(3), 377, doi:10.1016/S0039-6028(00)00436-2 (2000).

[316] Y. Ding and Z. L. Wang, Profile imaging of reconstructed polar and non-polar surfaces of ZnO, *Surf. Sci.* **601**(2), 425, doi:10.1016/j.susc.2006.07.063 (2007).

[317] R. Wahl, J. V. Lauritsen, F. Besenbacher, and G. Kresse, Stabilization mechanism for the polar ZnO(000$\bar{1}$)-O surface, *Phys. Rev. B* **87**(8), 085313, doi:10.1103/PhysRevB.87.085313 (2013).

[318] V. Staemmler, K. Fink, B. Meyer, D. Marx, M. Kunat, S. Gil Girol, U. Burghaus, and C. Wöll, Stabilization of polar ZnO surfaces: Validating microscopic models by using CO as a probe molecule, *Phys. Rev. Lett.* **90**(10), 106102, doi:10.1103/PhysRevLett.90.106102 (2003).

[319] M. Schiek, K. Al-Shamery, M. Kunat, F. Traeger, and C. Wöll, Water adsorption on the hydroxylated H-(1 × 1) O-ZnO(000$\bar{1}$) surface, *Phys. Chem. Chem. Phys.* **8**(13), 1505, doi:10.1039/b515418a (2006).

[320] M. Kunat, S. Gil Girol, T. Becker, U. Burghaus, and C. Wöll, Stability of the polar surfaces of ZnO: A reinvestigation using He-atom scattering, *Phys. Rev. B* **66**(8), 081402(R), doi:10.1103/PhysRevB.66.081402 (2002).

[321] M. Kunat, S. G. Girol, U. Burghaus, and C. Wöll, The interaction of water with the oxygen-terminated, polar surface of ZnO, *J. Phys. Chem. B* **107**(51), 14350, doi:10.1021/jp030675z (2003).

[322] J. V. Lauritsen, S. Porsgaard, M. K. Rasmussen, M. C. R. Jensen, R. Bechstein, K. Meinander, B. S. Clausen, S. Helveg, R. Wahl, G. Kresse, and F. Besenbacher, Stabilization principles for polar surfaces of ZnO, *ACS Nano* **5**(7), 5987, doi:10.1021/nn2017606 (2011).

[323] R. Jacobs, B. Zheng, B. Puchala, P. M. Voyles, A. B. Yankovich, and D. Morgan, Counterintuitive reconstruction of the polar O-terminated ZnO surface with zinc vacancies and hydrogen, *J. Phys. Chem. Lett.* **7**(22), 4483, doi:10.1021/acs.jpclett.6b02174 (2016).

[324] B. Meyer, First-principles study of the polar O-terminated ZnO surface in thermodynamic equilibrium with oxygen and hydrogen, *Phys. Rev. B* **69**(4), 045416, doi:10.1103/PhysRevB.69.045416 (2004).

[325] S. King, S. Parihar, K. Pradhan, H. Johnson-Steigelman, and P. Lyman, Observation of a $(\sqrt{3}\times\sqrt{3})R30°$reconstruction on O-polar ZnO surfaces, *Surf. Sci.* **602**(22), L131, doi:10.1016/j.susc.2008.09.025 (2008).

[326] R. Lindsay, C. A. Muryn, E. Michelangeli, and G. Thornton, ZnO(000$\bar{1}$)-O surface structure: Hydrogen-free (1 × 1) termination, *Surf. Sci.* **565**(2–3), L283, doi:10.1016/j.susc.2004.07.014 (2004).

[327] S. Erker, P. Rinke, N. Moll, and O. T. Hofmann, Doping dependence of the surface phase stability of polar O-terminated (000$\bar{1}$) ZnO, *New J. Phys.* **19**(8), 083012, doi:10.1088/1367-2630/aa79e7 (2017).

[328] Y. Yang, C. M. Schlepütz, F. Bellucci, M. W. Allen, S. M. Durbin, and R. Clarke, Structural investigation of ZnO O-polar (000$\bar{1}$) surfaces and Schottky interfaces, *Surf. Sci.* **610**, 22, doi:10.1016/j.susc.2012.12.018 (2013).

[329] M. Galeotti, A. Atrei, U. Bardi, G. Rovida, M. Torrini, E. Zanazzi, A. Santucci, and A. Klimov, Structure of the ZnO(000$\bar{1}$) surface studied by X-ray photoelectron diffraction, *Chem. Phys. Lett.* **222**(4), 349, doi:10.1016/0009-2614(94)87073-X (1994).

[330] S. E. Chamberlin, C. J. Hirschmugl, S. T. King, H. C. Poon, and D. K. Saldin, Role of hydrogen on the ZnO(000$\bar{1}$)–(1 × 1) surface, *Phys. Rev. B* **84**(7), 075437, doi:10.1103/PhysRevB.84.075437 (2011).

[331] M. Eremtchenko, J. Schaefer, and F. S. Tautz, Understanding and tuning the epitaxy of large aromatic adsorbates by molecular design, *Nature* **425**, 602, doi:10.1038/nature01901 (2003).

[332] M. Eremtchenko, D. Bauer, J. Schaefer, and F. Tautz, Structure, bonding, and growth at a metal–organic interface in the weak chemisorption regime: Perylene–Ag(111), *J. Mater. Res.* **19**(07), 2028, doi:110.1557/JMR.2004.0253 (2004).

[333] M. Eremtchenko, D. Bauer, J. A. Schaefer, and F. S. Tautz, Polycyclic aromates on close-packed metal surfaces: functionalization, molecular chemisorption and organic epitaxy, *New J. Phys.* **6**, 4, doi:10.1088/1367-2630/6/1/004 (2004).

[334] K. Manandhar and B. A. Parkinson, Photoemission and STM study of the morphology and barrier heights at the interface between perylene and noble metal (111) surfaces, *J. Phys. Chem. C* **114**(36), 15394, doi:10.1021/jp1008626 (2010).

[335] K. Manandhar, J. B. Sambur, and B. A. Parkinson, Morphologies, structures, and interfacial electronic structure of perylene on Au(111), *J. Appl. Phys.* **107**(6), 063716, doi:10.1063/1.3318682 (2010).

[336] K. Bobrov, N. Kalashnyk, and L. Guillemot, True perylene epitaxy on Ag(110) driven by site recognition effect, *J. Chem. Phys.* **142**(10), 101929, doi:10.1063/1.4913325 (2015).

[337] K. Bobrov, N. Kalashnyk, and L. Guillemot, Thermodynamic balance of perylene self-assembly on Ag(110), *J. Chem. Phys.* **145**(15), 154705, doi:10.1063/1.4964669 (2016).

[338] C. Seidel, R. Ellerbrake, L. Gross, and H. Fuchs, Structural transitions of perylene and coronene on silver and gold surfaces: A molecular-beam epitaxy LEED study, *Phys. Rev. B* **64**(19), 195418, doi:10.1103/PhysRevB.64.195418 (2001).

[339] H. Han, M. Hongying, C. Qiao, Y. Xinzheng, Q. Huiqin, Z. Jianhua, L. Haiyang, H. Pimo, and B. Shining, The electronic states of ordered thin films of perylene on Ag(110), *Physica B: Cond. Mat.* **352**(1–4), 36, doi:10.1016/j.physb.2004.06.035 (2004).

[340] L. Gao, Z. T. Deng, W. Ji, X. Lin, Z. H. Cheng, X. B. He, D. X. Shi, and H.-J. Gao, Understanding and controlling the weakly interacting interface in perylene/Ag(110), *Phys. Rev. B* **73**(7), 075424, doi:10.1103/PhysRevB.73.075424 (2006).

[341] J. Li, H. Li, P. Winget, and J.-L. Brédas, Electronic structure of the perylene–zinc oxide interface: Computational study of photoinduced electron transfer and impact of surface defects, *J. Phys. Chem. C* **119**(33), 18843, doi:10.1021/acs.jpcc.5b03596 (2015).

[342] I. Kröger, B. Stadtmüller, C. Kleimann, P. Rajput, and C. Kumpf, Normal-incidence X-ray standing-wave study of copper phthalocyanine submonolayers on Cu(111) and Au(111), *Phys. Rev. B* **83**(19), 195414, doi:10.1103/PhysRevB.83.195414 (2011).

[343] S. Duhm, C. Bürker, J. Niederhausen, I. Salzmann, T. Hosokai, J. Duvernay, S. Kera, F. Schreiber, N. Koch, N. Ueno, and A. Gerlach, Pentacene on Ag(111): Correlation of bonding distance with intermolecular interaction and order, *ACS Appl. Mater. Interfaces* **5**(19), 9377, doi:10.1021/am402778u (2013).

[344] T. Hosokai, private communication .

[345] B. Stadtmüller, D. Lüftner, M. Willenbockel, E. M. Reinisch, T. Sueyoshi, G. Koller, S. Soubatch, M. G. Ramsey, P. Puschnig, F. S. Tautz, and C. Kumpf, Unexpected interplay of bonding height and energy level alignment at heteromolecular hybrid interfaces, *Nat. Comms.* **5**, 3685, doi:10.1038/ncomms4685 (2014).

[346] E. Goiri, M. Matena, A. El-Sayed, J. Lobo-Checa, P. Borghetti, C. Rogero, B. Detlefs, J. Duvernay, J. Ortega, and de Oteyza, Self-assembly of bicomponent molecular monolayers: Adsorption height changes and their consequences, *Phys. Rev. Lett.* **112**(11), 117602, doi:10.1103/PhysRevLett.112.117602 (2014).

[347] D. G. de Oteyza, J. M. García-Lastra, M. Corso, B. P. Doyle, L. Floreano, A. Morgante, Y. Wakayama, A. Rubio, and J. E. Ortega, Customized electronic coupling in self-assembled donor-acceptor nanostructures, *Adv. Funct. Mater.* **19**(22), 3567, doi:10.1002/adfm.200901374 (2009).

[348] L. Kilian, E. Umbach, and M. Sokolowski, A refined structural analysis of the PTCDA monolayer on the reconstructed Au(111) surface - "Rigid or distorted carpet?", *Surf. Sci.* **600**(13), 2633, doi:10.1016/j.susc.2006.03.049 (2006).

[349] N. Nicoara, J. Méndez, and J. M. Gómez-Rodríguez, Visualizing the interface state of PTCDA on Au(111) by scanning tunneling microscopy, *Nanotechnology* **27**(47), 475707, doi:10.1088/0957-4484/27/47/475707 (2016).

[350] F. Silly, A. Q. Shaw, M. R. Castell, and G. A. D. Briggs, A chiral pinwheel supramolecular network driven by the assembly of PTCDI and melamine, *Chem. Commun.* **0**, 1907, doi:10.1039/B715658H (2008).

[351] T. Hosokai, K. Yonezawa, J. Yang, K. Koswattage, and S. Kera, Significant reduction in the hole-injection barrier by the charge-transfer state formation: Diindenoperylene contacted with silver and copper electrodes, *Org. Elec.* **49**, 39, doi:10.1016/j.orgel.2017.06.033 (2017).

[352] K. Balakrishnan, A. Datar, T. Naddo, J. Huang, R. Oitker, M. Yen, J. Zhao, and L. Zang, Effect of side-chain substituents on self-assembly of perylene diimide molecules: morphology control, *J. Am. Chem. Soc.* **128**(22), 7390, doi:10.1021/ja061810z (2006).

[353] M. C. R. Delgado, E.-G. Kim, D. A. d. S. Filho, and J.-L. Bredas, Tuning the charge-transport parameters of perylene diimide single crystals via end and/or core functionalization: A density functional theory investigation, *J. Am. Chem. Soc.* **132**(10), 3375, doi:10.1021/ja908173x (2010).

[354] C. Huang, S. Barlow, and S. R. Marder, Perylene-3,4,9,10-tetracarboxylic acid diimides: Synthesis, physical properties, and use in organic electronics, *J. Org. Chem.* **76**(8), 2386, doi:10.1021/jo2001963 (2011).

[355] M. Gsänger, J. Oh, M. Könemann, H. Höffken, A.-M. Krause, Z. Bao, and F. Würthner, A crystal-engineered hydrogen-bonded octachloroperylene diimide with a twisted core: An n-channel organic semiconductor, *Angew. Chem. Int. Ed.* **49**(4), 740, doi:10.1002/anie.200904215 (2010).

[356] E. Kozma and M. Catellani, Perylene diimides based materials for organic solar cells, *Dyes Pigment.* **98**(1), 160, doi:10.1016/j.dyepig.2013.01.020 (2013).

[357] L. Chen, C. Li, and K. Müllen, Beyond perylene diimides: synthesis, assembly and function of higher rylene chromophores, *J. Mater. Chem. C* **2**(11), 1938, doi:10.1039/c3tc32315c (2014).

[358] P. Erwin and M. E. Thompson, Elucidating the interplay between dark current coupling and open circuit voltage in organic photovoltaics, *Appl. Phys. Lett.* **98**(22), 223305, doi:10.1063/1.3595679 (2011).

[359] C. Li and H. Wonneberger, Perylene imides for organic photovoltaics: Yesterday, today, and tomorrow, *Adv. Mater.* **24**, 613, doi:10.1002/adma.201104447 (2012).

[360] W. Deng, Y. Shen, J. Qian, Y. Cao, and H. Yang, A perylene diimide crystal with high capacity and stable cyclability for Na-ion batteries, *ACS Appl. Mater. Interfaces* **7**(38), 21095, doi:10.1021/acsami.5b04325 (2015).

[361] Z. Zhang, J. Wang, D. Liu, W. Luo, M. Zhang, W. Jiang, and Y. Zhu, Highly efficient organic photocatalyst with full visible light spectrum through π–π stacking of TCNQ–PTCDI, *ACS Appl. Mater. Interfaces* **8**(44), 30225, doi:10.1021/acsami.6b10186 (2016).

[362] J. C. Swarbrick, J. Ma, J. A. Theobald, N. S. Oxtoby, J. N. O'Shea, N. R. Champness, and P. H. Beton, Square, hexagonal, and row phases of PTCDA and PTCDI on Ag–Si(111)$\sqrt{3}\times\sqrt{3}R30°$, *J. Phys. Chem. B* **109**(24), 12167, doi:10.1021/jp0508305 (2005).

[363] M. Mura, F. Silly, G. A. D. Briggs, M. R. Castell, and L. N. Kantorovich, H-bonding supramolecular assemblies of PTCDI molecules on the Au(111) surface, *J. Phys. Chem. C* **113**(52), 21840, doi:10.1021/jp908046t (2009).

[364] J. Hieulle and F. Silly, Localized intermolecular electronic coupling in two-dimensional self-assembled 3,4,9,10-perylenetetracarboxylic diimide nanoarchitectures, *J. Mater. Chem. C* **1**(30), 4536, doi:10.1039/c3tc30771a (2013).

[365] F. S. Tautz, Structure and bonding of large aromatic molecules on noble metal surfaces: The example of PTCDA, *Prog. Surf. Sci.* **82**, 479, doi:10.1016/j.progsurf.2007.09.001 (2007).

[366] K. Tojo and J. Mizuguchi, Refinement of the crystal structure of 3,4:9,10-perylenebis(dicarboximide), $C_{24}H_{10}N_2O_4$, at 263 K, *Z. Kristallogr. NCS* **2017**, 45, doi:10.1524/ncrs.2002.217.1.45 (2002).

[367] R. Stiufiuc, L. M. A. Perdigão, B. Grandidier, D. Deresmes, G. Allan, C. Delerue, D. Stiévenard, P. H. Beton, S. C. Erwin, M. Sassi, V. Oison, and J.-M. Debierre, Above-barrier surface electron resonances induced by a molecular network, *Phys. Rev. B* **81**(4), 045421, doi:10.1103/PhysRevB.81.045421 (2010).

[368] C. Emanuelsson, H. M. Zhang, E. Moons, and L. S. O. Johansson, Scanning tunneling microscopy study of thin PTCDI films on Ag/Si(111)-$\sqrt{3} \times \sqrt{3}$, *J. Chem. Phys.* **146**(11), 114702, doi:10.1063/1.4978470 (2017).

[369] C. Ludwig, B. Gompf, J. Petersen, R. Strohmaier, and W. Eisenmenger, STM investigations of PTCDA and PTCDI on graphite and MoS_2. A systematic study of epitaxy and STM image contrast, *Z. Physik B - Condensed Matter* **93**(3), 365, doi:10.1007/BF01312708 (1994).

[370] J. M. Topple, S. A. Burke, S. Fostner, and P. Grütter, Thin film evolution: Dewetting dynamics of a bimodal molecular system, *Phys. Rev. B* **79**(20), 205414, doi:10.1103/PhysRevB.79.205414 (2009).

[371] J. Megow, T. Körzdörfer, T. Renger, M. Sparenberg, S. Blumstengel, F. Henneberger, and V. May, Calculating optical absorption spectra of thin polycrystalline organic films: Structural disorder and site-dependent van der Waals interaction, *J. Phys. Chem. C* **119**(10), 5747, doi:10.1021/acs.jpcc.5b01587 (2015).

[372] O. Guillermet, A. Glachant, J. Hoarau, J. Mossoyan, and M. Mossoyan, Perylene tetracarboxylic diimide ultrathin film deposition on Pt(100): a LEED, AES, REELS and STM study, *Surf. Sci.* **548**(1–3), 129, doi:10.1016/j.susc.2003.10.054 (2004).

[373] O. Guillermet, M. Mossoyan-Déneux, M. Giorgi, A. Glachant, and J. Mossoyan, Structural study of vapour phase deposited 3,4,9,10-perylene tetracarboxylicacid diimide: Comparison between single crystal and ultra thin films grown on Pt(100), *Thin Solid Films* **514**(1–2), 25, doi:10.1016/j.tsf.2006.02.024 (2006).

[374] K. Aït-Mansour, M. Treier, P. Ruffieux, M. Bieri, R. Jaafar, P. Gröning, R. Fasel, and O. Gröning, Template-directed molecular nanostructures on the Ag/Pt(111) dislocation network, *J. Phys. Chem. C* **113**(19), 8407, doi:10.1021/jp901378v (2009).

[375] F. Loske, M. Reichling, and A. Kühnle, Deposition sequence determines morphology of C_{60} and 3,4,9,10-Perylenetetracarboxylic diimide islands on $CaF_2(111)$, *Jpn. J. Appl. Phys.* **50**(8), 08LB07, doi:10.1143/JJAP.50.08LB07 (2011).

[376] W. Braun, G. Gavrila, M. Gorgoi, and D. Zahn, Influence of the molecular structure on the interface formation between magnesium and organic semiconductors, *Radiat. Phys. Chem.* **75**(11), 1869, doi:10.1016/j.radphyschem.2005.07.057 (2006).

[377] P. Winget, L. K. Schirra, D. Cornil, H. Li, V. Coropceanu, P. F. Ndione, A. K. Sigdel, D. S. Ginley, J. J. Berry, J. Shim, H. Kim, B. Kippelen, J.-L. Brédas, and O. L. A. Monti, Defect-driven interfacial electronic structures at an organic/metal-oxide semiconductor heterojunction, *Adv. Mater.* **26**(27), 4711, doi:10.1002/adma.201305351 (2014).

[378] O. Boudrioua, H. Yang, P. Sonnet, L. Stauffer, A. J. Mayne, G. Comtet, G. Dujardin, Y. Kuk, S. Nagarajan, A. Gourdon, and E. Duverger, Large organic molecule chemisorption on the SiC(0001) surface, *Phys. Rev. B* **85**(3), 035423, doi:10.1103/PhysRevB.85.035423 (2012).

[379] S. M. Kozlov, F. Viñes, and A. Görling, Bandgap engineering of graphene by physisorbed adsorbates, *Adv. Mater.* **23**(22–23), 2638, doi:10.1002/adma.201100171 (2011).

[380] S. M. Kozlov, F. Viñes, and A. Görling, On the interaction of polycyclic aromatic compounds with graphene, *Carbon* **50**(7), 2482, doi:10.1016/j.carbon.2012.01.070 (2012).

[381] H. J. Karmel, J. J. Garramone, J. D. Emery, S. Kewalramani, M. J. Bedzyk, and M. C. Hersam, Self-assembled organic monolayers on epitaxial graphene with enhanced structural and thermal stability, *Chem. Commun.* **50**(64), 8852, doi:10.1039/C4CC02761B (2014).

[382] N. Tanigaki, C. Heck, and T. Mizokuro, Oriented thin films of perylenetetracarboxylic diimide on frictiontransferred polymer films, *Phys. Procedia* **14**, 119, doi:10.1016/j.phpro.2011.05.023 (2011).

[383] J. Taborski, P. Väterlein, H. Dietz, U. Zimmermann, and E. Umbach, NEXAFS investigations on ordered adsorbate layers of large aromatic molecules, *J. Electron Spectrosc. Relat. Phenom.* **75**, 129, doi:10.1016/0368-2048(95)02397-6 (1995).

[384] V. Chiş, G. Mile, R. Ştiufiuc, N. Leopold, and M. Oltean, Vibrational and electronic structure of PTCDI and melamine–PTCDI complexes, *J. Mol. Struct.* **924–926**, 47, doi:10.1016/j.molstruc.2008.12.038 (2009).

[385] L. Gisslén and R. Scholz, Crystallochromy of perylene pigments: Interference between Frenkel excitons and charge-transfer states, *Phys. Rev. B* **80**(11), 115309, doi:10.1103/PhysRevB.80.115309 (2009).

[386] M. Oltean, A. Calborean, G. Mile, M. Vidrighin, M. Iosin, L. Leopold, D. Maniu, N. Leopold, and V. Chiş, Absorption spectra of PTCDI: A combined UV–Vis and TD-DFT study, *Spectrochim. Acta Mol. Biomol. Spectrosc.* **97**, 703, doi:10.1016/j.saa.2012.07.056 (2012).

[387] M. Oltean, G. Mile, M. Vidrighin, N. Leopold, and V. Chiş, Weakly bound PTCDI and PTCDA dimers studied by using MP2 and DFT methods with dispersion correction, *Phys. Chem. Chem. Phys.* **15**(33), 13978, doi:10.1039/c3cp44644a (2013).

[388] J. Megow, Computing dispersive, polarizable, and electrostatic shifts of excitation energy in supramolecular systems: PTCDI crystal, *J. Chem. Phys.* **145**(9), 094109, doi:10.1063/1.4962179 (2016).

[389] J. N. O'Shea, A. Saywell, G. Magnano, L. M. Perdigño, C. J. Satterley, P. H. Beton, and V. R. Dhanak, Adsorption of PTCDI on Au(111): Photoemission and scanning tunnelling microscopy, *Surf. Sci.* **603**(20), 3094, doi:10.1016/j.susc.2009.08.024 (2009).

[390] P. Fenter, F. Schreiber, L. Zhou, P. Eisenberger, and S. R. Forrest, *In situ* studies of morphology, strain, and growth modes of a molecular organic thin film, *Phys. Rev. B* **56**, 3046, doi:10.1103/PhysRevB.56.3046 (1997).

[391] B. Krause, F. Schreiber, H. Dosch, A. Pimpinelli, and O. H. Seeck, Temperature dependence of the 2D-3D transition in the growth of PTCDA on Ag(111): A real-time X-ray and kinetic Monte Carlo study, *Europhys. Lett.* **65**(3), 372, doi:10.1209/epl/i2003-10090-6 (2004).

[392] L. Weinhardt, O. Fuchs, A. Fischer, M. Weigand, F. Meyer, A. Benkert, M. Blum, M. Bär, S. Pookpanratana, J. Denlinger, C. Heske, and E. Umbach, Site- and symmetry-resolved resonant X-ray emission study of a highly ordered PTCDA thin film, *J. Phys. Chem. C* **120**(16), 8607, doi:10.1021/acs.jpcc.5b12422 (2016).

[393] J. B. Gustafsson, H. M. Zhang, E. Moons, and L. S. O. Johansson, Electron spectroscopy studies of PTCDA on Ag/Si(111)$-\sqrt{3}\times\sqrt{3}$, *Phys. Rev. B* **75**(15), 155413, doi:10.1103/PhysRevB.75.155413 (2007).

[394] D. R. T. Zahn, G. N. Gavrila, and G. Salvan, Electronic and vibrational spectroscopies applied to organic/inorganic interfaces, *Chem. Rev.* **107**, 1161, doi:10.1021/cr050141p (2007).

[395] A. Nikitin, H. Ogasawara, D. Mann, R. Denecke, Z. Zhang, H. Dai, K. Cho, and A. Nilsson, Hydrogenation of single-walled carbon nanotubes, *Phys. Rev. Lett.* **95**(22), 225507, doi:10.1103/PhysRevLett.95.225507 (2005).

[396] Y. Zou, L. Kilian, A. Schöll, T. Schmidt, R. Fink, and E. Umbach, Chemical bonding of on Ag surfaces and the formation of interface states, *Surf. Sci.* **600**(6), 1240, doi:10.1016/j.susc.2005.12.050 (2006).

[397] H. Yang, O. Boudrioua, A. J. Mayne, G. Comtet, G. Dujardin, Y. Kuk, P. Sonnet, L. Stauffer, S. Nagarajan, and A. Gourdon, The paradox of an insulating contact between a chemisorbed molecule and a wide band gap semiconductor surface, *Phys. Chem. Chem. Phys.* **14**(5), 1700, doi:10.1039/C2CP23104B (2012).

[398] F. Ciccullo, S.-A. Savu, A. Gerbi, M. Bauer, R. Ovsyannikov, A. Cassinese, T. Chassé, and M. B. Casu, Chemisorption, morphology, and structure of a n-type perylene diimide derivative at the interface with gold: influence on devices from thin films to single molecules, *Chem. Eur. J.* **21**(9), 3766, doi:10.1002/chem.201404901 (2015).

[399] M. Häming, Electronic many-body effects in organic thin-films and interfaces, Phd thesis, Universität Würzburg (2011).

[400] D. M. Newns, Self-consistent model of hydrogen chemisorption, *Phys. Rev.* **178**, 1123, doi:10.1103/PhysRev.178.1123 (1969).

[401] J. K. Norsko, Chemisorption on metal surfaces, *Rep. Prog. Phys.* **53**(10), 1253, doi:10.1088/0034-4885/53/10/001 (1990).

[402] M. Yu, W. Xu, N. Kalashnyk, Y. Benjalal, S. Nagarajan, F. Masini, E. Lægsgaard, M. Hliwa, X. Bouju, A. Gourdon, C. Joachim, F. Besenbacher, and T. R. Linderoth, From zero to two dimensions: supramolecular nanostructures formed from perylene-3,4,9,10-tetracarboxylic diimide (PTCDI) and Ni on the Au(111) surface through the interplay between hydrogen-bonding and electrostatic metal-organic interactions, *Nano Res.* **5**(12), 903, doi:10.1007/s12274-012-0274-6 (2012).

[403] M. Sassi, V. Oison, and J.-M. Debierre, First principle study of a bimolecular thin film on Ag(111) surface, *Surf. Sci.* **602**(17), 2856, doi:10.1016/j.susc.2008.07.019 (2008).

[404] K. Glöckler, C. Seidel, A. Soukopp, M. Sokolowski, E. Umbach, M. Böhringer, R. Berndt, and W.-D. Schneider, Highly ordered structures and submolecular scanning tunnelling microscopy contrast of PTCDA and DM-PBDCI monolayers on Ag(111) and Ag(110), *Surf. Sci.* **405**, 1, doi:10.1016/S0039-6028(97)00888-1 (1998).

[405] A. Hauschild, R. Temirov, S. Soubatch, O. Bauer, A. Schöll, B. C. C. Cowie, T.-L. Lee, F. S. Tautz, and M. Sokolowski, Normal-incidence X-ray standing-wave determination of the adsorption geometry of PTCDA on Ag(111): Comparison of the ordered room-temperature and disordered low-temperature phases, *Phys. Rev. B* **81**(12), 125432, doi:10.1103/PhysRevB.81.125432 (2010).

[406] J. Schnadt, J. O'Shea, L. Patthey, J. Schiessling, J. Krempaský, M. Shi, N. Mårtensson, and P. Brühwiler, Structural study of adsorption of isonicotinic acid and related molecules on rutile TiO_2(110) II: XPS, *Surf. Sci.* **544**(1), 74, doi:10.1016/j.susc.2003.08.013 (2003).

[407] W. Doherty, S. Sorensen, and R. Friedlein, Selective hydrogen bond disruption in adenine monolayer films by reaction with water, *J. Electron. Spectrosc. Relat. Phenom.* **174**(1-3), 107, doi:10.1016/j.elspec.2009.05.001 (2009).

[408] F. Anger, J. O. Ossó, U. Heinemeyer, K. Broch, R. Scholz, A. Gerlach, and F. Schreiber, Photoluminescence spectroscopy of pure pentacene, perfluoropentacene, and mixed thin films, *J. Chem. Phys.* **136**, 054701, doi:10.1063/1.3677839 (2012).

[409] P. Rotter, B. A. J. Lechner, A. Morherr, D. M. Chisnall, D. J. Ward, A. P. Jardine, J. Ellis, W. Allison, B. Eckhardt, and G. Witte, Coupling between diffusion and orientation of pentacene molecules on an organic surface, *Nat. Mater.* **15**(4), 397, doi:10.1038/nmat4575 (2016).

[410] Y. Nakayama, Y. Uragami, M. Yamamoto, K. Yonezawa, K. Mase, S. Kera, H. Ishii, and N. Ueno, High-resolution core-level photoemission measurements on the pentacene single crystal surface assisted by photoconduction, *J. Phys.: Condens. Matter* **28**(9), 094001, doi:10.1088/0953-8984/28/9/094001 (2016).

[411] K. Broch, U. Heinemeyer, A. Hinderhofer, F. Anger, R. Scholz, A. Gerlach, and F. Schreiber, Optical evidence for intermolecular coupling in mixed films of pentacene and perfluoropentacene, *Phys. Rev. B* **83**, 245307, doi:10.1103/PhysRevB.83.245307 (2011).

[412] S. Kowarik, A. Hinderhofer, C. Wang, C. Weber, A. Gerlach, A. Hexemer, S. R. Leone, and F. Schreiber, Identification of an organic semiconductor superlattice structure of pentacene and perfluoro-pentacene through resonant and non-resonant X-ray scattering, *AIP Advances* **5**(11), 117241, doi:10.1063/1.4936884 (2015).

[413] M. Eremtchenko, R. Temirov, D. Bauer, J. Schaefer, and F. Tautz, Formation of molecular order on a disordered interface layer: Pentacene/Ag(111), *Phys. Rev. B* **72**(11), 115430, doi:10.1103/PhysRevB.72.115430 (2005).

[414] N. Koch, A. Vollmer, S. Duhm, Y. Sakamoto, and T. Suzuki, The effect of fluorination on pentacene/gold interface energetics and charge reorganization energy, *Adv. Mater.* **19**(1), 112, doi:10.1002/adma.200601825 (2007).

[415] L. Gross, F. Mohn, N. Moll, P. Liljeroth, and G. Meyer, The chemical structure of a molecule resolved by atomic force microscopy, *Science* **325**(5944), 1110, doi:10.1126/science.1176210 (2009).

[416] D. G. de Oteyza, Y. Wakayama, X. Liu, W. Yang, P. L. Cook, F. J. Himpsel, and J. E. Ortega, Effect of fluorination on the molecule–substrate interactions of pentacene/Cu(100) interfaces, *Chem. Phys. Lett.* **490**, 54, doi:10.1016/j.cplett.2010.03.006 (2010).

[417] H. Glowatzki, G. Heimel, A. Vollmer, S. L. Wong, H. Huang, W. Chen, A. T. S. Wee, J. P. Rabe, and N. Koch, Impact of fluorination on initial growth and stability of pentacene on Cu(111), *J. Phys. Chem. C* **116**(14), 7726, doi:10.1021/jp208582z (2012).

[418] S. Duhm, S. Hosoumi, I. Salzmann, A. Gerlach, M. Oehzelt, B. Wedl, T.-L. Lee, F. Schreiber, N. Koch, N. Ueno, and S. Kera, Influence of intramolecular polar

bonds on interface energetics in perfluoro-pentacene on Ag(111), *Phys. Rev. B* **81**(4), 045418, doi:10.1103/PhysRevB.81.045418 (2010).

[419] S. L. Wong, H. Huang, Y. L. Huang, Y. Z. Wang, X. Y. Gao, T. Suzuki, W. Chen, and A. T. S. Wee, Effect of fluorination on the molecular packing of perfluoropentacene and pentacene ultrathin films on Ag(111), *J. Phys. Chem. C* **114**(20), 9356, doi:10.1021/jp910581b (2010).

[420] C. Schmidt, T. Breuer, S. Wippermann, W. G. Schmidt, and G. Witte, Substrate induced thermal decomposition of perfluoro-pentacene thin films on the coinage metals, *J. Phys. Chem. C* **116**(45), 24098, doi:10.1021/jp307316r (2012).

[421] M. Marks, C. Schmidt, C. H. Schwalb, T. Breuer, G. Witte, and U. Höfer, Temperature dependent structural phase transition at the perfluoropentacene/Ag(111) interface, *J. Phys. Chem. C* **116**(2), 1904, doi:10.1021/jp2094577 (2012).

[422] B. Schuler, W. Liu, A. Tkatchenko, N. Moll, G. Meyer, A. Mistry, D. Fox, and L. Gross, Adsorption geometry determination of single molecules by atomic force microscopy, *Phys. Rev. Lett.* **111**(10), 106103, doi:10.1103/PhysRevLett.111.106103 (2013).

[423] J. Götzen, C. H. Schwalb, C. Schmidt, G. Mette, M. Marks, U. Höfer, and G. Witte, Structural evolution of perfluoro-pentacene films on Ag(111): Transition from 2D to 3D growth, *Langmuir* **27**(3), 993, doi:10.1021/la1022664 (2011).

[424] S. Kera, S. Hosoumi, K. Sato, H. Fukagawa, S.-i. Nagamatsu, Y. Sakamoto, T. Suzuki, H. Huang, W. Chen, A. T. S. Wee, V. Coropceanu, and N. Ueno, Experimental reorganization energies of pentacene and perfluoropentacene: effects of perfluorination, *J. Phys. Chem. C* **117**(43), 22428, doi:10.1021/jp4032089 (2013).

[425] T. Breuer, T. Maßmeyer, A. Mänz, S. Zoerb, B. Harbrecht, and G. Witte, Structure of van der Waals bound hybrids of organic semiconductors and transition metal dichalcogenides: The case of acene films on MoS_2, *Phys. Status Solidi RRL* **10**(12), 905, doi:10.1002/pssr.201600320 (2016).

[426] T. Nagata, T. Nakamura, R. Hayakawa, T. Yoshimura, S. Oh, N. Hiroshiba, T. Chikyow, N. Fujimura, and Y. Wakayama, Photoelectron spectroscopic study on monolayer pentacene thin-film/polar ZnO single-crystal hybrid interface, *Appl. Phys. Express* **10**(2), 025702, doi:10.7567/APEX.10.025702 (2017).

[427] I. Salzmann, S. Duhm, G. Heimel, M. Oehzelt, R. Kniprath, R. L. Johnson, J. P. Rabe, and N. Koch, Tuning the ionization energy of organic semiconductor films: the role of intramolecular polar bonds, *J. Am. Chem. Soc.* **130**(39), 12870, doi:10.1021/ja804793a (2008).

[428] C. B. France, P. G. Schroeder, J. C. Forsythe, and B. A. Parkinson, Scanning tunneling microscopy study of the coverage-dependent structures of pentacene on Au(111), *Langmuir* **19**, 1274, doi:10.1021/la026221v (2003).

[429] Y.-Y. Lo, J.-H. Chang, G. Hoffmann, W.-B. Su, C.-I. Wu, and C.-S. Chang, A comparative study on the adsorption behavior of pentacene and perfluoropentacene molecules on Au(111) surfaces, *Jpn. J. Appl. Phys.* **52**, 101601, doi:10.7567/JJAP.52.101601 (2013).

[430] X.-Q. Shi, Y. Li, M. A. Van Hove, and R.-Q. Zhang, Interactions between organics and metal surfaces in the intermediate regime between physisorption and chemisorption, *J. Phys. Chem. C* **116**(44), 23603, doi:10.1021/jp310007v (2012).

[431] R. P. Bula, I. M. Oppel, and H. F. Bettinger, Thermal generation of pentacenes from soluble 6,13-dihydro-6,13-ethenopentacene precursors by a diels–alder-retro-diels–alder sequence with 3,6-disubstituted tetrazines, *J. Org. Chem.* **77**(7), 3538, doi:10.1021/jo202450u (2012).

[432] S.-A. Savu, A. Sonström, R. Bula, H. F. Bettinger, T. Chassé, and M. B. Casu, Intercorrelation of electronic, structural, and morphological properties in nanorods of 2,3,9,10-tetrafluoropentacene, *ACS Appl. Mater. Interfaces* **7**(35), 19774, doi:10.1021/acsami.5b05622 (2015).

[433] S.-A. Savu, G. Biddau, L. Pardini, R. Bula, H. F. Bettinger, C. Draxl, T. Chassé, and M. B. Casu, Fingerprint of fractional charge transfer at the metal/organic interface, *J. Phys. Chem. C* **119**(22), 12538, doi:10.1021/acs.jpcc.5b03768 (2015).

[434] F. Anger, R. Scholz, E. Adamski, K. Broch, A. Gerlach, Y. Sakamoto, T. Suzuki, and F. Schreiber, Optical properties of fully and partially fluorinated rubrene in films and solution, *Appl. Phys. Lett.* **102**(1), 013308, doi:10.1063/1.4773520 (2013).

[435] F. Anger, H. Glowatzki, A. Franco-Cañellas, C. Bürker, A. Gerlach, R. Scholz, Y. Sakamoto, T. Suzuki, N. Koch, and F. Schreiber, Interface dipole and growth mode of partially and fully fluorinated rubrene on Au(111) and Ag(111), *J. Phys. Chem. C* **119**(12), 6769, doi:10.1021/jp511822g (2015).

[436] F. Anger, R. Scholz, A. Gerlach, and F. Schreiber, Vibrational modes and changing molecular conformation of perfluororubrene in thin films and solution, *J. Chem. Phys.* **142**(22), 224703, doi:10.1063/1.4922052 (2015).

[437] W. A. Ogden, S. Ghosh, M. J. Bruzek, K. A. McGarry, L. Balhorn, V. Young, L. J. Purvis, S. E. Wegwerth, Z. Zhang, N. A. Serratore, C. J. Cramer, L. Gagliardi, and C. J. Douglas, Partial fluorination as a strategy for crystal engineering of rubrene derivatives, *Cryst. Growth Des.* **17**(2), 643, doi:10.1021/acs.cgd.6b01497 (2017).

[438] H. Peisert, M. Knupfer, and J. Fink, Electronic structure of partially fluorinated copper phthalocyanine ($CuPCF_4$) and its interface to Au(100), *Surf. Sci.* **515**(2–3), 491, doi:10.1016/S0039-6028(02)01967-2 (2002).

[439] H. Peisert, M. Knupfer, T. Schwieger, G. G. Fuentes, D. Olligs, J. Fink, and T. Schmidt, Fluorination of copper phthalocyanines: Electronic structure and interface properties, *J. Appl. Phys.* **93**(12), 9683, doi:10.1063/1.1577223 (2003).

[440] T. Schwieger, H. Peisert, and M. Knupfer, Direct observation of interfacial charge transfer from silver to organic semiconductors, *Chem. Phys. Lett.* **384**(4–6), 197, doi:10.1016/j.cplett.2003.11.094 (2004).

[441] J. Meiss, A. Merten, M. Hein, C. Schuenemann, S. Schäfer, M. Tietze, C. Uhrich, M. Pfeiffer, K. Leo, and M. Riede, Fluorinated zinc phthalocyanine as donor for efficient vacuum-deposited organic solar cells, *Adv. Funct. Mater.* **22**(2), 405, doi:10.1002/adfm.201101799 (2012).

[442] M. Brendel, S. Krause, A. Steindamm, A. K. Topczak, S. Sundarraj, P. Erk, S. Höhla, N. Fruehauf, N. Koch, and J. Pflaum, The effect of gradual fluorination on the properties of F_nZnPc thin films and F_nZnPc/C bilayer photovoltaic cells, *Adv. Funct. Mater.* **25**(10), 1565, doi:10.1002/adfm.201404434 (2015).

[443] K. Toyoda, I. Hamada, S. Yanagisawa, and Y. Morikawa, Density-functional theoretical study of fluorination effect on organic/metal interfaces, *Org. Elec.* **12**(2), 295, doi:10.1016/j.orgel.2010.11.010 (2011).

[444] S.-A. Savu, M. B. Casu, S. Schundelmeier, S. Abb, C. Tönshoff, H. F. Bettinger, and T. Chassé, Nanoscale assembly, morphology and screening effects in nanorods of newly synthesized substituted pentacenes, *RSC Adv.* **2**(12), 5112, doi:10.1039/c2ra20168b (2012).

[445] S.-A. Savu, S. Abb, S. Schundelmeier, J. D. Saathoff, J. M. Stevenson, C. Tönshoff, H. F. Bettinger, P. Clancy, M. B. Casu, and T. Chassé, Pentacene-based nanorods on Au(111) single crystals: Charge transfer, diffusion, and step-edge barriers, *Nano Res.* **6**(6), 449, doi:10.1007/s12274-013-0322-x (2013).

[446] Y. Sakamoto, T. Suzuki, M. Kobayashi, Y. Gao, Y. Fukai, Y. Inoue, F. Sato, and S. Tokito, Perfluoropentacene: High-performance p–n junctions and complementary circuits with pentacene, *J. Am. Chem. Soc.* **126**, 8138, doi:10.1021/ja0476258 (2004).

[447] Y. Sakamoto and T. Suzuki, Perfluorinated and half-fluorinated rubrenes: Synthesis and crystal packing arrangements, *J. Org. Chem.* **82**(15), 8111, doi:10.1021/acs.joc.7b01383 (2017).

[448] S. Kera, H. Fukagawa, T. Kataoka, S. Hosoumi, H. Yamane, and N. Ueno, Spectroscopic evidence of strong π–π interorbital interaction in a lead-phthalocyanine bilayer film attributed to the dimer nanostructure, *Phys. Rev. B* **75**(12), 121305(R), doi:10.1103/PhysRevB.75.121305 (2007).

[449] M. Alagia, C. Baldacchini, M. G. Betti, F. Bussolotti, V. Carravetta, U. Ekström, C. Mariani, and S. Stranges, Core-shell photoabsorption and photoelectron spectra of gas-phase pentacene: Experiment and theory, *J. Chem. Phys.* **122**(12), 124305, doi:10.1063/1.1864852 (2005).

[450] C. Baldacchini, F. Allegretti, R. Gunnella, and M. G. Betti, Molecule-metal interaction of pentacene on copper vicinal surfaces, *Surf. Sci.* **601**(13), 2603, doi:10.1016/j.susc.2006.12.016 (2007).

[451] A. Basagni, L. Ferrighi, M. Cattelan, L. Nicolas, K. Handrup, L. Vaghi, A. Papagni, F. Sedona, C. D. Valentin, S. Agnoli, and M. Sambi, On-surface photo-dissociation of C–Br bonds: towards room temperature Ullmann coupling, *Chem. Commun.* **51**(63), 12593, doi:10.1039/C5CC04317D (2015).

[452] O. McDonald, A. Cafolla, Z. Li, and G. Hughes, Synchrotron photoemission studies of pentacene films on Cu(110), *Surf. Sci.* **600**(9), 1909, doi:10.1016/j.susc.2006.02.021 (2006).

[453] E. Barrena, D. G. de Oteyza, H. Dosch, and Y. Wakayama, 2D supramolecular self-assembly of binary organic monolayers, *ChemPhysChem* **8**(13), 1915–, doi:10.1002/cphc.200700494 (2007).

[454] A. El-Sayed, D. J. Mowbray, J. M. García-Lastra, C. Rogero, E. Goiri, P. Borghetti, A. Turak, B. P. Doyle, M. Dell'Angela, L. Floreano, Y. Wakayama, A. Rubio, J. E. Ortega, and D. G. de Oteyza, Supramolecular environment-dependent electronic properties of metal–organic interfaces., *J. Phys. Chem. C* **116**(7), 4780, doi:10.1021/jp211749g (2012).

[455] S. Duhm, private communication (2017).

[456] M. Suscavage, M. Harris, D. Bliss, P. Yip, S.-Q. Wang, D. Schwall, L. Bouthillette, J. Bailey, M. Callahan, D. C. Look, D. C. Reynolds, R. L. Jones, and C. W. Litton, High quality hydrothermal ZnO crystals, *MRS Internet J. Nitride Semicond. Res.* **4**(S1), 287, doi:10.1557/S109257830000260X (1999).

[457] W. Lin, D. Chen, J. Zhang, Z. Lin, J. Huang, W. Li, Y. Wang, and F. Huang, Hydrothermal growth of ZnO single crystals with high carrier mobility, *Cryst. Growth Des.* **9**(10), 4378, doi:10.1021/cg900339u (2009).

[458] D. Ehrentraut, K. Maeda, M. Kano, K. Fujii, and T. Fukuda, Next-generation hydrothermal ZnO crystals, *J. Cryst. Growth* **320**(1), 18, doi:10.1016/j.jcrysgro.2011.01.005 (2011).

[459] E. N. Kaufmann (Editor), Characterization of materials (Wiley, 2012), 2nd edition, doi:10.1002/0471266965.

[460] J. Götzen and G. Witte, Rapid preparation of highly ordered ultraflat ZnO surfaces, *App. Surf. Sci.* **258**(24), 10144, doi:10.1016/j.apsusc.2012.06.094 (2012).

[461] N. Abedi and G. Heimel, Correlating core-level shifts and structure of zinc-oxide surfaces, *Phys. Status Solidi B* **252**(4), 755, doi:10.1002/pssb.201451469 (2015).

[462] J. Dumont, B. Hackens, S. Faniel, P.-O. Mouthuy, R. Sporken, and S. Melinte, ZnO(0001) surfaces probed by scanning tunneling spectroscopy: Evidence for an inhomogeneous electronic structure, *Appl. Phys. Lett.* **95**(13), 132102, doi:10.1063/1.3238288 (2009).

[463] K. Ozawa, Y. Oba, K. Edamoto, M. Higashiguchi, Y. Miura, K. Tanaka, K. Shimada, H. Namatame, and M. Taniguchi, Valence-band structure of the polar ZnO surfaces studied by angle-resolved photoelectron spectroscopy, *Phys. Rev. B* **79**(7), 075314, doi:10.1103/PhysRevB.79.075314 (2009).

[464] Y. T. Law, T. Skála, I. Píš, V. Nehasil, M. Vondráček, and S. Zafeiratos, Bimetallic nickel–cobalt nanosized layers supported on polar ZnO surfaces: Metal–support interaction and alloy effects studied by synchrotron radiation X-ray photoelectron spectroscopy, *J. Phys. Chem. C* **116**(18), 10048, doi:10.1021/jp301219u (2012).

[465] A. Calzolari, M. Bazzani, and A. Catellani, Dipolar and charge transfer effects on the atomic stabilization of ZnO polar surfaces, *Surf. Sci.* **607**, 181, doi:10.1016/j.susc.2012.09.004 (2013).

[466] JoVE Science Education Database. *Organic Chemistry*, Degassing liquids with freeze-pump-thaw cycling, JoVE, Cambridge, MA, USA (2017).

[467] K. Jacobi, G. Zwicker, and A. Gutmann, Work function, electron affinity and band bending of zinc oxide surfaces, *Surf. Sci.* **141**(1), 109, doi:10.1016/0039-6028(84)90199-7 (1984).

[468] S. Hövel, C. Kolczewski, M. Wühn, J. Albers, K. Weiss, V. Staemmler, and C. Wöll, Pyridine adsorption on the polar ZnO(0001) surface: Zn termination versus O termination, *J. Chem. Phys.* **112**(8), 3909, doi:10.1063/1.480942 (2000).

[469] K. Diller, F. Klappenberger, M. Marschall, K. Hermann, A. Nefedov, C. Wöll, and J. V. Barth, Self-metalation of 2H-tetraphenylporphyrin on Cu(111): An X-ray spectroscopy study, *J. Chem. Phys.* **136**(1), 014705, doi:10.1063/1.3674165 (2012).

[470] J. R. Williams, M. Kobata, I. Pis, E. Ikenaga, T. Sugiyama, K. Kobayashi, and N. Ohashi, Polarity determination of wurtzite-type crystals using hard x-ray photoelectron diffraction, *Surf. Sci.* **605**(13-14), 1336, doi:10.1016/j.susc.2011.04.036 (2011).

[471] J. R. Williams, I. Píš, M. Kobata, A. Winkelmann, T. Matsushita, Y. Adachi, N. Ohashi, and K. Kobayashi, Observation and simulation of hard X-ray photoelectron diffraction to determine polarity of polycrystalline zinc oxide films with rotation domains, *J. Appl. Phys.* **111**(3), 033525, doi:10.1063/1.3682088 (2012).

[472] I. Bartoš and O. Romanyuk, Polarity of wurtzite crystals by photoelectron diffraction, *Appl. Surf. Sci.* **315**, 506, doi:10.1016/j.apsusc.2014.01.038 (2014).

[473] H. Noei, H. Qiu, Y. Wang, E. Löffler, C. Wöll, and M. Muhler, The identification of hydroxyl groups on ZnO nanoparticles by infrared spectroscopy, *Phys. Chem. Chem. Phys.* **10**(47), 7092, doi:10.1039/b811029h (2008).

[474] R. Lindsay, E. Michelangeli, B. G. Daniels, T. V. Ashworth, A. J. Limb, G. Thornton, A. Gutiérrez-Sosa, A. Baraldi, R. Larciprete, and S. Lizzit, Impact of defects on the surface chemistry of ZnO$(000\bar{1})-$O, *J. Am. Chem. Soc.* **124**(24), 7117, doi:10.1021/ja025904u (2002).

[475] C. Tang, M. J. S. Spencer, and A. S. Barnard, Activity of ZnO polar surfaces: an insight from surface energies, *Phys. Chem. Chem. Phys.* **16**(40), 22139, doi:10.1039/C4CP03221G (2014).

[476] H.-W. Ra, K. S. Choi, C. W. Ok, S. Y. Jo, K. H. Bai, and Y. H. Im, Ion bombardment effects on ZnO nanowires during plasma treatment, *App. Phys. Lett.* **93**(3), 033112, doi:10.1063/1.2965109 (2008).

[477] A. Önsten, D. Stoltz, P. Palmgren, S. Yu, T. Claesson, M. Göthelid, and U. O. Karlsson, SO_2 interaction with Zn(0001) and ZnO(0001) and the influence of water, *Surf. Sci.* **608**, 31, doi:10.1016/j.susc.2012.09.007 (2013).

[478] M. D. McCluskey, M. C. Tarun, and S. T. Teklemichael, Hydrogen in oxide semiconductors, *J. Mater. Res.* **27**(17), 2190, doi:10.1557/jmr.2012.137 (2012).

[479] M. Henderson, The interaction of water with solid surfaces: Fundamental aspects revisited, *Surf. Sci. Rep.* **46**(1–8), 1, doi:10.1016/S0167-5729(01)00020-6 (2002).

[480] F. Viñes, A. Iglesias-Juez, F. Illas, and M. Fernández-Garcáa, Hydroxyl identification on ZnO by infrared spectroscopies: Theory and experiments, *J. Phys. Chem. C* **118**(3), 1492, doi:10.1021/jp407021v (2014).

[481] H. Ye, G. Chen, H. Niu, Y. Zhu, L. Shao, and Z. Qiao, Structures and Mechanisms of Water Adsorption on ZnO(0001) and GaN(0001) Surface, *J. Phys. Chem. C* **117**(31), 15976, doi:10.1021/jp312847r (2013).

[482] Y. Liu, W. Xu, Y. Shan, and H. Xu, High reactivity of the ZnO(0001) polar surface: The role of oxygen adatoms, *J. Phys. Chem. C* **121**(15711—15718), 29, doi:10.1021/acs.jpcc.7b03326 (2017).

[483] L. Ericsson, H. Zhang, and K. Magnusson, Photoemission study of ZnO nanocrystals: Thermal annealing in UHV and induced band bending, *Surf. Sci.* **612**, 10, doi:10.1016/j.susc.2013.02.001 (2013).

[484] R. Schlesinger, F. Bianchi, S. Blumstengel, C. Christodoulou, R. Ovsyannikov, B. Kobin, K. Moudgil, S. Barlow, S. Hecht, S. Marder, F. Henneberger, and N. Koch, Efficient light emission from inorganic and organic semiconductor hybrid structures by energy-level tuning, *Nat. Comms.* **6**, 6754, doi:10.1038/ncomms7754 (2015).

[485] J. Stähler and P. Rinke, Global and local aspects of the surface potential landscape for energy level alignment at organic-ZnO interfaces, *Chem. Phys.* **485–486**, 149, doi:10.1016/j.chemphys.2016.11.017 (2017).

[486] O. T. Hofmann and P. Rinke, Band bending engineering at organic/inorganic interfaces using organic self-assembled monolayers, *Adv. Electron. Mater.* **3**(6), 1600373, doi:10.1002/aelm.201600373 (2017).

[487] R. Schlesinger, Y. Xu, O. T. Hofmann, S. Winkler, J. Frisch, J. Niederhausen, A. Vollmer, S. Blumstengel, F. Henneberger, P. Rinke, M. Scheffler, and N. Koch, Controlling the work function of ZnO and the energy-level alignment at the interface

to organic semiconductors with a molecular electron acceptor, *Phys. Rev. B* **87**(15), 155311, doi:10.1103/PhysRevB.87.155311 (2013).

[488] A. M.-C. Ng, A. B. Djurišić, K.-H. Tam, W.-M. Kwok, W.-K. Chan, W. Y. Tam, D. L. Phillips, and K.-W. Cheah, Organic nanoclusters on inorganic nanostructures for tailoring the emission properties of organic materials, *Adv. Funct. Mater.* **18**(4), 566, doi:10.1002/adfm.200700264 (2008).

[489] A. M. C. Ng, X. Y. Chen, F. Fang, A. B. Djurišić, and W. K. Chan, 3,4,9,10-perylenetetracarboxylicdiimide/ZnO hybrid nanomaterials, *Opt. Mater.* **32**(12), 1578, doi:10.1016/j.optmat.2010.06.009 (2010).

[490] Y. Xu, O. T. Hofmann, R. Schlesinger, S. Winkler, J. Frisch, J. Niederhausen, A. Vollmer, S. Blumstengel, F. Henneberger, N. Koch, P. Rinke, and M. Scheffler, Space-charge transfer in hybrid inorganic-organic systems, *Phys. Rev. Lett.* **111**(22), 226802, doi:10.1103/PhysRevLett.111.226802 (2013).

[491] M. Gruenewald, L. K. Schirra, P. Winget, M. Kozlik, P. F. Ndione, A. K. Sigdel, J. J. Berry, R. Forker, J.-L. Brédas, T. Fritz, and O. L. A. Monti, Integer charge transfer and hybridization at an organic semiconductor/conductive oxide interface, *J. Phys. Chem. C* **119**(9), 4865, doi:10.1021/jp512153b (2015).

[492] K. Ozawa, S. Munakata, K. Edamoto, and K. Mase, Electron donor molecule on the oxide surface: influence of surface termination of ZnO on adsorption of tetrathiafulvalene, *J. Phys. Chem. C* **115**(44), 21843, doi:10.1021/jp207769x (2011).

[493] K. Ozawa, M. Suzuki, R. Tochikubo, H. Kato, Y. Sugizaki, K. Edamoto, and K. Mase, Electron-donor dye molecule on ZnO($10\bar{1}0$), (0001), and ($000\bar{1}$) studied by photoelectron spectroscopy and X-ray absorption spectroscopy, *J. Phys. Chem. C* **120**(16), 8653, doi:10.1021/acs.jpcc.6b00454 (2016).

[494] L. L. Kelly, D. A. Racke, H. Kim, P. Ndione, A. K. Sigdel, J. J. Berry, S. Graham, D. Nordlund, and O. L. A. Monti, Hybridization-induced carrier localization at the C_60/ZnO interface, *Adv. Mater.* **28**(20), 3960, doi:10.1002/adma.201503694 (2016).

[495] H. Li, E. L. Ratcliff, A. K. Sigdel, A. J. Giordano, S. R. Marder, J. J. Berry, and J.-L. Brédas, Modification of the gallium-doped zinc oxide surface with self-assembled monolayers of phosphonic acids: A joint theoretical and experimental study, *Adv. Funct. Mater.* **24**(23), 3593, doi:10.1002/adfm.201303670 (2014).

[496] H. Li and J.-L. Bredas, Comparison of the impact of zinc vacancies on charge separation and charge transfer at ZnO/Sexithienyl and ZnO/fullerene interfaces, *Adv. Mater.* **28**(20), 3928, doi:10.1002/adma.201503262 (2016).

[497] I. Beinik, M. Hellström, T. N. Jensen, P. Broqvist, and J. V. Lauritsen, Enhanced wetting of Cu on ZnO by migration of subsurface oxygen vacancies, *Nat. Comms.* **6**, 8845, doi:10.1038/ncomms9845 (2015).

[498] T. Becker, M. Kunat, C. Boas, U. Burghaus, and C. Wöll, Adsorption dynamics of CO on the polar surfaces of ZnO, *J. Chem. Phys.* **113**(15), 6334, doi:10.1063/1.1309131 (2000).

[499] P. Palmgren, T. Claesson, A. Önsten, B. Agnarsson, M. Månsson, O. Tjernberg, and M. Göthelid, Band bending and structure dependent HOMO energy at the ZnO(0001)-titanyl phthalocyanine interface, *Surf. Sci.* **601**(18), 4222, doi:10.1016/j.susc.2007.04.113 (2007).

[500] R. Einholz, T. Fang, R. Berger, P. Grüninger, A. Früh, T. Chassé, R. F. Fink, and H. F. Bettinger, Heptacene: Characterization in solution, in the solid state, and in films, *J. Am. Chem. Soc.* **139**(12), 4435, doi:10.1021/jacs.6b13212 (2017).

[501] F. De Angelis, M. Gaspari, A. Procopio, G. Cuda, and E. Di Fabrizio, Direct mass spectrometry investigation on Pentacene thin film oxidation upon exposure to air, *Chem. Phys. Lett.* **468**(4–6), 193, doi:10.1016/j.cplett.2008.12.048 (2009).

[502] A. Vollmer, H. Weiss, S. Rentenberger, I. Salzmann, J. Rabe, and N. Koch, The interaction of oxygen and ozone with pentacene, *Surf. Sci.* **600**, 4004, doi:10.1016/j.susc.2005.11.067 (2006).

[503] L. Ferrighi, I. Píš, T. H. Nguyen, M. Cattelan, S. Nappini, A. Basagni, M. Parravicini, A. Papagni, F. Sedona, E. Magnano, F. Bondino, C. Di Valentin, and S. Agnoli, Control of the intermolecular coupling of dibromotetracene on Cu(110) by the sequential activation of C–Br and C–H bonds, *Chem. Eur. J.* **21**(15), 5826, doi:10.1002/chem.201405817 (2015).

[504] I. Píš, L. Ferrighi, T. H. Nguyen, S. Nappini, L. Vaghi, A. Basagni, E. Magnano, A. Papagni, F. Sedona, C. Di Valentin, S. Agnoli, and F. Bondino, Surface-confined polymerization of halogenated polyacenes: The case of dibromotetracene on Ag(110), *J. Phys. Chem. C* **120**(9), 4909, doi:10.1021/acs.jpcc.5b12047 (2016).

[505] M. Scheele, W. Brütting, and F. Schreiber, Coupled organic–inorganic nanostructures (COIN), *Phys. Chem. Chem. Phys.* **17**(1), 97, doi:10.1039/C4CP03094J (2015).

[506] U. Becker and M. F. Hochella, The calculation of STM images, STS spectra, and XPS peak shifts for galena: New tools for understanding mineral surface chemistry, *Geochim. Cosmochim. Acta* **60**(13), 2413, doi:10.1016/0016-7037(96)00094-4 (1996).

[507] J. Muscat and C. Klauber, A combined ab initio and photoelectron study of galena (PbS), *Surf. Sci.* **491**(1–2), 226, doi:10.1016/S0039-6028(01)01408-X (2001).

[508] J. Muscat and J. Gale, First principles studies of the surface of galena PbS, *Geochim. Cosmochim. Acta* **67**(5), 799, doi:10.1016/S0016-7037(02)00978-X (2003).

[509] J.-X. Ma, Y. Jia, Y.-L. Song, E.-J. Liang, L.-K. Wu, F. Wang, X.-C. Wang, and X. Hu, The geometric and electronic properties of the PbS, PbSe and PbTe (001) surfaces, *Surf. Sci.* **551**(1–2), 91, doi:10.1016/j.susc.2003.12.003 (2004).

[510] K. S. Knight, A high-resolution neutron powder diffraction investigation of galena (PbS) between 10 K and 350 K: no evidence for anomalies in the lattice parameters or atomic displacement parameters in galena or altaite (PbTe) at temperatures corresponding to the saturation of cation disorder, *J. Phys.: Condens. Matter* **26**(38), 385403, doi:10.1088/0953-8984/26/38/385403 (2014).

[511] T. Kendelewicz, P. Liu, G. E. Brown, and E. J. Nelson, Atomic geometry of the PbS(100) surface, *Surf. Sci.* **395**(2–3), 229, doi:10.1016/S0039-6028(97)00627-4 (1998).

[512] G. M. Rangger, O. T. Hofmann, L. Romaner, G. Heimel, B. Bröker, R.-P. Blum, R. L. Johnson, N. Koch, and E. Zojer, F4TCNQ on Cu, Ag, and Au as prototypical example for a strong organic acceptor on coinage metals, *Phys. Rev. B* **79**(16), 165306, doi:10.1103/PhysRevB.79.165306 (2009).

[513] H. Méndez, G. Heimel, A. Opitz, K. Sauer, P. Barkowski, M. Oehzelt, J. Soeda, T. Okamoto, J. Takeya, J.-B. Arlin, J.-Y. Balandier, Y. Geerts, N. Koch, and I. Salzmann, Doping of organic semiconductors: Impact of dopant strength and electronic coupling, *Angew. Chem. Int. Ed.* **52**(30), 7751, doi:10.1002/anie.201302396 (2013).

[514] H. Méndez, G. Heimel, S. Winkler, J. Frisch, A. Opitz, K. Sauer, B. Wegner, M. Oehzelt, C. Röthel, S. Duhm, D. Többens, N. Koch, and I. Salzmann, Charge-transfer crystallites as molecular electrical dopants, *Nat. Commun.* **6**, 8560, doi:10.1038/ncomms9560 (2015).

[515] P. K. Koech, A. B. Padmaperuma, L. Wang, J. S. Swensen, E. Polikarpov, J. T. Darsell, J. E. Rainbolt, and D. J. Gaspar, Synthesis and application of 1,3,4,5,7,8-hexafluorotetracyanonaphthoquinodimethane (F6-TNAP): A conductivity dopant for organic light-emitting devices, *Chem. Mater.* **22**(13), 3926, doi:10.1021/cm1002737 (2010).

[516] B. Lüssem, M. L. Tietze, H. Kleemann, C. Hoßbach, J. W. Bartha, A. Zakhidov, and K. Leo, Doped organic transistors operating in the inversion and depletion regime, *Nat. Commun.* **4**, 2775, doi:10.1038/ncomms3775 (2013).

[517] C. Brülke, T. Heepenstrick, N. Humberg, I. Krieger, M. Sokolowski, S. Weiß, F. S. Tautz, and S. Soubatch, Long vertical distance bonding of the hexagonal boron nitride monolayer on the Cu(111) surface, *J. Phys. Chem. C* **121**(43), 23964, doi:10.1021/acs.jpcc.7b06107 (2017).

[518] P. J. Blowey, L. A. Rochford, D. A. Duncan, D. Warr, T.-L. Lee, D. P. Woodruff, and G. Costantini, Probing the interplay between geometric and electronic structure in a two-dimensional K-TCNQ charge transfer network, *Faraday Discuss.* **204**, 97, doi:10.1039/C7FD00093F (2017).

[519] Q. Wang, A. Franco-Cañellas, P. Ji, C. Bürker, R.-B. Wang, K. Broch, P. K. Thakur, T.-L. Lee, H. Zhang, A. Gerlach, L. Chi, S. Duhm, and F. Schreiber,

Bilayer formation vs molecular exchange in organic heterostructures: Strong impact of subtle changes in molecular structure, *J. Phys. Chem. C* **122**(17), 9480, doi:10.1021/acs.jpcc.8b01529 (2018).

[520] B. Stadtmüller, M. Willenbockel, S. Schröder, C. Kleimann, E. M. Reinisch, T. Ules, S. Soubatch, M. G. Ramsey, F. S. Tautz, and C. Kumpf, Modification of the PTCDA-Ag bond by forming a heteromolecular bilayer film, *Phys. Rev. B* **91**(15), 155433, doi:10.1103/PhysRevB.91.155433 (2015).

[521] M. Gruenewald, C. Sauer, J. Peuker, M. Meissner, F. Sojka, A. Schöll, F. Reinert, R. Forker, and T. Fritz, Commensurism at electronically weakly interacting phthalocyanine/PTCDA heterointerfaces, *Phys. Rev. B* **91**(15), 155432, doi:10.1103/PhysRevB.91.155432 (2015).

[522] B. Stadtmüller, M. Gruenewald, J. Peuker, R. Forker, T. Fritz, and C. Kumpf, Molecular exchange in a heteromolecular PTCDA/CuPc bilayer film on Ag(111), *J. Phys. Chem. C* **118**(49), 28592, doi:10.1021/jp5078104 (2014).

[523] P. Borghetti, D. G. de Oteyza, C. Rogero, E. Goiri, A. Verdini, A. Cossaro, L. Floreano, and J. E. Ortega, Molecular-level realignment in donor–acceptor bilayer blends on metals, *J. Phys. Chem. C* **120**(11), 5997, doi:10.1021/acs.jpcc.5b11373 (2016).

[524] B. Stadtmüller, S. Schröder, F. C. Bocquet, C. Henneke, C. Kleimann, S. Soubatch, M. Willenbockel, B. Detlefs, J. Zegenhagen, T.-L. Lee, F. S. Tautz, and C. Kumpf, Adsorption height alignment at heteromolecular hybrid interfaces, *Phys. Rev. B* **89**(16), 161407(R), doi:10.1103/PhysRevB.89.161407 (2014).

[525] I. Kröger, B. Stadtmüller, C. Stadler, J. Ziroff, M. Kochler, A. Stahl, F. Pollinger, T.-L. Lee, J. Zegenhagen, F. Reinert, and C. Kumpf, Submonolayer growth of copper-phthalocyanine on Ag(111), *New J. Phys.* **12**, 083038, doi:10.1088/1367-2630/12/8/083038 (2010).

[526] C. Kleimann, B. Stadtmüller, S. Schröder, and C. Kumpf, Electrostatic interaction and commensurate registry at the heteromolecular F_{16}CuPc-CuPc interface, *J. Phys. Chem. C* **118**(3), 1652, doi:10.1021/jp411289j (2014).

[527] F. Schaefers, M. Mertin, and M. Gorgoi, KMC-1: A high resolution and high flux soft X-ray beamline at BESSY, *Rev. Sci. Instrum.* **78**(12), 123102, doi:10.1063/1.2808334 (2007).

[528] M. Gorgoi, S. Svensson, F. Schäfers, W. Braun, and W. Eberhardt, Hard X-ray high kinetic energy photoelectron spectroscopy at the KMC-1 beamline at BESSY, *Eur. Phys. J. Spec. Top.* **169**(1), 221, doi:10.1140/epjst/e2009-00996-5 (2009).

[529] M. Gorgoi, S. Svensson, F. Schäfers, G. Öhrwall, M. Mertin, P. Bressler, O. Karis, H. Siegbahn, A. Sandell, H. Rensmo, W. Doherty, C. Jung, W. Braun, and W. Eberhardt, The high kinetic energy photoelectron spectroscopy facility at BESSY progress and first results, *Nucl. Instr. Meth. Phys. Res. A* **601**(1–2), 48, doi:10.1016/j.nima.2008.12.244 (2009).

[530] M. Gorgoi, N. Mårtensson, and S. Svensson, HAXPES studies of solid materials for applications in energy and information technology using the HIKE facility at HZB-BESSY II, *J. Electron Spectrosc. Relat. Phenom.* **200**, 40, doi:10.1016/j.elspec.2015.05.005 (2015).

Acronyms

Materials

Ag	silver	
Au	gold	
Cu	copper	
CuPc	copper(II)-phthalocyanine	$C_{32}H_{16}N_8Cu$
DIP	diindenoperylene	$C_{32}H_{16}$
F4TCNQ	2,3,5,6-tetrafluoro-7,7,8,8-tetracyanoquinodimethane	$C_{12}F_4N_4$
F6TCNNQ	2,2'-(perfluoronaphthalene-2,6-diylidene)dimalononitrile	$C_{16}F_6N_4$
F4PEN	2,3,9,10-tetrafluoropentacene	$C_{22}H_{10}F_4$
NTCDA	1,4,5,8-naphthalene-tetracarboxylicacid-dianhydride	$C_{14}H_4O_6$
P2O	6,13-pentacenedione	$C_{22}H_{12}O_2$
P4O	pentacene-5,7,12,14-tetraone	$C_{22}H_{10}O_4$
PbS	lead sulfide	
PEN	pentacene	$C_{22}H_{14}$
Perylene	perylene	$C_{20}H_{12}$
PFP	perfluoropentacene	$C_{22}F_{14}$
PTCDA	3,4,9,10-perylene-tetracarboxylic-dianhydride	$C_{24}H_8O_6$
PTCDI	3,4,9,10-perylene-tetracarboxylic-diimide	$C_{24}H_{10}O_4N_2$
TAT	7,8,15,16-tetraazaterrylene	$C_{26}H_{12}N_4$
ZnO	zinc oxide	

Analysis techniques

AFM	atomic force microscopy
HAXPS/HXPS	hard X-ray photoelectron spectroscopy
IPES	inverse photoelectron spectroscopy
LEED	low-energy electron diffraction
NEXAFS	near edge X-ray absorption fine structure
NIXSW	normal-incidence x-ray standing wave
PES	photoelectron spectroscopy
PhD	photoelectron diffraction
STM	scanning tunneling microscopy
SXPS	soft X-ray photoelectron spectroscopy
UPS	UV photoelectron spectroscopy
XPS	X-ray photoelectron spectroscopy
XSW	X-ray standing wave

Concepts

BE	binding energy (also E_B)
CLS	core-level shift (also CS)
COM	conjugated organic molecule
CS	chemical shift
CT	charge transfer
d_H	adsorption distance
DFT	density functional theory
DOS	density of states
EA	electron affinity
EDC	energy distribution curve
ELA	energy level alignment
E_B	binding energy (also BE)
E_{Bragg}	Bragg energy
E_F	Fermi energy, Fermi level, Fermi edge
E_{kin}	kinetic energy
E_{Vac}	vacuum energy
f_H	coherent fraction
FWHM	full width at half maximum
HIB	hole injection barrier
HOMO	highest occupied molecular orbital
HR	high-resolution
IE	ionization energy
ID	interface dipole
IMFP	inelastic mean free path
LT	low temperature
LUMO	lowest unoccupied molecular orbital
ML	monolayer
OMBD	organic molecular beam deposition
P_H	coherent position
QCM	quartz crystal microbalance
RT	room temperature
SECO	secondary-electron cut-off
SIAS	surface-induced aromatic stabilization
vdW	van der Waals
UHV	ultra-high vacuum
WF	work function (also ϕ)
Y_P	photoelectron yield
ϕ	work function (also WF)

List of publications

1. J. Niederhausen, A. Franco-Cañellas, S. Erker, M. Oehzelt, T. Schultz, P. Amsalem, P. K. Thakur, K. Broch, D. A. Duncan, A. Zykov, S. Kowarik, T.-L. Lee, A. Gerlach, O. T. Hofmann, F. Schreiber an N. Koch, The structure of single-crystalline ZnO surfaces, *in preparation*.
2. A. Franco-Cañellas, J. Niederhausen, K. Broch, A. Hinderhofer, A. Greco, D. A. Duncan, P. K. Thakur,T.-L. Lee, A. Gerlach, S. Duhm, N. Koch and F. Schreiber, *in preparation*.
3. Q. Wang*, A. Franco-Cañellas*, P. Ji, C. Bürker, K. Broch, P. K. Thakur, T.-L. Lee, B. Wang, H. Zhang, A. Gerlach, L. Chi, S. Duhm and F. Schreiber, Bilayer Formation vs Molecular Exchange: Strong Impact of Subtle Changes in Molecular Structure, *J. Phys. Chem. C* **122**(17), 9480, doi:10.1021/acs.jpcc.8b01529 (2018).
4. A. Franco-Cañellas, Q. Wang, K. Broch, B. Shen, A. Gerlach, H. F. Bettinger, S. Duhm and F. Schreiber, Resolving intramolecular-distortion changes induced by partial fluorination of an hydrocarbon core adsorbed on Cu(111), *Phys. Rev. Materials* **2**(4), 044002, doi:10.1103/PhysRevMaterials.2.044002 (2018).
5. A. Franco-Cañellas, Q. Wang, K. Broch, D. A. Duncan, P. K. Thakur, L. Liu, S. Kera, A. Gerlach, S. Duhm and F. Schreiber, Metal-organic interface functionalization via acceptor end groups: PTCDI on coinage metals, *Phys. Rev. Materials* **1**(1), 013001(R), doi:10.1103/PhysRevMaterials.1.013001 (2017).
6. A. Yang*, A. Franco-Cañellas*, M. Sato, B. Wang, R.-B. Wang, H. Koike, I. Salzmann, P. K. Thakur, T.-L. Lee, L. Liu, S. Kera, A. Gerlach, K. Kanai, J. Fan, F. Schreiber and S. Duhm, Nitrogen substitution impacts organic-metal interface energetics, *Phys. Rev. B* **94**(15), 155426, doi:10.1103/PhysRevB.94.155426 (2016).
7. C. Bürker, A. Franco-Cañellas, K. Broch, T.-L. Lee, A. Gerlach, and F. Schreiber, Surface reactions studied with X-ray standing waves, *Diamond Annual Review 2014-/15* (2015).
8. F. Anger, H. Glowatzki, A. Franco-Cañellas, C. Bürker, A. Gerlach, R. Scholz, Y. Sakamoto, T. Suzuki, N. Koch and F. Schreiber, Interface Dipole and Growth Mode of Partially and Fully Fluorinated Rubrene on Au(111) and Ag(111), *J. Phys. Chem. C* **119**(12), 6769, doi:10.1021/jp511822g (2015).
9. C. Bürker, A. Franco-Cañellas, K. Broch, T.-L. Lee, A. Gerlach, and F. Schreiber, Self-Metalation of 2*H*-Tetraphenylporphyrin on Cu(111) Studied with XSW: Influence of the Central Metal Atom on the Adsorption Distance, *J. Phys. Chem. C* **118**(25), 13659, doi:10.1021/jp503046w (2014).

(*) These authors contributed equally.

Zusammenfassung

Organische Halbleiter sind auf Kohlenstoff basierende Materialen mit vielversprechenden funktionalen Eigenschaften, die drauf ausgerichtet sind, ihre anorganischen Gegenspieler zu ersetzen und/oder zu ergänzen (z.B. Silizium). Sie können günstig hergestellt werden, sie sind flexibel und ihre Eigenschaften können chemisch abgestimmt werden –alles für die Verbraucherelektronik attraktive Eigenschaften. Schon jetzt sind Smartphones und Fernsehgeräte mit organischen LED erhältlich. Zudem wurden interessante Prototypen organischer "roll-up" Solarzellen bereits vorgestellt. Dennoch steht der Durchbruch dieser Materialien noch bevor, da grundlegende Aspekte bezüglich (nicht nur) des Ladungstransportes immer noch die gesamte Effizienz einschränken. In diesem Zusammenhang beeinflusst die Angleichung der Energie-Niveaus zwischen den Molekülen und der Elektrode die Ladungsinjektionen/Energiegewinnung und ist deshalb für einen optimalen Ladungstransfer durch die Grenzfläche verantwortlich. Eine gezielte Beeinflussung des "Energy-level alignment" (ELA) erfordert eine vollständige Beschreibung der Grenzflächeneigenschaften: sowohl der elektronischen und chemischen als auch der strukturellen Adsorptionsabstände bzw. der molekulare Verzerrung. Chemische Funktionalisierung der Polymere oder kleinerer Moleküle durch die Ergänzung von Seitengruppen mit starken elektronischen Donator- oder Akzeptorverhalten stellt einen Weg dar, um das ELA zu optimieren. In der vorliegenden Arbeit verwenden wir elementspezifische Techniken wie Röntgenphotoelektronenspektroskopie (XPS) und stehende Röntgenwellen (XSW), um zu untersuchen, wie eine Substitution von Stickstoff und Fluor in prototypischen und gut untersuchten π-konjugierten organischen Molekülen die geometrischen, chemischen und elektronischen Eigenschaften dieser Moleküle beeinflusst, wenn diese sich auf Metall-Einkristall-Substraten mit unterschiedlicher Reaktivität anlagern. Wir zeigen, dass die Kombination von hochauflösenden XPS mit XSW Messungen eine leistungsfähige Methode ist, um diesem Problem beizukommen, da die Adsorptionsdistanz und molekulare Distorsion problemlos mit veränderten Features im XPS-spektrum verbunden werden können, wie z.B. die Satellitenstruktur, Verbreiterung oder Peakverschiebung. Insbesondere untersuchen wir die Adsorption von Perylene und Pentacene Derivaten auf unterschiedlichen Oberflächen aus Metall und Halbleitern, und zwar die (111) Oberflächen von Gold, Silber und Kupfer und die polaren (000$\pm$1) Oberflächen von Zinkoxid (ZnO). Schließlich zeigen wir zudem, dass diese Methode erfolgreich ausgeweitet werden kann, um die Entwicklung der bloßen ZnO Oberfläche unter bestimmten Verfahren in Echtzeit zu untersuchen. ZnO ist ein vielversprechender transparenter anorganischer Halbleiter, der leicht in unterschiedlichen Nanostrukturen hergestellt werden kann. Zu seinen unterschiedlichen Oberflächen gibt es noch viele offene Fragen, da die Struktur der Oberflächen immer noch zur Diskussion steht, zusammen mit dem Vorhandensein möglicher Relaxationen. Mit der chemischen und strukturellen Information stellen wir neue Ergebnisse über das gesamte Oberflächenverhalten und unterschiedliche Präparationsbedingungen zur Verfügung.

Acknowledgements

I would like to use the last pages of this thesis to thank all the people that helped to make it possible.

As there is no other way, I start thanking Prof. Frank Schreiber for giving me the opportunity to do my PhD in his group, for his inspiring supervision and trust. I am also grateful to Prof. Martin Oettel for agreeing to serve as the second reporter.

I want to especially thank Dr. Alexander Gerlach for his inestimable help, advice and patience, without him this work would not have been the same.

Also, a very warm thank you goes for Prof. Steffen Duhm. I have learned a lot through our numerous discussion and collaborations. I also appreciate his invitation to visit him in Suzhou. In the same terms, I want to very much thank Dr. Jens Niederhausen for his valuable help with the ZnO business, his support during numerous beamtimes and long email discussions. I also want to acknowledge our collaborators Dr. Marcus Scheele, Prof. Bettinger, Dr. Oliver T. Hofmann and Simon Erker for giving me the opportunity to work and learn with and from them.

The experiments at the beamline I09 of the Diamond Light Source have been a fundamental part of this work and their success was made possible by the excellent facilities and the inestimable support of its staff, Dr. Tien-Lin Lee, Dr. Pardee Kumar Thakur, Dr. David A. Duncan and Dave McCue. It was a great pleasure working with them. I also want to acknowledge all the people who accompanied us during the beamtimes, especially JProf Katharina Broch, Dr. Christoph Bürker and Dr. Alexander Hinderhofer. I use the opportunity to thank Qi Wang for her help with the UPS and LEED measurements.

I would like to thank my colleagues at the Soft Matter group, especially Soeren Claas, Christoph Bürker and Falk Anger, who enormously helped me at the beginning. I am also indebted to all the proof-readers, especially Clemens Zeiser and Miriam Klopotek, and Frau Maurer and Frau Rotschke for their help during all these years with administrative work. Also, I would like to praise Bernd Hofferberth and Bernhard Degel for their highly appreciated help with the in-house experimental setup.

Last but definitely not least, I would like to thank all the marvelous people that I have met during this time in Tübingen. Without you it would not have been the same. This work is also yours. The dearest and last thank you goes to Tabea Heitz and to my family and friends back at home, you have always walked this journey with me.

Per haver suspès física a la Sele encara hem arribat prou lluny.